PENNSTATE

DEPARTMENT OF METEOROLOGY

Final Report

Numerical Study of the Role of Shallow Convection in Moisture Transport and Climate

Grant No. NAG8-1530

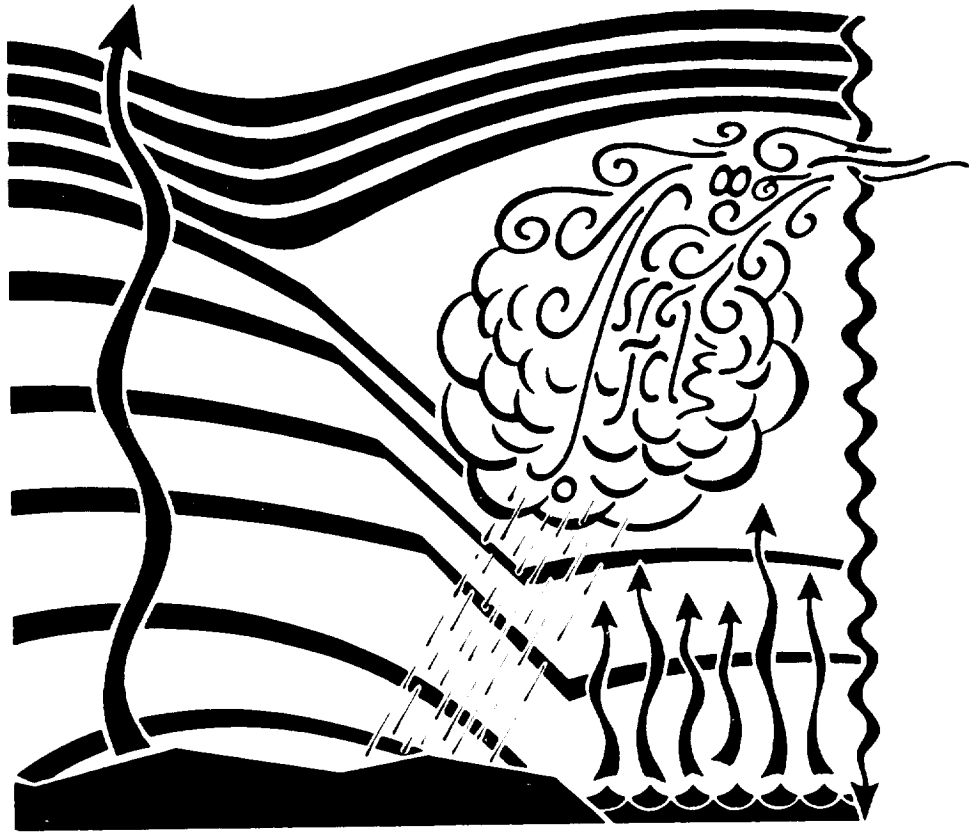

By:
Nelson L. Seaman, P.I.
David R. Stauffer, Co-P.I.
And
Ricardo C. Munoz

Final Report
for

NUMERICAL STUDY OF THE ROLE OF SHALLOW CONVECTION ON MOISTURE TRANSPORT AND CLIMATE

NOAA/NASA Joint GEWEX/GCIP Program
Grant No. NAG8-1530

1 June 1998 - 31 May 2001-12-05

Sumitted to:

Dr. James Arnold
Global Hydrology and Climate Center
NASA
320 Sparkman Drive
Huntsville, AL 35805

By

Nelson L. Seaman, P.I.
David R. Stauffer, Co-P.I.
and
Ricardo C. Munoz

The Pennsylvania State University
Department of Meteorology
502 Walker Building
University Park, PA 16802

Ph.: 814-863-1583
Fax: 814-865-3663
Email: seaman@ems.psu.edu

December 10, 2001

EXECUTIVE SUMMARY

The **objective** of this investigation was to study the role of shallow convection on the regional water cycle of the Mississippi and Little Washita Basins of the Southern Great Plains (SGP) using a 3-D mesoscale model, the PSU/NCAR MM5. The underlying premise of the project was that current modeling of regional-scale climate and moisture cycles over the continents is deficient without adequate treatment of shallow convection.

At the beginning of the study, it was hypothesized that an improved treatment of the regional water cycle can be achieved by using a 3-D mesoscale numerical model having high-quality parameterizations for the key physical processes controlling the water cycle. These included a detailed land-surface parameterization (the Parameterization for Land-Atmosphere-Cloud Exchange [PLACE] sub-model of Wetzel and Boone, 1995), an advanced boundary-layer parameterization (the 1.5-order turbulent kinetic energy [TKE] predictive scheme of Shafran et al., 2000), and a more complete shallow convection parameterization (the hybrid-closure scheme of Deng et al., 2002a,b) than are available in most current models. PLACE is a product of researchers working at NASA's Goddard Space Flight Center in Greenbelt, MD. The TKE and shallow-convection schemes are the result of model development at Penn State.

The long-range goal is to develop an integrated suite of physical sub-models that can be used for regional and perhaps global climate studies of the water budget. Therefore, the work plan focused on integrating, improving, and testing these parameterizations in the MM5 and applying them to study water-cycle processes over the SGP. These schemes have been tested extensively through the course of this study and the latter two have been improved significantly as a consequence.

The work conducted in this study provided the first insertion of the PLACE scheme into the MM5v3 model (the latest version of the MM5). The result is a fully coupled comprehensive parameterization of land-surface processes (PLACE) in the MM5 mesoscale model. Care has been taken to ensure appropriate initialization of the surface fields and definition of parameters. An offline PLACE system forced by observations was constructed and refined for this study to initialize 3-D MM5-PLACE. Extensive analysis of model results was performed against ARM-CART and Oklahoma Mesonet data. Utilization of MM5 with PLACE for a summer convective case has shown that the coupled model better captured the spatial distribution of moisture in the boundary layer. The observed west-east gradient in afternoon surface-layer moisture across Oklahoma was reproduced by the PLACE-MM5 runs, but not by the simpler force-restore Slab model within MM5. Based on fine-scale data for the subgrid soil-moisture heterogeneity, we have shown that it has a positive impact in the computation of surface fluxes of water vapor and sensible heat.

It was found through extensive testing in 3-D and 1-D frameworks that the PLACE land-surface scheme performed at about the same level of accuracy as other land-surface schemes used to represent the surface fluxes over the Great Plains in normal operations. In some cases, PLACE was able to perform better than alternative schemes. However, in many situations, it was found that a more simple force-restore land-surface contained originally in the Blackadar boundary layer parameterization (Zhang and Anthes 1982), known as the Blackadar slab scheme, generally provided about the same level of skill or better. Thus, while the results of MM5-PLACE simulations were as good or better than any others known to be done with PLACE, it proved difficult to show an overall clear advantage when PLACE is used.

The underlying reason for this result is attributed mostly to the uncertainty involved in defining many of the key soil and vegetation parameters that must be defined in order to run PLACE. Even with the best soil-characteristic data sets currently available, such as the State Soil Geographical Database (STATSGO), PLACE produced soil-moisture evolutions that did not always agree well with soil-moisture measurements over the Great Plains. Work is currently underway at Penn State to evaluate MM5-PLACE during July 1997 using ESTAR soil moisture and NDVI-based leaf-area index and vegetation fraction.

The 1.5-order TKE-predicting turbulence scheme of Shafran et al. (2000) worked reasonably well in dry (unsaturated) conditions, but was found to have deficiencies in saturated layers. A reformulation was introduced that now accounts for the effects of saturation on the calculations in the buoyancy-production term of the turbulent kinetic energy equation, the stability parameters and turbulent length scales. This saturation dependency is missing in many current numerical models. The change allows the turbulence sub-model to generate more intense mixing in clouds, especially near cloud tops where the longwave radiative flux divergence can cause intense cooling. The consequence of this improvement is a more realistic thermodynamic and moisture structure in cloudy layers and better representation of fog layers.

Extensive evaluations and testing of the shallow-cloud parameterization also were conducted in the course of this investigation. It was found that this convection sub-model contained several layer-dependent formulations for some key quantities related to the cloud-base mass flux. In particular, the discrete thickness of the model layers tended to cause a discontinuous behavior of the mass-flux calculations that sometimes led to erratic behavior of the convection scheme. This behavior occurred even for vertical configurations that are considered to be very good for 3-D models (e.g., layer thicknesses of only ~40 m in the boundary layer and

the cloud layer). Further work led to changes in the formulations of the shallow convection scheme so that the dependency on discrete layer thickness was reduced or eliminated. The consequence was that the key quantities of the shallow-convection scheme, including mass flux and detrainment rates, now evolve in a generally smooth manner as the clouds develop and grow. Not only does the reformulation provide a more realistic shallow-cloud structure, but it also makes the evolution of calculated water-budget terms smoother and much easier to interpret.

Following the extensive testing of each individual parameterization, several combined experiments were conducted in the 3-D MM5 using PLACE or the Blackadar slab land-surface scheme, and the improved versions of the PSU 1.5-order TKE-predicting turbulence scheme and shallow-convection scheme. These experiments showed that the MM5 can produce fairly realistic distributions of shallow convective cloud fields in stratocumulus and fair-weather cumulus (humilis) conditions. Cloud area and liquid water content are reasonable and are within the accuracy expected, given typical uncertainties in the initial atmospheric and soil states. The vertical structure for the resolved-scale temperature and moisture fields in the cloud layer appear to evolve in a generally realistic way, although further testing is required.

The coupling of the PLACE-MM5 model with the new PSU shallow convection scheme in MM5 and applied to the same case has shown that we are able to include in our simulations important physical interactions that control the development of convection over land (cloud-radiative interactions, cloud-surface interactions, and cloud-boundary layer interactions). This evaluation of the complete 3-D modeling system in a complex convective situation over land has also suggested several improvements that are being tested in the new parameterizations, especially in the shallow convection and turbulence sub-models. We have shown that, as we are able to incorporate more physically realistic interactions in our model system, the accuracy of

each sub-model must be increased. Otherwise there is a possibility that the simulations may diverge from the observations even more rapidly than without the inclusion of these physical processes. However, our results also suggest that the inclusion of these complex physical interactions is crucial if one wants to better simulate the development and evolution of convection over land.

Due to the extensive development, testing and refinement work related to improving the key parameterizations used in this study, it was impossible to perform as many 3-D experiments with the finished system as were originally intended. We had expected to conduct and evaluate MM5 runs for 1-3 months in the summertime environment in the Southern Great Plains (SGP), but had to restrict the experimentation to two cases in April and July of 1997. Now that the parameterizations have been enhanced, it is recommended that future numerical work be conducted to expand the testing to seasonal time scales so that meaningful water budgets can be calculated over the SGP.

Publications resulting from NOAA/NASA support under Project NAG8-1530:

Deng, A., N.L. Seaman and J.S. Kain, 1998: A Parameterization for Detraining Cumulus-Cloud Mass into Dissipating Layer Clouds. 12th AMS Conference on Numerical Weather Prediction, January 11-16, Phoenix, Arizona, 120-123.

Deng, A., 1999: A shallow convection parameterization scheme for mesoscale models. Ph. D. Thesis, The Pennsylvania State University, 152 pp.

Deng, A.J., N.L. Seaman and J.S. Kain, 1999: Evaluation of the Penn State Shallow Convection Scheme in the Marine Atmosphere Using the ASTEX First Lagrangian Experiment. 9th PSU/NCAR Mesoscale Model Users' Workshop. Boulder, CO, 23-25 June, 116-119.

Seaman, N.L,, A.J. Deng, and J.S. Kain, 1999: Evaluation of the Penn State Shallow Convection Scheme Over Land. 9th PSU/NCAR Mesoscale Model Users' Workshop. Boulder, CO, 23-25 June, 164-167.

Stauffer, D.R., R.C. Munoz and N.L. Seaman, 1999: In-Cloud Turbulence and Explicit Microphysics in the MM5. 9th PSU/NCAR Mesoscale Model Users' Workshop. Boulder, CO, 23-25 June, 177-180.

Deng, A., N.L. Seaman, and A.M. Lario-Gibbs, 2000: A Shallow Convection Scheme for 3-D Regional Scale Air Quality Applications. 11th Conf. on Applications of Air Pollution Meteorology with A&WMA. AMS, Long Beach, CA, 9-14 January, 102-106.

Munoz, R., D.R. Stauffer and N.L. Seaman, 2000a: Use of a water-tracer modeling methodology to characterize the atmospheric water budget along North-Central Chile. 6th Int'l. Conf. On S. Hemi. Meteor. And Oceanography., AMS, Santiago, Chile, 3-7 April, 220-221.

Munoz, R.C., D.R. Stauffer and N.L. Seaman, 2000b: Treatment of buoyancy production at a cloudy-clear interface in a TKE model. 14th AMS Symp. on Bound. Layer and Turbulence. Aspen, CO, 7-11 Aug., 62-65.

Munoz, R.C., J.C. Wyngaard and D.R. Stauffer, 2000: Morning transition of the temperature profile close to the surface. 14th AMS Symp. on Bound. Layer and Turbulence. Aspen, CO, 7-11 Aug., 198-201.

Stauffer, D.R., B.P. Reen, and R.C. Munoz, 2000: Modeling atmospheric boundary layer structure during SGP-97. 10th PSU/NCAR Mesoscale Model Users' Workshop. Boulder, CO, 23-25 June, 44-48.

Deng, A., N.L. Seaman, D.R. Stauffer and R.C. Munoz, 2001: Application of the PSU shallow convection parameterization scheme in 3-D environments. 9th AMS Conf. on Meso. Proc., Ft. Lauderdale, FL, 30 July - 2 Aug., 50-54.

Lynn, B.H., D.R. Stauffer, P.J. Wetzel, W.-K. Tao, P. Alpert, N. Perlin, R.D. Baker, R. Munoz, A. Boone and Y. Jia, 2001: Improved simulation of Florida summer convection using the PLACE land model and a 1.5-order turbulence parameterization coupled to the Penn State/NCAR mesoscale model. *Mon. Wea. Rev.*, **129**, 1441-1461.

Munoz, R.C., N.L. Seaman, D.R. Stauffer and A. Deng, 2001: Modeling the interaction between boundary layer and shallow clouds using a TKE and a shallow convection parameterization. 9th AMS Conf. on Mesoscale Proc.., Ft. Lauderdale, FL, 30 July - 2 Aug., 26-30.

Reen, B.P., D.R. Stauffer, K.J. Davis and A.R. Desai, 2001: On the added value of high-resolution remotely sensed soil moisture data in a mesoscale model. 9th AMS Conf. on Mesoscale Proc.., Ft. Lauderdale, FL, 30 July - 2 Aug., J129-J133.

Stauffer, D.R., R.C. Munoz, and N.L. Seaman, 2001: On the importance of saturation effects in the turbulence scheme of a mesoscale model. 9th AMS Conf. on Mesoscale Proc., Ft. Lauderdale, FL, 30 July - 2 Aug., 1-5.

Munoz, R.C., N.L. Seaman, D.R. Stauffer and A. Deng, 2001: Sensitivities of shallow cloud fields to environmental and surface variables in the new PSU shallow convection scheme. NASA GSFC Cumulus Parameterization Workshop, Greenbelt, MD, 3-5 Dec., 16 pp.

Deng, A., N.L. Seaman and J.S. Kain, 2002a: A shallow-convection parameterization for mesoscale models. Part I: Sub-model description and preliminary applications. Submitted to, *J. Atmos. Sci.*, **59**, 36 pp.

Deng, A., N.L. Seaman and J.S. Kain, 2002b: A shallow-convection parameterization for mesoscale models. Part II: Verification and sensitivity study. Submitted to, *J. Atmos. Sci.*, **59**, 35 pp.

CONTENTS

1. INTRODUCTION

1.1 Objective

The **objective** of this investigation was to study the role of shallow convection on the regional water cycle of the Mississippi and Little Washita Basins using a 3-D mesoscale model, the PSU/NCAR MM5. The underlying premise of the project was that current modeling of regional-scale climate and moisture cycles over the continents is deficient without adequate treatment of shallow convection.

It was hypothesized that an improved treatment of the regional water cycle can be achieved by using a 3-D mesoscale numerical model having a detailed land-surface parameterization, an advanced boundary-layer parameterization, and a more complete shallow convection parameterization than are available in most current models. The methodology was based on the application in the MM5 of new or recently improved parameterizations covering these three physical processes. Therefore, the work plan focused on integrating, improving, and testing these parameterizations in the MM5 and applying them to study water-cycle processes over the Southern Great Plains (SGP):

(1) the Parameterization for Land-Atmosphere-Cloud Exchange (PLACE) described by Wetzel and Boone (1995),

(2) the 1.5-order turbulent kinetic energy [TKE]-predicting scheme of Shafran et al. (2000), and

(3) the hybrid-closure sub-grid shallow convection parameterization of Deng (1999).

Each of these schemes has been tested extensively through this study and the latter two have been improved significantly to extend and their capabilities.

1.2 Background

The summertime regional-scale water budget over continents is an important factor in the overall global water cycle. Although horizontal transport in numerical models is relatively straightforward, improvement of vertical transports, especially for moisture, represents a crucial need. Summer regimes in middle latitudes generally do not exhibit the strong dynamical forcing and large-scale vertical motion fields common in winter cyclones. Instead, vertical moisture transport is highly dependent on radiation-driven sub-grid scale physical processes (Dickinson 1995). These include land-surface fluxes, boundary layer turbulent processes, and both shallow and deep convection.

Modeling of regional-scale climate and moisture cycles is incomplete without adequate treatment of shallow convection (Dickinson 1995, Wetzel and Boone 1995), which strongly affects the surface fluxes, the upper boundary of the mixed layer and the development of convective precipitation. Shallow convection is defined here as the process by which air parcels become saturated, such that non-precipitating, buoyancy-driven clouds form, dissipate, and interact with their environment. Although shallow convective clouds can form at any level in the atmosphere, our attention is confined to the layer near the top of the planetary boundary layer, where these clouds are most often observed. Shallow convection includes both cumulus and

stratocumulus clouds types of various depths and area coverage, and may involve both water and ice phases.

Despite the acknowledged importance of shallow convection in moisture transport and climate studies, it is often treated in a relatively simply manner in regional and global-scale numerical models. For example, Betts and Miller (1986) employ a simple adjustment scheme that drives the environment toward a pre-determined state, but does not provide many details of the cloud structure. In addition, their approach for shallow convection appears to be best adapted to the tropical marine environment. Seth and Giorgi (1996) studied how organized mesoscale circulations induced by vegetation can affect vertical transports of heat and moisture. Using a regional-scale climate-adapted version of the hydrostatic MM4 model (RegCM2), they found important effects on monthly precipitation resulting from land-surface heterogeneity. However, their model treats the effects of shallow clouds only in a very crude sense. This could be a serious omission because of the strong influence these clouds have on the radiation budget and vertical moisture transport.

Although shallow convection produces very little (if any) precipitation and does not affect its environment nearly as much or as rapidly as deep precipitating convection, its effects are not trivial. Shallow convection can be important for altering local and regional-scale precipitation patterns and the structure of temperature, water vapor, and mixing depth in the turbulent boundary layer. In a similar way, shallow-cloud patterns and their area coverage are affected by horizontal heterogeneity in the land-surface processes, even over fairly small areas (Wetzel and Boone 1995, Wetzel et al. 1996). Shallow convection at the top of the mixed layer can act as a sink for boundary-layer moisture, while transporting water, aerosols and chemical species into the middle troposphere. Shallow clouds also have an impact on subsequent

convective precipitation by changing the environmental temperature and moisture structure in which deep clouds must grow. By using up some of the convective available potential energy (CAPE) of boundary-layer air, shallow convection can delay or in some cases even prevent the onset of deep convection. In other cases convection could occur sooner due to pre-conditioning of the environment.

1.3 Organization

Section 2 documents the shallow-convection parameterization, which is the central sub-model needed for this investigation. This parameterization, developed by Deng (1999) is currently under review for publication (Deng et al. 2002a,b), so its design is presented here to assist in understanding the work carried out through this study. The PLACE land-surface scheme and the TKE-predicting turbulence scheme already have been described in the literature by Wetzel and Boone (1995) and Shafran et al. (2000), so it is unnecessary to repeat those descriptions here.

Next, Section 3 describes the most important 1-D experimentation conducted in this study, using a single column model (SCM) based on the vertical structure of the MM5 model, and the offline (stand-alone) PLACE methodology used to initialize the 3-D MM5 PLACE. This 1-D framework proved very helpful for understanding and refining the parameterizations for turbulence and shallow convection. Section 4 describes the 3-D numerical experiments carried out in the MM5 and discusses the implications of the model results. Finally, Section 5 summarizes what has been learned through this study and some of the most important work remains for the future.

2. THE SHALLOW CONVECTION PARAMETERIZATION

The Kain-Fritsch (1990) deep-convection scheme is the progenitor for the present shallow-cloud development. In the Kain-Fritsch (KF) scheme, if a cloud updraft fails to reach a critical depth necessary to support rain (i.e., shallow cloud only), it is assumed to disappear without having any impact at all on its environment. Here, we seek especially to describe how those shallow clouds grow and interact with their surroundings. The major elements of the shallow-cloud scheme are:

- definition of initial cloud-parcel characteristics and the convective trigger mechanism;
- a convective-cloud sub-model based on the parcel buoyancy equation,
- closure assumptions that determine the cloud-base mass flux; and
- a prognostic scheme for the area and water content of clouds that result from the detrainment of the convective-updraft air.

The cloud parameterization is designed to represent the physical linkage between the turbulent *planetary boundary layer* (PBL) and moist convective processes in a multi-layer framework. We define the PBL as the layer beginning at the surface and extending upward to the point where surface-based turbulence rapidly decreases with height. Although the top of this layer can be identified in a model by the drop-off in turbulent kinetic energy, it also tends to be characterized by a sharp jump in the potential temperature. Thus, it can be distinguished from the *cloud-topped boundary layer* (CTBL) discussed by some investigators (e.g., Albrecht 1979, Agee 1987), which includes the PBL plus a shallow-cloud layer having distinctly different stability characteristics.

We assume that shallow convective clouds consist of active updrafts and (approximately) *neutrally buoyant clouds* (NBCs). The NBCs represent either the remnants of previous updrafts or the cloud mass dispelled from currently active updraft cores. This production of NBCs from

detrained updraft air is consistent with the conceptual model of shallow convection presented by Wyant et al. (1997). The most vigorous convective updrafts generally cover less than 10% of a grid area, while the associated NBCs may cover a much greater fraction of the sky. Although the shallow updrafts are assumed to produce no rain, the NBCs may generate some light precipitation. In general, most of the updraft mass is detrained near the cloud tops as it reaches or overshoots the equilibrium level. Over time, this detrainment process and the consequent induced subsidence can change or even dominate the thermal and moisture structure of the mesoscale environment. If the shallow-cloud updraft exceeds a critical depth (defined as D_{KF} = 4 km in this application), it is considered to transition to deep convection (thunderstorm), often with heavy precipitation and strong moist downdrafts (Kain and Fritsch 1990). On the other hand, under conditions with a strong capping inversion and large vertical moisture flux, the detrainment process can lead to an accumulation of vapor and detrained cloud mass at the inversion base, so that a solid stratus deck may develop. Thus, the shallow convection can have a direct link to both resolved stratiform cloud and sub-grid deep convective cloud, both of which can be active precipitation generators. In many 3-D models, representation of the physical relationships among these three types of cloud is weak at best.

2.1 Cloud-Parcel Initial Characteristics

The parameterization is built as a one-dimensional column sub-model. Active cloud updrafts are triggered when parcels originating in the PBL are able to reach their *lifting condensation level* (LCL). The characteristics of a potential cloud-initiating parcel are defined by its virtual potential temperature, θ_{vp}, water-vapor mixing ratio, q_{vp}, and vertical velocity. The values of θ_{vp} and q_{vp} for the parcel are defined at each time step from the average ambient values of the model layers in the lowest 20% of the PBL or in the lowest two model layers, whichever is deeper. The underlying assumptions are that energetic turbulent eddies are initiated near the surface and that the largest (and most buoyant) of these rise with only modest dilution through the entire PBL to approach or reach their LCL. The LCL for these parcels is calculated according to the method of Fritsch and Chappell (1980) and may lie below or above the PBL top.

In theory, an ensemble of shallow clouds could be created by defining different parcels with initial characteristics based on a probability distribution about θ_{vp} and q_{vp}, but that approach has not been introduced here.

Following eddy-transport theory, we hypothesize that these cloud-forming parcels have positively correlated thermal, moisture and vertical velocity perturbations. The eddy vertical velocity, w_T, is scaled to the maximum turbulent kinetic energy (TKE) in the PBL according to

$$w_T = \sqrt{\frac{2}{3} \cdot TKE_{MAX}} \,, \tag{2.1}$$

where the constant $2/3$ results from the TKE definition, assuming that the turbulence is isotropic. We then define the release height of the cloud-initiating parcel, z_R, to be the lower of two levels: the top of the PBL (h_{PBL}) or the LCL. The total vertical velocity of the cloud-initiating parcel is estimated as $w_P = \overline{w} + w_T$, where $\overline{w}$ is the resolved-scale vertical motion at z_R. The TKE is calculated using a 1.5-order turbulence scheme (Gayno 1994, Shafran et al. 2000). Typically, in a weakly forced marine boundary layer w_T is only ~0.1-0.3 $\mathrm{m\,s^{-1}}$. Over land in a shear-driven nocturnal boundary layer, w_T may grow to ~0.3-0.8 $\mathrm{m\,s^{-1}}$, while during the afternoon in a convectively unstable boundary layer it can easily reach ~1-2 $\mathrm{m\,s^{-1}}$. If a cloud-initiating parcel fails to reach the LCL, it is assumed to return to its point of origin in the PBL without affecting the environment.

Additional factors (e.g., sub-grid terrain irregularity or land-use variability) also may contribute to the parcel vertical velocity in certain cases, but most of these are ignored at present. However, nonhydrostatic pressure-gradient forces beneath strong deep-cloud updrafts (Schlesinger 1984), w_{NH}, are considered when the cloud depth, D_c, becomes greater than the critical Kain-Fritsch depth, D_{KF} = 4 km. In this case, w_{NH} is defined as a simple function of $w(z_{1000})^{\tau-1}$, which is the parcel vertical velocity at 1 km above the cloud base from the previous time step, according to

$$w_{NH} = \begin{cases} 0.15 \cdot [w(z_{1000})^{\tau-1} - w_P] & \text{if } w(z_{1000})^{\tau-1} - w_P > 0 \text{ and } D_C > D_{KF} \\ 0 & \text{otherwise} \end{cases} \qquad (2.2)$$

The parameter 0.15 in (2.2) yields a magnitude of w_{NH} in the range $0.5 < w_{NH} < 1.5 \text{ m s}^{-1}$ when deep convection is present. The total parcel vertical velocity at z_R, therefore, is given by:

$$w_R = \overline{w} + w_T + w_{NH} = w_P + w_{NH} \qquad (2.3)$$

If the cloud-initiating parcel reaches the LCL, a convective-cloud updraft forms. Its subsequent acceleration and mixing with the environment are calculated using the entraining-detraining cloud model of Kain and Fritsch (1990). The entrainment rate at any level is a function of the radius of the updraft, R_C, and the local parcel buoyancy with respect to its environment. While the Kain-Fritsch deep-convection scheme assumes a constant updraft radius of 1.5 km, the shallow-convection scheme allows the radius R_C to grow smoothly from a minimum of $R_{C\min} = 0.15 \text{ km}$ to a maximum of $R_{C\max} = 1.50 \text{ km}$, which occurs when the shallow convection transitions to deep precipitating convection.

For our purposes, we assume that the most significant factors controlling R_C are the depth of the boundary layer, h_{PBL}, and the depth of the cloud ($D_C = z_T - z_B$, where z_T is the height of cloud top and $z_B = LCL$ is the cloud-base height). The calculation of the cloud depth is described below in Section 2.2. For simplicity all updrafts in a grid cell are considered to have equal radius and depth at a given time. This uniform geometry is convenient, although an ensemble of different cloud sizes would be more realistic (e.g., Siebesma and Cuijpers 1995). The dependency of R_C on boundary layer depth is assumed to be greatest for comparatively shallow cloud depths and shallow boundary-layer depths. These basic assumptions are approximated in the following relationship for the cloud-updraft radius (when $D_C < D_{KF}$).

$$R_C = \frac{b - \sqrt{b^2 - 12\eta h_{PBL}}}{4} \quad \text{and} \quad R_{C\min} \le R_C \le R_{C\max} \qquad (2.4)$$

where $b = \frac{7 + 2\eta h_{PBL}}{2}$, $\eta = \frac{12 D_C}{4 - D_C}$, and R_C, D_C and h_{PBL} are in km. Figure 2.1.1 demonstrates the relationship between R_C, D_C and h_{PBL} given by (2.4). For deep boundary layers notice that even fairly shallow clouds have large radii, while for very shallow boundary layers, the clouds must become quite deep before large radii develop. When $D_C \geq D_{KF}$, $R_C = 1.5\text{km}$ and thermodynamic control is passed to the KF deep convection scheme, which includes convective rainfall and moist downdraft development. Obviously, the specific values used in this formulation are somewhat arbitrary, but the distributions appear to be qualitatively consistent with reality. The application of R_C was most effective when averaged over 2-3 time steps.

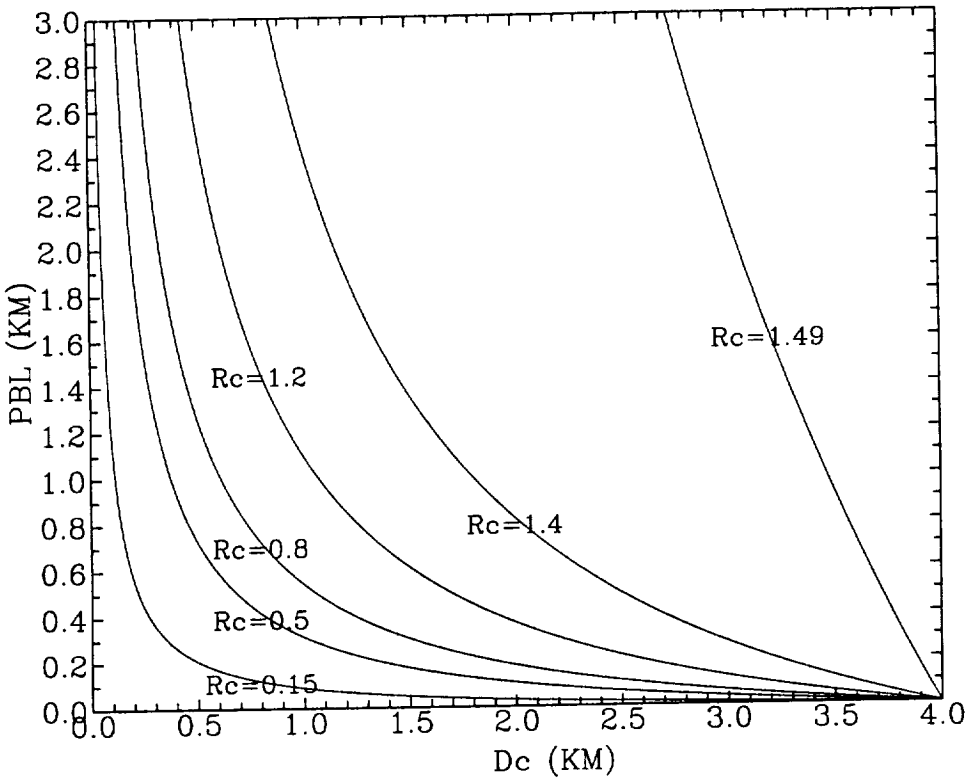

Figure 2.1.1. Relationship between updraft radius (R_C , km), PBL height (h_{PBL} , km) and cloud depth (D_C , km).

2.2 The Convective-Cloud Sub-Model

As mentioned in Section 2.1, the KF 1-D entraining-detraining cloud model is used to calculate the updraft vertical velocity and liquid-water profiles based on the parcel buoyancy equation. Unlike KF, however, clouds are not assumed to grow instantly to their mature equilibrium level as soon as a cloud is triggered. Here, the cloud top grows at a rate proportional to the maximum vertical velocity of the updraft, $W_{\max}$, estimated to be

$$\frac{dz_T}{dt} = 0.2 \cdot W_{\max} \tag{2.5}$$

until the equilibrium level is reached. The empirical factor 0.2 imposes a reasonable cloud growth rate (e.g., see Simpson 1983), so that under deep-convection conditions, it usually takes 20-30 minutes to reach the tropopause from the level of free convection (LFC). This approach allows detrainment from the growing cloud top to moisten the environment, which is oversimplified in the instantaneous cloud growth of the KF scheme. The interpretation of the 0.2 factor is that cloud-top growth is slowed because the updraft must push aside environmental air to continue its upward progress, while the parcel buoyancy equation merely describes the cloud's velocity profile in its full-grown state.

Although the thermal and moisture characteristics of the cloud-forming parcel are defined from the lowest 20% of the PBL (Section 2.1), its mass is taken directly from the sub-cloud layers nearest to the cloud base. The depth of this updraft source layer, D_S, grows as a function of the updraft radius from a minimum of 100 m to a maximum of 600 m, according to

$$D_S = d_1 + 1000(R_C - R_{C\min})/d_2 \tag{2.6}$$

with the constraint $D_S \le h_{PBL}$ and where $d_1 = 100\,\text{m}$ and $d_2 = 2.7$. Thus, as clouds grow wider and deeper they are expected to have greater mass flux at cloud base and are likely to entrain air from a deeper sub-cloud layer. To satisfy continuity requirements, subsidence is induced in the cloud environment to compensate for the mass extracted from the PBL source layer. If the cloud remains "shallow", ($D_C < D_{KF}$), no sub-grid scale convective downdrafts are allowed to form, so all compensation for the upward mass flux must occur through this subsidence mechanism.

It should be noted that, although the growth of the updrafts occurs gradually, there is still only one size of clouds allowed in a particular grid column in the present formulation. That is, unlike the atmosphere, we do not attempt at this time to represent an ensemble of cloud sizes, as has been done for deep convection by Arakawa and Schubert (1974).

2.3 Cloud Updraft Closure Assumptions

The cloud-base mass flux closure is adopted to determine the intensity of sub-grid convection from resolved-scale quantities. The grid-cell mass flux at cloud base is defined as:

$$\mu_B = N(\pi R_C^2 \rho w_B) \tag{2.7}$$

where N is the number of updrafts in the cell, w_B is the parcel vertical velocity at cloud base, ρ is the parcel air density (here, R_C is in m). Generally, closure requires that either μ_B or N must be specified to allow the other quantity to be diagnosed. Of course, for any scheme, errors may occur in the calculation of N, R_C, or w_B, but the key is to estimate μ_B with reasonable accuracy so as to simulate realistic measurable cloud-field characteristics (e.g., cloud fraction, depth, liquid-water path length, etc.). Moreover, as stated above, we have made the simplifying assumption that all shallow clouds in a grid cell have the same geometry, rather than use a more realistic distribution of cloud sizes. Thus, the calculations for N and R_C, in particular, should not be considered literal, but merely provide a qualitative estimate needed for the mass flux calculations.

As part of the preliminary development of the updraft module for the shallow-convection scheme, five different mass-flux closure assumptions were tested. Brief descriptions and comments about these closures are as follows:

2.3.1 Boundary-Layer Vapor Balance (BLVB)

Used by Tiedtke (1989) to simulate subtropical trade cumuli, this closure assumes total water vapor in the PBL is constant (in the absence of rain). That is, the rate of vapor removal from the PBL by cloud-base updrafts is balanced by the sum of surface evaporation and

entrainment flux at the PBL top. Thus, N_1 (the number of cloud updrafts for the BLVB closure) can be diagnosed from (2.7) by defining $q_v\mu_B$ as the sum of these two fluxes. Although the BLVB closure was found to be reasonable for many marine environments, it greatly underestimated the cloud-base mass flux in continental applications (not shown) and therefore was eliminated from further consideration.

2.3.2 *Convective Available Potential Energy (CAPE) Removal*

This closure assumes that total cloud-base mass flux proceeds at a rate necessary to stabilize the column over a deep-convective time period, which is generally about 30 minutes (Fritsch and Chappell 1980, Kain and Fritsch 1990). Similar to the BLVB closure, the CAPE-Removal closure diagnoses the number of updrafts in the grid cell, N_2, from (2.7) using the CAPE-derived μ_B. The CAPE closure often works poorly in shallow-convection environments where the cloud depths are about 1 km or less (i.e., there is little or no CAPE in the shallow-cloud layer). Nevertheless, it is still attractive for cases in which most of the shallow cloud lies above the LFC. Application of N_2 was found to be most effective when averaged over ~15 time steps.

2.3.3 *Boundary-Layer Depth (BLD) Relationship*

This closure assumes that the number of updrafts for a shallow-convection environment, N_3, is a direct function of the scale of the largest, most-energetic turbulent eddies in the PBL. Thus, N_3 depends on the depth of that layer. Since the maximum amplitude of the eddy vertical velocity spectra occurs at wavelength $\sim 1.5h_{PBL}$ (Young 1987), we hypothesize that under convective conditions, this geometry can be used to estimate the distribution and number of cloud-initiating updrafts in a grid cell according to

$$N_3 = \frac{\Delta X \Delta Y}{(1.5h_{PBL})^2} \tag{2.8}$$

where $\Delta X \Delta Y$ is the grid-cell area. The total mass flux, μ_B, can then be calculated from (2.7). A similar closure has been used by other investigators to study boundary-layer rolls (Stull 1988), so (2.8) could be modified for use in strongly sheared environments. The BLD closure was tested in both continental and marine environments and found to be suitable for fairly shallow cloud depths (D_C < 2 km). However, it sometimes caused large oscillations in the mass flux due to feedbacks between h_{PBL}, N_3 and μ_B.

2.3.4 TKE-Based Closure

This closure operates on the assumption that shallow clouds basically are driven by the TKE in the PBL. Specifically, it scales the shallow-cloud mass flux by the magnitude of the maximum diagnosed TKE in the layer. The closure requires that we define four quantities: M_S, an upper bound on the amount of mass that can be processed by the shallow clouds (given as the total mass in the updraft source layer at the time the scheme is called); τ_{SC}, a characteristic relaxation time scale; and TKE_U, and TKE_L, which are upper and lower bounds on the TKE used for the mass-flux calculations. The relaxation time scale is defined as $\tau_{SC} = b_1(D_S / w_B)$, where D_S is the depth of the updraft source layer, w_B, is the cloud-base updraft velocity, and b_1 = 4.5 is an empirical constant. Then, letting TKE_S be the maximum diagnosed TKE in the source layer and setting the constraints TKE_L, = 1.0 J kg^{-1} and TKE_U = 10.0 J kg^{-1}, we obtain

$$TKE_1 = \begin{cases} TKE_L & for \quad TKE_S < TKE_L \\ TKE_S & for \quad TKE_L \le TKE_S \le TKE_U \\ TKE_U & for \quad TKE_S > TKE_U \end{cases}, \tag{2.9}$$

where TKE_1 becomes the effective maximum value of TKE in the source layer. Given these reasonable constraints, the maximum mass flux that could occur is given by

$$\mu_B(\max) = \frac{M_S}{\tau_{SC}} \tag{2.10}$$

and the actual mass flux given by the closure becomes

$$\mu_B = (\frac{TKE_1}{TKE_U})\mu_B(\max). \tag{2.11}$$

For this closure the number of clouds in the grid cell can be recovered from the cloud-base mass flux as $N_4 = \mu_B/\mu_{BS}$, where (2.7) defined the single-cloud mass flux as $\mu_{BS} = \pi R_C^2 \rho w_B$.

To interpret (2.11), let us describe the *"shallow-convection period"* to be the time required for N_4 updrafts to remove all of the mass from the source layer, M_S, (and assuming no compensating mass flux into the layer). Then, (2.10) and (2.11) reveal that when $TKE_I = TKE_U$ (i.e., when $TKE_S \geq 10.0$ J kg^{-1}), the shallow-convection period equals τ_{SC}; however, when $TKE_I < TKE_U$ (the normal condition), mass removal occurs more slowly by the factor TKE_U/TKE_I. For example, in a typical convectively unstable continental environment, we might find that $TKE_I \sim$ 2.0 J kg^{-1}, $w_B \sim 1.15$ m s^{-1} and D_S is ~300 m. Thus, the relaxation time scale indicating the shortest period for processing all mass in the source layer is $\tau_{SC} \sim 0.33$ h, but because TKE_I is not sufficient to support the maximum mass flux, the actual shallow-convection period is ~1.67 h. However, in a weakly forced marine environment where the prevailing sensible heat flux is often < 10 Wm^{-2}, it is common for $TKE_S < 1.0$ J kg^{-1}. In this situation, we may find D_S ~200 m and $w_B \sim 0.25$ m s^{-1}, so the relaxation time scale is $\tau_{SC} \sim 1$ h, while the shallow-convection period becomes ~10 h. Tests of the TKE-based closure showed it to operate well for most shallow clouds ($D_C < 2$ km), while it damped most of the feedback oscillations that were characteristic of the BLD closure.

2.3.5 Hybrid Closure

Since the TKE-based closure was found to work well for fairly shallow convective clouds and the CAPE-removal closure was found to work better for deeper clouds (D_C approaching D_{KF}), a simple *hybrid closure* is proposed to represent the intermediate range of cloud depths. When cloud tops are above the LFC, but have depths less than D_{KF} (which describes a large percentage of convective cases), the clouds are assumed to be in transition from the TKE-based closure to the CAPE-removal closure. A simple linear averaging is used in this case, although refined transition functions could be hypothesized. First, the number of updrafts is calculated according to each of the two closures (N_2 and N_4). Then, the final number of updrafts is

estimated based on the fraction of the cloud depth that lies above the LFC relative to the distance between the LFC and the height D_{KF} above cloud base, given by

$$N = fN_2 + (1-f)N_4 \tag{2.12}$$

where $f = h_3/h_1$ is a ratio of two length scales (km), such that $h_3 = D_C - h_2$, $h_1 = D_{KF} - h_2$. Here, $h_2 = z_{LFC} - z_B$, and z_{LFC} is the height of the LFC. Normally, $N_2 < N_4$, because the CAPE-removal closure hypothesizes that stabilization of a deep cloud layer occurs rather rapidly as a result of a few vigorous updrafts. This agrees with the general observation that the number of growing clouds in an area decreases as their size (depth and width) increases due to compensating subsidence in the cloud environment.

To summarize, the shallow-convection parameterization may use any of three mass-flux closure assumptions (type 2, 4 or 5), determined by D_C, z_T and z_{LFC}, according to

$$\begin{array}{ll} z_T \le z_{LFC} & \rightarrow \text{TKE - based closure only} \\ z_T > z_{LFC} \text{ and } D_C < D_{KF} & \rightarrow \text{Hybrid closure} \\ D_C \ge D_{KF} & \rightarrow \text{CAPE - removal closure only} \end{array} \tag{2.13}$$

which provides a smooth transition from one closure to another as the cloud depth grows. It also should be remembered that the uniform updraft geometry used in the present formulation represents a simplification, while the atmosphere typically exhibits an ensemble of cloud depths (see Sec. 2.2). Using LES, Siebesma and Cuijpers (1995) showed that a variety of cloud sizes contributes to a reduction in the updraft mass flux with height. While this effect is not considered in the present version of the parameterization, their LES results suggest that the updraft mass flux could perhaps be modified to account for a distribution of cloud sizes.

2.4 Prognostic Scheme for Neutrally Buoyant Cloud Fraction and Cloud Water

Most cloud parameterizations designed for the mesoscale consider only deep convection in detail. In these schemes, detrained cloudy air generally is fed back directly to the resolved scale, where it evaporates immediately until the grid-cell saturates (e.g., Kain and Fritsch 1993). This "all-or-nothing" approach for post-convective layer-cloud formation is an oversimplification and can have negative impacts on other aspects of model performance, such as radiative

processes and latent heating. In deep thunderstorms, large detrainment rates near the tropopause often cause a small to moderate-sized grid cell (DX ≤ 25 km) to saturate quite rapidly, so that little damage is done by neglecting sub-grid layer clouds. However, in the case of smaller shallow clouds, it may take many hours (if ever) for detrained cloud water to saturate a layer.

A more realistic representation is to detrain convective cloud mass from updrafts into a class of sub-grid clouds having nearly neutral buoyancy (e.g., Wyant et al. 1997). Once the detrained updraft air becomes part of these sub-grid NBCs, it can spread as layer clouds, initiate light precipitation, or slowly evaporate into the sub-saturated grid volume. While some existing schemes have attempted to treat this detrained cloud mass in large-scale models (e.g., Tiedtke 1989, 1993), they often rely on a moisture-balance closure and so may not be versatile enough for both continental and marine environments.

2.4.1 Basic Equations

The mass-conserving equations for the rate of change of sub-grid cloud area (a) and cloud water/ice content (l_c) for the NBCs are given by:

$$\frac{\partial a}{\partial t} = S_a + D_a - \vec{v} \cdot \nabla_H a - w\frac{\partial a}{\partial z} \tag{2.14}$$

$$\frac{\partial l_c}{\partial t} = S_l + D_{mix} + D_{pre} + D_{ics} + D_{CTEI} - \vec{v} \cdot \nabla_H l_c - w\frac{\partial l_c}{\partial z} \tag{2.15}$$

Here, S_a and S_l are sources of cloud area and condensed water content ejected from convective updrafts, respectively. The term D_a (dissipation of cloud area) represents evaporation due to mixing at the sides of the cloud; D_{mix} is the depletion of water liquid/ice content due to vertical mixing; D_{pre} is water depletion due to precipitation (drizzle); D_{ics} is a depletion rate contributed by an ice settling process and D_{CTEI} is water depletion due to cloud-top entrainment instability. The horizontal and vertical advection terms are represented by $-\vec{v} \cdot \nabla_H \chi$ and $-w\partial\chi/\partial z$, where χ is either l_c or a. The grid-averaged condensed water content (l) is related to the sub-grid

NBC water content (l_c) according to $l = al_c$. When a = 1.0 (saturated conditions), then $l = l_c = q_c$, where q_c is the model's explicit (resolved-scale) cloud-water mixing ratio.

2.4.2 *Formation of Neutrally Buoyant Clouds*

Convection produces a variety of clouds either directly, such as cumulus and cumulonimbus, or indirectly, such as stratocumulus and anvils. A realistic parameterization for clouds of convective origin, but which have nearly neutral buoyancy, is obtained by considering their source to be condensates produced in sub-grid cumulus updrafts (active convective clouds) and later detrained at the sub-grid scale into the non-convective environment. The following equations represent the source terms for the sub-grid NBCs described in (2.14) and (2.15):

$$S_a = -\tilde{w}\frac{\partial a}{\partial z} + \frac{R_{ud}}{M_L} \tag{2.16}$$

$$S_l = \left(\frac{\partial l}{\partial t} - l_c S_a\right)\Big/ a \tag{2.17}$$

where

$$\frac{\partial l}{\partial t} = -\tilde{w}\frac{\partial l}{\partial z} + \frac{R_{ud}}{M_L} l_u \tag{2.18}$$

$\tilde{w}$ is the convection-induced sub-grid-scale subsidence, R_{ud} (kg [air] s^{-1}), is the updraft detrainment rate from the parcel-buoyancy scheme, and M_L(kg) is total mass of air in a grid cell for a given model layer. The liquid/ice water content in the updraft core is given by l_u. Note that the volume of detrained updraft air increases the area of the NBC (a), while its liquid water content (l_c) is solved as a residual term in (2.17) to satisfy the mass-conservation constraint $l = al_c$.

2.4.3 *Evaporation of Clouds*

In (2.14) and (2.15), there are several processes through which the NBC can dissipate. Following Tiedtke (1993), the area decreases through cloud-edge evaporation, according to

$$D_a = -\frac{a}{l_c} K(q_s - q_v) \tag{2.19}$$

where $K = 10^{-5}$ s^{-1} is a horizontal diffusion coefficient; and q_v and q_s are the resolved-scale specific humidity and saturation specific humidity, respectively. This yields a dissipation time scale on order of a day for $l_c = 1.0$ g kg^{-1} air. The dissipation rate becomes significantly greater, however, when the cloud water content becomes small ($l_c < 0.1$ g kg^{-1} air). Thus, in effect, this term accounts for the final dissipation of clouds from which most of the condensate has already been depleted by other processes.

2.4.4 Depletion of Water Liquid/Ice Content by In-Cloud Mixing Processes

Cloud water in the sub-model can be mixed downward (but not upward) inside the NBC by vertical diffusion induced by turbulence and radiation flux divergence, given by

$$D_{mix} = \frac{1}{a}\frac{\partial}{\partial z}[(K_v + K_r)\frac{\partial(al_c)}{\partial z}] \tag{2.20}$$

where K_v is the local diffusion coefficient derived from the TKE. The additional radiation-induced diffusion coefficient is given by

$$K_r = \frac{l_B^2}{\theta}[\left|\frac{\partial\theta}{\partial t}\right|_{LW}\left|\frac{\Delta z_T}{15}\right| + \left|\frac{\partial\theta}{\partial t}\right|_{SW}\left|\frac{\Delta z_T}{50}\right|] \tag{2.21}$$

where K_r is a maximum at the cloud top and decreases linearly downward over a maximum cloud depth of 1000 m. In (2.21), l_B is the Blackadar length scale provided by the turbulence scheme (Shafran et al. 2000), θ is the potential temperature of the environmental air and Δz_T is the model layer thickness at cloud the top. The terms $\left.\frac{\partial\theta}{\partial t}\right|_{LW}$ and $\left.\frac{\partial\theta}{\partial t}\right|_{SW}$ are the longwave cooling rate at cloud top and the daytime solar heating just below cloud top, respectively, provided by the radiation scheme. This K_r term would be unnecessary if very high vertical resolutions were possible, but in typical mesoscale models with $\Delta z_T \geq 50$ m, it accounts for radiation-induced turbulence occurring at scales that too small to be represented accurately by K_v, which is derived from grid-resolved quantities in the turbulence scheme.

Cloud water also can evaporate into clear air at the exposed cloud base through the same vertical diffusion terms. The finite-differenced form of these diffusion terms is one-sided so that the water flux is downward only, while mixing into layers above the cloud is prohibited. These vertical mixing terms become the most important water depletion process when the liquid/ice content is in the range of $0.1 < l_c < 0.5$ g kg^{-1}, where neither sub-grid precipitation (Sec. 2.4.5) or horizontal diffusion processes (Sec. 2.4.3) are effective.

2.4.5 Precipitation Processes

Precipitation can form in the NBCs through auto-conversion and accretion, exactly as for resolved-scale layer clouds. Here, we use the simple water/ice cloud scheme of Dudhia (1989), without a mixed phase, for which auto-conversion begins at $l_c > 0.5g$ kg^{-1} (a similar threshold exists for initiating auto-conversion of ice, based on activation of ice nuclei below 273 K). It is feasible to introduce a mixed-phase explicit precipitation scheme for use with the shallow-cloud scheme, but that is not done here. Also, cloud-ice particles are assumed to fall slowly through an ice-settling process described by Grell et al. (1994). The ice settling prevents long-term retention of low-density cirrus clouds that are unable to produce significant snowfall rates.

2.4.6 Cloud-Top Entrainment Instability (CTEI)

Deardorff (1980) proposed that shallow clouds can dissipate through a mechanism called cloud-top entrainment instability (CTEI). If a parcel of dry air is entrained into the cloud top, it induces mixing and evaporation. As a result, the density of the parcel may become greater than (θ_v less than) that of surrounding cloudy air, causing unstable acceleration of the parcel downward through the cloud. The depletion rate of the cloud liquid due to the CTEI, following Deardorff, is parameterized as

$$D_{CTEI} = -10^{-4} \frac{r - r_{\min}}{r_{\max} - r_{\min}} l_c \qquad (2.22)$$

Deardorff (1980) shows that $r = \Delta h / L\Delta(q_v + l_c)$, where the moist static energy is given by $h = C_P T + gz + Lq_v$, Δh represents the jump of h across the cloud top, $\Delta(q_v + l_C)$ is the jump of total water across the cloud-top, L is the latent heat of vaporization, and C_P is the specific heat at constant pressure. In (2.22) r_{min} and r_{max} are CTEI initiation criteria given by Deardorff (1980) and MacVean and Mason (1990). If $r \le r_{min}$, then r is set equal to r_{min} and the depletion rate goes to zero; if $r \ge r_{max}$ then r is set equal to r_{max}, which gives the maximum depletion rate, $-10^{-4} l_C$ kg kg^{-1} s^{-1}. Because CTEI-induced downdraft cooling is expected to be confined to the upper portion of the cloud layer (Randall 1980), the depletion due to CTEI is applied only in the uppermost 100 m of the NBC.

Deardorff (1980) originally proposed CTEI as a possible dominant mechanism for the breakup and evaporation of a stratus deck. Although subsequent observational and modeling research has suggested that this is generally not the case, the process is included in the NBC sub-model as a contributing factor for cloud water depletion.

3. EXPERIMENTATION IN A SINGLE COLUMN MODEL

3.1 The 1-D MM5

The initial testbed for the shallow-convection parameterization has been a 1-D version of the Penn State/NCAR mesoscale model (MM5), which is based on the non-hydrostatic numerical framework of the 3-D parent model (Grell et al. 1994). In addition to the shallow-convection scheme, the 1-D model contains a full set of MM5 physical parameterizations, including a 1.5-order turbulence sub-model (Shafran et al. 2000), an explicit moisture scheme (Dudhia 1989) that predicts resolved-scale liquid/ice cloud and precipitation, and a two-stream broadband column radiation sub-model (Dudhia 1989). The land-surface scheme can be chosen to be either

the Blackadar Slab model or PLACE. As discussed in Sec. 2, it also contains the KF (1990) deep convection parameterization. Moreover, the user can specify 3-D large-scale dynamical tendencies, such as advection and subsidence. Of these, the interaction between the shallow convection and radiation requires special note.

To function correctly with the shallow convection sub-model, the radiation scheme must be applied separately to the sub-grid clear and cloudy areas of the column. Like many other schemes, however, Dudhia's radiation assumes that a grid cell is either totally clear or totally cloudy. Furthermore, the shallow-cloud area predicted by (2.14) is a function of height. To solve this problem efficiently, the column's sub-grid NBC is partitioned into three idealized parts (see Fig. 3.1.1): (1) clear throughout the model depth, (2) sub-grid upright cloud through the full depth of the convective layer (often this is a fairly small fraction of the grid area), and (3) broad stratiform sub-grid cloud (often near the top of the convective updraft, referred to here as the "anvil" for convenience). The radiation-induced thermal tendencies are calculated and applied separately to each fraction of the cell area. The convective updraft is detrained completely into the NBC after each time step, and so does not contribute to the radiation tendencies. Deng (1999) gives details of the methodology used for the sub-grid partitioning represented in Figure 3.1.1.

If the partitioned sub-grid cloud areas 2 and 3 in the figure ($\overline{a}_2$ and $\overline{a}_3$) were used directly for the radiation calculations, however, the true cloud effects would be underestimated. The "effective" cloud fraction (i.e., the area as viewed from above) must be somewhat greater than the idealized distribution of Fig. 3.1.1 because (2.14) implicitly assumes that clouds in adjacent layers always have the maximum possible overlap in the vertical. While this maximum-overlap assumption gives a reasonable first guess for clouds of convective origin, it is not likely

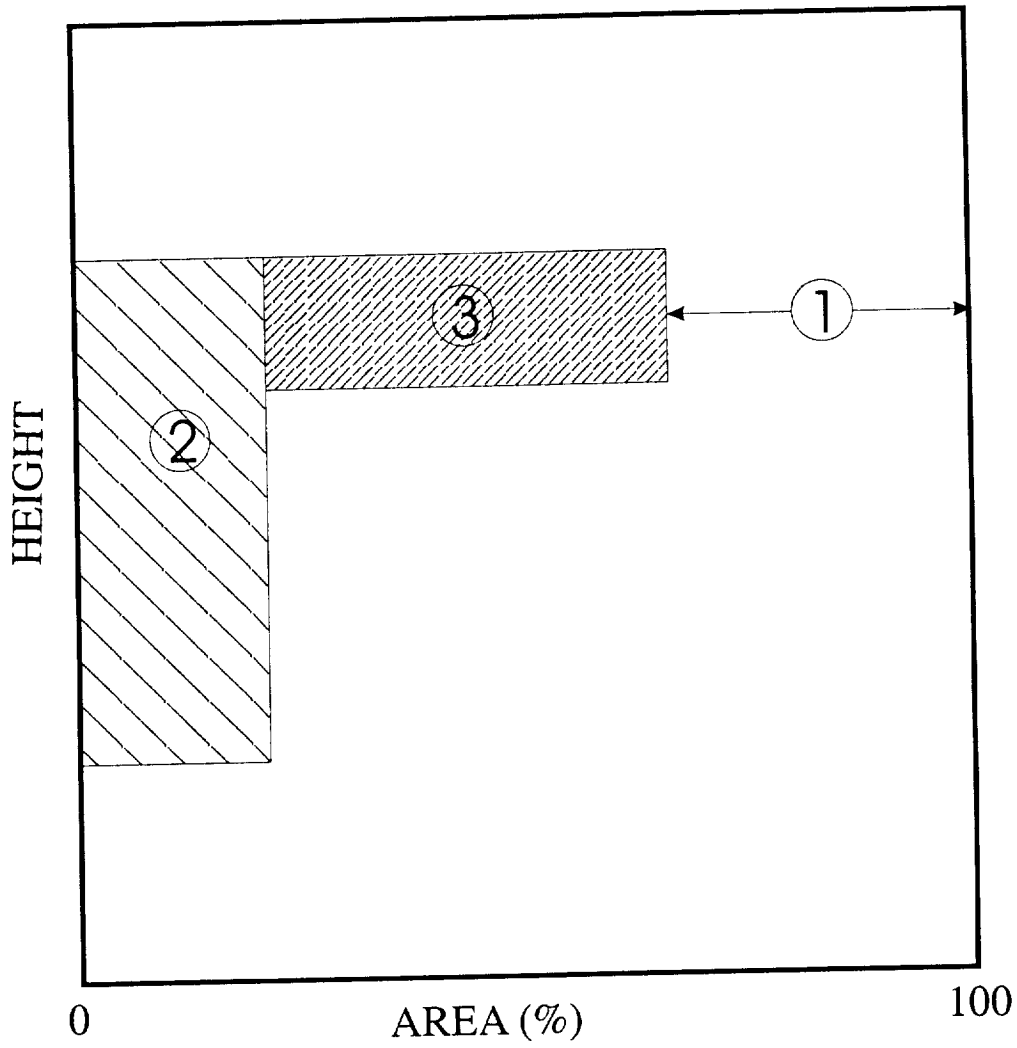

Figure 3.1.1. Schematic diagram showing idealized partition of NBC in a grid column into (1) clear, (2) upright cloud, and (3) anvil cloud.

to be accurate because in nature many dissipating NBCs are no longer linked vertically by an active updraft. An additional fractional area, a_s, is postulated to be a function of the environmental relative humidity, RH, so that the total or "effective" cloud fraction, a_e, can be written as

$$a_e = (1-a)a_s + a \tag{3.1}$$

where a is the fraction predicted using (2.14). Following Xu and Randall (1996), the additional fraction, a_s, is parameterized according to

$$a_S = RH^{\alpha_1}[1-\exp(\frac{-\alpha_3(l_c+q_c)}{[(1-RH)q_S]^{\alpha_2}})] \quad \text{if } RH<1 \tag{3.2}$$

where $a_S = 1$ if $\mathrm{RH} \geq 1$ and α_1, α_2 and α_3 are empirical constants defined as 0.25, 0.49 and 100, respectively. Note that the cloud liquid/ice content used in (3.2) appears as the sum of the cloud liquid/ice at the sub-grid scale, l_c, and the resolved scale, q_c. However, when a layer becomes saturated, l_c converts into q_c, while $q_c = 0$ when the layer is sub-saturated, so only one of these two quantities can actually be non-zero at a given time.

As a brief example, Fig. 3.1.2 shows the resultant area of effective cloud, a_e (thin solid curve), in a marine stratocumulus case where the maximum predicted cloud area from (2.14) is $a_{\max} = 0.44$ (shaded region) and $RH_{\max} = 0.93$ (heavy solid curve) at 1451 m. Notice that, in the cloud layers with lower relative humidity (~0.85-0.90), the effective cloud fraction is only about 5-10% greater than the calculated NBC fraction. However, near the cloud top, where the relative humidity is greatest, a_e exceeds the NBC fraction by nearly 40%.

The surface radiation flux, R_S, (for either LW or SW flux) is given by

$$R_S = \overline{a}_{e2}R_2 + \overline{a}_{e3}R_3 + (1-\overline{a}_{e2}-\overline{a}_{e3})R_{clr} \tag{3.3}$$

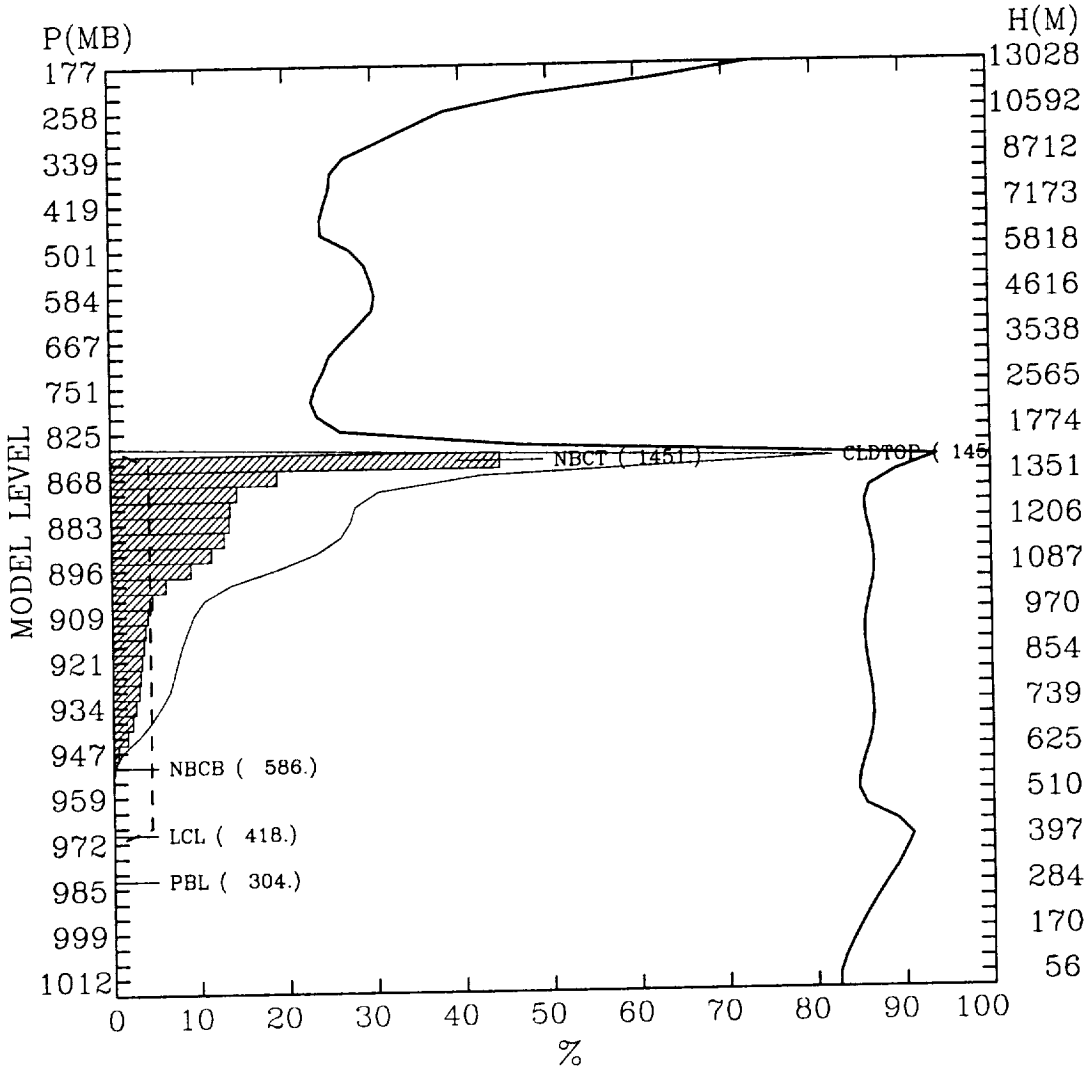

Figure 3.1.2. Model-predicted cloud fraction (%) and resolved-scale relative humidity, RH (%), versus pressure (mb) and height (m) at 1200 UTC, 11 June 1992 (Hour 5) for ASTEX at 28.00°N, 24.22°W. Shading indicates NBC fraction (%), the dashed line is the area of shallow-cloud updraft (%), the thin solid curve is the effective cloud area for radiation calculations (%), and the heavy curve is RH (%). LCL denotes the lifting condensation level, PBL is the boundary layer top, CLDTOP is top of updraft, and NBCT and NBCB are the top and base of NBCs, respectively.

where $\overline{a}_{e2}$ and $\overline{a}_{e3}$ are the vertically averaged effective cloud fractions and R_2 and R_3 are the surface fluxes contributed from the sub-grid upright and anvil portions of the NBC, respectively. The term R_{clr} is the surface flux contributed by the clear portion of the grid element. Finally, Fig. 3.1.3 presents the evolution of the surface radiation fluxes for each of these three sub-grid components and the net grid-averaged surface radiation determined by (3.3) for three days during the same marine stratocumulus case (11-14 June 1992) from which Figure 3.1.2 is taken.

Naturally, calling the Dudhia (1989) radiation sub-model three times for each grid cell to account for sub-grid cloud effects involves extra calculations, compared to the usual approach when there are no sub-grid clouds. The added computational load due to the multiple applications of the radiation module can be offset in part by not calling the scheme each time step. It should be sufficient to call it about once every 10-15 minutes, unless the cloud field is changing very rapidly. Furthermore, multiple calls to the radiation module could be avoided, in principle, by developing an equivalent grid-averaged representation for the radiative properties of the sub-grid cloudy and clear portions of the column. However, this latter concept is more complex than merely spreading the sub-grid cloud water horizontally across the grid cell. Such an approach is beyond the scope of the present study.

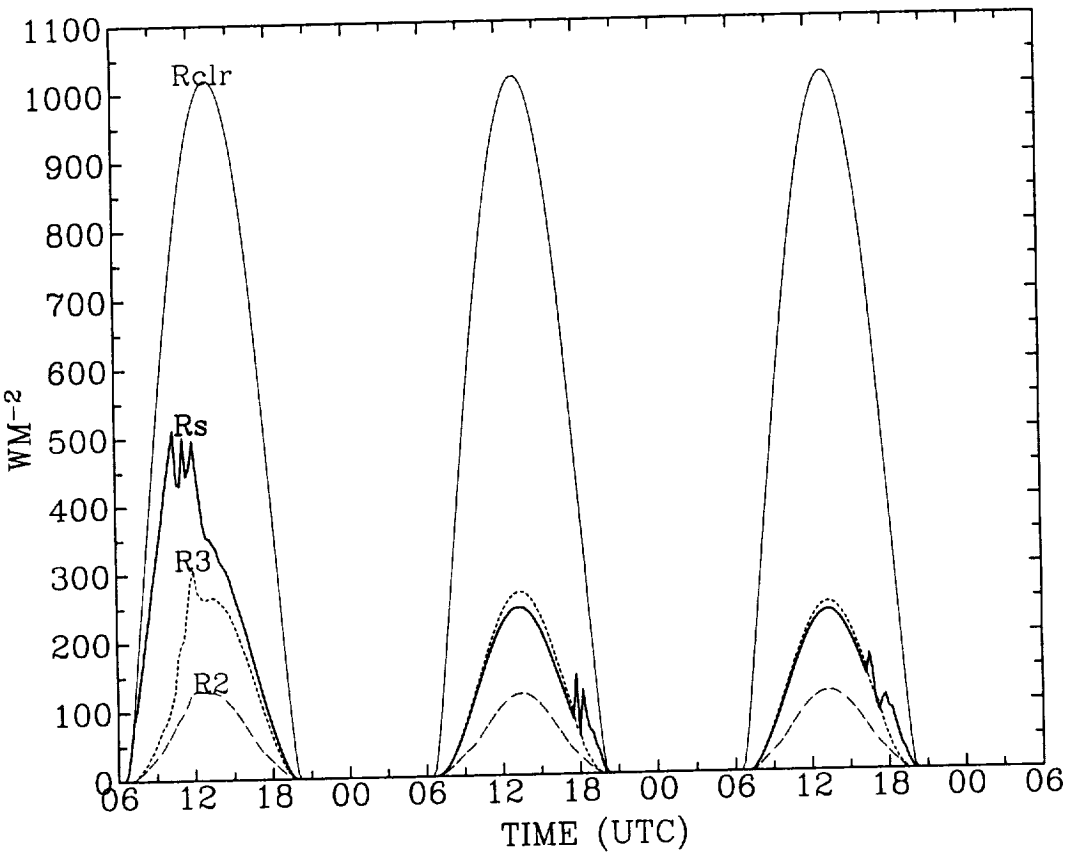

Figure 3.1.3. Model surface solar fluxes for 0600 UTC, 11 June to 0600 UTC, 14 June 1992 for ASTEX at 28.00°N, 24.22°W. Thin solid line is the clear-sky solar flux (R_{clr}), dashed line is the solar flux for upright cloud (R_2), dotted line is solar flux for the anvil cloud (R_3), and heavy solid line (R_S) is the area-weighted average flux.

3.2 Offline (Stand-Alone) Experiments with PLACE

3.2.1 Introductory Remarks

We describe in this section the offline (stand-alone) PLACE-related work for this study. The offline version of the PLACE model was forced by meteorological observations (rather than an atmospheric model) to create the initial conditions for the 3-D coupled MM5-PLACE simulations discussed in Section 4. The objectives of this work were (1) to produce realistic and consistent initial fields for the soil variables required by the coupled 3-D MM5-PLACE model, and (2) to examine the overall performance of PLACE over a large domain and over a long period when forced with analyzed data and using currently available characterizations of soil and vegetation fields. This offline PLACE modeling system and its results are described below.

3.2.2 Model Description

The stand-alone version of PLACE was constructed starting from the real-time Soil Hydrology Model (SHM) modeling framework already available at Penn State (Smith et al. 1994). The SHM system produced an archive of analyzed meteorological fields that had been used to feed the SHM model in real time for several years, including the summer of 1997, which is the period that we have focused on for testing and application of the MM5-PLACE model. The available fields provided by the SHM archive are 12-h precipitation, daily cloudiness, daily values of wind speed and indirect measures of temperature and humidity. In order to produce a more realistic representation of the diurnal cycle in the forcing, the SHM-preprocessor programs were re-run to construct meteorological forcings every three hours for wind speed, air

temperature, water mixing ratio and surface pressure. A simple radiative model, also from the SHM, is used to calculate radiative forcings for PLACE based on the cloud fields.

Figure 3.2.1 shows a schematic of the PLACE stand-alone model. Whenever possible the surface characterization fields and parameters used in the stand-alone runs were the same as those available in the standard MM5V3 modeling system, so that the results could be used directly as initial conditions in the coupled MM5-PLACE model runs. The next subsection compares the analyzed forcing fields with available measurements in the main area of interest.

3.2.3 Verification of the Forcings

The most important forcing for a land-surface model is precipitation. In Fig. 3.2.2a, we compare for the month of July 1997 the time series of daily precipitation amounts averaged over 110 Oklahoma Mesonet Stations with the analyzed precipitation amounts coming from the SHM-real-time system, for the grid points closest to the station locations. (The Mesonet data were acquired through another related NASA grant to study the effects of surface heterogeneity during the Southern Great Plains 1997 [SGP97] study period). Conventional analyses were not available for days 14, 15, and 22, so fields from the previous days were repeated to fill the gaps. The main precipitation events over the region are well captured in the analyzed data. An apparent exception of this is the precipitation amounts for 9 July 1997. The analysis shows significant precipitation that was not measured at the stations. Study of the horizontal distribution of the analyzed precipitation and of radar data shows that indeed there existed a significant precipitation event close to the limits of the Mesonet region, so that a small location error in the analysis appears to have produced a large bias in the total precipitation of the analysis for the Mesonet points. Figure 3.2.2b shows a scatter plot of daily averaged

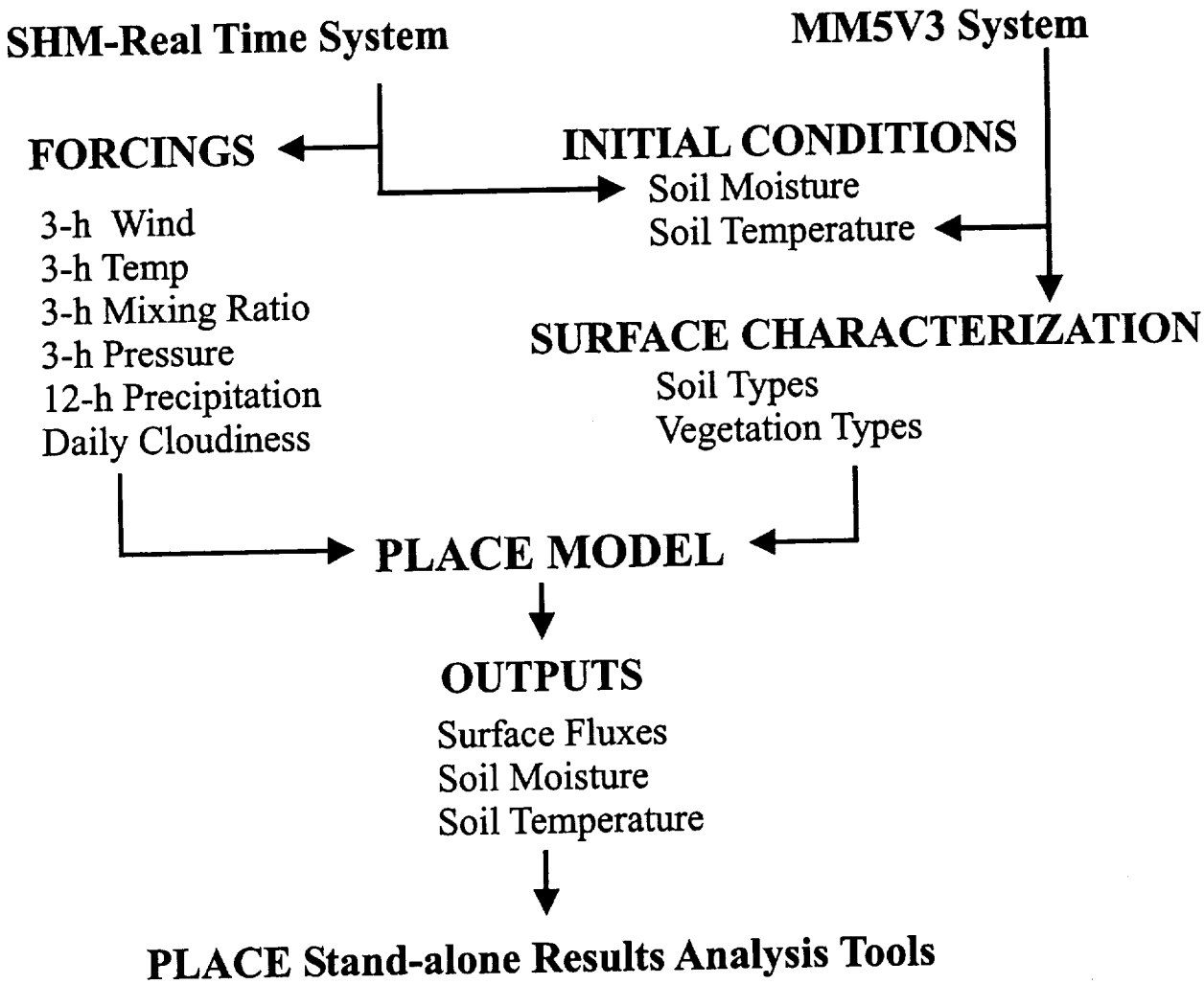

Figure 3.2.1 Schematic of PLACE Stand-Alone Model

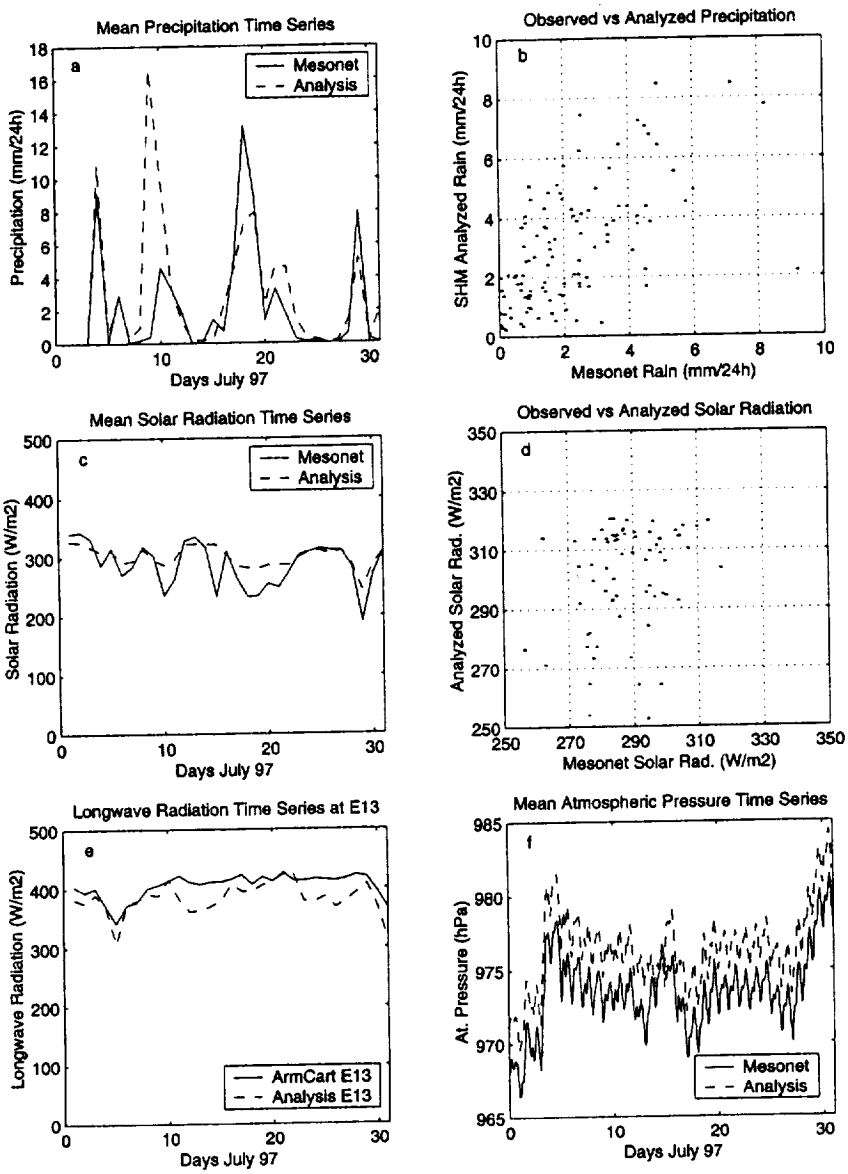

Figure 3.2.2 Comparison of forcings of stand-alone PLACE model and Mesonet station measurements for July 1997. a) Time series of measured and analyzed mean daily precipitation amounts, b) Scatter plot of mean daily precipitation for all stations, c) Time series of measured and analyzed mean daily solar radiation, d) Scatter plot of mean daily solar radiation for all stations, e) Time series of measured and analyzed mean daily longwave radiation at station E13, f) Time series of measured and analyzed mean atmospheric surface pressure.

precipitation measured and analyzed for the same 110 Mesonet stations with precipitation data. The daily averages are computed for the full month of July 1997. Although the figure shows considerable scatter, there is no significant bias between measured and analyzed precipitation.

Figures 3.2.2c and 3.2.2d show a similar analysis, but for analyzed and measured solar radiation (67 stations with full solar radiation measurements are used in this analysis). The analyzed solar radiation data appear to underestimate the shortwave radiation reaching the ground for clear conditions and overestimate it in cloudy conditions. Figure 3.2.2e is a check for the longwave radiation reaching the surface. Longwave radiation is not measured over the Mesonet stations, so that the comparison shown in the figure is restricted to station E13 of the ARM-CART site (siros datastream). The model longwave radiation reproduces reasonably well the measured flux. Finally, Fig. 3.2.2f compares time series of atmospheric surface pressure averaged for the Mesonet stations and the corresponding analyzed fields. The mean surface pressure bias is around 2-3 hPa. These analysis errors may be related in part to the relatively coarse 36-km terrain fields in the offline PLACE domain (Fig. 3.2.3), compared to the actual terrain at the Mesonet sites.

Figure 3.2.4 shows temporal and spatial verifications of meteorological forcings of the PLACE stand-alone system. Analyzed fields of air temperature (panels a and b), water vapor mixing ratio (panels c and d), and wind speed (panels e and f) agree reasonably well with the independent high-resolution measurements available in the Mesonet. Although the forcings that feed the offline PLACE may be further improved by using the Oklahoma Mesonet data, the offline PLACE must be run over the entire 36-km continental-scale MM5 domain (see Fig. 3.2.3) where special data do not exist, and these Mesonet data will also serve as an independent

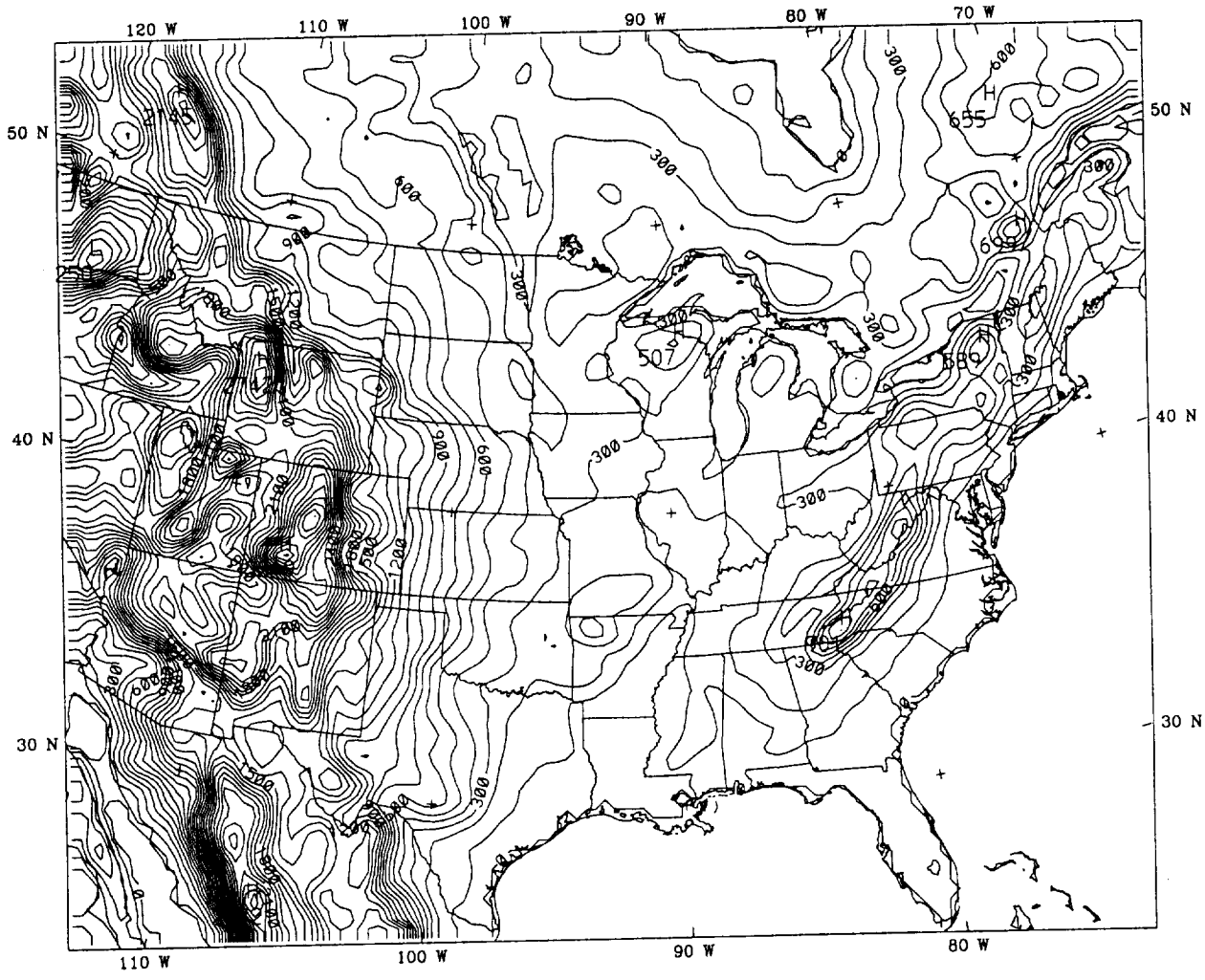

Figure 3.2.3 Model 36-km domain and topography.

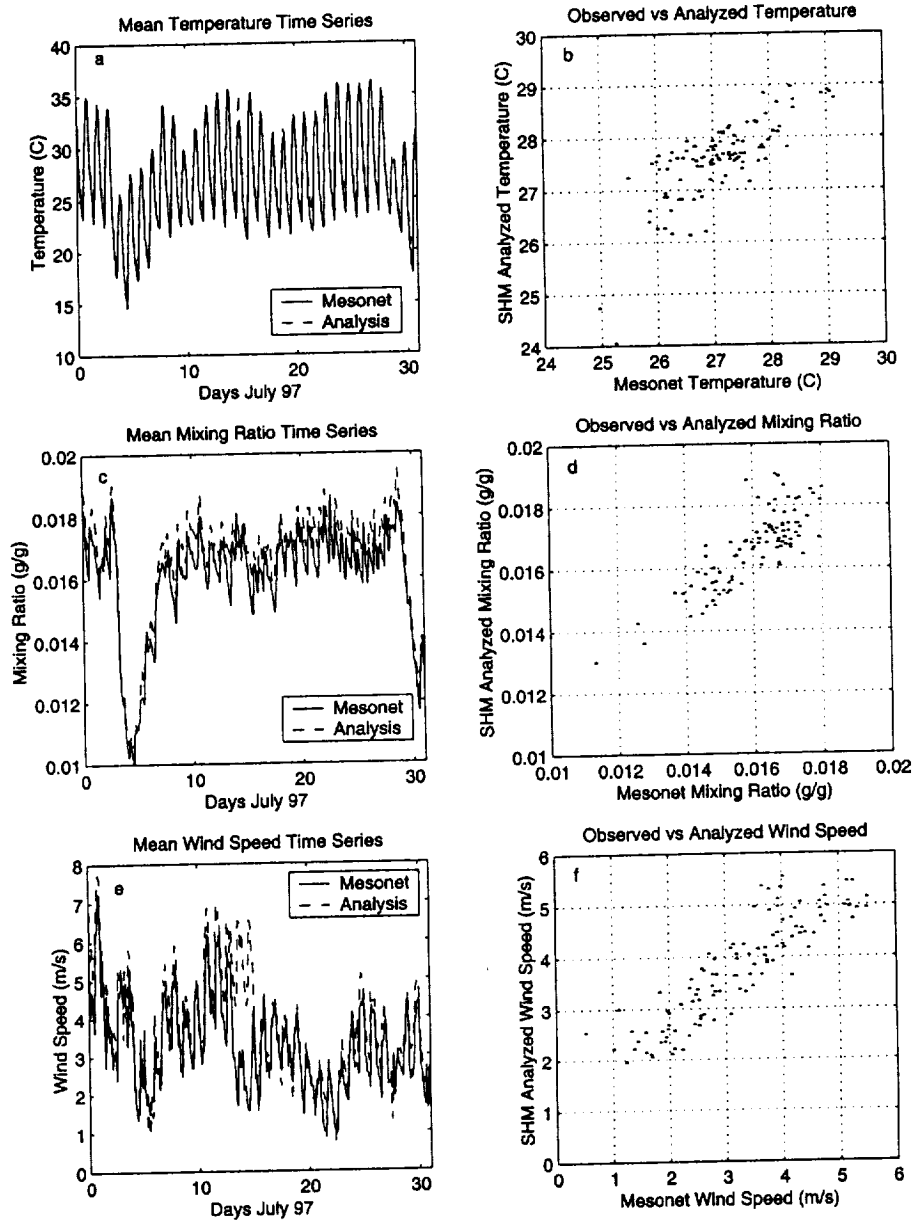

Figure 3.2.4 Comparisons of forcings to stand-alone PLACE model and stations measurements for July 1997. a) Time series of measured and analyzed mean temperature, b) Scatter plot of mean daily temperature for all stations, c) Time series of measured and analyzed mean water vapor mixing ratio, d) Scatter plot of mean daily water vapor mixing ratio for all stations, e) Time series of measured and analyzed mean wind speed, f) Scatter plot of mean daily wind speed for all stations.

verification of the 3-D MM5-PLACE surface fields in section 4.1. Thus, this independent verification of the conventional analyses used to force offline PLACE against the Mesonet data shows that these data are reasonably accurate for the purpose of creating the initial conditions for the MM5-PLACE 3-D experiments.

3.2.4 Model Settings and Parameter Specifications

The model domain (Fig. 3.2.3) is based on the SHM real-time system (Smith et al. 1994). It covers most of the continental United States with 94 points in the N-S direction and 114 points in the W-E direction. All the work presented in this report uses this 36-km domain. The time step used in the stand-alone runs of PLACE is 10 minutes. Although PLACE has the capability of handling several mosaic tiles in each grid cell, only one tile has been used in these runs. Whenever possible the surface characterization and the soil and vegetation parameters are taken from the MM5V3 system. The soil is characterized based on the 16-category STATSGO soil map. The land-use/vegetation characterization is based on the 24-type USGS classification scheme that is available as a standard MM5 option. Some of the parameters of PLACE that are not specified in the MM5V3 land-surface model have been defined with the help of the PLACE developer, Dr. Peter Wetzel. Among these parameters are the vegetation leaf area index (LAI) that has been set at a value of 7. The map of vegetation fraction used in these runs comes from the climatological vegetation fraction map available in MM5V3 for the month of July. A more detailed description of the soil and vegetation parameters required by PLACE, and their definition in the results presented here can be found in Munoz (2002). The results presented in subsequent sections correspond to an offline model run that was initialized on 1 June 1997.

The PLACE model uses 7 soil temperature layers defined at 0-2 cm below the surface, 2-

5 cm, 5-10 cm, 10-15 cm, 15-50 cm, 50-90 cm and 90-130 cm. Its 5 soil moisture layers are located at 0-2 cm, 2-5 cm, 5-15 cm, 15-50 cm and 50-130 cm. The initial soil moisture field was derived from the moisture field at 1 June 1997 of the SHM-real-time-model. The soil moisture profile at the PLACE levels was obtained by linear interpolation of the SHM soil moisture profile. The initial soil temperature profile was calculated as a linear interpolation between a surface soil temperature and a deep soil temperature field. The upper field is calculated as the daily average of the air temperature, and the deep soil temperature is the climatological deep soil temperature field available in the MM5V3 system.

3.2.5 Offline PLACE Results

Results presented in this section are obtained using the model settings and parameters described above, with the only exception that the precipitation forcing used was obtained from the measurements at each individual Mesonet station. This procedure allowed us to perform a more extensive comparison between model results and point measurements than if we used the analyzed precipitation fields. Although the latter fields had not shown any significant bias with respect to the measurements (except July 9, as noted earlier), the variance between measurements and analysis made the evaluation of the PLACE model at the station level less revealing. However, the gridded fields of soil variables used as initial conditions for the 3-D MM5-PLACE runs are produced by using the analyzed precipitation fields as forcing for the stand-alone PLACE model.

3.2.5.1 Soil Moisture

Figure 3.2.5 shows daily time series of observed and modeled soil moisture averaged

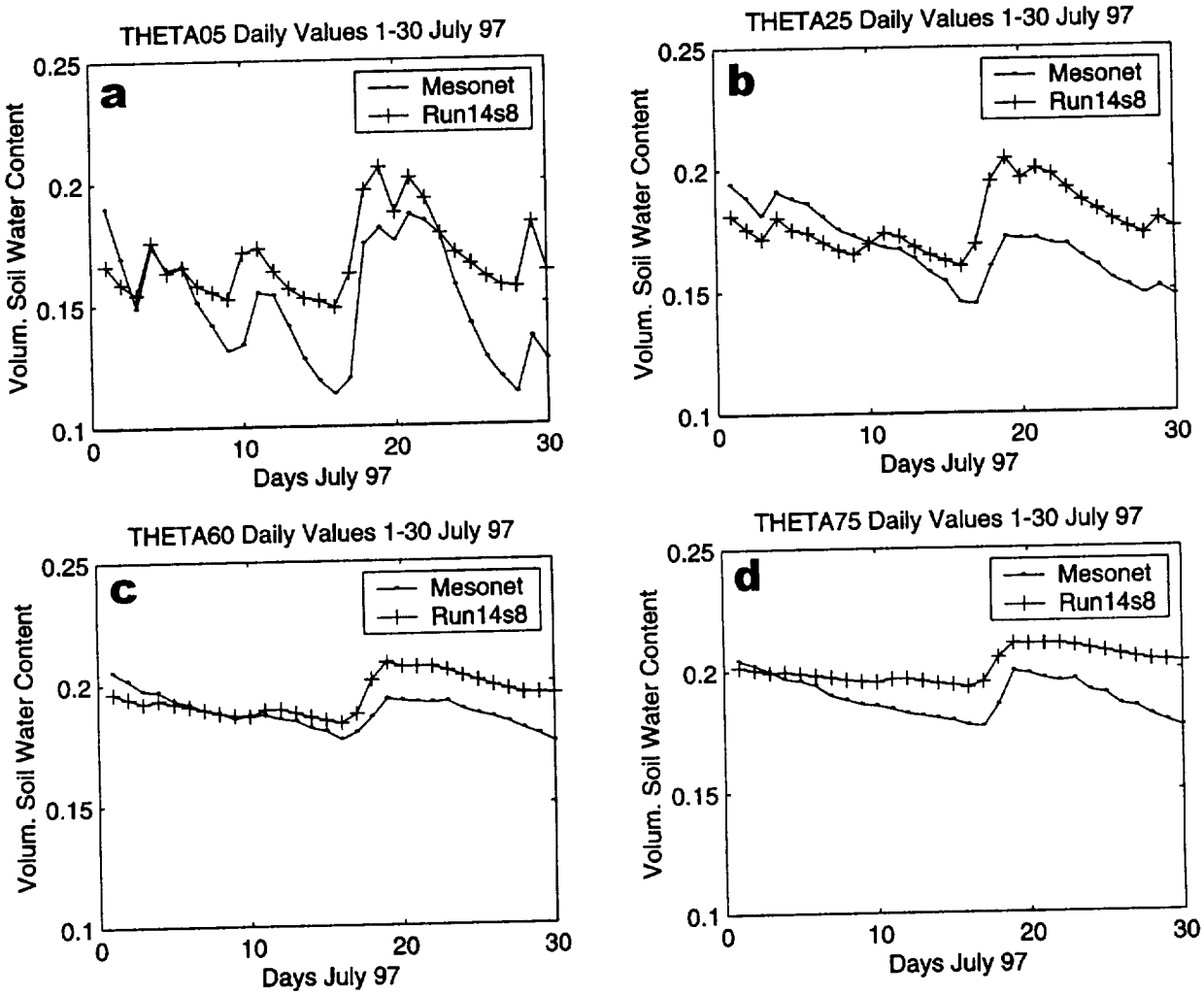

Figure 3.2.5 Time series of measured and modeled volumetric soil moisture content averaged over 35 Mesonet stations with full soil moisture data for July 1997. a) 5 cm depth, b) 25 cm depth, c) 60 cm depth, d) 75 cm depth.

over 35 Mesonet stations, for the period 1 to 30 July 1997, and for the four levels with measurements (model results have been interpolated to the measurement levels). Soil moisture at 5 cm depth (panel a) in the measurements and the model results responds strongly to the precipitation events during the month. The rain episodes produce increments of similar magnitude in the model as in the observations. The drying trend in between rain events, however, is different in the model as compared to the data. The data show larger drying rates at this level. The second level at 25-cm depth (panel b) shows a remarkable similarity between the observed and measured mean drying trends during the month. Both time series averaged over the 35 Mesonet stations show a systematic difference that is due to an initial error and to the effects of the rain event around July 10 that is significant in the model results, but is only slightly noted in the observations. Mean results for the 60-cm deep soil moisture (panel c) are also similar between model and observations, again with a slightly larger drying in the observations than in the model results. The same is evident at the depth of 75 cm (panel d).

Figure 3.2.6 shows number histograms of soil moisture at different levels, as derived from model results and observations. The difference in the shapes of the histograms is significant. Model results show a tendency to peak at middle values of soil moisture, while observed histograms are highly skewed with larger frequencies at the low soil moisture range. A secondary maximum in the observed histograms occurs at the high soil moisture range, especially in the deeper soil layers. Therefore, the PLACE model is having some difficulty simulating the very low and very high soil moisture values, especially in the deeper soil layers. Deep soil values may be improved by extending the length of the PLACE simulation to several months.

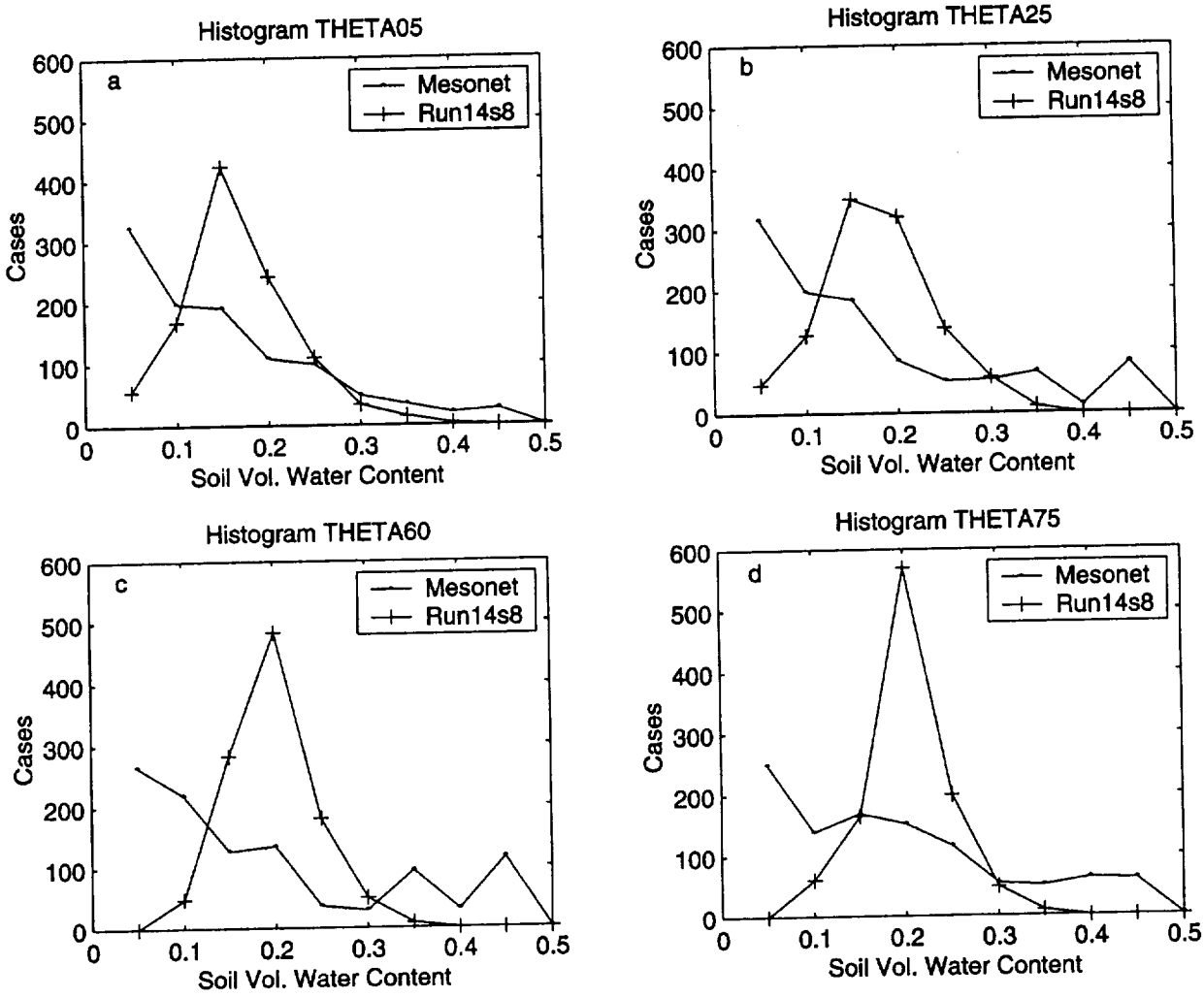

Figure 3.2.6 Number histograms of measured and modeled soil moisture contents for July 1997. a) 5 cm depth, b) 25 cm depth, c) 60 cm depth, d) 75 cm depth.

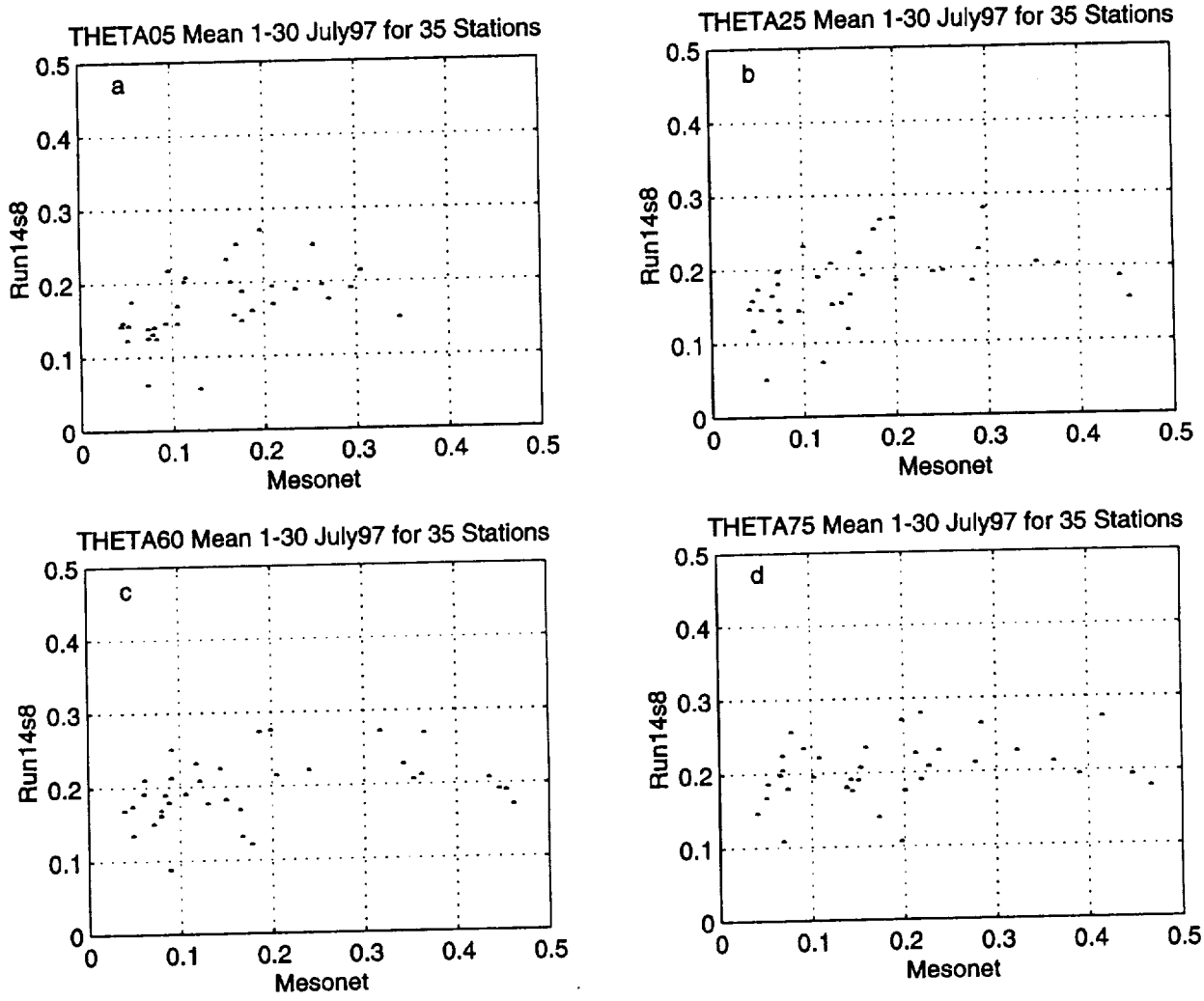

Figure 3.2.7 Scatter plot of monthly mean soil moisture for 35 Mesonet stations with full soil moisture data for July 1997. a) 5 cm depth, b) 25 cm depth, c) 60 cm depth, d) 75 cm depth.

Figure 3.2.7 shows the dispersion between monthly mean soil-moisture values from the measurements and the model results, for the four levels with data. It is apparent that the model is unable to capture the regions with larger soil moisture values in the data. This bias could be due to excessively rapid drying in the model or simply due to soil moisture parameters that are different between model and observation sites (for example, a saturation moisture that is smaller in the model than in the measurements). We investigate this problem further by displaying the dispersion between the observed and modeled maximum and minimum soil moisture at each station, as shown in Fig. 3.2.8. Panel a shows the scatter between monthly minimum soil moisture at 5-cm depth (minimum values are paired independent of the day that they have been reached). The minimum values of soil moisture are in many cases significantly greater than the corresponding values in the observations. The scatter of maximum values at 5-cm depth (panel b) shows a smaller bias between model and observations in the middle soil moisture range. The largest soil moisture amounts, however, are consistently underestimated by the model. Similar conclusions are drawn for the level 25-cm deep, as shown in panels c and d.

Figure 3.2.9 shows time series of the correlation coefficients between observed and modeled soil moisture for the four depths with data. A significant increase in the model-observation correlations is evident during the rainy episodes, especially in the two uppermost levels. The two lower levels show a steady increase in the correlation through the monthly period, suggesting that a longer model run could improve the correlations between model and measurements at the deeper levels. The two lines in these panels correspond to the sensitivity to the precipitation forcing used in the model. Run 14s8 (continuous line) used the observed precipitation rates starting on 1 July 1997 (during June 1997 it used the analyzed precipitation fields), while run 14s8s1 used the measured precipitation rates from the start on 1 June 1997.

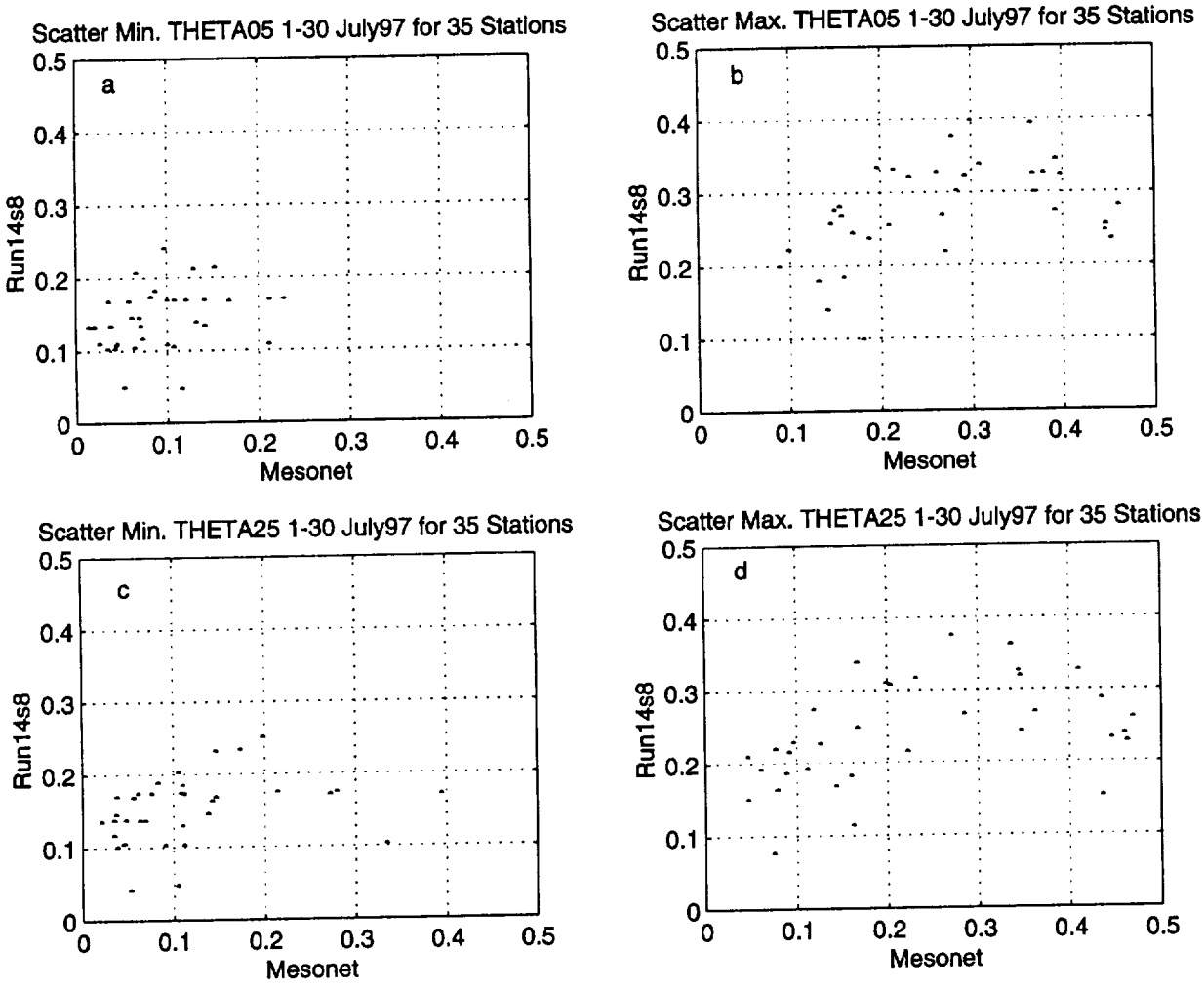

Figure 3.2.8 Scatter plot of monthly minimum and maximum soil moisture for 35 Mesonet stations with full soil moisture data for July 1997. a) minimum soil moisture at 5 cm depth, b) maximum soil moisture at 5 cm depth, c) minimum soil moisture at 25 cm depth, d) maximum soil moisture at 25 cm depth.

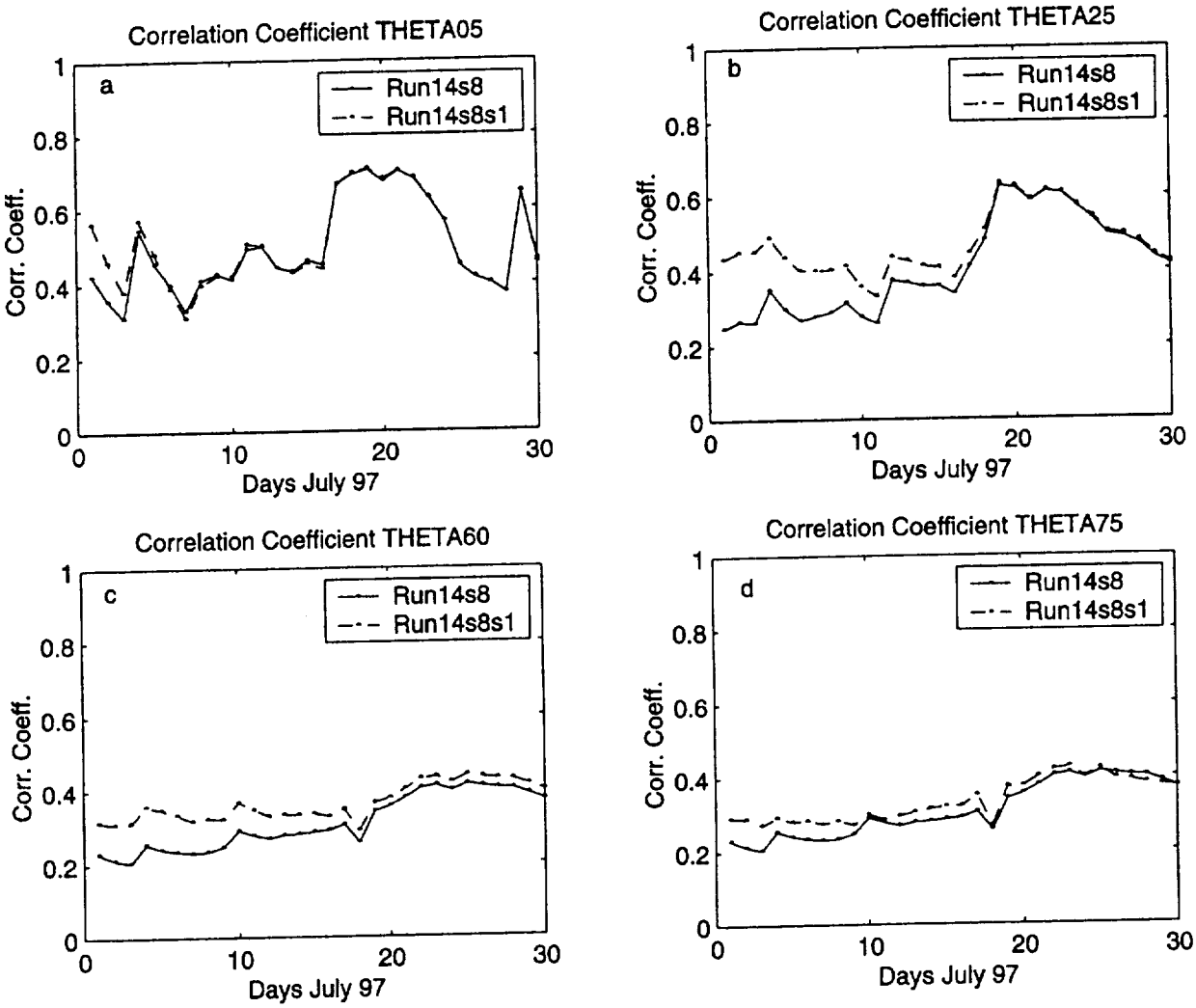

Figure 3.2.9 Time series of correlation coefficients between observed and measured soil moisture contents for the 35 Mesonet stations with full soil moisture data for July 1997. Model run Run14s8 is driven by point-measured precipitation starting on 1 July, and run Run14s8s1 uses point-measured precipitation starting from 1 June. a) 5 cm depth, b) 25 cm depth, c) 60 cm depth, d) 75 cm depth.

The effect of using better precipitation forcing is evident in the lower layers. The uppermost layer shows larger correlation coefficients only during the first days of July. The monthly correlation between model and observations for each station is represented in Fig. 3.2.10 for all four levels. The uppermost levels show only positive correlations. The lower levels show more variable correlations, with some stations showing negative values and others showing values closer to 1.

Another way of studying the spatial variability in the observations and in the model results is by grouping the stations in four regions, each covering (overlapping) regions of approximately 2x2 degrees. These regions are defined as A, B, C, D, from the westernmost to the easternmost part of Oklahoma. Figure 3.2.11 shows the mean time series of soil moisture in the four regions according to the available measurements. A significant west-east gradient in soil moisture is apparent from this figure. The western portion of the Mesonet is significantly drier than the eastern part. This gradient is more noticeable in the second layer (panel b). The upper layer is more affected by the rain distribution, and the lower layers appear to be more homogeneous in soil moisture, with the exception of region A that is drier in all four levels. The corresponding regional averages from the model results are presented in Fig. 3.2.12. The west-east gradient is not well reproduced in the model results. Only at the end of the month has a gradient developed after the large precipitation event around 19 July 1997.

The mean vertical soil-moisture profile is shown in Fig. 3.2.13, where the mean profiles are plotted for observations and model results. A mean overestimation in the soil moisture profile is evident from the figure, although the vertical gradients of soil moisture are similar below 20-cm depth. The model results show a systematic minimum in the second level.

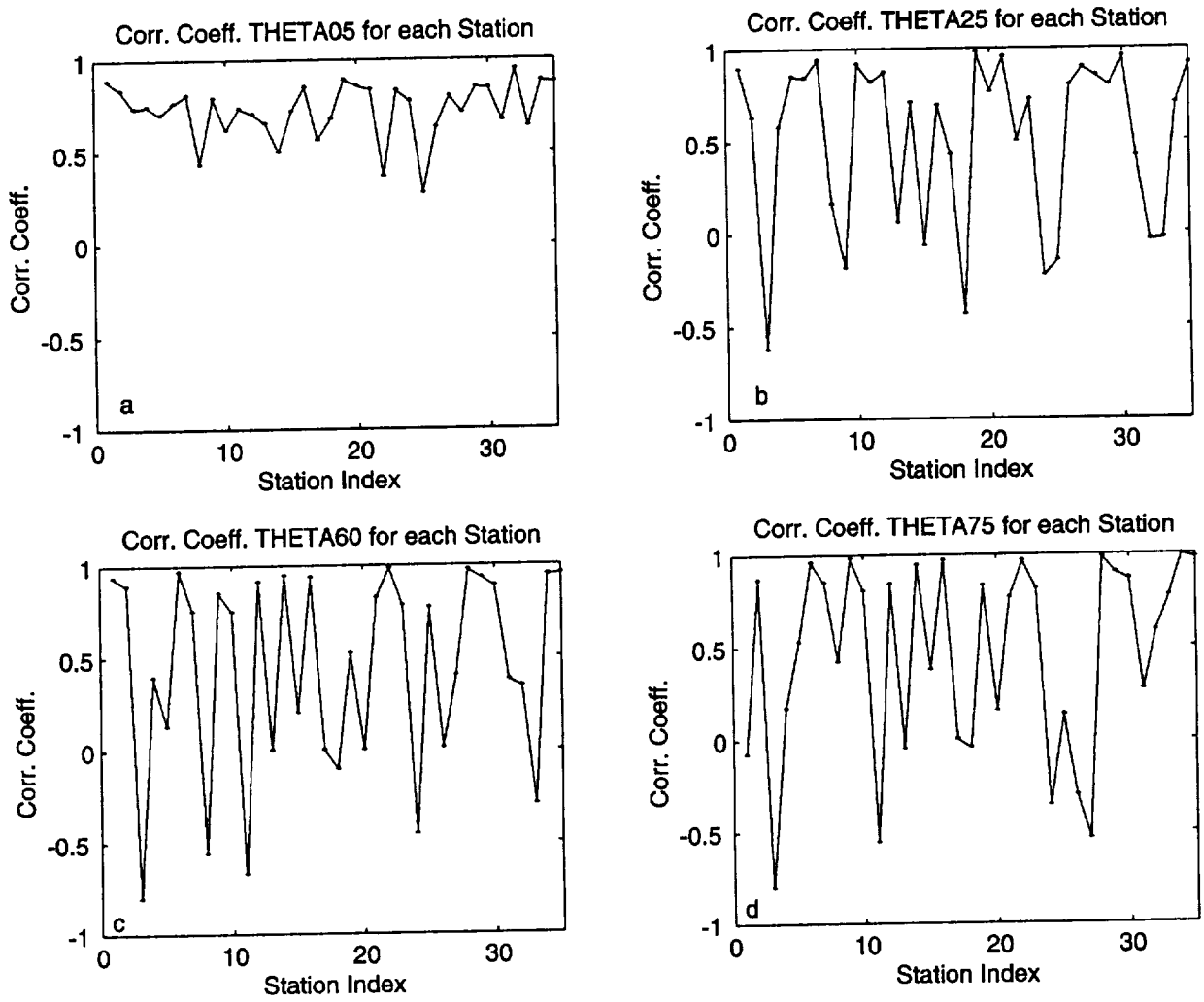

Figure 3.2.10 Monthly correlation coefficients between model and measured soil moisture contents for 35 Mesonet stations with full soil moisture data for July 1997 (station index does not correspond to Mesonet station number). a) 5 cm depth, b) 25 cm depth, c) 60 cm depth, d) 75 cm depth.

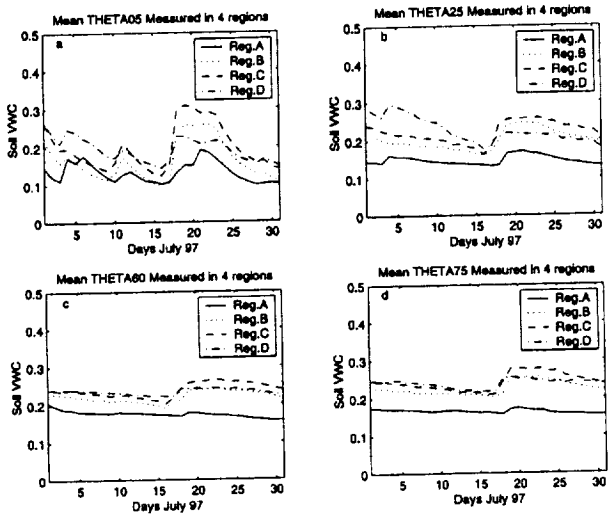

Figure 3.2.11 Time series of measured volumetric soil moisture content at 35 Mesonet stations with full soil moisture data for July 1997 and for the four regions described in the text (Region A is the westernmost and Region D is easternmost). a) 5 cm depth, b) 25 cm depth, c) 60 cm depth, d) 75 cm depth.

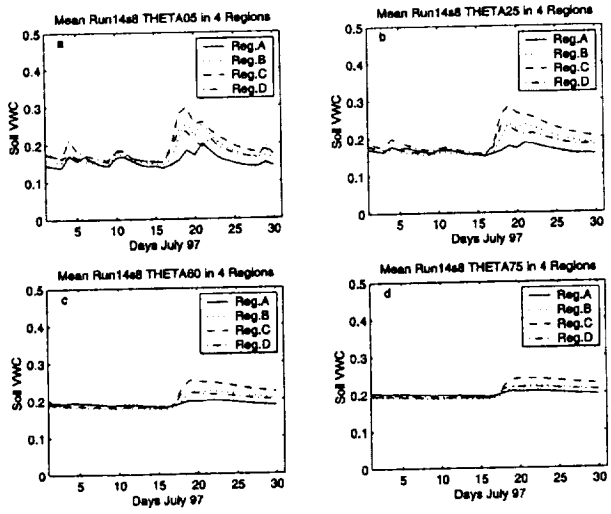

Figure 3.2.12 Same as in Fig. 3.2.10, but for model results.

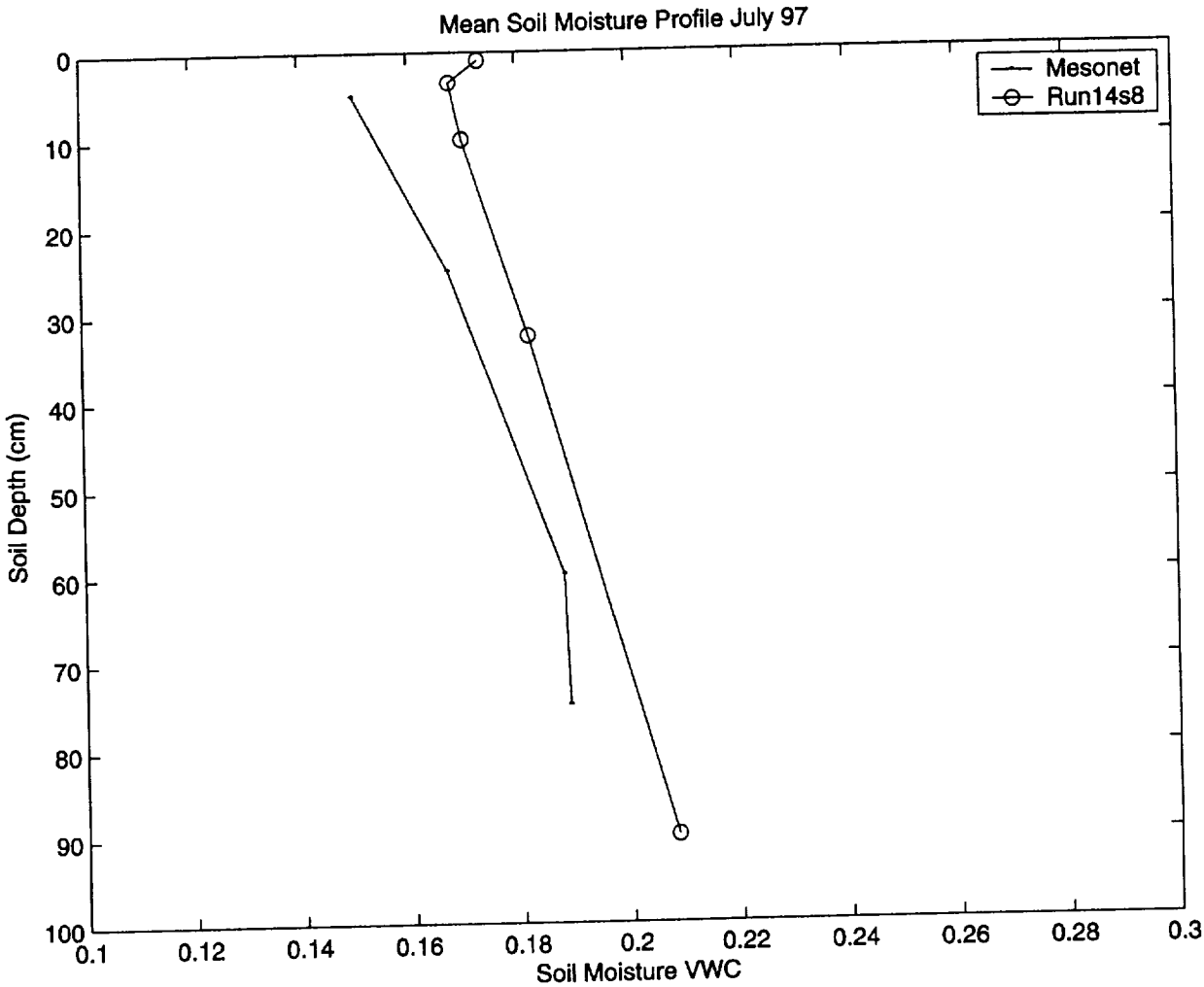

Figure 3.2.13 Measured and observed mean vertical profiles of soil moisture for 35 Mesonet stations with full soil moisture data for July 1997.

This may be due to a possible specification error in the root fraction at this level (0.5), which may make it too large. Further experimentation with longer PLACE integrations is necessary to obtain definitive conclusions.

Finally, it has been possible to compare the offline PLACE model results to high resolution surface soil moisture derived from the Electronically Scanned Thinned Array Radiometer (ESTAR) instrument flown on a P3 aircraft during SGP97 (Jackson et al., 1999). An example of this comparison is shown in Fig. 3.2.14 taken from Reen et al. (2001). The figure shows a cross section of soil moisture content along one of the ESTAR southwest-northeast flight paths on 12 July 1997. The cross section is around 400 km long and the ARM-CART Central Facility at Lamont, Oklahoma, is located near grid cell 95 in the figure. The 800-m resolution ESTAR data and the offline PLACE data were both averaged to a 4-km grid for this comparison. On this day there was a general north-south gradient in soil moisture with warmer, drier conditions towards the south largely due to the convective precipitation that occurred the day before in the northern region. In spite of the coarse 36-km resolution of the PLACE stand-alone results, the spatial variability at this scale is remarkably well captured by the model results on this day.

3.2.5.2 Soil Temperature

Most Mesonet stations have measurements of soil temperature at 10-cm depth and about half of these also have measurements at 5-cm and 30-cm depths. Panels a, b, and c of Fig. 3.2.15 show monthly time series of the soil temperature at different levels averaged over all stations with data (and over all 111 Mesonet stations in the case of model results). The two types of data lines correspond to measurements below bare soil (TB05 and TB10) and below a sod

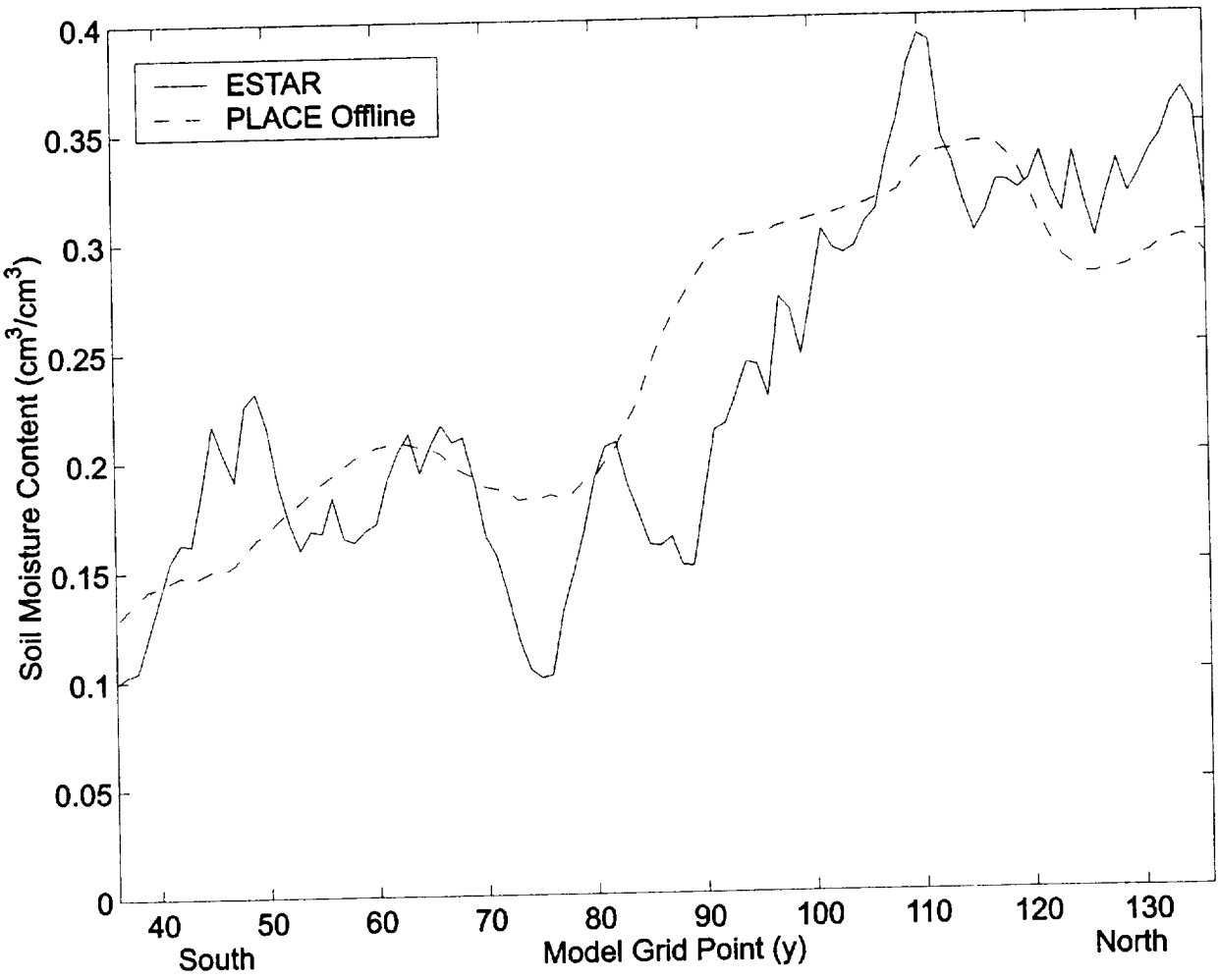

Figure 3.2.14 Offline PLACE versus ESTAR soil moisture contents for 12 July 1997. Each model cell y-value represents an east-west 4-km grid average across the width of the ESTAR data area (from Reen et al. 2001).

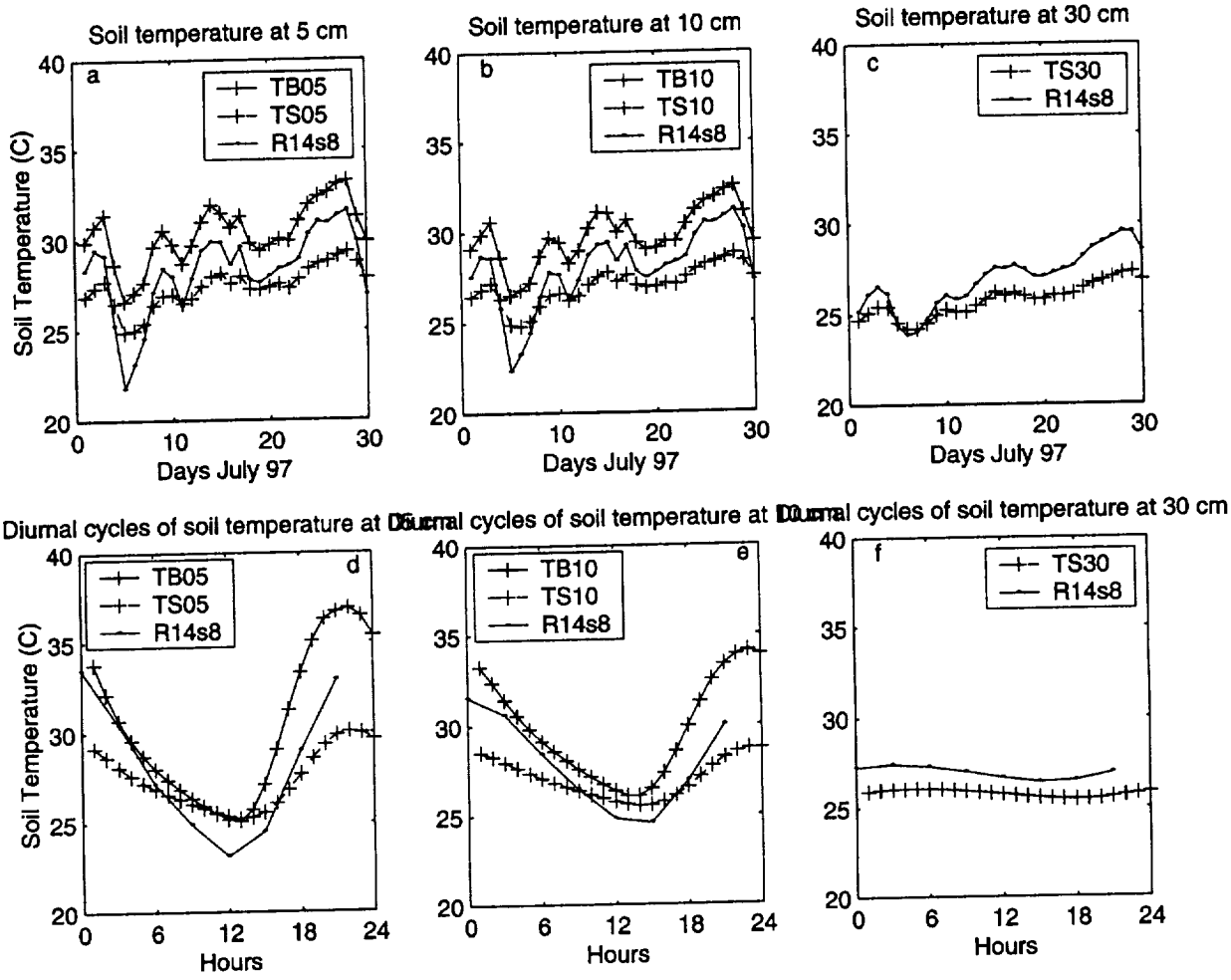

Figure 3.2.15 Comparison of observed and modeled soil temperature. a) Soil temperature at 5 cm depth averaged over all Mesonet stations with data and all 111 stations in the case of model results. TB05 is measured below bare soil and TS05 is measured below a sod cover. b) as a) but for 10 cm depth, c) as a) but for 30 cm depth, d) Mean diurnal cycles for July 1997 at 5 cm depth, e) as d) but for 10 cm depth, f) as d) but for 30 cm depth.

cover (TS05, TS10, and TS30). The measured mean temperatures below bare soil are consistently higher than below sod cover, also have a larger diurnal amplitude (not shown). The model soil temperatures in the upper two layers fall between the two measured averaged series, with the exception of the period around 6 July, when the model temperatures dropped more than the observations. The slight warming trend of the observed deep soil temperature is slightly smaller than the monthly trend of the model results. Panels d, e, and f of the same figure show diurnal cycles of measurements and model results at the three levels with data. The amplitude of the mean diurnal cycles in the model agrees well with the measured cycles at the different soil depths.

3.2.5.3 Surface Fluxes

Comparison of modeled and observed surface fluxes is always complicated by the local character of the measurements. Mesonet stations do not have flux measurements. Stations in the SGP ARM-CART site include EBBR and eddy correlation measurements of fluxes. Many stations, however, present measurement problems during extended periods. We restrict our comparison here to ARM-CART stations E9 and E15 that do not report data quality problems during July 1997. Figures 3.2.16 and 3.2.17 summarize the analysis of the sensible and latent heat fluxes measured at these stations. Diurnal cycles of fluxes are shown in panels a and c of Fig. 3.2.16. In both stations the surface fluxes appear to be dominated by the latent heat fluxes, especially at station E9. Panels b and d illustrate the diurnal cycle of the variability in these measurements. Noise in the data is relatively large during the night and in the diurnal transition periods, where the Bowen ratio method of determining fluxes usually has problems. The fluxes between hours 15 and 21 are averaged for each day and presented in the monthly time series in

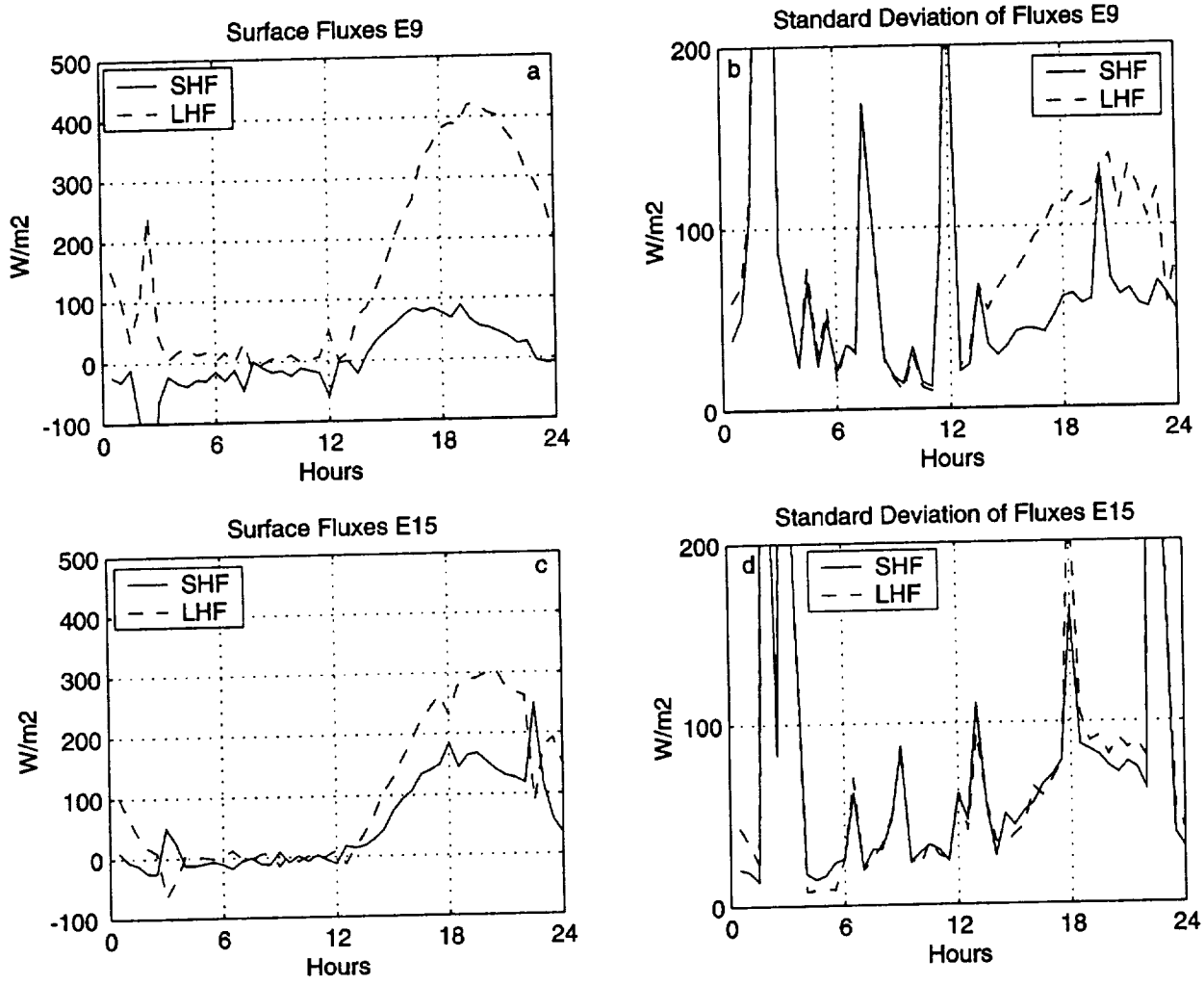

Figure 3.2.16 Measured surface fluxes at two ARM-CART EBBR stations. a) Mean diurnal cycles of sensible and latent heat fluxes for station E9 during July 1997. b) Mean diurnal cycles of standard deviation of surface fluxes for station E9 during July 1997. c) As a) but for station E15. d) As b) but for station E15.

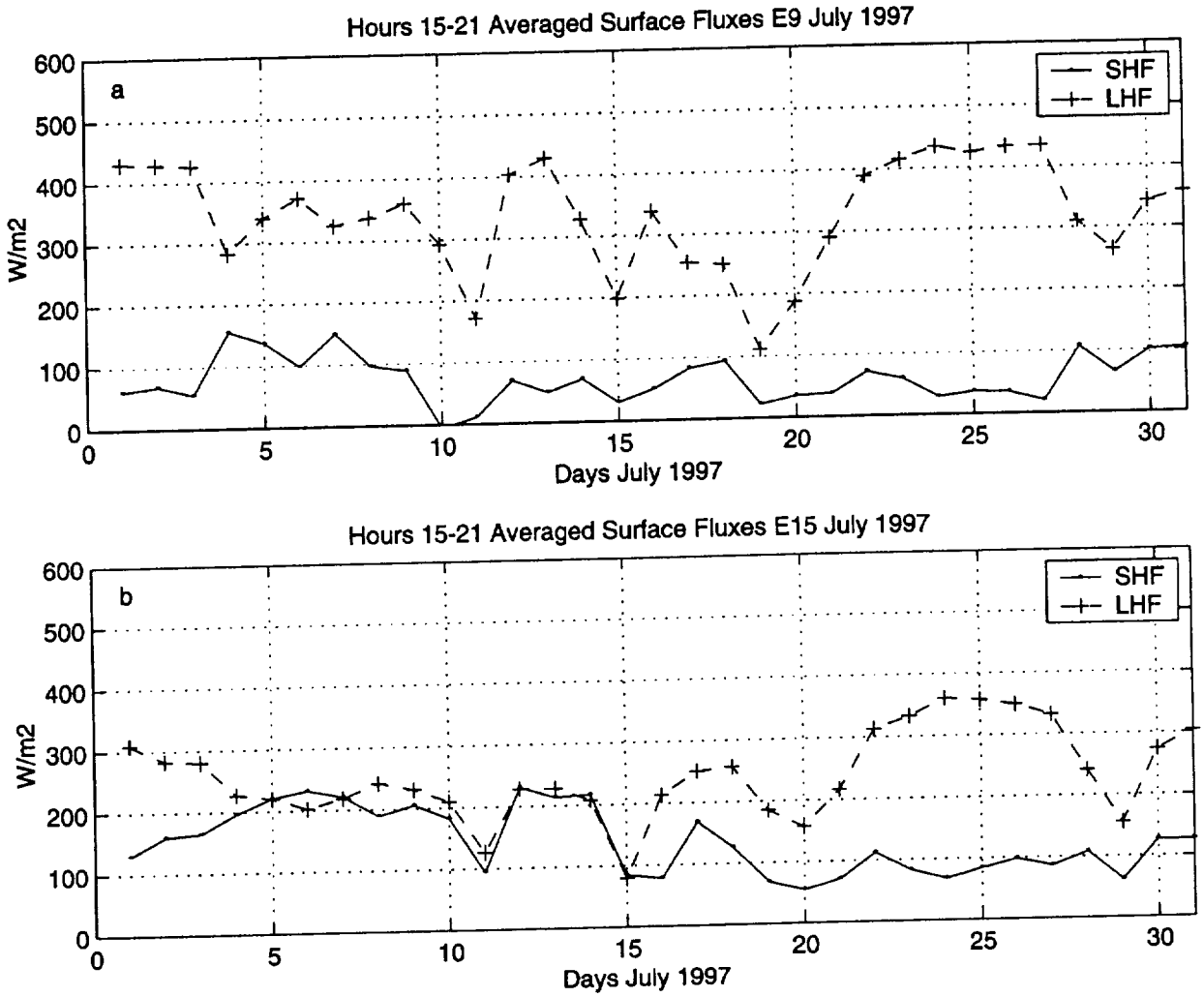

Figure 3.2.17 Monthly time series of diurnal surface fluxes at two ARM-CART EBBR stations. Each daily value is the average of measurements between 15 UTC and 21 UTC. a) Station E9, b) Station E15.

Figure 3.2.17. The dominance of latent heat fluxes at station E9 is again evident. The low values of sensible heat flux during the afternoon at E9 for the entire month is intriguing. There appears to be some source of water nearby. Station E15 also has Bowen ratios less than one for more than two-thirds of the month, but it has Bowen ratio near one (i.e., comparable latent and sensible heat fluxes) during the period of 5 to 15 of July 1997.

The corresponding diurnal cycles and monthly time series of fluxes for offline PLACE model results are shown in Fig. 3.2.18. Mean model results for station E9 are also dominated by the latent flux, although not as strongly as in the observations. Station E15 has more comparable fluxes. The 3-hourly noise evident in these diurnal cycles is probably an artifact of the meteorological forcing supplied to the model that changes every three hours. Panels c and d of the same figure roughly follow the corresponding observed time series. The most evident problem in the model results is when the sensible heat flux remains very low and even negative during daytime. This may be due to the use of one cloud field for the entire day in the radiation model. The corresponding observed fluxes become small, but usually remain positive. Overall, the offline PLACE results are representing fairly well the land-surface conditions and its daily variability.

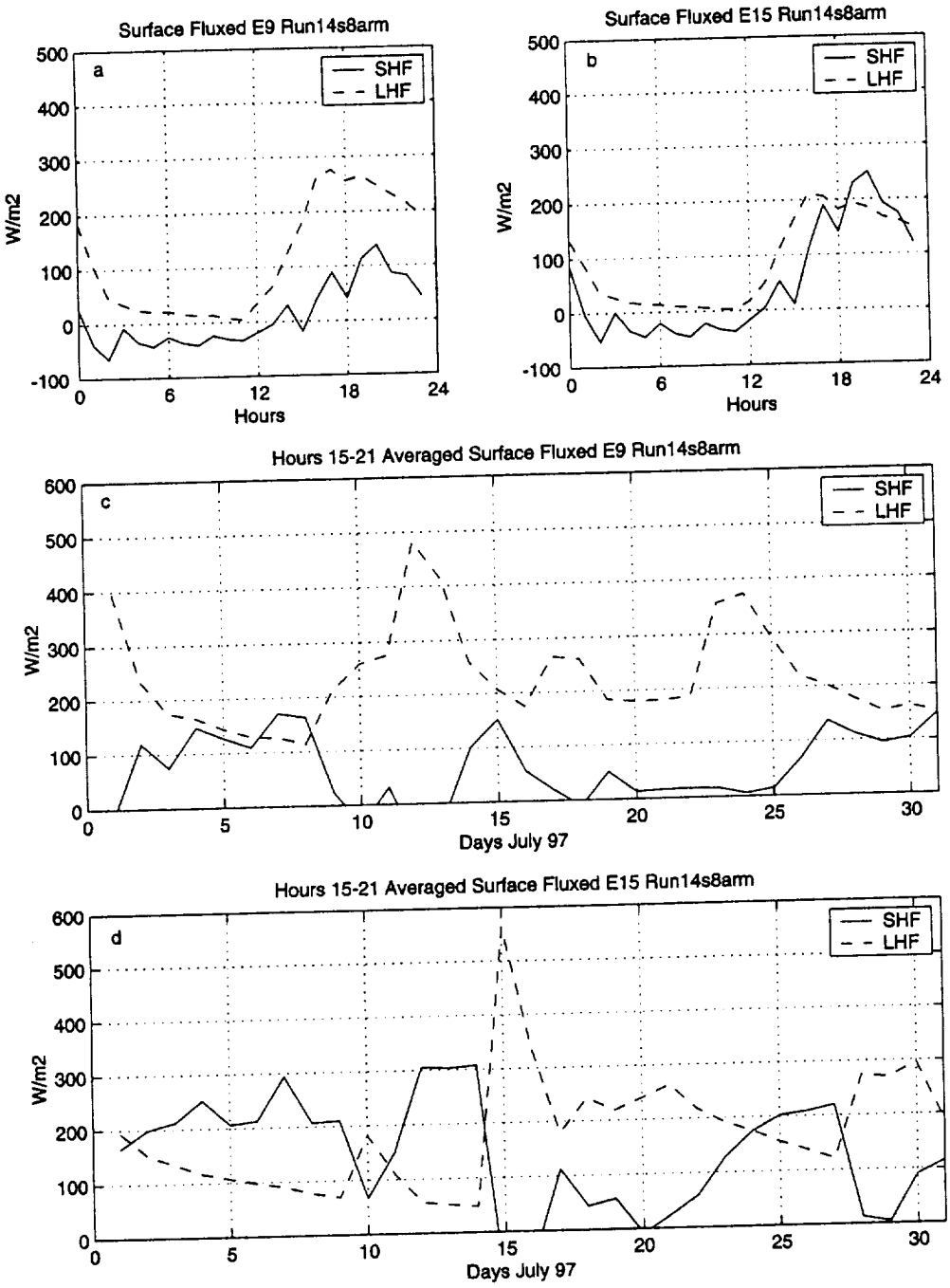

Figure 3.2.18 Analysis of modeled surface fluxes for two ARM-CART EBBR stations. a) Mean diurnal cycle of surface fluxes at station E9 for July 1997. b) As a) but for station E15. c) As Figure 3.2.17a but for model results. d) As Figure 3.2.17b but for model results.

3.3 The Improved Shallow-Convection Scheme

3.3.1 Removal of Stochastic Behavior in the Mass Flux Calculations

3.3.1.1 Introductory Remarks

In order to use the shallow convection parameterization to investigate the interaction among shallow clouds and other physical processes like radiation, turbulence, deep convection and surface processes, it is necessary first to make sure that the parameterization is working in a physically plausible way. This means that, among other things, it appropriately conserves quantities like water or energy and that it produces realistic tendencies. It also means that it has a smooth behavior, in the sense that for small changes in the variables input to the scheme, it produces smoothly varying tendencies.

Preliminary application of the shallow scheme has shown that the latter conditions are not fully satisfied and that several improvements to the shallow scheme are necessary if one wants to use it with the purposes of regional climate and atmospheric water-budget studies. This section describes the most important problems encountered in the original scheme of Deng (1999) and points to suggested solutions and improvements.

For the purpose of this report we divide the shallow-cloud scheme into three main parts. Part 1 will be referred to as the updraft algorithm. It defines the initial parcel that is used to determine the convective amount (intensity) and calculates the updraft mass fluxes for that parcel

as a function of the given environmental sounding. Part 2 of the shallow parameterization will be referred to as the closure algorithm. It computes the environmental tendencies derived from the updraft mass flux profile and evaluates the change in available buoyant energy due to those tendencies. It also determines how much convection will occur, given an appropriate closure condition. The final part of the shallow-cloud scheme, Part 3, calculates the dissipation of shallow cloud variables in the neutrally buoyant cloud mass that is detrained from the shallow-cloud updrafts. The following portions of this section describe the problems and improvements for each of the three parts of the scheme and illustrate results using the original formulation versus the improved scheme.

3.3.1.2 Improvements to the Kain-Fritsch Updraft Algorithm

Preliminary runs with the shallow convection scheme have shown a large degree of discontinuous behavior in its solutions. This feature hinders the attainment of quasi-equilibrium conditions, as well as making the physical interpretation of model results quite difficult. One of the underlying reasons for the discontinuous behavior of the shallow convection scheme is that its cloud-updraft model is based on the Kain-Fritsch (1990) deep-convection scheme. The latter was designed to calculate a mean updraft condition to be used for a convective period lasting on the order of a half hour or so. Therefore, the discontinuous features of its cloud model had little impact over a period of several time steps. When a new Kain-Fritsch updraft was determined a half hour later, it would be calculated on the basis of what could be (by that time) a very different environment. However, the original shallow-convection scheme calculates a new updraft at every time step using this same Kain-Fritsch cloud model, which causes the discontinuous

tendencies that become painfully evident.

3.3.1.2.1 Case 0: A Simple Case with Discontinuities

As the first step in the investigation, we isolated the algorithm that computes the source conditions for the shallow clouds. In essence it corresponds to the source algorithm in the Kain-Fritsch (1990) cloud model, with some modifications regarding the source layer and the initial level of the updraft parcels defined for the shallow convection scheme. To test the scheme we used the thermodynamic sounding shown in Figure 3.3.1. It consists of a 500-m mixed layer capped by a deep isothermal layer. The water vapor mixing ratio is constant in almost all the lower atmosphere above 990 mb. For this case the lowest two layers of the sounding, comprising a depth of about 10 mb (~100 m), define the thermodynamic properties of the updraft parcel. The mixing ratio of these two layers is moister than in the upper levels, but is kept constant in all calculations shown in this section. The temperature of the two lowest layers will be varied to study the continuity (smoothness) characteristics of the cloud model. The temperature of these two layers is varied by increments of 0.04 K over a range of 4 K (for a total of 100 experiments). We will refer to this experiment as Case 0. Figure 3.3.1 shows the coldest and the warmest soundings used. All other conditions are held constant (unless stated otherwise), including a constant PBL height of 50 mb (~500 m) and a constant initial velocity of the updraft (0.2 m/s).

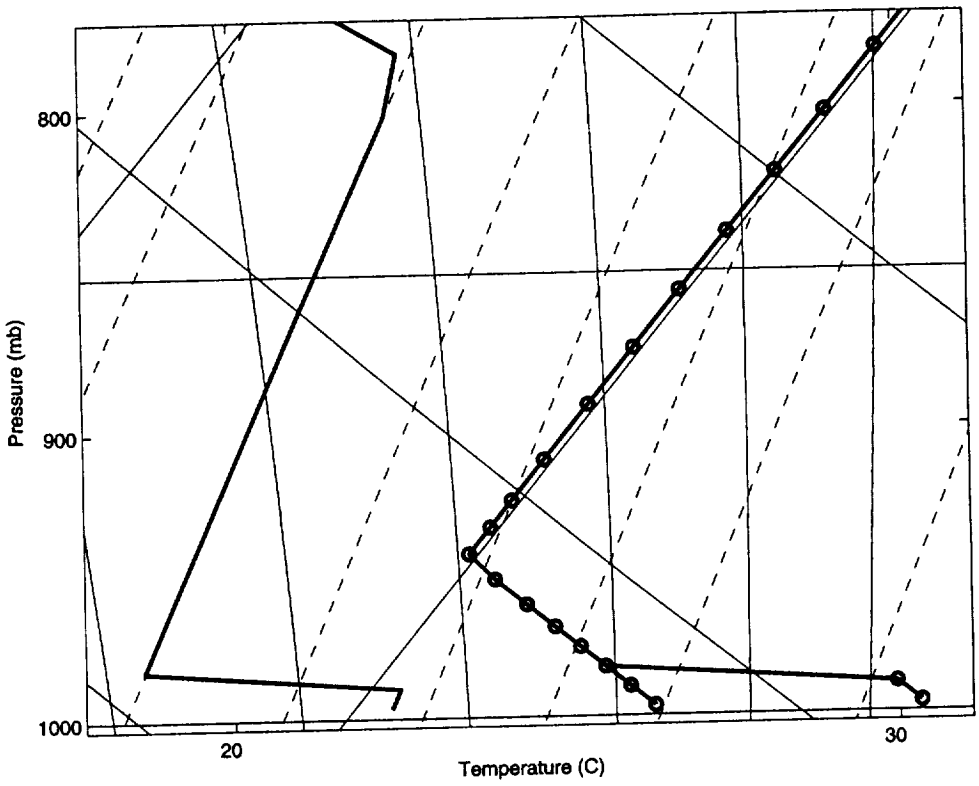

Figure 3.3.1 Skew-T diagram for environmental sounding used in the tests. The two lowest grid layers have a temperature that is varied between the two temperature soundings shown in the figure. Model levels are denoted by circles on the temperature sounding.

3.3.1.2.2 Discontinuities of the Original Shallow Scheme

To illustrate the discontinuous behavior of the original updraft scheme, Figure 3.3.2 shows the mass fluxes in the series of 100 experiments of Case 0 at level 11 (915 mb), as a function of the temperature perturbation in the surface layer. Several jumps are present in the series, where small changes in the temperature of the initial updraft parcel produce large changes in the mass flux profile. Since the shallow-cloud tendencies, as well as the tendencies fed into the grid-resolved variables, depend directly on the mass flux profile, it appears that the current scheme can produce abrupt changes in the calculated grid-scale tendencies.

Further analyses of these results have shown that the jumpiness in the mass flux is due in part to the large importance given to the grid layers in the scheme's computations. For example, the detrainment at the top of the updraft is performed over an integer number of layers (up to the level LTOP, which is the layer in which the cloud top is diagnosed). Therefore, when the number of detraining layers changes from, say, 1 to 2, the mass fluxes change abruptly and significantly in all layers involved. Other layers that have an important impact on the results are the layer of equilibrium temperature (LET) and the layer defining the thermodynamic properties of the starting updraft. Whenever these layers change by a unit (one whole layer), the updraft mass flux distribution can change drastically.

Figure 3.3.3 shows the series of important heights diagnosed with the original updraft algorithm, as a function of the perturbation temperature. ZPBL is the assumed PBL height that is set constant at 500 m in all calculations. The fine line labeled ZLCL is the diagnosed lifting

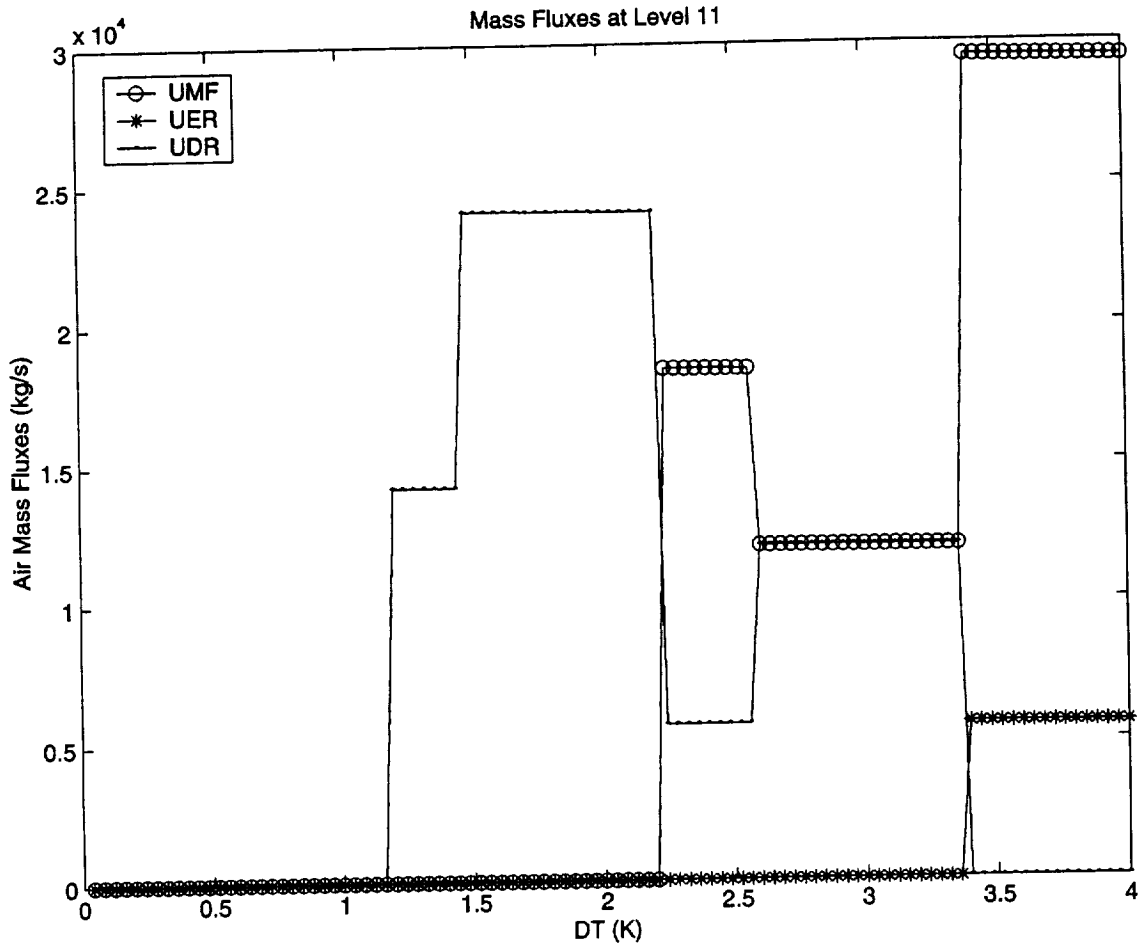

Figure 3.3.2 Diagnosed mass fluxes for the original updraft algorithm at Level 11 as a function of perturbation temperature in the initial shallow-cloud updraft parcel. UMF: mass flux at the top of the layer. UER: entrainment flux in the layer. UDR: detrainment flux in the layer.

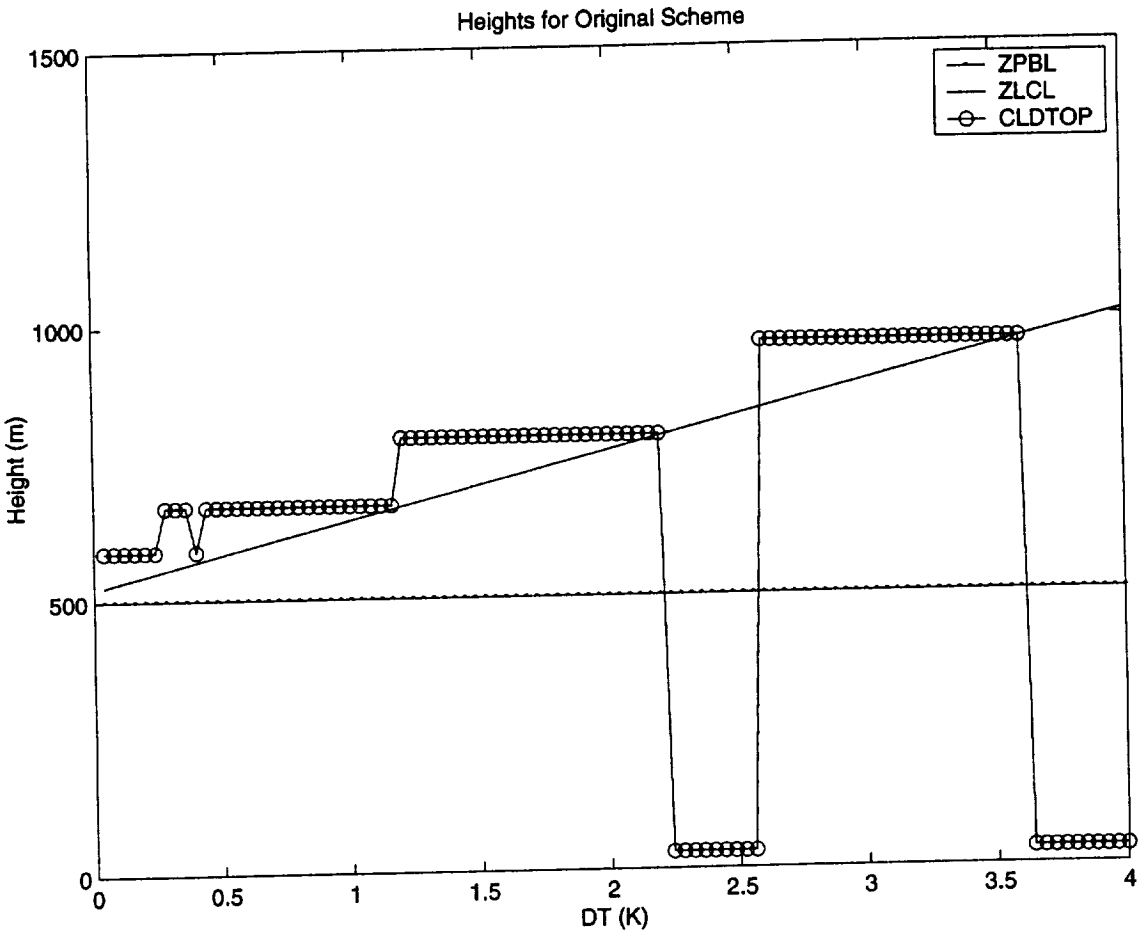

Figure 3.3.3 Important heights diagnosed with the original shallow-cloud updraft algorithm. ZPBL: height of the PBL. ZLCL: lifting condensation level. CLDTOP: cloud top height.

condensation level that is based on the temperature and moisture of the surface layer. Here, the updraft release height is always at ZPBL because ZPBL < ZLCL in all of the 100 experiments of Case 0. Finally, the line with circles labeled as CLDTOP is the diagnosed top of the updraft (or cloud). The discrete behavior of the cloud top is a serious problem that complicates the interpretation of the scheme's results and has feedbacks to many of the shallow-cloud scheme's calculations. Also, there are two regions in Figure 3.3.3 where CLDTOP drops suddenly to a minimum value. These regions correspond to conditions for which the algorithm diagnoses no shallow clouds because the condition ZLCL > CLDTOP is met. A further discussion of the appropriateness and implicaitons of this condition is presented below. While it is true that the series of LET and LTOP must jump between integer numbers (because they refer to grid levels), it is not necessary true that the algorithm has to reflect these discontinuities in such a strong way. In fact, LET and LTOP represent the integer locations of well defined heights that are continuous in the vertical, namely, the height of no-buoyancy (ZLET) and the height of zero vertical velocity for the updraft parcel (ZTOP), respectively.

As it is now, the shallow cloud scheme is activated (i.e., produces condensed water mass, which is a source of NBC and defines cloud mass fluxes) depending on the relationship between the ZLCL and CLDTOP. If CLDTOP > ZLCL, then the cloud model is activated and mass fluxes are calculated. Although this condition appears reasonable, a closer look indicates that its consequences are not completely straightforward. Figure 3.3.4 shows the total detrained mass fluxes of water vapor and liquid water that are diagnosed by the original scheme. Again, the discreteness of the fluxes is evident in the figure. The two regions with large drops in the vapor detrainment fluxes in Panel *a* correspond to the experiments in which the shallow scheme does

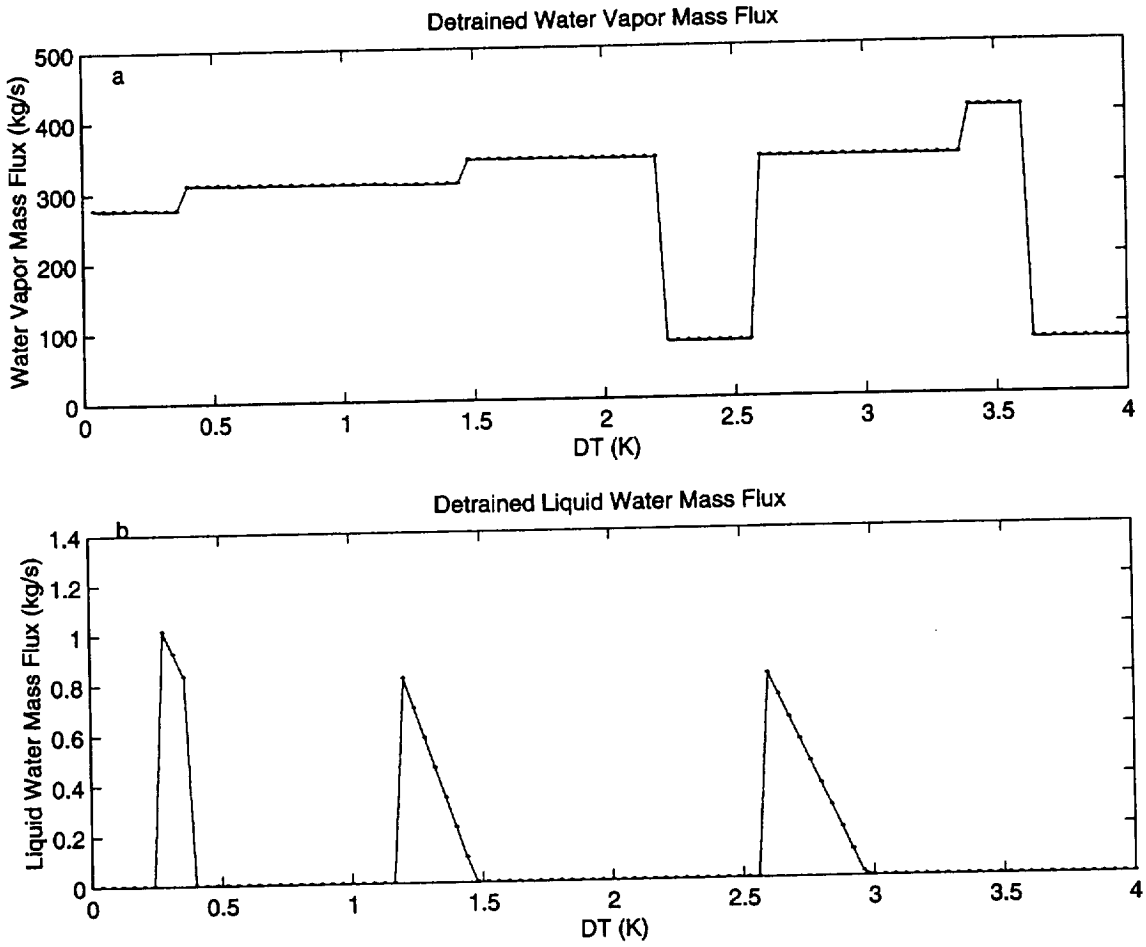

Figure 3.3.4 Sources of detrained updraft water vapor and liquid water diagnosed with the original updraft algorithm. (a) Total detrained water vapor flux (regions with low values around DT = 2.5 K and DT = 4 K are not fed back to the calling model because CLDTOP<ZLCL). (b) Total detrained liquid water.

not activate because of the triggering condition discussed above (also see Figure 3.3.3). The detrained liquid water (that defines the source of shallow water clouds) is also discontinuous.

Two subtle effects of the shallow-cloud triggering condition are illustrated in Figure 3.3.4. First, ZLCL is calculated with an undiluted parcel, but the CLDTOP calculations include the effects of dilution with the environment. Thus, it is possible that, although CLDTOP > ZLCL, the environmental dilution precludes the updraft from actually reaching saturation. In this condition the algorithm will produce mass flux profiles and shallow-cloud tendencies, but there will be no production of liquid water at all! This situation is seen in the figure in the region 2.2 K > DT > 1.5 K, where the cloud fluxes are active, but there is no liquid-water detrainment.

The second effect is also illustrated in Figure 3.3.4. The discrete character of CLDTOP produces abrupt changes in the status of the triggering condition, as can be seen in the regions around DT=2.2K (ON to OFF) and DT=2.55K (OFF to ON). Especially when the jump is from OFF to ON, the jump in the shallow-cloud parameterization tendencies can be large, because there already is a large updraft occurring when the ON condition is triggered.

Another discontinuity that the updraft algorithm possesses, but which has not been illustrated here, is in the definition of the thermodynamic properties of the cloud-initiating parcel. A discrete number of model layers near the surface is considered at each time step to define these properties, so that as the ZPBL grows continuously, the source layer grows discretely. That is, the source layer is defined as two or more discrete model layers, beginning from the surface. Understanding and correcting this problem is more straightforward than the problems with the cloud model described previously.

In summary the problems detected in the updraft algorithm of the shallow-cloud scheme can lead to discontinuities in the mass flux profiles that may arise from: (a) discrete definition of the updraft-property layer, (b) discrete definition of the releasing layer for cloud-initiating parcels, and (c) discrete definitions of the LET layer and the upper moist detrainment layer. Furthermore, a problem with the triggering condition has been identified. The use of ZLCL in defining the triggering condition appears to be inappropriate and unnecessary. The improved updraft scheme developed in this study tries to use corresponding continuous definitions for these significant levels in its calculations. Results with the revised scheme are presented below in the next sections.

3.3.1.2.3 Basic Results with the Improved Updraft Algorithm

The revised shallow-cloud updraft scheme tries to retain the physical basis of the original Kain-Fritsch scheme and its conservative properties, while also stressing the importance that its diagnosed mass fluxes should be smooth and continuous. To attain this goal, the revised scheme requires that the environmental and/or initial updraft properties must change in a smooth and continuous manner. Here, we only present the results for the same experimental conditions (Case 0) discussed in the previous section, but using the revised shallow-cloud updraft scheme.

Figure 3.3.5 shows the mass fluxes at level 11, using the revised updraft scheme (compare to Figure 3.3.2). The new results are indeed smooth and continuous. The results in the

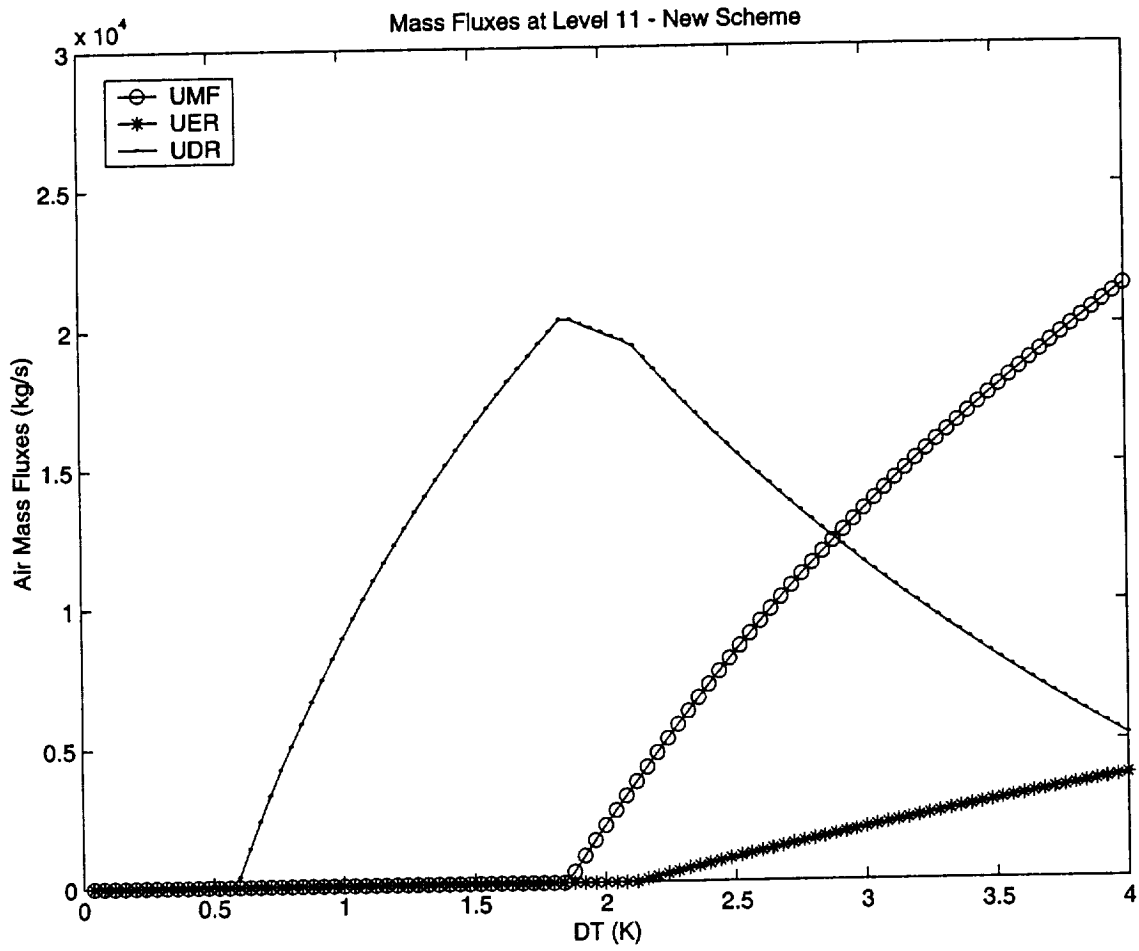

Figure 3.3.5 Diagnosed mass fluxes using the revised updraft algorithm at Level 11 as a function of perturbation temperature in the initial shallow-cloud updraft parcel. UMF: mass flux at the top of the layer. UER: entrainment flux in the layer. UDR: detrainment flux in the layer.

figure clearly show that, as DT grows, the evolution of detrainment rate, the increase of mass flux, and later the development of entrainment each have a simple physical meaning that is consistent with the expected behavior at a fixed height when the updraft grows in depth through that level.

Figure 3.3.6 shows the corresponding series of significant heights to be compared with Figure 3.3.3. The updraft top height, ZTOP, increases smoothly and continuously as the updraft-initiating parcel becomes warmer. This figure also shows some additional relevant heights that are diagnosed with the new scheme. Of particular interest is the height labeled as ZLCLU that corresponds to the height where the entraining/detraining updraft reaches saturation and condensed water begins to form. In this example, ZLCLU is significantly higher than ZLCL, the lifting condensation level based on the undiluted initial parcel (which of course is exactly the same as the one diagnosed by the original shallow-cloud scheme in Figure 3.3.3). Also, the level ZLET is the no-buoyancy level that corresponds to the LET level of the original scheme.

Finally, Figure 3.3.7 shows the total detrained water vapor and liquid water fluxes, which can be compared to the corresponding fluxes of Figure 3.3.4. The smoothness of the new fluxes contrasts dramatically with those calculated using the original scheme. In particular, the liquid water fluxes are non-zero in the entire domain of this test. Furthermore, they appear to have a weak minimum at intermediate values of initial parcel temperature (DT ~ 3 K). One would expect that the sources and tendencies derived from the shallow convection scheme will also behave in a more physically plausible way.

It is now possible to seek a physical interpretation for the behavior of the shallow

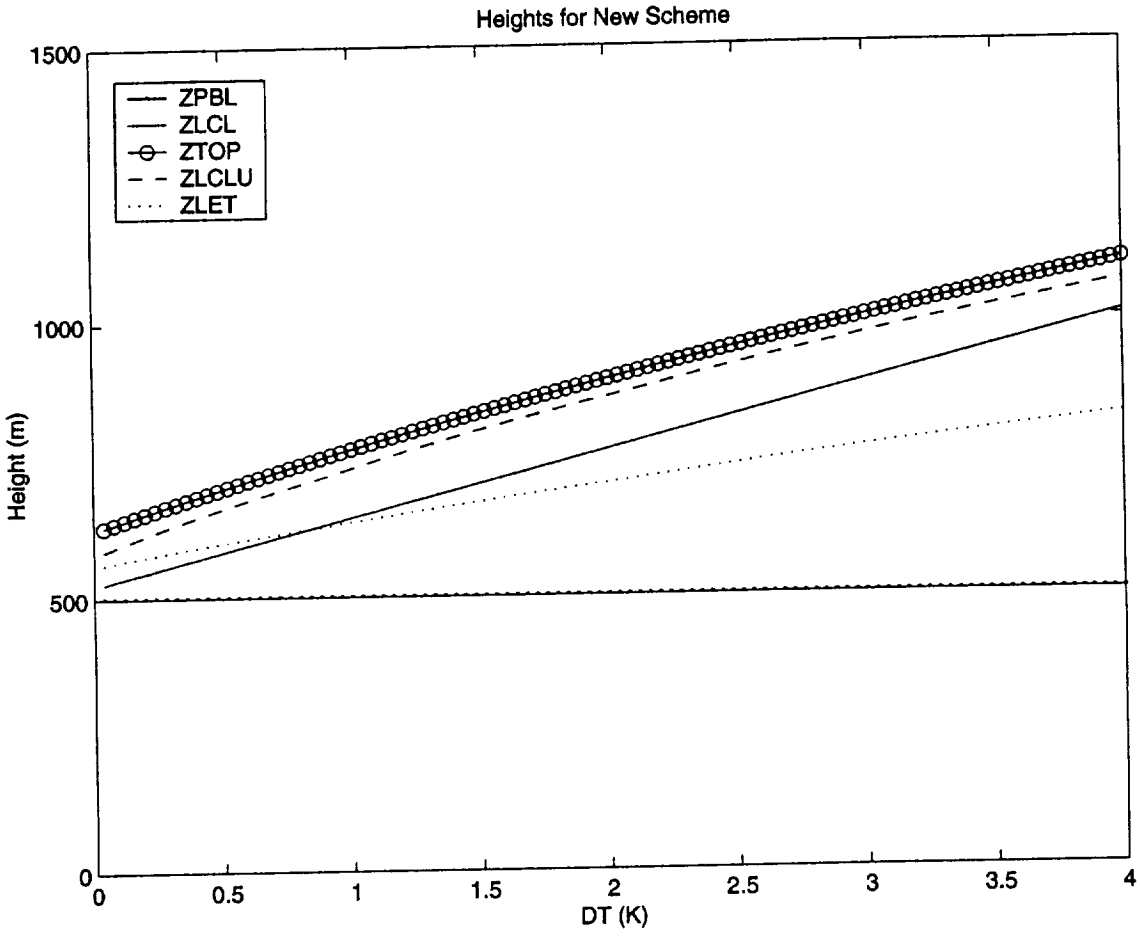

Figure 3.3.6 Important heights diagnosed with the revised shallow-cloud updraft algorithm. ZPBL: height of the PBL. ZLCL: lifting condensation level. ZTOP is the height of the updraft top. ZLCLU is the height where the updraft becomes saturated. ZLET. is the no-buoyancy level.

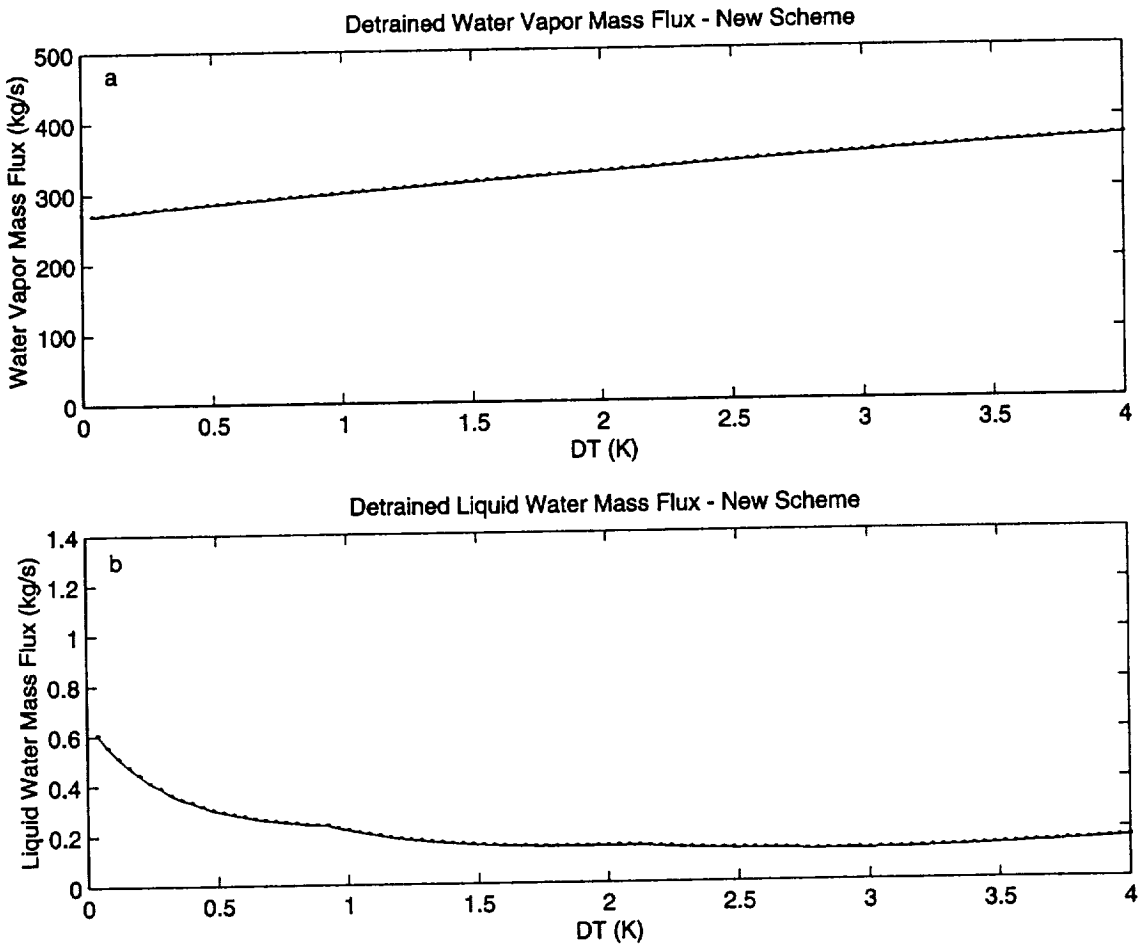

Figure 3.3.7 Sources of detrained updraft water vapor and liquid water diagnosed with the revised updraft algorithm. (a) Total detrained water vapor flux (regions with low values around DT = 2.5 K and DT = 4 K are not fed back to the calling model because CLDTOP<ZLCL). (b) Total detrained liquid water.

convection scheme, which was not possible in the original scheme due to the discontinuous behavior of the liquid fluxes in Figure 3.3.4b. A close inspection of Figure 3.3.7b, however, still shows some artifacts in the experiment series of fluxes, but they are minor compared to the original results and should not preclude the continuation of this work. Therefore, we were able to move forward with a broader series of tests.

3.3.1.2.4 Further Results with the Improved Updraft Algorithm

In this section we present results from the revised shallow-cloud updraft algorithm using changes in other conditions affecting the cloud-initiating parcels.

3.3.1.2.4.1 Case 1: Changes in the PBL Height

For Case 1, the PBL height was varied from 400 to 700 m in 100 steps of 3 m each. All other conditions were held constant as in Case 0. (Note that the temperature perturbation of the surface layer in Case 1 and the following cases is fixed at 2 K, exactly in the middle of the sensitivity range applied in the previous section.) Changing the PBL height directly affects the releasing height of the updraft-initiating parcel, as well as the other properties of the initial parcel. The latter effect is due to the fact that the scheme assumes that the initial parcel has the average properties of the surface-based source layer corresponding to 20% of the PBL depth. Figure 3.3.8 summarizes the results for this sensitivity test for the improved (left panels) and

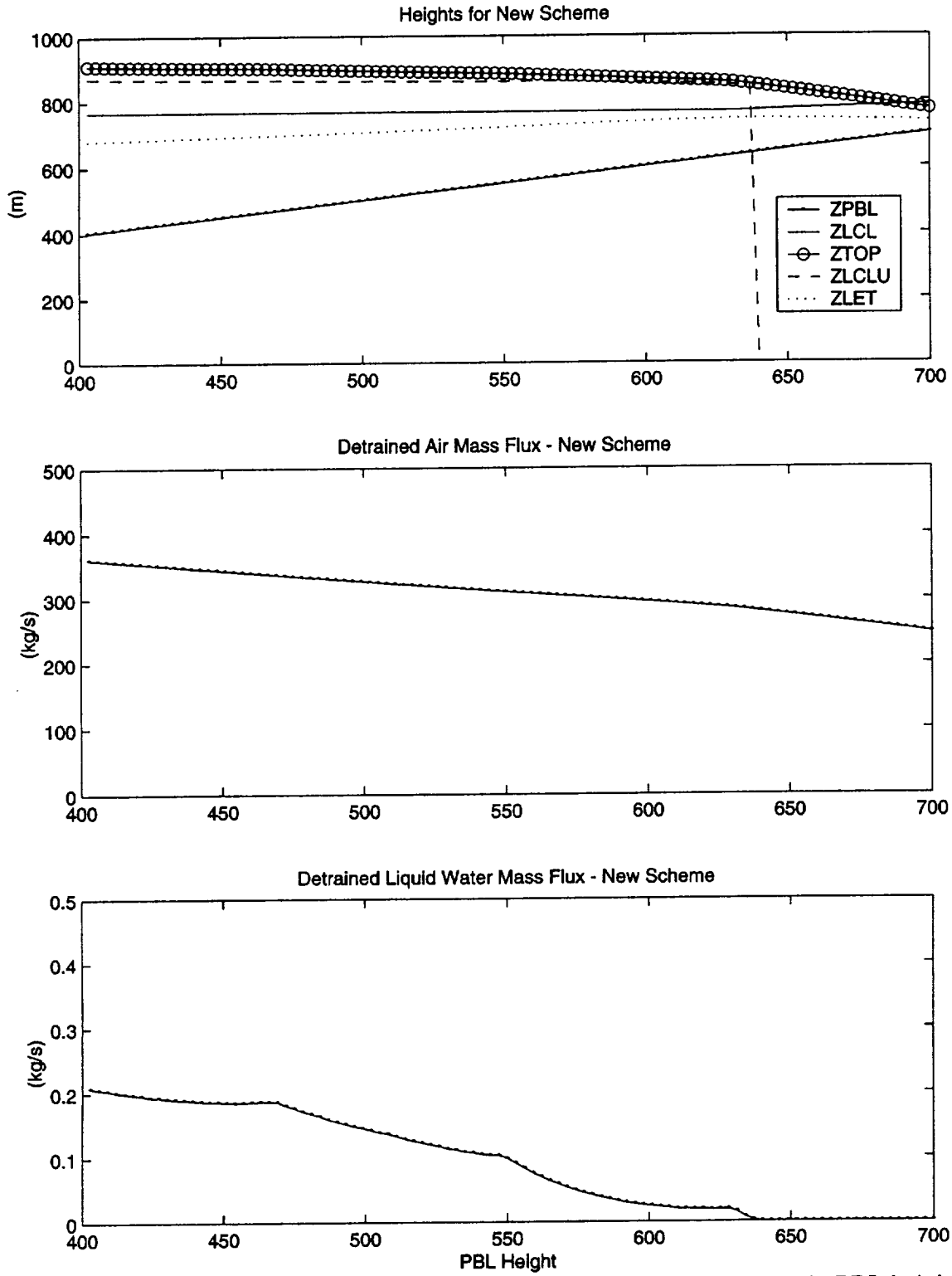

Figure 3.3.8. Results from the shallow convection as a function of change in PBL height. Figures 3.3.8a are computed with the revised updraft algorithm. Figures 3.3.8b are based on the original updraft algorithm. Upper panels are critical heights, middle panels are total detrained air mass fluxes, and lower panels are total liquid water fluxes.

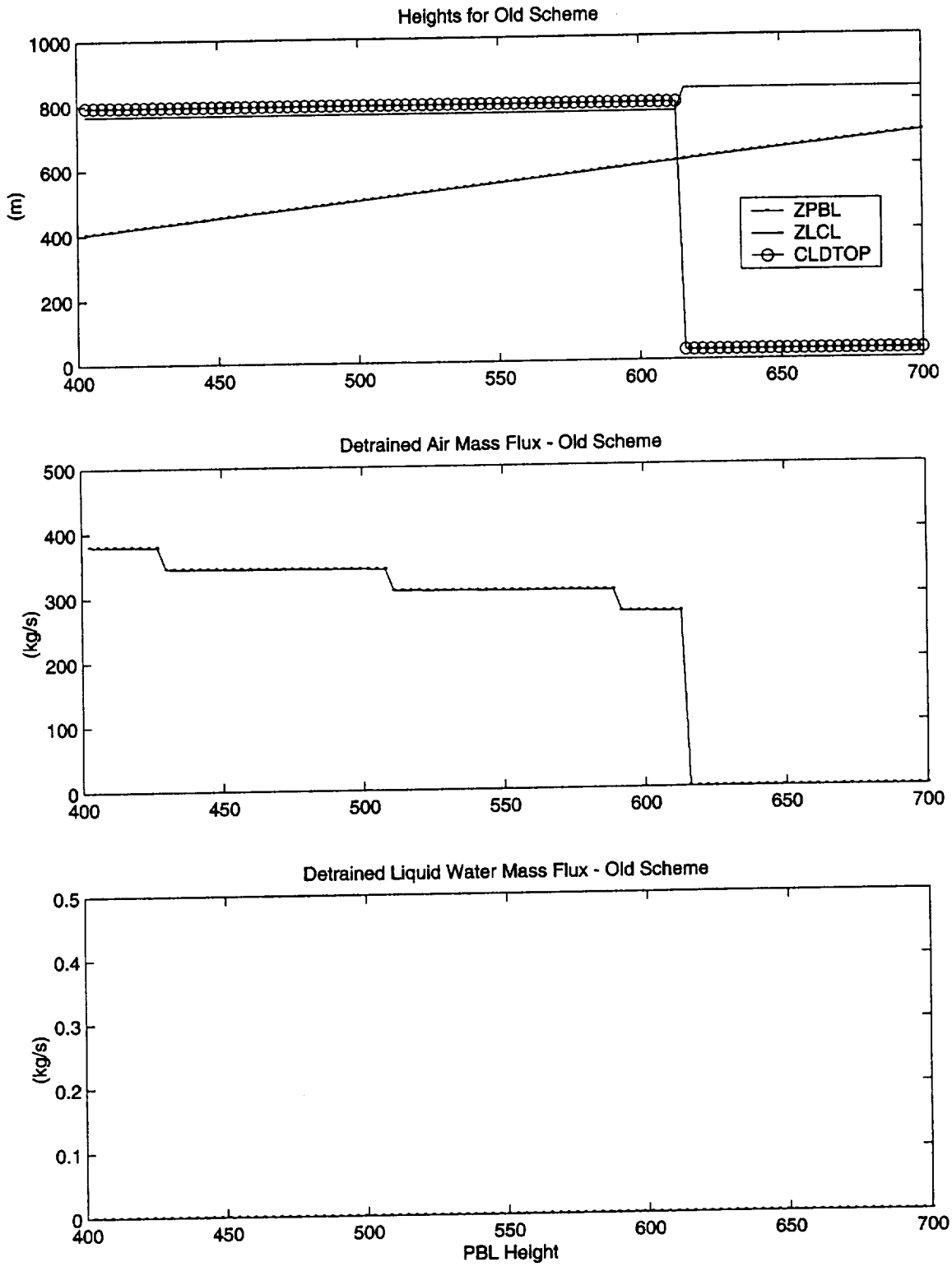

Figure 3.3.8b (Continued)

original (right panels) updraft algorithms. The upper panels show the series of heights for the two schemes. The old scheme maintains a constant cloud-top height until the diagnosed ZLCL abruptly rises at ZPBL~615 m (because an extra integer layer was considered in the surface source layer), causing the scheme to suddenly shut off. The revised scheme, however, diagnoses a gradual change in all heights, including a gradual increase of the ZLCL as the surface layer grows in depth along with the ZPBL.

The middle panels show the total detrained air mass fluxes. Again, the original scheme is highly discontinuous and the mass flux stops abruptly. The new scheme, on the other hand, diagnoses a gradual decrease of the mass fluxes as the release height increases. The physical reason for this is that the density of the initial parcel decreases as the release height slowly rises. Finally, the bottom panels show the diagnosed total liquid water detraining fluxes. In this case the old scheme does not produce any liquid water, although the updraft scheme is active in most of the series. Again, this is because of the dilution effect on the parcels and the detrainment algorithm used by the scheme. On the other hand, the new scheme produces a continuous source of liquid water as long as ZLCLU is lower than ZTOP (see upper panels). When that condition is not true the liquid fluxes drop smoothly to zero.

3.3.1.2.4.2 Case 2: Changes in Initial Vertical Speed

In the next series of tests the initial vertical speed of the updraft parcel is varied from 0.2 to 10.2 ms^{-1} in 100 steps of 0.2 ms^{-1} each, while all other conditions are held constant, as in the

temperature tests (Case 0). Figure 3.3.9 shows results for Case 2 based on the original and revised updraft algorithms. The most relevant differences produced by the improved algorithm are the smoothness in the liquid water fluxes and the height variations, compared to the original approach.

3.3.1.2.4.3 Case 3: Changes in Mixing Ratio of the Surface Layer

Finally, the tests are repeated, but now changing the water vapor mixing ratio of the surface source layer that helps to define the thermodynamic properties of the updraft-initiating parcel. All other variables in Case 3, plus the temperature of the source layer, are fixed as in the initial test, Case 0. The increase of the mixing ratio in the surface layer makes the LCL of the parcel (for both dilute and undilute versions) decrease and also induces a change in the saturation state of the updraft.

Figure 3.3.10 shows the results for this series of tests. The variation of the heights is more complex in this case. The ZLCL, as well as the ZLCLU, decreases as the initial parcel becomes more humid. When ZLCL becomes lower than ZPBL, the parcels are released from the ZLCL. The discontinuous behavior of the liquid water detrainment mass fluxes calculated with the old scheme represents a serious inconsistency that is greatly reduced with the revised scheme. Although the improved updraft algorithm is still not completely smooth, the mass flux perturbations are greatly reduced so that their impacts on the NBCs and the feedbacks to the resolved-scale tendencies should remain negligible.

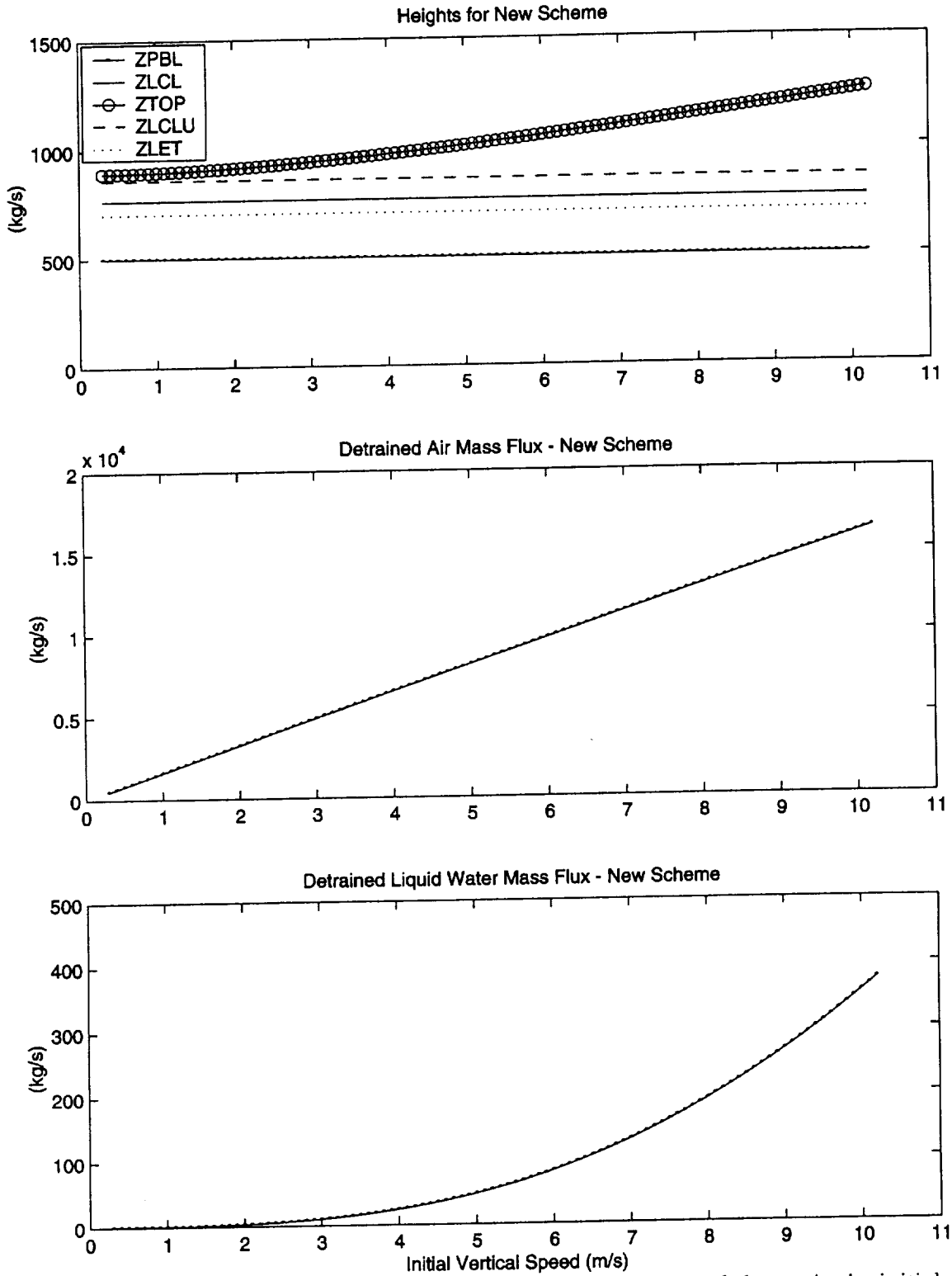

Figure 3.3.9. Results from the shallow convection as a function of change in the initial vertical speed of the updraft parcel. Figures 3.3.9a are computed with the revised updraft algorithm. Figures 3.3.9b are based on the original updraft algorithm. Upper panels are critical heights, middle panels are total detrained air mass fluxes, and lower panels are total liquid water fluxes.

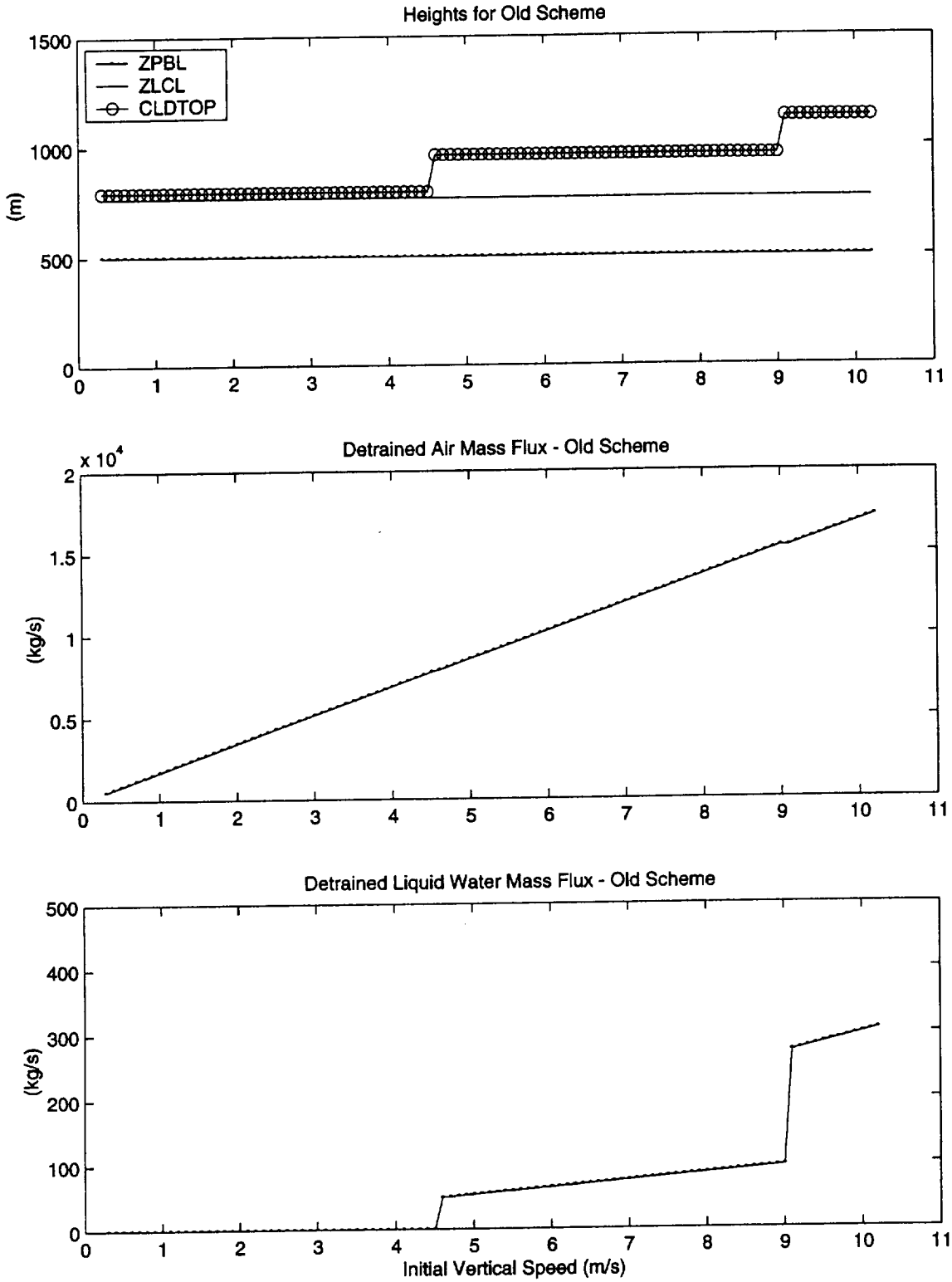

Figure 3.3.9b (Continued)

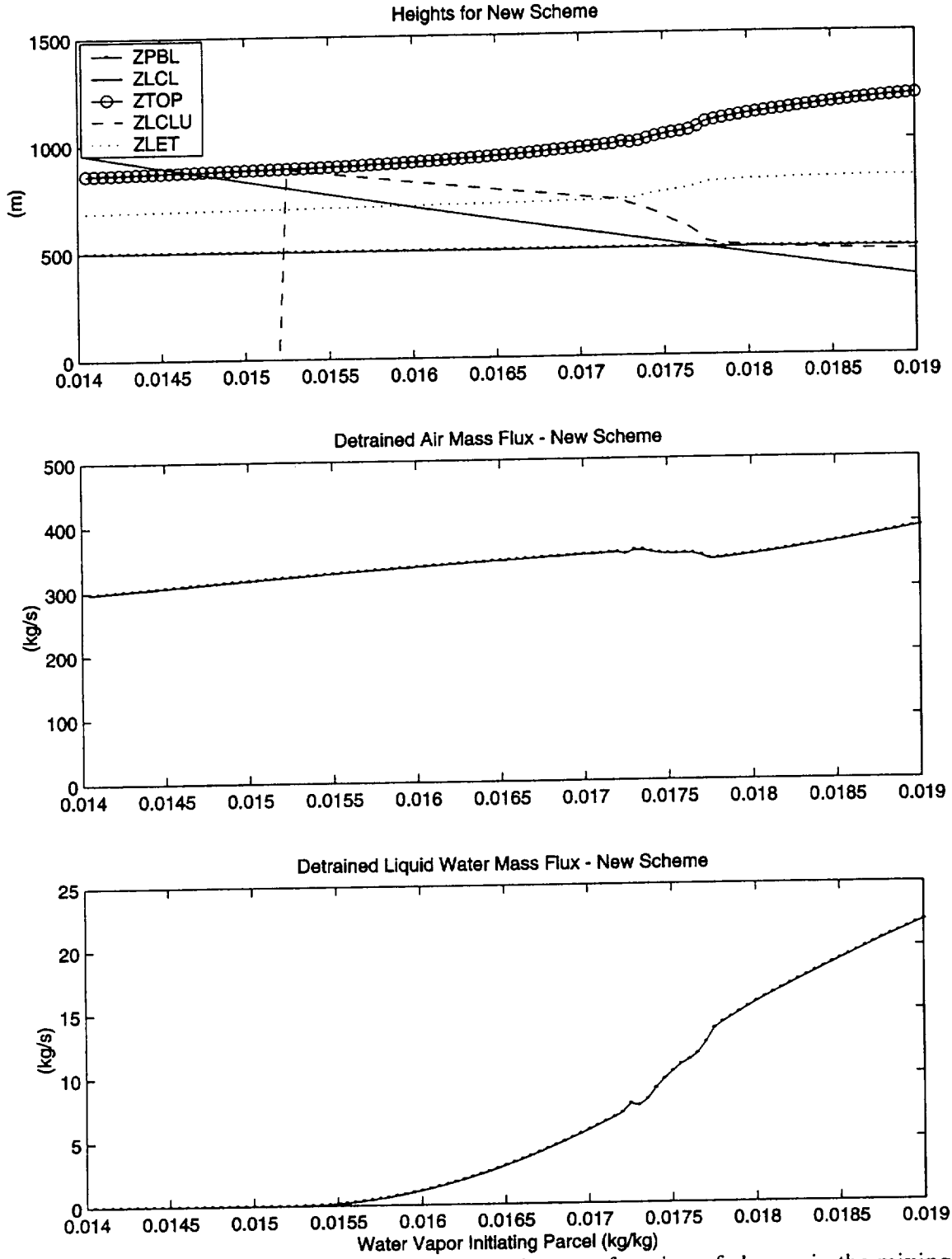

Figure 3.3.10 Results from the shallow convection as a function of change in the mixing ratio of the surface layer. Figures 3.3.10a are computed with the revised updraft algorithm. Figures 3.3.10b are based on the original updraft algorithm. Upper panels are critical heights, middle panels are total detrained air mass fluxes, and lower panels are total liquid water fluxes.

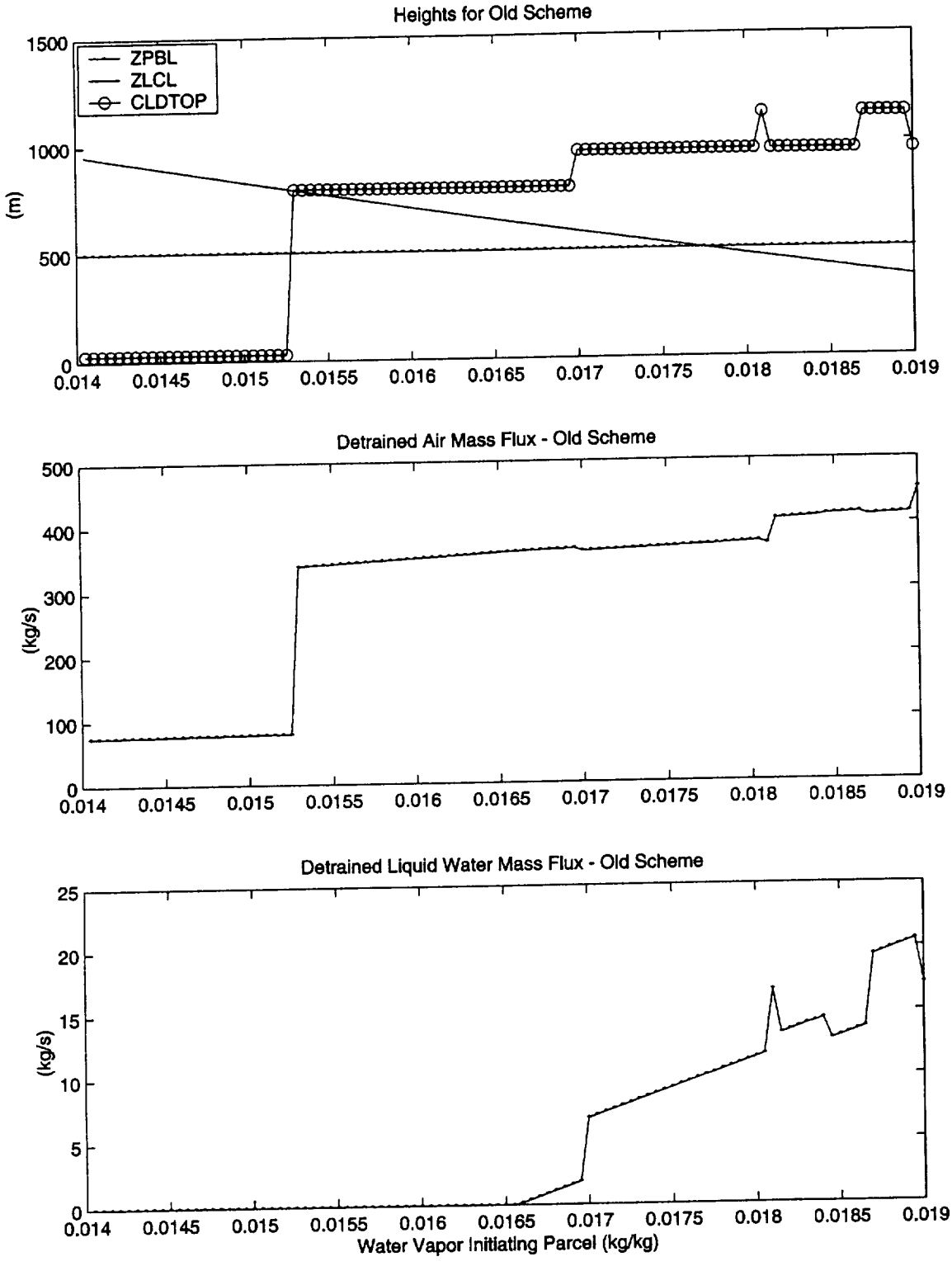

Figure 3.3.10b (Continued)

3.3.1.3 Improvements to the Closure Algorithm

With the improved updraft algorithm it is possible now to test the second part of the shallow-convection code. In this part, the closure algorithm is used to derive tendencies for the environmental thermodynamic profiles based on the updraft mass fluxes. The available buoyant energy (ABE) closure algorithm (ABE is the same as CAPE used in the Kain-Fritsch deep convection scheme) determines the amount of convection according to the change in ABE induced by the unit updraft. In the shallow convection scheme this ABE closure is supplemented with a TKE closure that determines the amount of convection according to the TKE in the boundary layer. The TKE closure is most appropriate for very shallow clouds driven primarily by boundary layer turbulence. For intermediate cloud depths, a hybrid regime is defined in which the amount of convection is interpolated between the rates calculated by the ABE and the TKE closures.

3.3.1.3.1 Case 0: Results with Original Closure Algorithm

We next applied the original closure algorithm to the same Case 0 discussed in Section 3.3.1.2 in which the temperature of the surface layer is varied in a set of 100 small increments of 0.04 K. Here, we used the revised updraft algorithm from that previous section to derive the updraft mass fluxes that are input to the closure algorithm. Results are presented in Figures 3.3.11 and 3.3.12.

Figure 3.3.11a shows the ABE calculated by the updraft algorithm for the undiluted

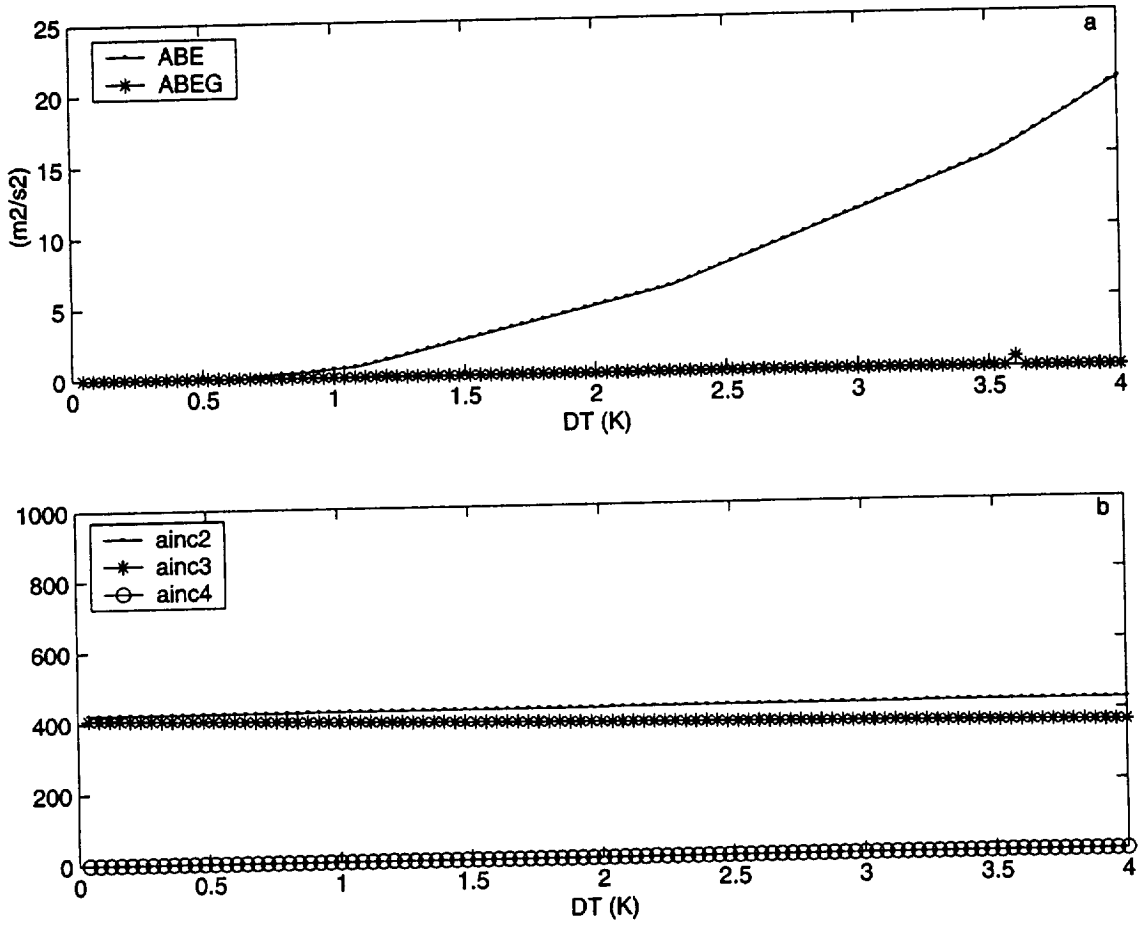

Figure 3.3.11 Results for Case 0 using the original closure algorithm. (a) ABE: buoyant energy obtained in undilute updraft algorithm. ABEG: buoyant energy calculated in the original closure algorithm. (b) Updraft multiplication factors calculated in the original closure algorithm. AINC2 is the multiplication factor calculated with the shallow TKE closure, AINC4 is calculated with the ABE closure, and IINC3 is the multiplication factor for the hybrid (transition) closure.

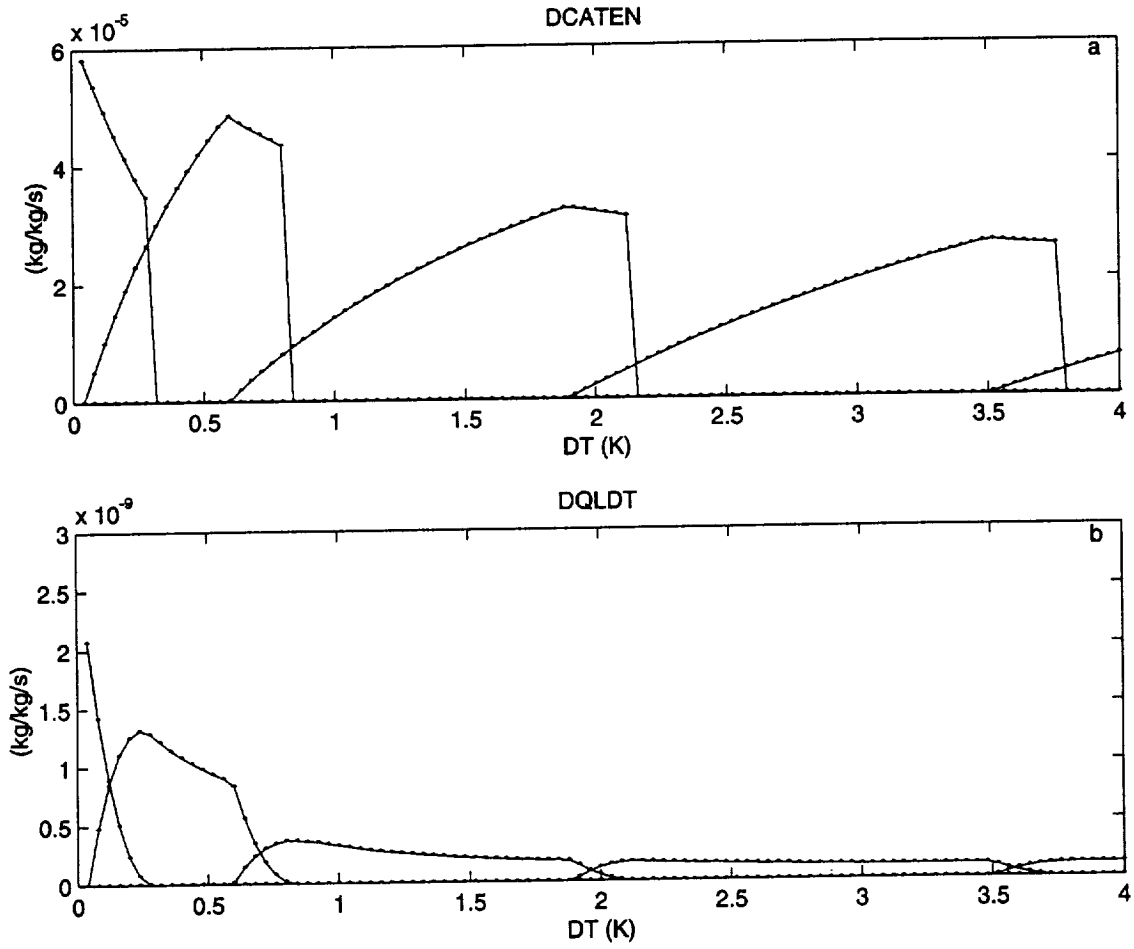

Figure 3.3.12 Neutrally buoyant cloud source rates, based on detrainment from the shallow cloud updraft calculated with the original closure algorithm for Case 0. (a) Cloud area fraction source rate. (b) Liquid water source rate.

parcel used to compute the updraft. Also shown is the ABE diagnosed by the original closure algorithm (ABEG). Note that there is a large discrepancy between these two values of ABE. The reason is that the computation of the ABE in the closure algorithm is performed for a parcel starting at the undilute LCL, without regard to the fact that the parcel in the updraft algorithm can originate at the PBL. This condition occurs quite often, whenever the LCL is above the PBL. It represents a lack of consistency between the two sections of code that can have serious consequences because the ABE closure is highly dependent on the difference between the updraft ABE and the closure ABE (ABEG). In the original code both buoyant energies often are calculated for parcels with different properties! The apparent solution for this inconsistency is to use the same parcel in the closure section as it was used in the updraft scheme. Figure 3.3.11b shows the convective amplification factors calculated by the three shallow-cloud closure regimes. These factors are the numbers by which the initial updraft mass flux has to be multiplied in order to attain closure. AINC2 is the multiplication factor calculated for the TKE closure, AINC4 is the factor calculated for the ABE closure, and AINC3 is the hybrid (or, transition) closure factor (the one that would be used in the case shown in the figure). The figure shows that values of AINC2 are almost constant for all 100 experiments in the series. The values of AINC4 are very close to zero, but are not exactly zero. In each case the original closure algorithm sees an initial non-zero value of ABE coming from updraft algorithm and then calculates a new ABEG which is zero (because a different parcel was used). In effect, the closure algorithm thinks that it has overestimated the convective factor, AINC4, and therefore reduces the factor by 50%. The procedure is repeated until the maximum number of iterations is reached (10) and that value is selected as the final AINC. The transition factor for the hybrid closure, AINC3, is close to AINC2 with a decreasing tendency as the temperature perturbation

increases.

Figure 3.3.12 shows the source rates for the key NBC (neutrally buoyant cloud) variables diagnosed by the original closure scheme. Figure 3.3.12a shows the source rate of cloudy area fraction and Figure 3.3.12b is the source rate for liquid water. The series shows the rates for each of the different layers at which updraft mass is detrained, but the individualization of each layer is irrelevant for the present discussion. The salient feature of Figure 3.3.12a is the discontinuous series of the cloudy area source term. With all the effort put into producing continuous updraft fluxes, one wonders how these source rates can collapse abruptly to zero. The reason lies in the algorithm that computes the tendencies of the NBC variables. We saw in the section discussing the updraft algorithm that an updraft can exist without producing any liquid water. That means that one can have a non-zero detrainment mass flux with a zero liquid-water detrainment rate. The original code assumed that any detrainment flux produces a cloudy area fraction, which is not the case when the detrainment has no liquid water. As the liquid water source term in Figure 3.3.12b goes to zero the cloud-area source term may not go to zero, which means that a "dry" detrainment is being computed as a source for the cloudy area! The solution to this problem requires just to keep track of the effective air mass flux that is detrained when liquid water is present and to use only this portion to compute the cloud area source term.

3.3.1.3.2 Case 0: Results with Revised Closure Algorithm

Figures 3.3.13 and 3.3.14 show results obtained with the revised closure algorithm described above. The ABE series shown in Figure 3.3.13a is the same as that shown for the

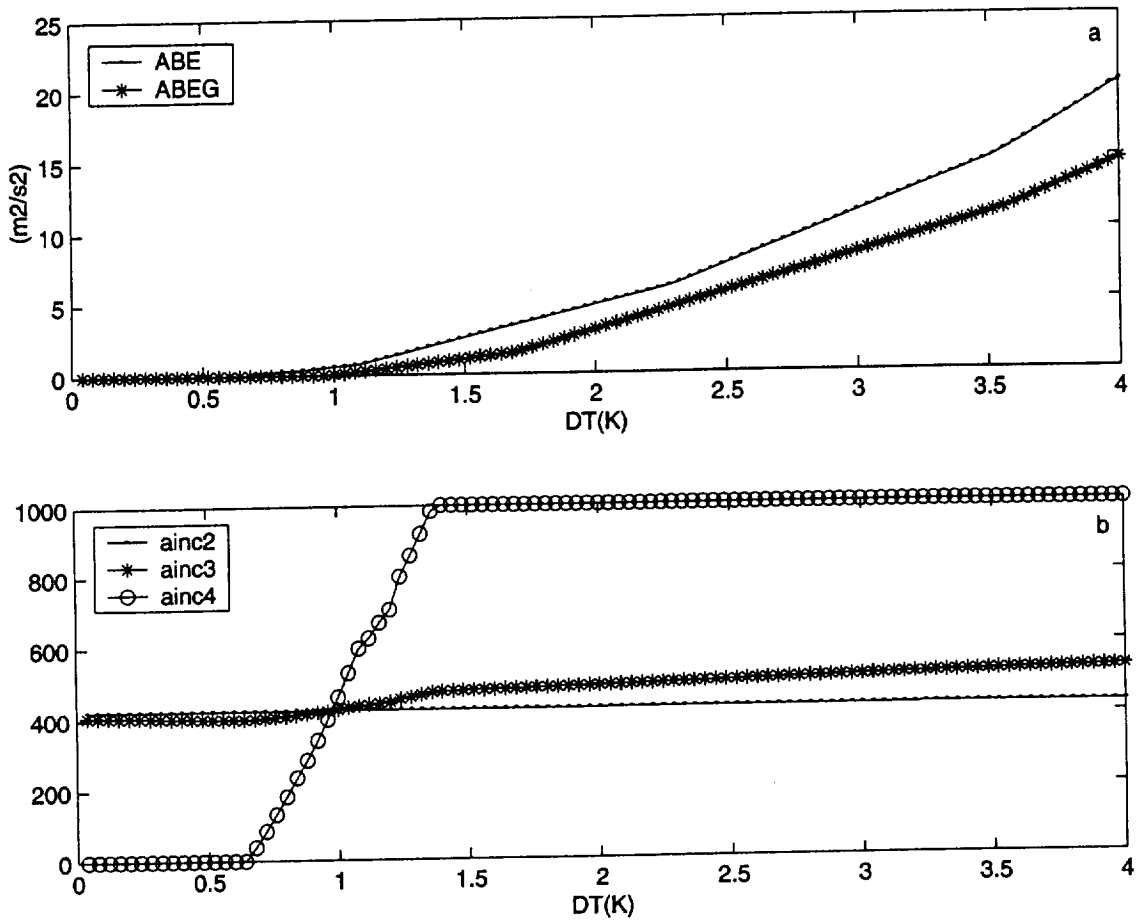

Figure 3.3.13 Results for Case 0 using the revised closure algorithm. (a) ABE: buoyant energy obtained in undilute updraft algorithm. ABEG: buoyant energy calculated in the original closure algorithm. (b) Updraft multiplication factors calculated in the original closure algorithm. AINC2 is the multiplication factor calculated with the shallow TKE closure, AINC4 is calculated with the ABE closure, and IINC3 is the multiplication factor for the hybrid (transition) closure.

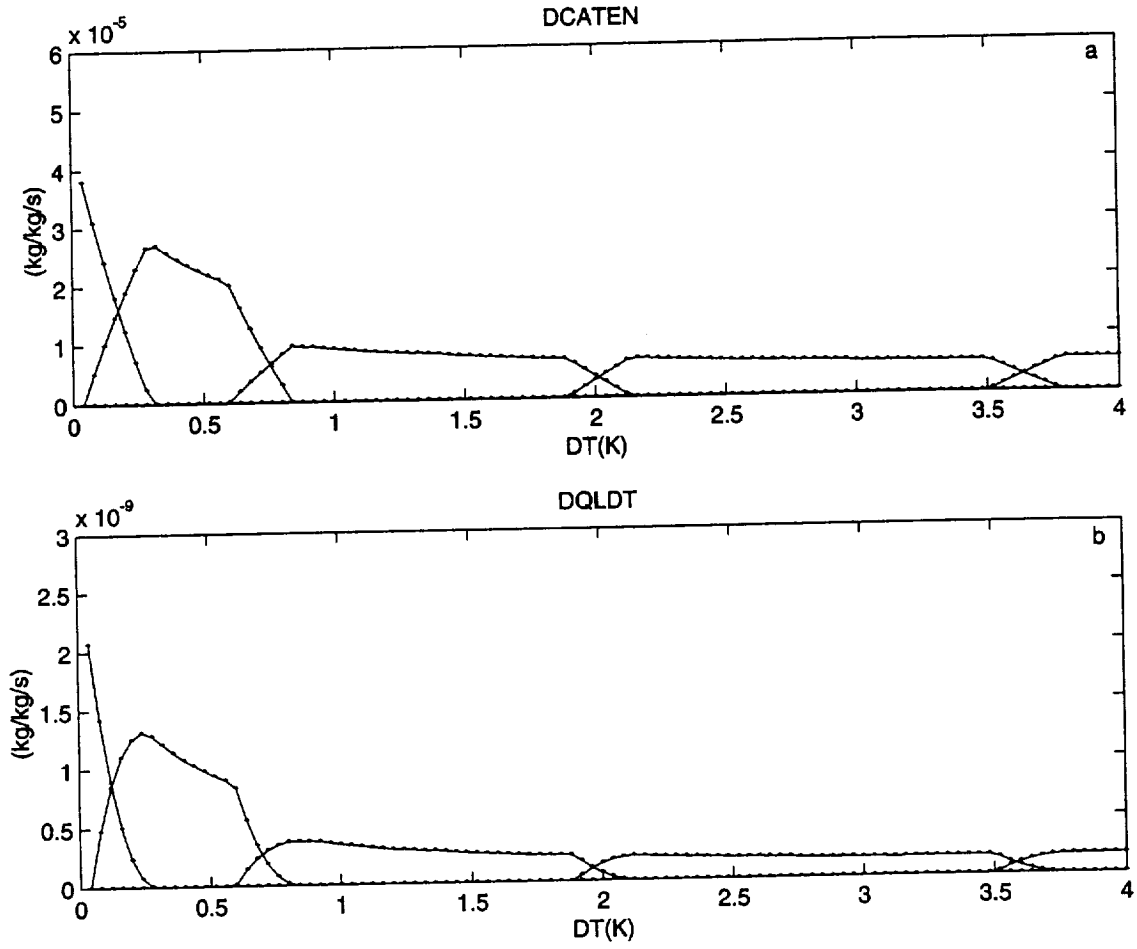

Figure 3.3.14 Neutrally buoyant cloud source rates, based on detrainment from the shallow cloud updraft calculated with the revised closure algorithm for Case 0. (a) Cloud area fraction. source rate. (b) Liquid water source rate.

original scheme in Figure 3.3.11a, because both are based on the same shallow-cloud updraft scheme. However, although the final ABEG series is lower than ABE, it is still non-zero. The similarity in the shapes of the ABE and ABEG series in Figure 3.3.13a is an indication that the same parcel properties and updraft algorithm are being used to calculate ABE in the updraft algorithm and in the closure algorithm. Meanwhile, Figure 3.3.13b shows the convective factors calculated with the revised closure scheme. The TKE convective multiplication factor, AINC2, is similar to that obtained with the original scheme. However, the ABE convective factor, AINC4, is substantially different. Instead of remaining zero it increases rapidly as the temperature perturbation increases, from zero to the maximum allowed value of 1000. Thus, the resulting hybrid-closure multiplication factor, AINC3, increases slightly instead of decreasing, as occurred with the original scheme (compare to Figure 3.3.11b). The fact that the convective fluxes grow when calculated according to the revised closure algorithm as the initial updraft parcel becomes warmer has more physical appeal than the opposite case found with the original closure algorithm.

Next, Figure 3.3.14 shows the source rates for the NBC determined from the shallow-cloud updraft variables, as calculated according to the revised closure algorithm. Now the cloudy-area tendencies in Figure 3.3.14a are continuous and go to zero as the liquid-water source rates go to zero in Figure 3.3.14b. Again, this is physically more consistent behavior than the results obtained with the original algorithm.

At this point it is illustrative to check the updraft and closure algorithms to see exactly what type of thermodynamic profiles they produce and to see how the reduction in ABE is being accomplished. Figure 3.3.15 shows a Skew-T diagram with results based for Case 0 and for the

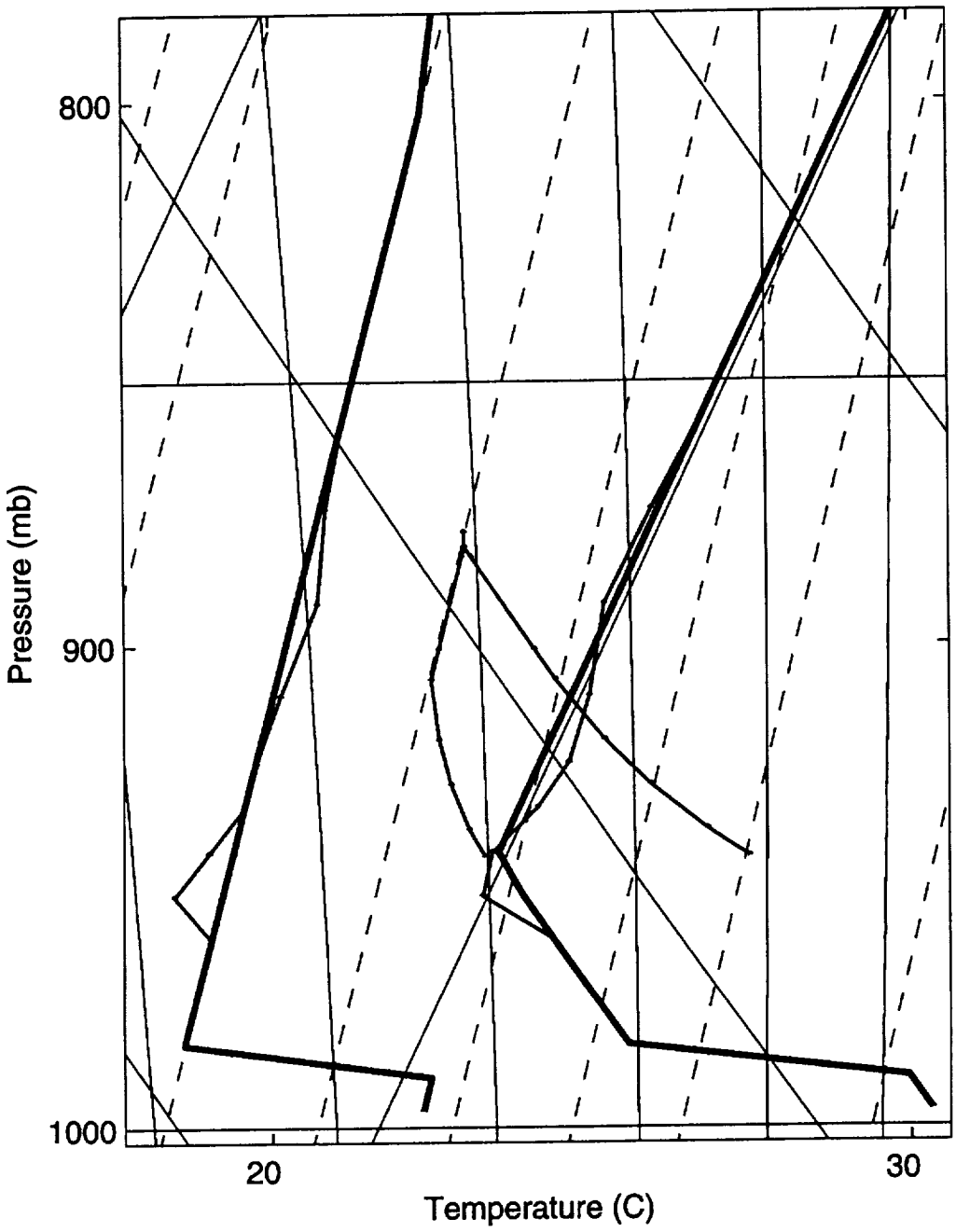

Figure 3.3.15 Skew-T diagram for results with revised algorithms in Case 0, shown for the largest surface temperature perturbation (4 K). A description of the lines is given in the text.

maximum perturbation in the surface layer temperature (i.e., DT=4 K). The bold lines in the figure represent the environmental temperature and dew point profiles. The fine line soundings correspond to the final soundings calculated with the closure scheme (i.e., the soundings towards which the closure scheme will calculate its tendencies). The short fine lines correspond to the parcel trajectories in temperature and dew point for the shallow-cloud updraft parcel calculated with the updraft algorithm. Several features are to be noted in this figure. First, the ABE is calculated (approximately) as the positive area between the parcel temperature path and the environmental temperature sounding. We see then that the final environmental sounding indeed has a lower ABE than the initial sounding. The decrease in ABE, however, is not large. Also, just by looking at the initial and final environmental temperature profiles, one can see an upper level cooling and a lower level warming that are induced by the convective scheme. This suggests a tendency for the profile to destabilize due to the convection! In other words, by reducing the ABE relative to the updraft parcel, the instability of the environmental sounding actually is increased. This is a very interesting result and appears to match the expected behavior of shallow cloud fields that, in certain circumstances, they can tend to destabilize the initial environment. Given that the initial temperature profile in these experiments is isothermal above the boundary layer (i.e., very stable) and that convection should move the thermal profile towards a moist adiabatic condition, the result in Figure 3.3.15 is indeed consistent with expectations.

A final feature to observe in this diagram is the tendency for the environmental soundings below the shallow-cloud updraft. Strong drying and cooling can be observed in the region just below the updraft base near 960 mb. The reason for this is that the source of the updraft mass flux is located there, but the thermodynamic properties of the shallow-cloud updraft are taken

from the surface layer (985-1000 mb). Therefore, when the surface layer is moister and warmer than the mass-source layers, the energy and water budget equations can induce strong tendencies in the mass-source layers. This behavior may not be physically realistic. Perhaps a better approach would be to assign the full boundary layer (BL) to be the source of the updraft mass flux. In this way the effect on the tendencies would be reduced and probably would be smoothed out quite easily later on by the mixing forced by the model's turbulence parameterization.

3.3.1.3.3 Further Results with Revised Closure Algorithm

3.3.1.3.3.1. Revised Closure Algorithm in Case 1

We present here results of an experiment series based on the revised shallow-cloud updraft and closure algorithms for Case 1, in which the PBL height was increased in steps of 3 m from 400 to 700 m. Figure 3.3.16 shows the series of ABE (Fig. 3.3.16a), convective multiplication factors (Fig. 3.3.16b), and the NBC source rates for cloud area and liquid water content (Figs. 3.3.16c and d). For lower parcel releasing heights (i.e., at the lower values of the BL height), the parcels have non-zero ABE that decrease slowly as the PBL grows. Figure 3.3.16b shows that the convection multiplication factors diagnosed by the revised closure algorithm also decrease slightly for shallow PBLs. For larger PBL heights (>550 m) the initial ABE drops rapidly to zero and the convective factors also decrease, especially AINC4, which comes from the ABE closure. The hybrid-closure multiplication factor, AINC3, is only slightly

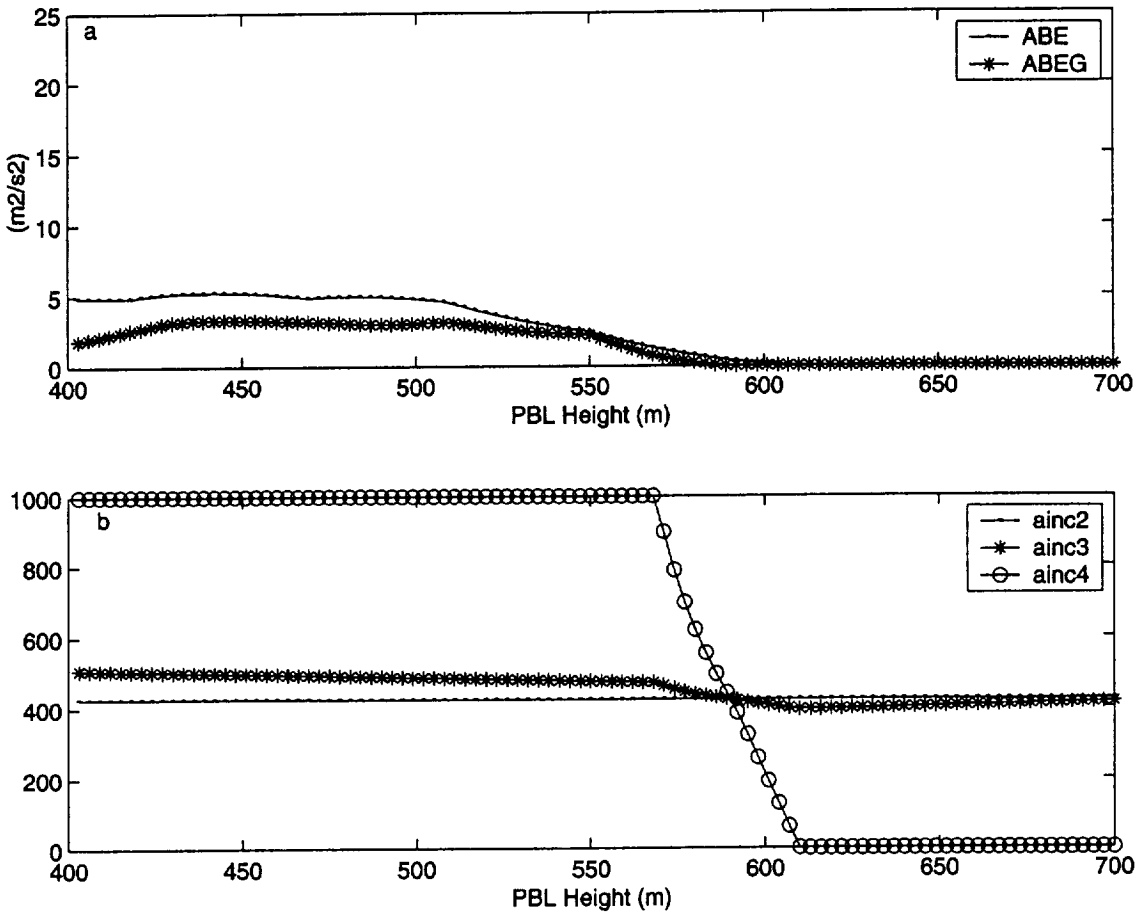

Figure 3.3.16 Results for the shallow convection scheme with the revised closure algorithm in Case 1. (a) Initial and final buoyant energies, (b) Convective multiplication factors.

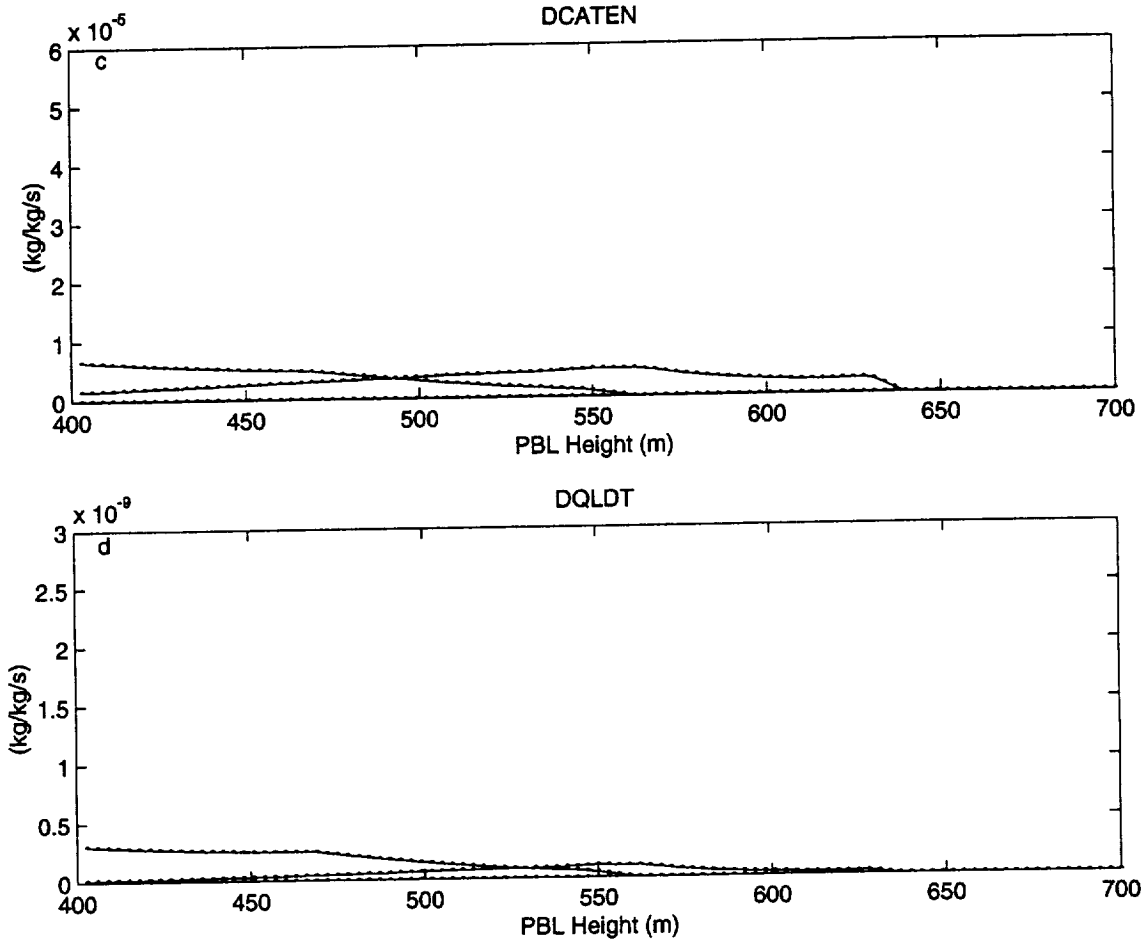

Figure 3.3.16 (Continued) Results for the shallow convection scheme with the revised closure algorithm in Case 1. (c) Cloudy area source rates, (d) Liquid water source rates.

reduced because it is dominated by the TKE closure, which is more or less constant in this case.

Figure 3.3.17 shows Skew-T diagrams for the lowest and highest PBL heights considered in the Case 1 computations. In the first case (left panel) the initial ABE is related to the positive area between the updraft path and the original temperature profile. This ABE decreases in the target environmental profiles as there is warming in the lower levels of the updraft layer. The updraft parcel path can be seen to reach saturation at ~900 mb. Intense drying and cooling is seen at ~960 mb (below the updraft base), which once again is related to the definition of the updraft mass-source layer. In the right panel of Figure 3.3.17, results for the highest PBL height are illustrated., Here, the updraft parcel is everywhere cooler than the environment, which explains the zero ABE diagnosed in this case (see Fig. 3.3.16a). The TKE closure still diagnoses a convective flux that slightly modifies the environment, even though the updraft fails to reach saturation.

3.3.1.3.3.2 Revised Closure Algorithm in Case 2

Results for Case 2, in which the initial vertical velocity of the shallow-cloud updraft parcel is incremented between 0.2 and 10.2 ms^{-1}, can be seen in Figures 3.3.18 and 3.3.19. The series of ABE in Figure 3.3.18 shows that the final ABEG is always lower that the initial ABE, and in most cases it is zero. The convective multiplication factors in Figure 3.3.18b show that AINC4 decreases as the initial vertical velocity increases. This is natural because, as the initial speed of the parcel increases, so also does the mass flux of the "unit" updraft. Thus, the final updraft mass flux corresponds to a decreasing amplification factor for the initial updraft.

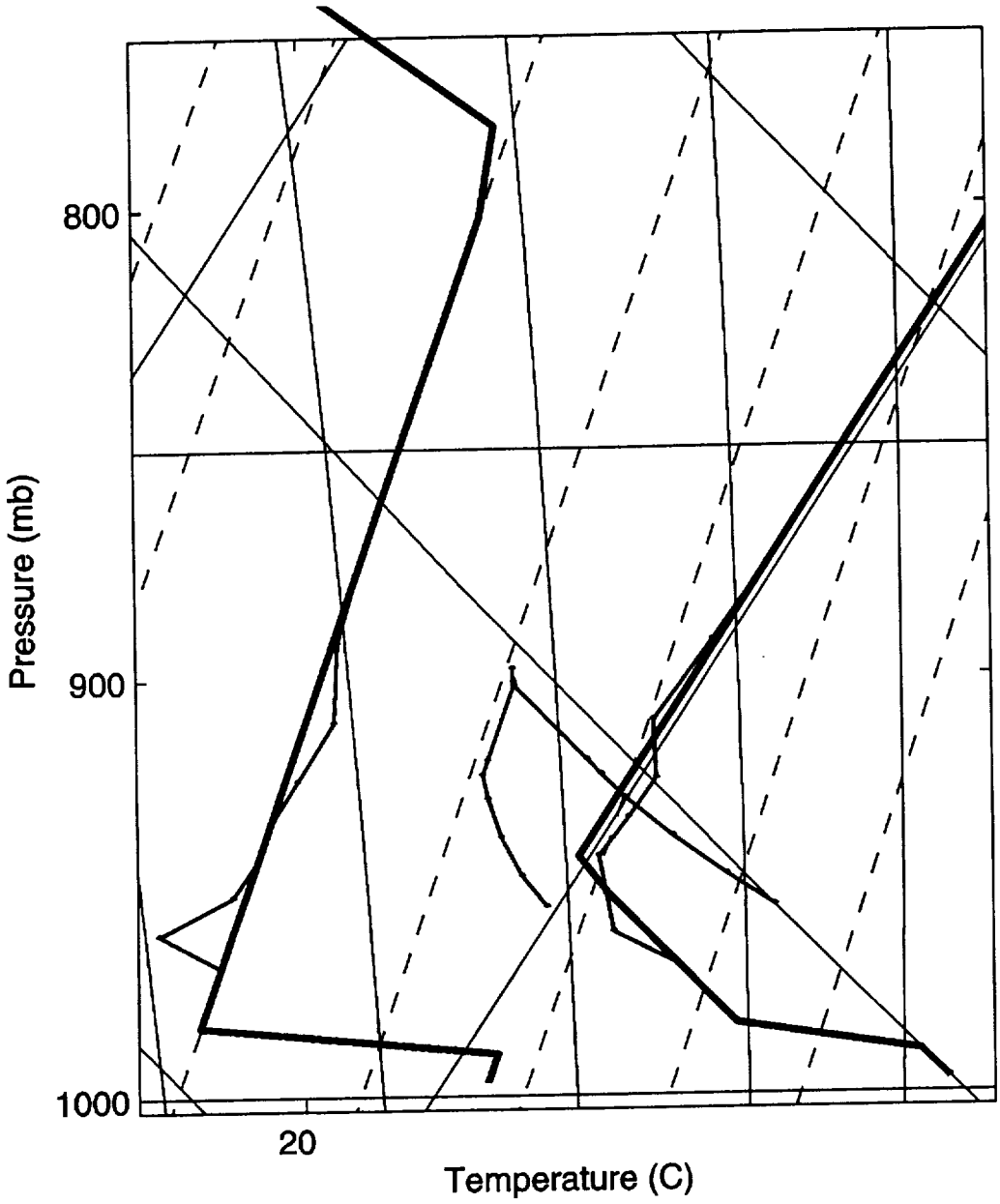

Figure 3.3.17 Skew-T diagram for shallow convection results with the revised algorithms for Case 1. (a) Using lowest PBL height. (b) Using highest PBL height.

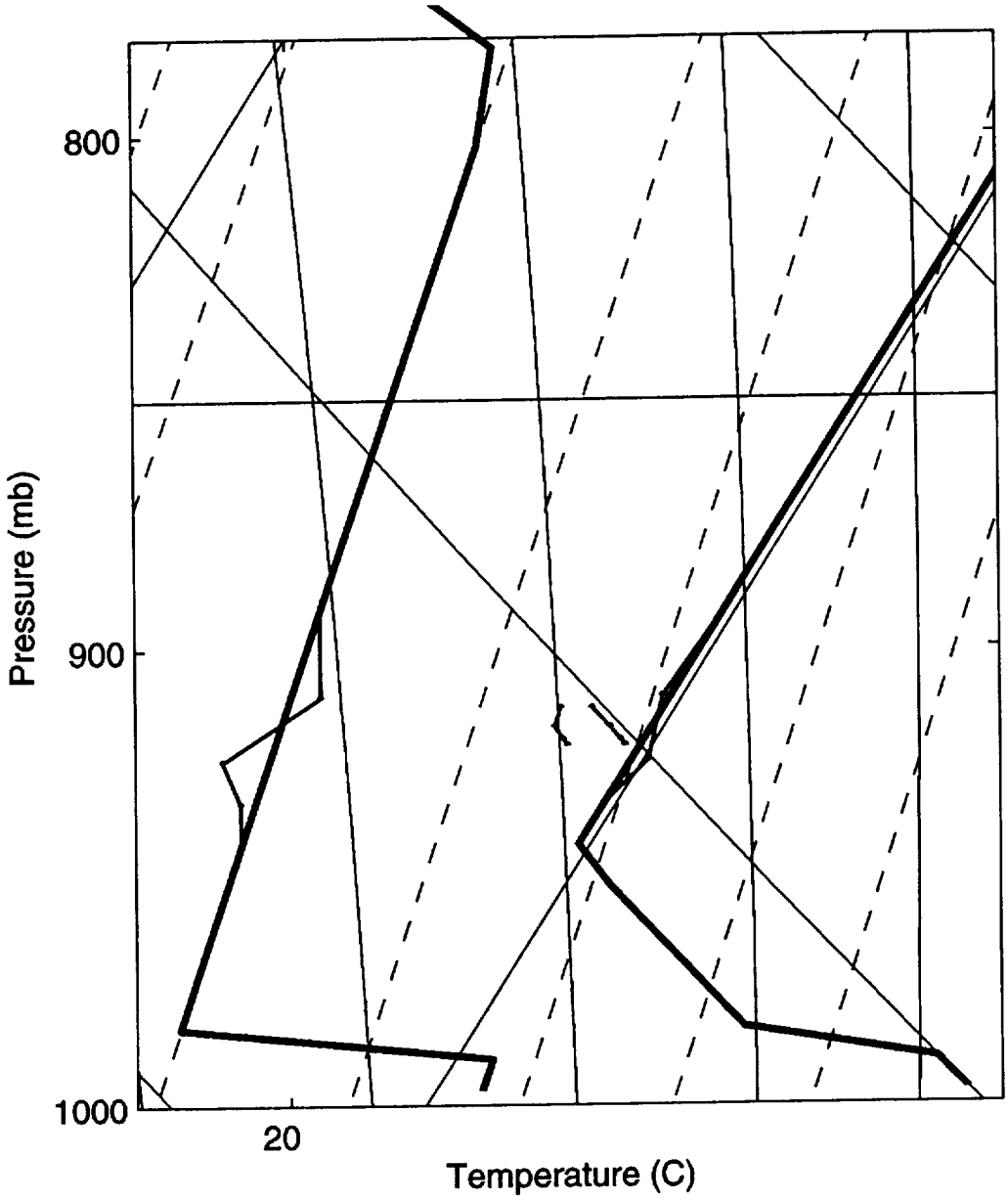

Figure 3.3.17 (Continued) Skew-T diagram for shallow convection results with the revised algorithms for Case 1. (a) Using lowest PBL height. (b) Using highest PBL height.

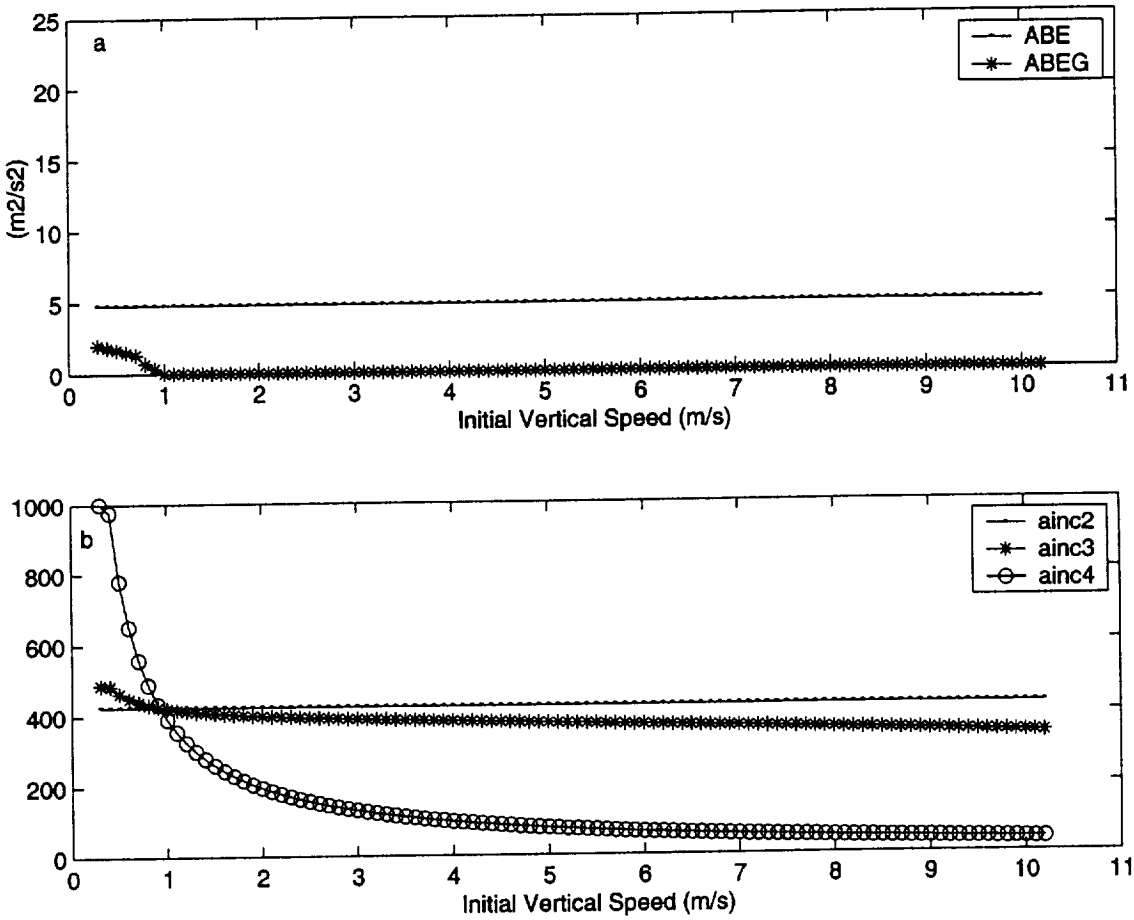

Figure 3.3.18 Results for the shallow convection scheme with the revised closure algorithm in Case 2. (a) Initial and final buoyant energies, (b) Convective multiplication factors.

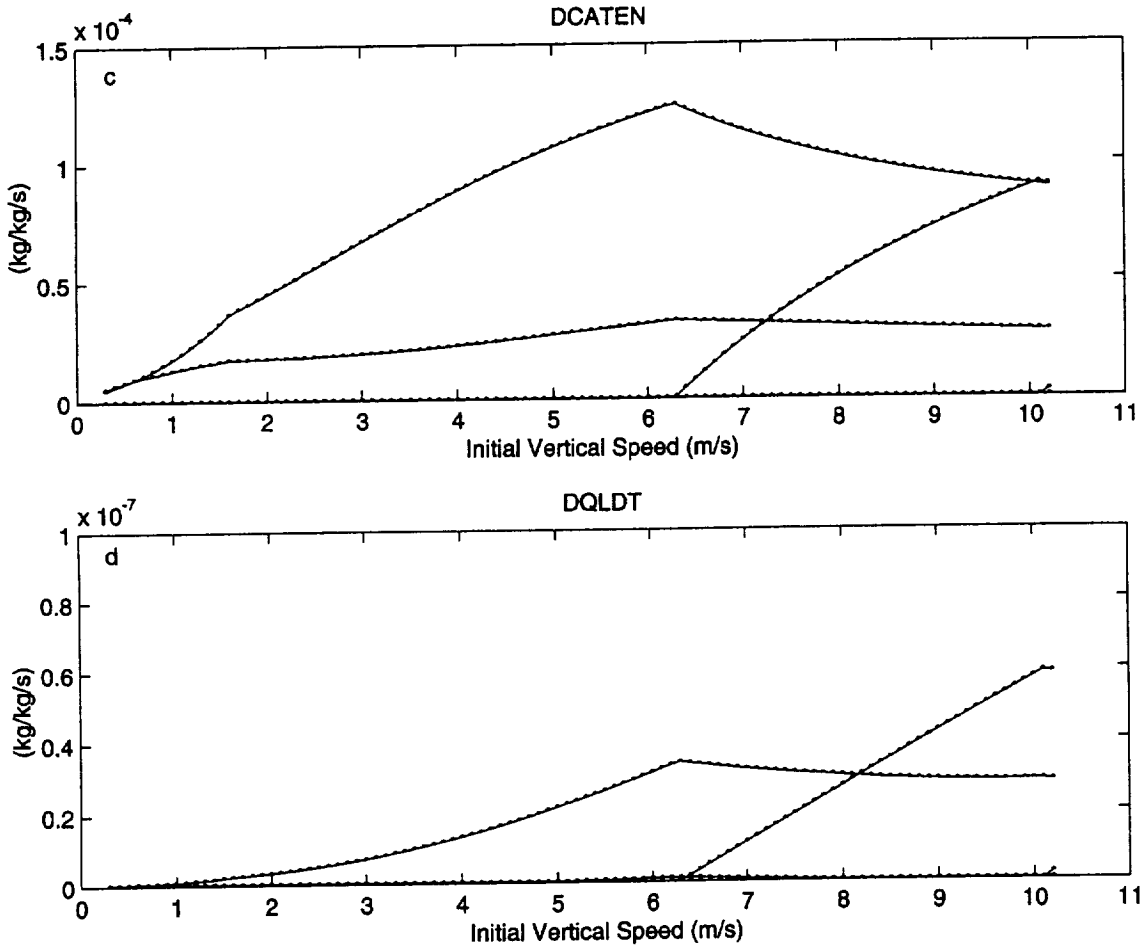

Figure 3.3.18 (Continued) Results for the shallow convection scheme with the revised closure algorithm in Case 2. (c) Cloudy area source rates, (d) Liquid water source rates.

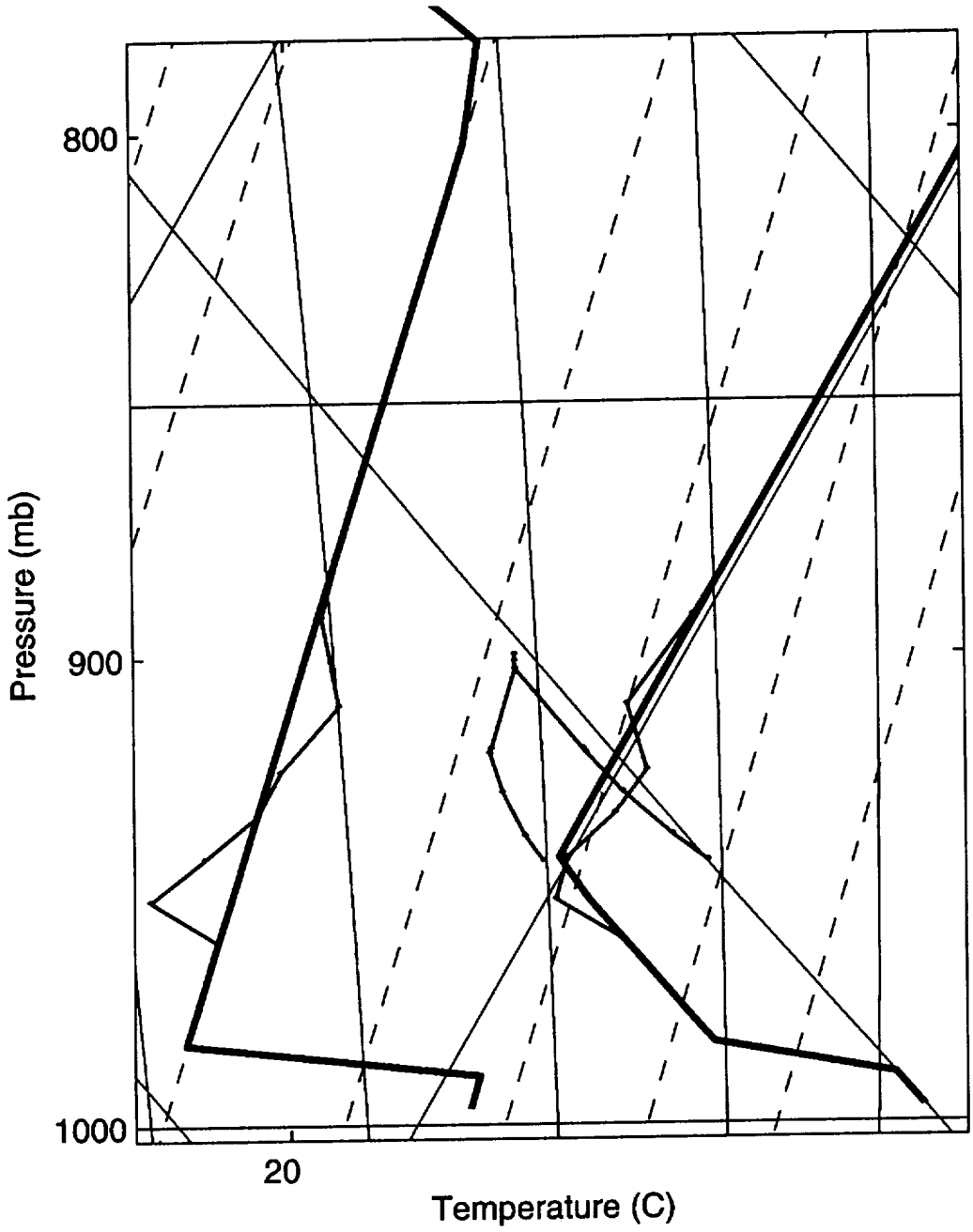

Figure 3.3.19 Skew-T diagrams for results of shallow convection scheme with the revised algorithms for Case 2. (a) Using smallest initial vertical speed. (b) Using maximum initial vertical speed.

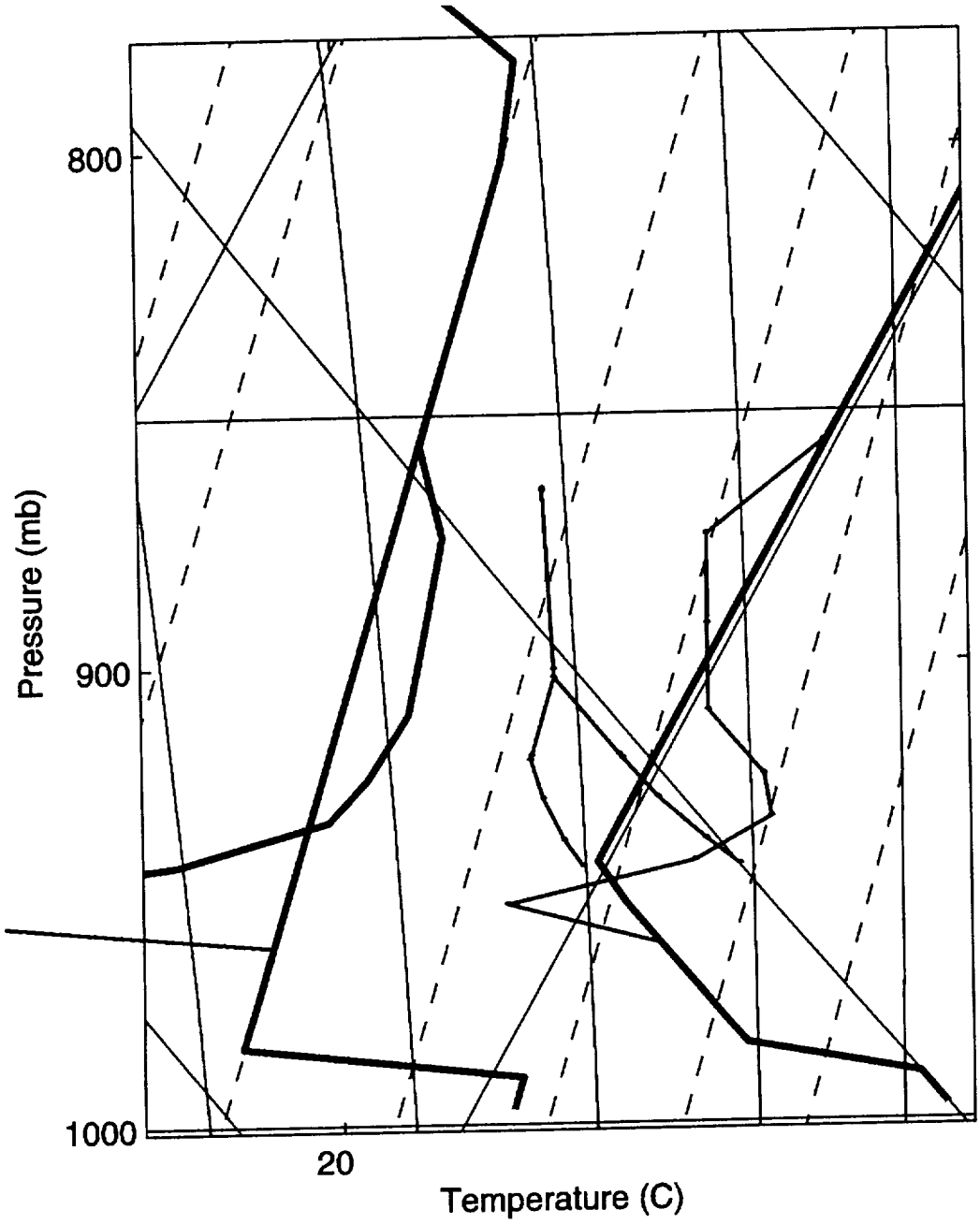

Figure 3.3.19 (Continued) Skew-T diagrams for results of shallow convection scheme with the revised algorithms for Case 2. (a) Using smallest initial vertical speed. (b) Using maximum initial vertical speed.

Figure 3.3.19 shows the Skew-T diagrams corresponding to the lowest (0.2 ms^{-1}) and highest (10.2 ms^{-1}) initial vertical velocities. In Fig. 3.3.19a we see that there exists some initial ABE that decreases as the environment is modified by convection. The updraft reaches saturation in the upper levels near 900 mb. In Figure 3.3.19b for the highest vertical velocities, the induced tendencies are much greater than for the other case with low vertical velocities. The final ABE is zero (when the virtual effect of water vapor is considered). The updraft extends through a deep layer (up to ~860 mb), where it is saturated and where liquid water is being detrained. The drying of the updraft mass-source layer below the updraft base in this case is very large and most probably is unphysical.

3.3.1.3.3.3 Revised Closure Algorithm in Case 3

Results obtained with the revised updraft and closure algorithms for Case 3 are shown in Figures 3.3.20 and 3.3.21. Figure 3.3.20a shows that as the water vapor content of the shallow-cloud updraft parcel increases, the convective multiplication factor for the ABE closure increases rapidly. Due to the TKE dominance in the hybrid (transition) closure, however, the ABE is only partially reduced in the final environmental profile (Fig. 3.3.20b). As the initial parcel becomes saturated, the induced tendencies grow substantially. This is especially evident in the Skew-Ts presented in Figure 3.3.21. Note that in the right panel of that figure, the parcel trajectory is saturated aloft from the shallow-cloud updraft base (where the temperature and dew point lines overlap at ~965 mb). The temperature sounding of the parcel trajectory is, however,

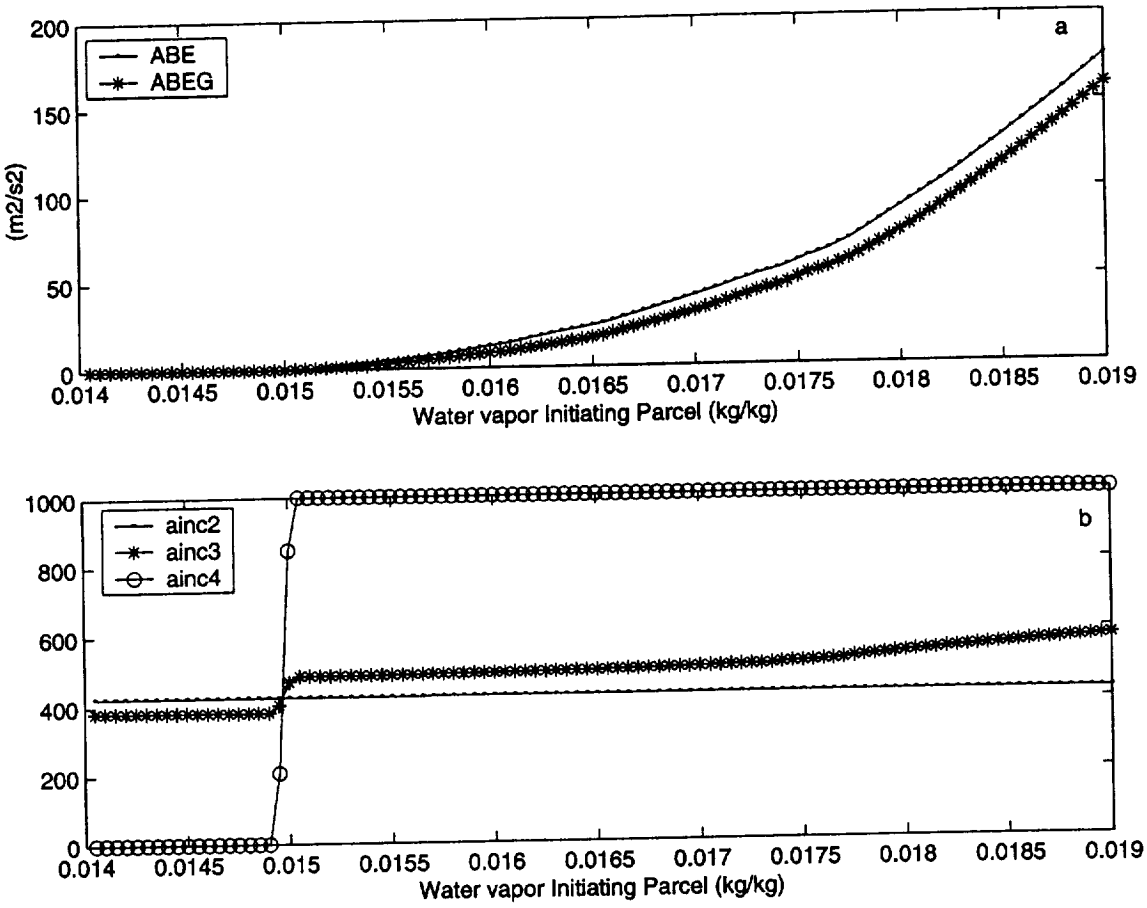

Figure 3.3.20 Results for the shallow convection scheme with the revised closure algorithm in Case 3. (a) Initial and final buoyant energies, (b) Convective multiplication factors.

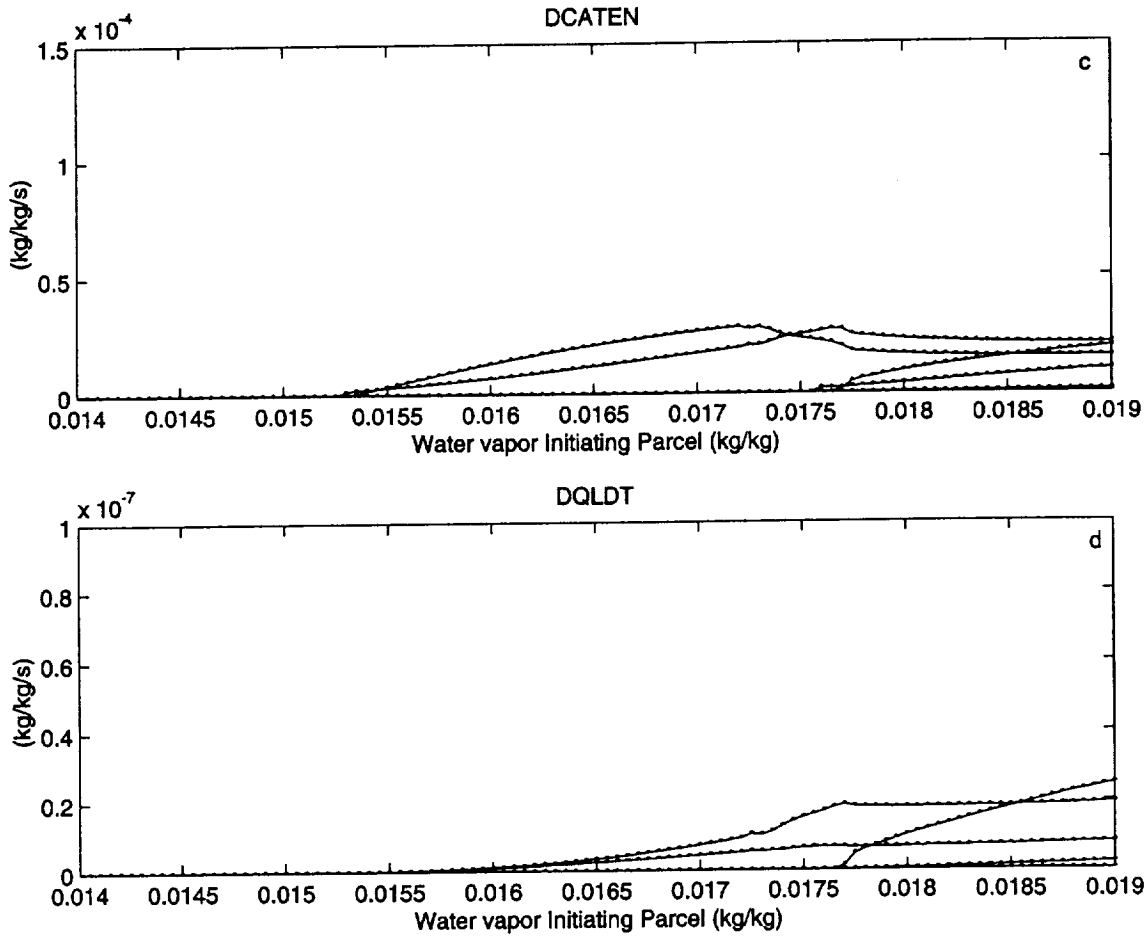

Figure 3.3.20 (Continued) Results for the shallow convection scheme with the revised closure algorithm in Case 3. (c) Cloudy area source rates, (d) Liquid water source rates.

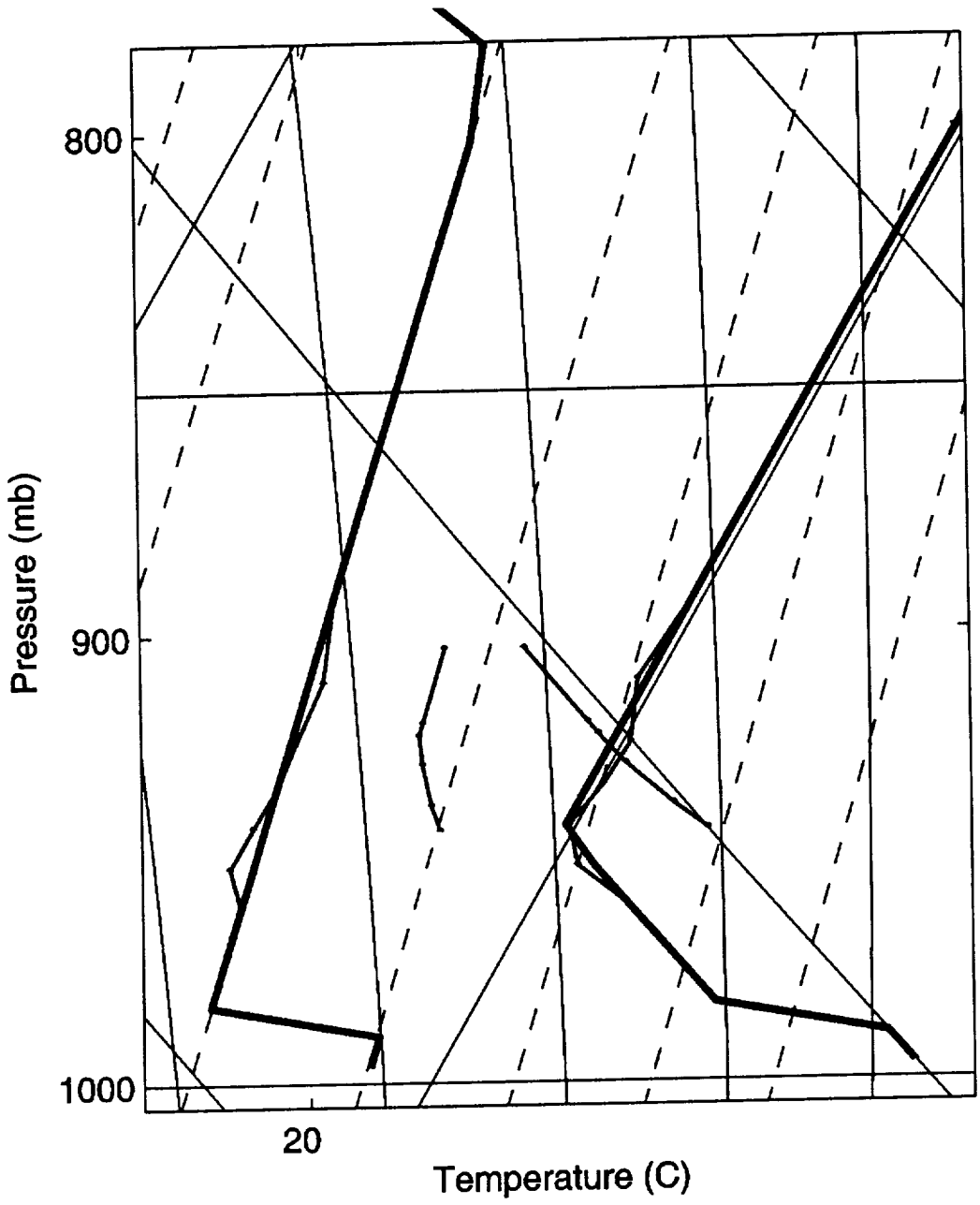

Figure 3.3.21 Skew-T diagram for results with revised algorithms in Case 3. (a) Using the smallest water vapor surface perturbation. A description of the lines is given in the text following Figure 3.3.15.

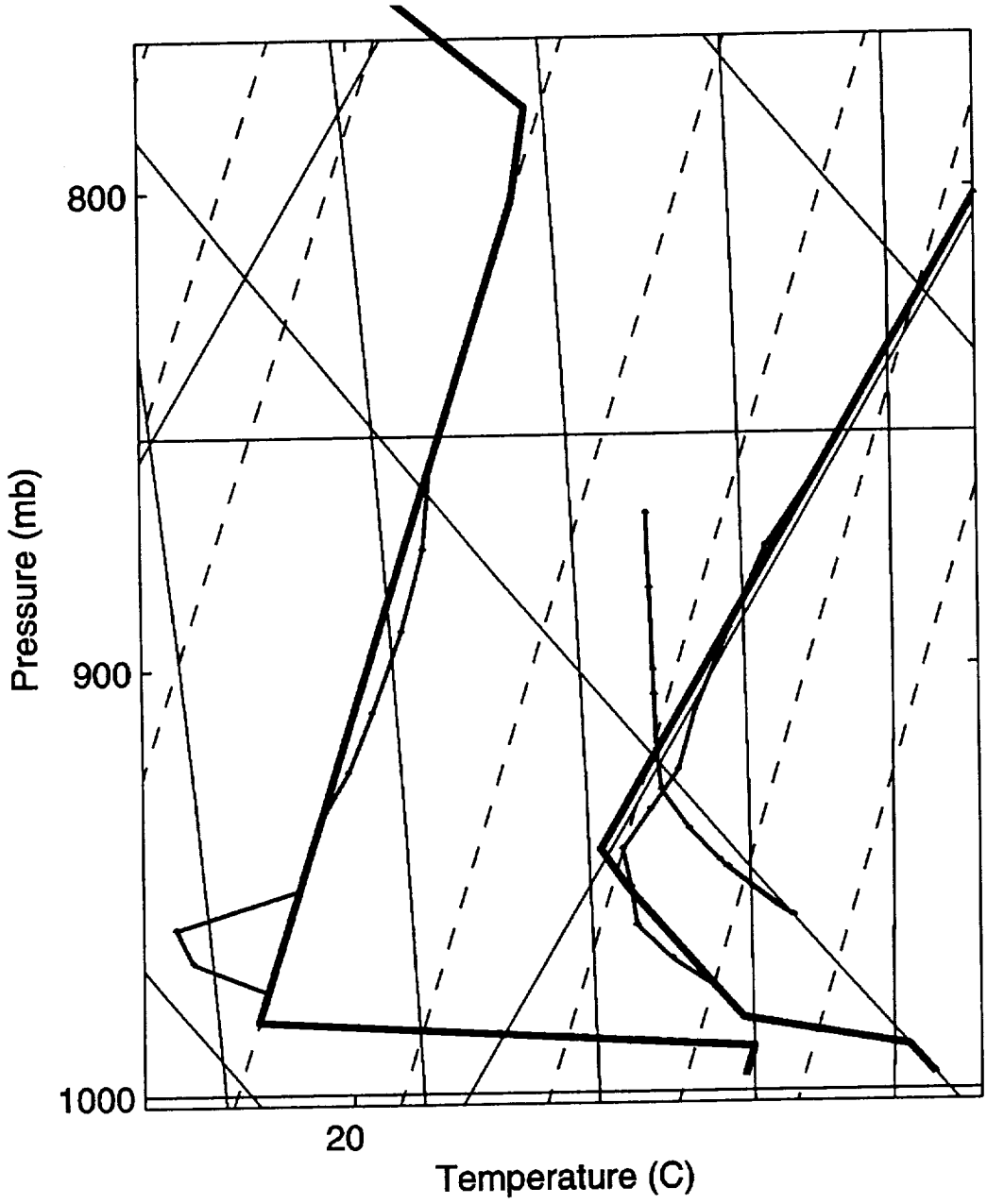

Figure 3.3.21 (Continued) Skew-T diagram for results with revised algorithms in Case 3. (b) Using the largest water vapor surface perturbation. A description of the lines is given in the text following Figure 3.3.15.

significantly different than the moist adiabat. This effect is due to the entrainment of environmental air into the cloud updraft. A test of this case with entrainment set to zero yields, quite naturally, a moist adiabat trajectory on the Skew-T (not shown).

3.3.1.3.3.4 Extension of the Mass-Source Layer to the Full PBL

As pointed out previously restricting the shallow-cloud updraft mass-source layer to the upper levels of the PBL, while taking its thermodynamic properties from near the surface, can induce large tendencies in the region of the mass source layer. These large tendencies appear to be unphysical. Therefore, a test was conducted by modifying this algorithm to redefine the mass-source layer as the complete PBL. Figures 3.3.22 and 3.3.23 show results for Case 0 with this modification of the source-layer algorithm. In the shallow-cloud updraft layer above 950 mb (in Figure 3.3.23), the results are similar to those obtained previously (in Figure 3.3.15), but the tendencies in the PBL shown in the Skew-T diagram of Figure 3.3.23 are much smaller than in the previous Case 3 experiment in which the mass-source layer was restricted to the upper portion of the PBL.

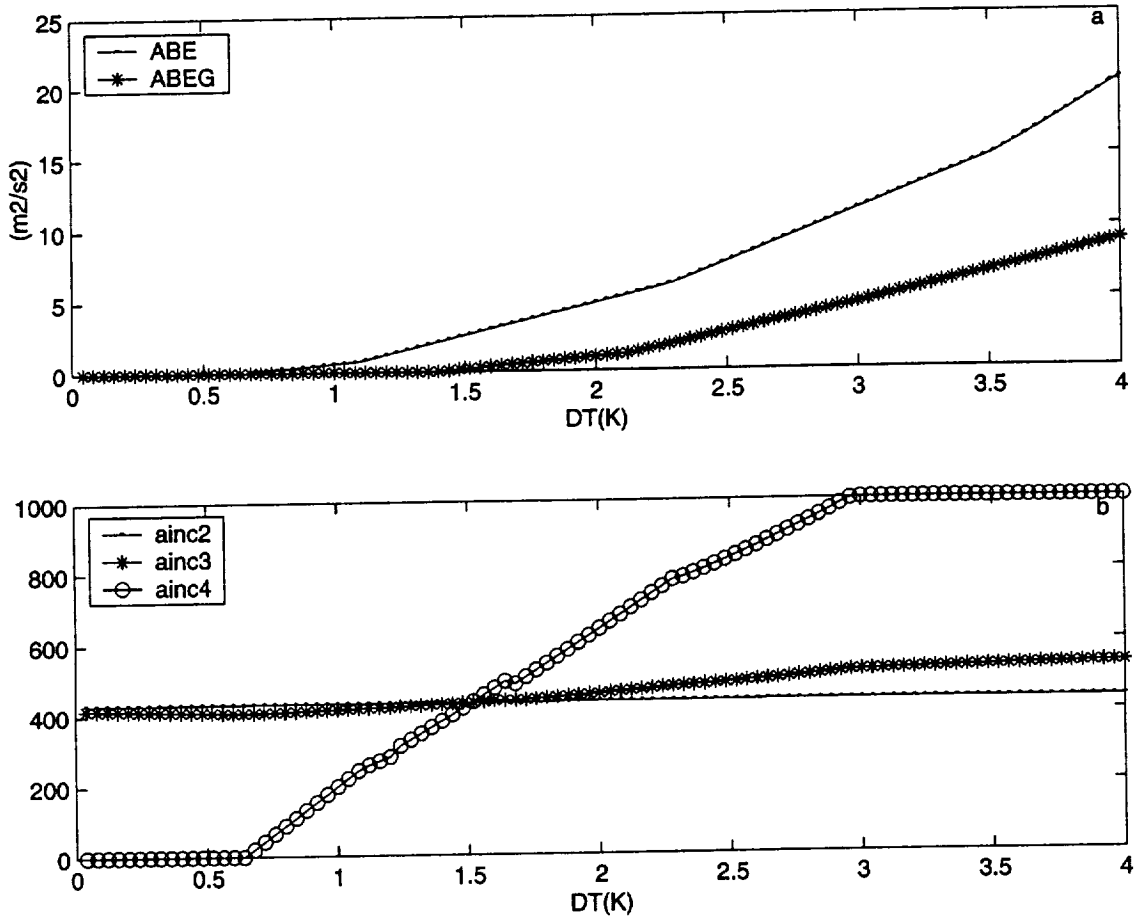

Figure 3.3.22 Results for the shallow convection scheme with the revised closure algorithm in Case 0 with the mass-source layer extended to the entire PBL. (a) Initial and final buoyant energies, (b) Convective multiplication factors.

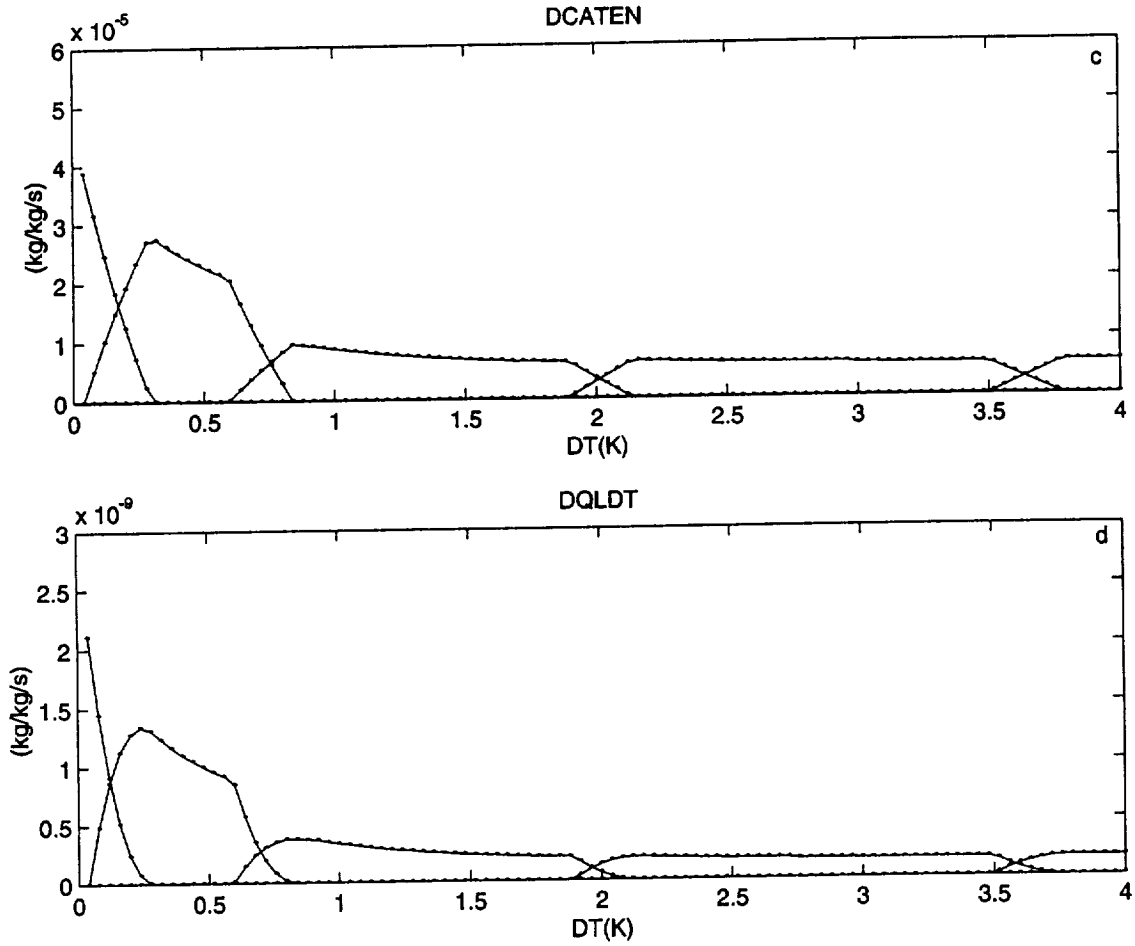

Figure 3.3.22b Results for the shallow convection scheme with the revised closure algorithm in Case 0 with the mass-source layer extended to the entire PBL. (c) Cloudy area source rates, (d) Liquid water source rates.

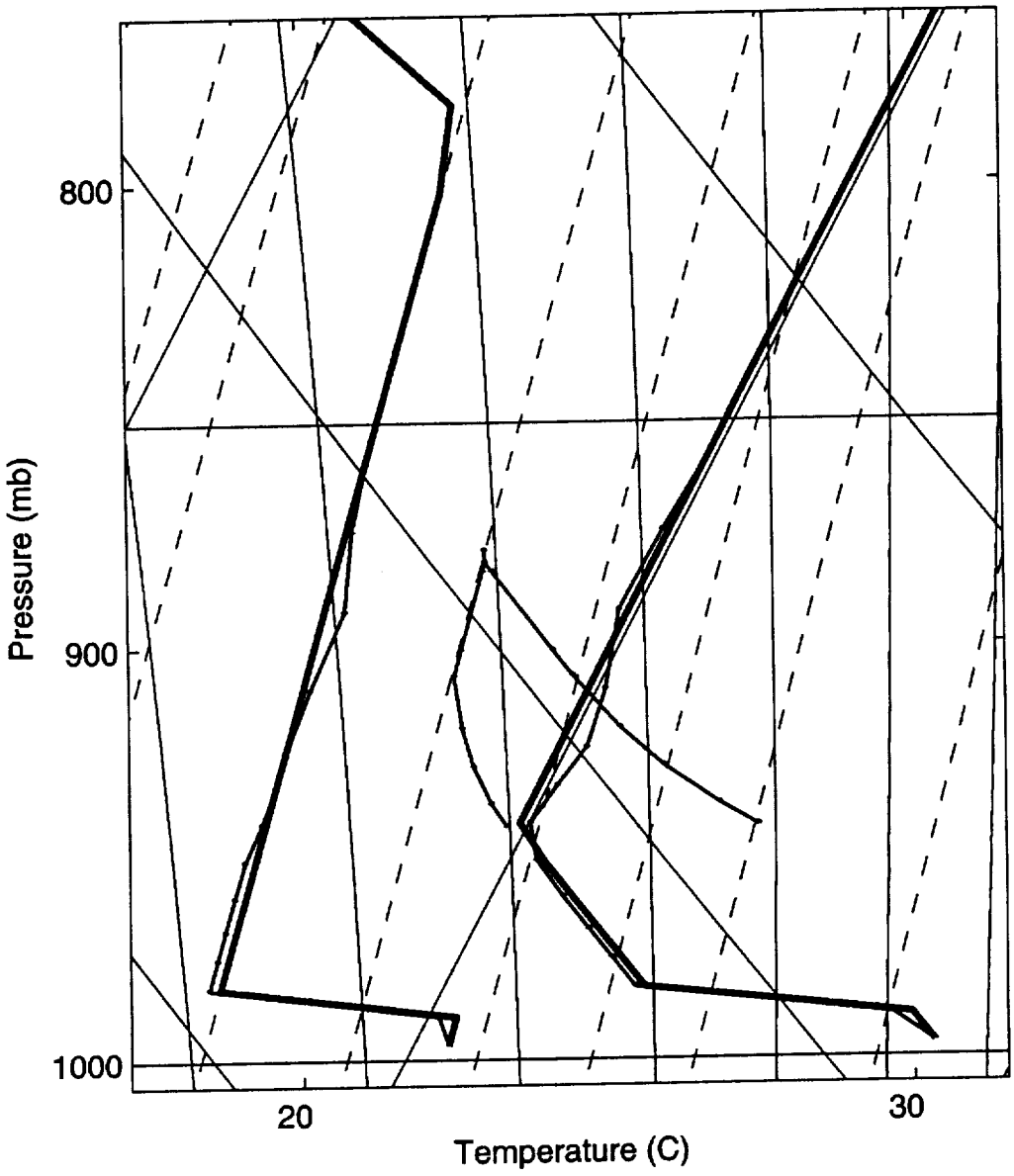

Figure 3.3.23 Skew-T diagram for results of the shallow convection scheme with revised algorithms in Case 0, but for the mass-source layer extended to the full PBL. The results are based shown for the largest surface temperature perturbation (4 K). A description of the lines is given in the text following Figure 3.3.15.

3.3.2 Calibration and Sensitivity Tests

3.3.2.1 Introductory Remarks

We describe here improvements and sensitivities of the Penn State (PSU) shallow convection parameterization. The original parameterization was developed in Deng (1999) and has been described in Deng et al. (2002a, 2002b). In Muñoz et al. (2001) the scheme was applied in the 3-D MM5 model Version 3.3 to simulate a summertime convection case over the central U.S. (see Section 4.3). Although the results were encouraging because the shallow convection scheme was able to partially capture the spatial distribution of shallow clouds, they also showed some systematic underprediction of cloudiness and a general patchiness in the cloud fields, that prompted the revisions and improvements described here.

The PSU shallow convection scheme can be considered an extension of the Kain-Fritsch (KF) deep convection parameterization scheme (Kain and Fritsch, 1990) to account for the effects of shallow non-precipitating clouds. As a standard convection parameterization scheme, the PSU shallow convection scheme consists of a *triggering condition*, a *cloud model* and a *closure assumption*. Because it is designed to represent shallow convection, however, the new scheme differs from other convection parameterizations in several respects. On the one hand some important elements of deep convection parameterizations lose their importance when applied to shallow convection, such as the triggering condition and the downdraft sub-model. The first has less importance because shallow clouds are much more numerous in a given area than deep-convection events. Also, since shallow clouds are by definition non-precipitating (or

nearly so), they do not require consideration of downdrafts that are formed by the evaporation of precipitating hydrometeors.

On the other hand, the representation of shallow clouds in mesoscale models poses some problems that are not as relevant in the deep convection case. For example, it is important to call the parameterization scheme much more often than the deep-convection routines, since the shallow clouds interact rapidly with many of the other physics of the calling model, mainly the land-surface, turbulence and radiative parameterizations. If the shallow convection is called infrequently, these interactions may be lost or distorted. Another important special feature of shallow clouds is that they have much smaller thermodynamic perturbations, compared with the deep-convection case. This characteristic makes the definition of the initial properties of the updraft parcel a very sensitive part of the parameterization. It also demands that updraft and mixing algorithms that have proven useful in the parameterization of deep convection be re-evaluated in the more subtle conditions occurring in shallow convection, where the buoyancy or liquid water content of the updraft may differ only marginally with respect to the environment.

A final special feature of the shallow-convection scheme is its treatment of the liquid water generated in the updraft. Unlike the Kain-Fritsch deep-convection scheme, where detrained liquid water is fed back immediately into the resolved water variables, the shallow scheme retains the detrained condensed water in sub-grid cloud variables (area and water content of sub-grid neutrally buoyant clouds, NBCs). The water mass of the NBCs is gradually put back into the resolved-scale variables by means of mixing and other parameterized processes.

This section describes further tests and improvements of the shallow-convection scheme, in addition to those discussed in Section 3.3.1, aimed at making it more robust and useful in the

parameterization of shallow convection for mesoscale and climate models. It also validates the improved scheme against a published data set from a trade-wind shallow convection case.

3.3.2.2 New Features in the Shallow Convection Parameterization

3.3.2.2.1 Parcel Properties

The original shallow scheme defines the thermodynamic properties of the updraft initiating parcel based on the average properties of the lowest 20% of the planetary boundary layer (PBL). The starting height of the updraft is defined as the minimum between the PBL height and the lifting condensation level (LCL) of the initial updraft parcel. The results shown in this section have been obtained with a simpler definition of the initial parcel properties. The buoyancy at the top of the PBL is calculated and a given perturbation to this value is assigned to the parcel, which is also considered to be saturated, but with no liquid water content. The buoyancy perturbation is a parameter of the scheme, as well as the perturbation of the initial vertical velocity. As we show later, very small buoyancy perturbations are sufficient to create a shallow-cloud layer. This new scheme is simpler than the original scheme and concentrates on the important physical variable (initial buoyancy) more than on a prescribed fraction of the PBL. Note that this new approach does not imply that the PBL top and cloud layer base are forced to coincide, since entrainment of dry air can preclude the parcel from producing liquid water near the updraft's base.

3.3.2.2.2 Updraft Model

Two problems have been found when applying the Kain-Fritsch cloud model in the shallow-convection scheme. These problems are not significant for the use of the K-F cloud model in the case of deep-convection parameterization, but they become important when used in the context of shallow convection, as was explained in the introduction.

The continuous use of the shallow-convection parameterization (i.e., it being called every time step) uncovered the degree of discretization inherent in the original K-F updraft scheme (see Section 3.3.1). The updraft is discretized on the same vertical grid layers as in calling model, which can have serious consequences. For example, in the time step when the detrainment layer at the top of the updraft includes an additional layer, the updraft mass fluxes can decrease abruptly by a significant percentage (from 100% to 50% in the case that the detrainment layer comprises initially one and then two model layers). These sudden jumps in the mass-flux profiles produce noise in the time evolution of the shallow-convection tendencies, which makes interpretation of the results more difficult and precludes attainment of quasi-equilibrium conditions.

The proposed solution to this discretization problem is to make the updraft algorithm able to recognize when a given model layer includes a significant transition level. We define four types of significant transition levels where

1. buoyancy changes sign,
2. liquid water becomes positive,
3. vertical velocity becomes zero.
4 mass flux becomes zero.

Once the algorithm recognizes the existence of a significant transition, it iterates inside the model layer to find its exact location, and then inserts this height into the updraft vertical layers. The transitions of types 3 and 4 also define the top of the shallow-could updraft. The logic of the new algorithm is somewhat more complex than that of the original scheme, but it results in an updraft that evolves smoothly as the environment and the initial parcel properties gradually change.

The second problem relates to the small thermodynamic perturbations associated with the shallow clouds. Figure 3.3.24 is taken from Kain and Fritsch (1990), and it shows the conceptual scheme used to define the detrainment and entrainment fractions in the original K-F updraft scheme. The updraft parcel is mixed in different proportions with an environmental parcel. In the figure the buoyancy of the resulting mixed parcel is plotted against the fraction of environmental air used. The point of crossover, where the mixed parcel has zero buoyancy with respect to the environment, is the critical mixing fraction that is used later to define the entrainment and detrainment rates. The larger the critical mixing fraction is, the larger the entrainment, and vice-versa.

This conceptual scheme is appealing and has been applied for a long time in the K-F deep-convection parameterization. Note however how the virtual temperature perturbation of the updraft in Figure 3.3.24 is rather large, as well as its water content that controls the maximum virtual cooling of the mixed parcels. In shallow clouds the thermodynamic perturbations are smaller, as well as the liquid water content, and this mixing algorithm tends to produce entrainment and detrainment that are mutually exclusive (i.e., all entrainment or all detrainment in a given layer). In the limit, for example, when the updraft parcel has no liquid water content,

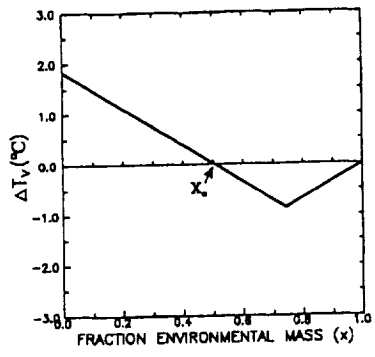

Figure 3.3.24. Virtual temperature of a parcel resulting from the mixture of updraft and environmental air (taken from Kain and Fritsch, 1990).

the scheme has a flip-flop behavior where full entrainment is diagnosed if the updraft is buoyant or full detrainment is diagnosed if it is not. Conceptually the applicability of the original K-F mixing algorithm near cloud base is questionable, since there has been little time for mixing to take place, so that the buoyancy of mixed parcels may not be very relevant to the definition of the entrainment and detrainment profiles. Along these lines, the change to the algorithm that we test here is to alter the definition of the critical mixing fraction in regions near cloud base (which mainly affects shallow clouds). In these regions the critical mixing fraction is defined solely on the basis of the buoyancy of the updraft parcel with respect to the environment, using a smooth function of the form:

$$\Psi_m = \frac{T_{v,u} - T_{v,\min}}{2DTM}, 0 < \Psi_m < 1 \tag{3.4}$$

where $T_{v,min} = T_{v,env}$ - DTM, $T_{v,u}$ is the virtual temperature of the updraft parcel and $T_{v,env}$ is the virtual temperature of the environment.

The actual mixing fraction used in the entrainment/detrainment diagnosis is a weighted average of the K-F mixing fraction and the new critical mixing fractions, in the form:

$$\Psi = e^{-\frac{z}{DELZS}}\Psi_{KF} + (1 - e^{-\frac{z}{DELZS}})\Psi_m \tag{3.5}$$

where Ψ_{KF} is the critical mixing fraction diagnosed with the standard KF algorithm. The two new parameters introduced by this scheme are DTM and DELZ, and are subject to sensitivity evaluations in the next section.

3.3.2.2.3 Closure

In the results presented here we restrict the scheme to use only the TKE closure algorithm described in Deng et al. (2002a, 2002b), with no use of the transitional closure regime between TKE and CAPE closures. This is so because we intend to test the scheme in a purely shallow-convective situation. Evaluation of the transitional closure algorithm will be performed in future work.

3.3.2.3 A trade wind boundary layer case

As a reference for the calibration and sensitivity analysis presented later we use a trade wind boundary layer case described by Siebesma and Cuijpers (1995). They showed observations and LES results for an undisturbed period of the BOMEX experiment. Figure 3.3.25 shows vertical profiles of mass flux (Panel a), entrainment rate (Panel b) and detrainment rate (Panel c). The LES results correspond to averages for the last 4 h of a 7-h simulation, and they report results obtained with two different methods of defining the updrafts. The case is forced by prescribed subsidence and radiative-cooling profiles, constant humidity advection, and constant sea-surface temperature. In our model calculations we use the same forcings and the

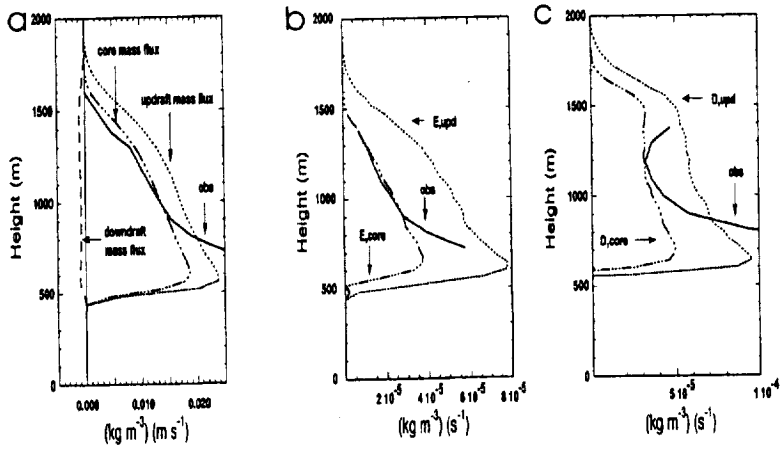

Figure 3.3.25. Mass flux profiles for BOMEX trade wind case. a) Mass flux profile, b) Entrainment rate profile, c) detrainment flux profile. Bold lines are profiles derived from budgets of observed data, and other two lines are derived from LES results with two methods of defining updrafts. (taken from Siebesma and Cuijpers, 1995).

same initial soundings. One of the main conclusions in Siebesma and Cuijpers (1995) is that, compared to LES results, current mass-flux parameterization schemes appear to underestimate the mixing between updrafts and environment by an order of magnitude.

3.3.2.4 Parameter Sensitivities

The parameter sensitivities described in this section are based on an experiment called Case 08, the parameters for which are shown in Table 1.

Table 1. Parameter values used in the basic sensitivity cases Case 08 and Case 10.

Parameter	Case08	Case10
DTVI	0.10	0.05
ENTPAR	0.15	0.10
CLOSVAL	20	20
DELZS	300	500
DTM	0.20	0.25
DIFFK	0.00001	0.00005

Figure 3.3.26 shows sensitivities of the new scheme to DTVI, the initial buoyancy perturbation of the updraft parcel (panels a, b, and c), and to ENTPAR, the entrainment parameter defined by the K-F standard scheme (panels d, e, and f). The vertical profiles shown correspond to 4-hour averages for mass fluxes (left panels), entrainment rates (center panels), and detrainment rates (right panels).

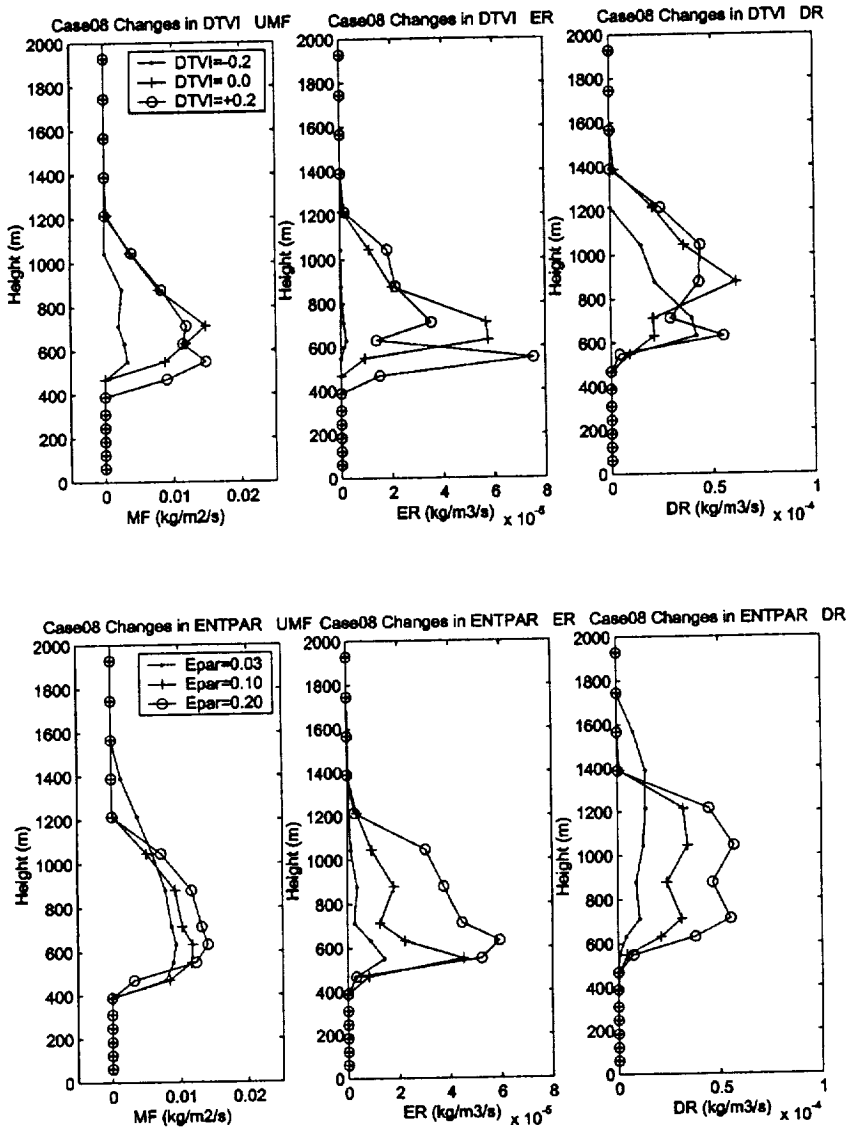

Figure 3.3.26. Sensitivity of new shallow convection scheme to initial parcel buoyancy perturbation DTVI (upper panels) and KF entrainment parameter ENTPAR (lower panels). a and d) are mass flux profiles, b and e are entrainment rate profiles, c and f) are detrainment rate profiles.

The sensitivities for DTVI include initial parcels that are negatively buoyant (DTVI=-0.2 K), neutrally buoyant (DTVI=0.0 K), and positively buoyant (DTVI=+0.2 K). The negatively buoyant initial parcels produce a shallower updraft layer and weak mass flux profiles dominated entirely by detrainment. The other two cases show similar mass flux profiles, except for larger entrainment rates near the updraft base in the case of the buoyant initial parcel. As the initial buoyancy increases, the mass flux near the base increases and the base height itself decreases, possibly due to the effect of the induced subsidence on the boundary layer growth.

Sensitivity of the new scheme to the K-F entrainment parameter is shown in the bottom three panels of Figure 3.3.26. Here, as ENTPAR increases from 0.03 m/Pa (the default value in K-F) to 0.20 m/Pa the entrainment and detrainment fluxes increase considerably. The case with lower entrainment also produces a deeper updraft.

The three upper panels of Figure 3.3.27 show the sensitivity of flux profiles for changes in the closure parameter, CLOSVAL. This parameter controls the magnitude of the mass flux at the updraft base when the TKE closure assumption is used. Panel a) clearly shows the influence of this parameter on the base mass flux. Increased cloud-base mass flux produces entrainment and detrainment profiles consistently larger, although the updraft top is not very sensitive to this parameter. The updraft base, however, decreases as the mass flux increases.

The three lower panels in Figure 3.3.27 show the sensitivity of the scheme to DELZ, the scale height that controls the relative importance of the original K-F mixing fraction and the new definition of the critical mixing fraction (see section 3.3.2.2.2). This parameter greatly influences the entrainment/detrainment ratio in the middle levels of the updraft, where the new buoyancy-based critical mixing fraction tends to increase the magnitude of the entrainment and

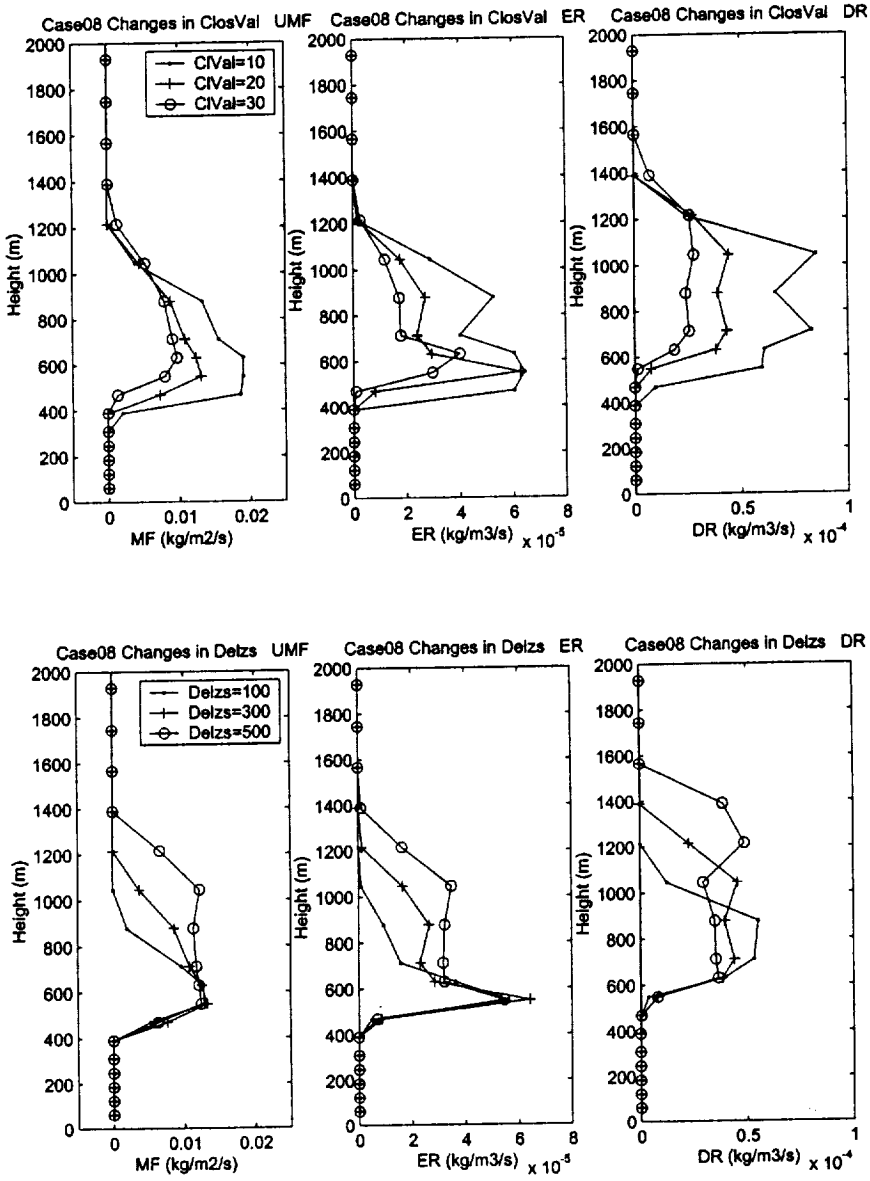

Figure 3.3.27. Sensitivity of new shallow convection scheme to closure parameter CLOSVAL (upper panels) and height scale DELZS (variables in lower panels are defined as in Figure 3.3.26).

decrease the detrainment. As a result the updraft layer is deeper and the detrainment increases in the updraft top layers.

Figure 3.3.28 shows sensitivities of the new scheme to the parameter DTM. This parameter controls the smoothness of the buoyancy transition. As DTM decreases the transition becomes steeper and the critical mixing fraction jumps faster from 0.0 to 1.0 (see Section 3.3.2.2.2). Panel a) in the figure now shows the average cloud-area fraction calculated for three values of DTM. Panels b) and c) show mean entrainment and detrainment rates profiles, respectively. Panels d), e), and f) show the standard deviation of the corresponding profiles for the same 4-h period in which the averages where performed. It is hard to find a systematic sensitivity in the mean profiles, but the influence of this parameter in the standard deviation is noticeable. In fact, as DTM becomes smaller the variability of the mass flux profiles increases significantly. This variability represents the abrupt changes from which the diagnosed updraft suffers on a time-step-to-time-step basis, as the buoyancy of the updraft parcel changes slightly. Note that the variability in the cloud-area fraction profile (note shown) does not change significantly, because it can be considered as a time integrated variable of the NBC, rather than an instantaneous function of the updraft characteristics.

3.3.2.5 Validation and Physical Sensitivities

Based on the sensitivities shown previously, a suitable set of parameters was selected that produces mass flux profiles and cloud area fractions that resemble those presented by Siebesma and Cuijpers (1995). This set of parameters is shown in Table 1 in the column labeled Case 10. For this case we performed sensitivity analyses with respect to changes in the prescribed

forcings. We report here sensitivities due to the specification of the subsidence profile and the sea-surface temperature.

The three upper panels of Figure 3.3.29 show changes in the vertical profiles of cloud area, entrainment rates and detrainment rates when the subsidence profile of the basic case (Case 8) is multiplied by a constant factor of 0.5, 1.0, and 2.0. For increased subsidence the updraft top is lower and the updraft layer becomes shallower. Cloud cover and mass fluxes close to the updraft top are greatly affected by changes in the subsidence, but are not affected so much near updraft base.

The three lower panels of the same figure show sensitivities to sea-surface temperatures that vary -1, 0 or +1 K with respect to the basic case (Case 8). Larger sea-surface temperatures increase cloud area fractions, updraft depth and entrainment and detrainment fluxes.

We finally illustrate in Figure 3.3.30 the effects of the shallow-convection scheme on the thermodynamic sounding of the environmental column. Panel a) is the initial Skew-T sounding for Case 10. Panel b) shows the sounding after seven hours when the shallow-convection scheme was not used, and Panel c) is the corresponding 7-h sounding when the shallow convection scheme was active. Among the several effects of the shallow-convection scheme on the thermodynamic profile we can mention: (1) shallow convection precludes the top of the boundary layer of becoming saturated, (2) the cloud layer becomes more humid, especially in its upper part, (3) the trade-wind inversion at the top of the cloud layer is more highly intensified (larger temperature gradient) when using the shallow-convection scheme, and 4) the top of the mixed layer develops a small temperature inversion. All of these effects appear physically realistic and consistent with the conceptual understanding of the trade-wind boundary layer. In the case that did not use the shallow convection parameterization, the top of the PBL becomes

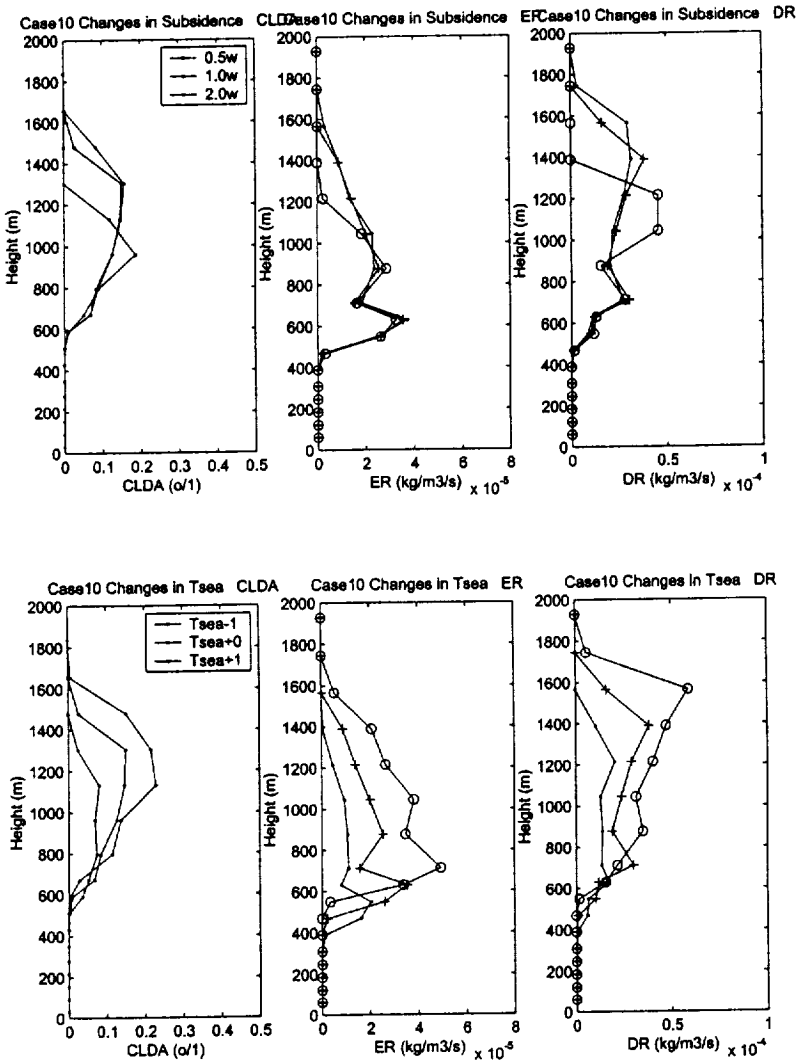

Figure 3.3.29. Sensitivity of new shallow-convection scheme to forcings. Upper panels show sensitivities to subsidence profile, and lower panels are sensitivities to sea surface temperature. . Panels a) and d) are cloud area profiles, Panels b) and e) are entrainment rate profiles, and Panels c) and f) are detrainment rate profiles.

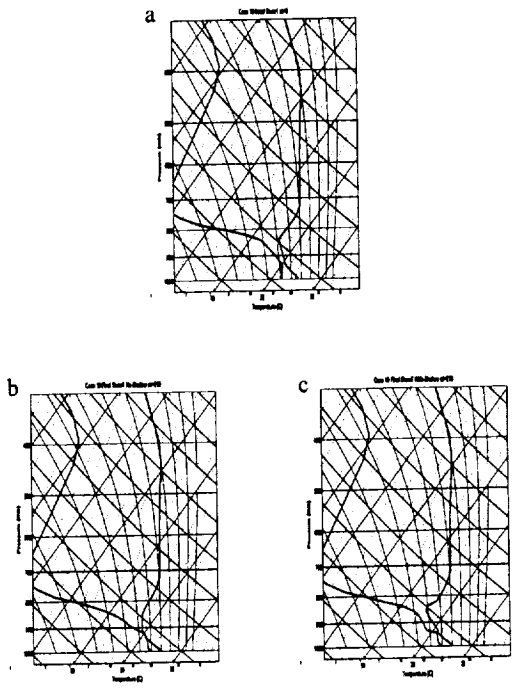

Figure 3.3.30. a) Initial sounding for trade-wind boundary layer case. b) Sounding after 7-h run without using the shallow convectionl parameterization, c) Same as b), but with the use of the shallow-convection parameterization.

fully saturated (stratus development), even though the 1.5-order TKE-predicting turbulence scheme has been corrected for the effects of saturation on the buoyancy production of TKE.

3.3.2.6 Conclusions

We have described here several improvements to the PSU shallow-convection scheme that make it more robust for its use in mesoscale models. The changes are demanded by the special features of shallow convection, especially because of the more subtle thermodynamic perturbations associated with shallow clouds that require more frequent use of the parameterization. The improvements have been made mainly in the Kain-Fritsch updraft algorithm that also is used in the shallow-convection parameterization.

Use of the improved scheme in the modeling of a trade-wind boundary layer case shows that the entrainment parameter of the K-F updraft model may be significantly smaller than required to reproduce the characteristics of observed and LES-derived mass flux profiles, as presented in Siebesma and Cuijpers (1995). This conclusion is consistent with that reported by the authors of the same paper. Moreover, with the correction of the entrainment parameter, the new shallow-convection scheme appears to perform reasonably well for reproducing the mass flux profiles, while showing physically realistic sensitivities to its important parameters and to changes in the prescribed forcings.

A final point of discussion concerns the shape of the detrainment profile obtained with the shallow-convection parameterization. Generally, it proved difficult to produce detrainment profiles that had maximum values close to cloud base and decreased with height, as it is typically the case in observed or LES-simulated shallow-cloud layers. In most of the results presented

here the detrainment profiles have a tendency to be uniform or increase with height. That is, the detrainment profile tends to peak in the aptly named detrainment layer at the top of the updraft. This appears to be a consistent shortcoming of many one-cloud convection schemes. However, it is interesting to note that in Panel c of Figure 3.3.28, the detrainment profile obtained with DTM=0.05 K has a shape that indeed tends to decrease with height. As discussed in Section 3.3.2.4, a small value of DTM corresponds to a more intermittent updraft. This observation immediately suggests that a possible way of improving the performance of a one-cloud convection scheme like this may be to add an additional degree of variability to the properties of the initial updraft parcel on successive time steps by changing its buoyancy, vertical velocity or mass flux according to a prescribed distribution function. The diagnosed updrafts on successive time steps would then show "noise", but this will be controlled by known and physically consistent causes, more than by numerical or algorithmic reasons. Over a number of time steps, the resulting forcing of the environment by the shallow convection would have the effect of an ensemble of shallow-cloud sizes without having to calculate the effect of the entire ensemble at every time step. This approach could be computationally simple and efficient, and hence it may be beneficial for the representation of the overall process of shallow convection. Further investigations along this line will be pursued in the future.

4. EXPERIMENTATION IN THE 3-D MM5

4.1 TKE-Predicting Turbulence Scheme in the 3-D MM5

4.1.1. Introductory Remarks

One area that is often overlooked in numerical weather prediction is proper treatment of turbulence in a saturated environment. The Blackadar planetary boundary layer (PBL) scheme (Grell et al. 1994, Zhang and Anthes 1982), for example, often produces dry-adiabatic or other absolutely unstable profiles in saturated layers. Although moist corrections for the vertical diffusion in cloudy layers have been added to the Richardson number (which appears in the computation of the mixing coefficient within the scheme), these problems have persisted and still occur quite regularly. This section presents some important considerations for representing atmospheric turbulence in layers saturated with respect to liquid or ice.

4.1.2 The TKE-Predicting Sub-Model for Turbulence

The 1.5-order turbulence sub-model that has been developed at Penn State (Gayno 1994, Gayno et al. 1994, Shafran et al. 2000) is now an option in version 3 of the MM5. The original version of this scheme, also known as the Gayno-Seaman scheme, is based on the work of Musson-Genon (1987) and Ballard et al. (1991). Although the scheme also contains a subgrid fog parameterization, it will not be discussed here and it is not included in the V3 release. The

fog module is still under development and will be included in a future release of the PSU TKE sub-model.

Although TKE-based schemes are often called PBL schemes, they are actually turbulence parameterizations for the entire atmosphere. The so-called "1.5-order closure" (Mellor and Yamada 1974, Yamada 1977) includes a prognostic second-order equation for only the momentum variance, or the turbulent kinetic energy (TKE). It has been shown that 1.5-order schemes are reasonably accurate and more computationally efficient than the complete second order schemes. The remainder of this section presents some special considerations for representing turbulent and microphysical processes in saturated layers, including important improvements to the scheme beyond that described in Shafran et al. (2000).

4.1.2.1 The TKE Equation

As described in Shafran et al. (2000), a prognostic equation for TKE, comprised of source and sink terms due to buoyancy, shear, transport and dissipation, is integrated forward in time, along with the other mixing variables. (We have recently included the advection of TKE, which may be important for accurate simulation of the PBL on fine grids in transition zones between land and water, dry land and moist land, etc.) The vertical mixing coefficients are proportional to the predicted TKE profiles in time and space. The mixed-layer height is also diagnosed from the TKE profiles using minimum TKE threshold conditions.

4.1.2.2. The Conservative Mixing Variables

At the beginning of an advection time step, the surface fluxes are computed using the same Monin-Obukhov similarity parameterization (Slab) used in the Blackadar scheme and described by Zhang and Anthes (1982). The MM5 temperature and moisture fields are then transformed into variables that are conservative during condensation and evaporation processes. The TKE sub-model converts the potential temperature (θ), vapor mixing ratio (q_v) and liquid water mixing ratio (q_l) into liquid water potential temperature (θ_l) and total water mixing ratio (q_t), following Betts (1973) and given by

$$\theta_l = \theta - \frac{\theta}{T}\frac{L_{lv}}{c_p} q_l \tag{4.1}$$

$$q_t = q_v + q_l , \tag{4.2}$$

where T is temperature, L_{lv} is the latent heat of vaporization, and c_p is the specific heat at constant pressure. The mixing is then performed on the liquid water potential temperature and total water mixing ratio, and these fields are converted back to the native MM5 variables at the end of the time step

Although the vertical mixing of *conservative* variables helps to reduce the occurrence of unrealistic thermal profiles in saturated layers, moist-adiabatic cloud layers are still not assured. We realized that the buoyancy production term within the TKE equation was based on the standard eddy-diffusivity formulation for the virtual potential temperature flux. This formulation, however, is only valid in a cloud-free environment. If a model uses this formulation when a dry-adiabatic layer first saturates, the virtual potential temperature gradient will be close

to zero and produce no additional source of TKE to increase the eddy diffusivity and mix the dry-adiabatic profile towards a moist-adiabatic profile.

4.1.2.3 Improvements for Saturated Layers

The equation for TKE in turbulent flow includes a buoyant production/destruction term given by

$$BP = \frac{g}{\theta_v} \overline{w'\theta'}_v \tag{4.3}$$

where g is gravity, θ_v is virtual potential temperature, and $\overline{w'\theta'}_v$ is the buoyancy flux. When buoyant production (BP) is positive it produces TKE and when it is negative it is a sink of TKE. Although it is possible to compute BP using an eddy diffusivity formulation for the flux,

$$\overline{w'\theta'_v} = -K \frac{\partial \theta_v}{\partial z} \ , \tag{4.4}$$

θ_v is not a conservative variable in saturated conditions. Thus, this eddy diffusivity formulation for the buoyancy flux is not generally valid. To obtain a general expression for buoyancy flux, we can use the definition of θ_v, and relate it to the conservative variables given in (4.1) and (4.2). Following Deardorff (1976),

$$\overline{w'\theta'_v} = A\,\overline{w'\theta'_l} + B\,\overline{w'q'_t} \tag{4.5}$$

where all variables are as defined above, and A and B are functions of the basic thermodynamic variables. We can then re-write (4.5) using eddy diffusivity K as

$$\overline{w'\theta_v'} = -KA\frac{\partial \theta_l}{\partial z} - KB\frac{\partial q_t}{\partial z}. \tag{4.6}$$

Note that (4.6) is equivalent to (4.4) for unsaturated conditions, but for these "dry" conditions there are different functions for A and B.

Because the TKE is often defined at the boundaries of the grid volumes where the temperature and moisture fields are defined, a problem occurs when computing the buoyancy production at a vertical boundary between saturated and unsaturated air. Neither the saturated or unsaturated formulation for buoyant production of TKE is strictly correct in this boundary region (e.g., Sommeria and Deardorff 1977, Munoz et al. 2000). For the purpose of this study we simply use the unsaturated formulation in the boundary zones.

We also re-formulated the dissipation of TKE used by Ballard et al. (1991) to include moist effects in the stability parameter, N^2, the Brunt-Vaisala frequency, in saturated layers. The computation of the Blackadar length scale used in the dissipation was also re-designed to better represent the vertical turbulent scales in saturated and unsaturated layers, based on the predicted TKE profile and local minima.

We have benchmarked this TKE sub-model and saturation effects on turbulence against that of Duynkerke and Driedonks (1987) for two cloud-topped PBL cases. One case was forced by only surface buoyancy fluxes while the other case was forced by radiative forcing at the top of the cloud. The 1-D MM5 results compared favorably with their one-dimensional results (not

shown). In this section we extend our work to three dimensions to demonstrate the importance of saturation effects on turbulence within a mesoscale model.

Another limitation of the original version of the TKE sub-model described by Shafran et al. (2000) is that cloud ice cannot be treated properly using liquid water potential temperature and total water defined by (4.1) and (4.2). Therefore, we have recently replaced the liquid water potential temperature variable in the scheme by an ice-liquid water potential temperature θ_{il}, as described by Tripoli and Cotton (1981),

$$\theta_{il} = \theta[1 - \frac{L_{lv} q_l}{c_p \max(T,253)} - \frac{L_{iv} q_i}{c_p \max(T,253)}] \tag{4.7}$$

where all symbols are as above, q_i is the cloud ice mixing ratio, L_{iv} is the latent heat for ice-vapor phase changes, and the max(T,253) is an empirical correction which improves diagnosis of θ from θ_{il} at temperatures colder than 253 K. The total water mixing ratio, modified to include the cloud ice mixing ratio q_i, is given by

$$q_t = q_v + q_l + q_i \,. \tag{4.8}$$

Since an equilibrium condition cannot be assumed for the ice phase, an additional mixing variable was needed for the transformation of total water mixing ratio back to the native MM5 moisture variables. Currently, the TKE submodel only allows "simple ice" (no mixed phase) microphysics, and a mixing equation for the cloud liquid/ice is included in the scheme, in

addition to the one for the total water defined by (4.8). The vapor mixing ratio is computed as a residual by subtracting the cloud liquid/ice mixing ratio from the total water mixing ratio.

Additional work has focused on making the TKE sub-model more robust, as well as more efficient. The counter-gradient terms for the TKE flux proposed by Ballard et al. 1991 were found to be a source of numerical instability. These correction terms were designed to account for the counter-gradient TKE flux observed in the lower third of the convective PBL. However, after several failed attempts to make these terms numerically stable, we have decided to remove them from the TKE flux formulation. These counter-gradient correction terms to the TKE flux, which are often ignored in other TKE formulations (e.g., Musson-Genon 1987), did not appear to have any significant positive effect on the model solutions.

An improved algorithm to define a smaller time step within the TKE sub-model to assure numerical stability has also been implemented. The surface-layer (lowest model layer) equations are solved explicitly while all layers above the surface layer are solved implicitly. Thus the most restrictive numerical stability criterion for the surface-layer diffusive equation for each north-south "j-slice" is used to determine the sub-model time step for that slice. This allows shallower surface layers to be used without needing to reduce the advection time step used to integrate the rest of the model equations.

4.1.3. Results with the Improved TKE Formulations for Saturation

We have benchmarked this new version of the TKE sub-model against that of Duynkerke and Driedonks (1987) for two cloud-topped PBL cases using the 1-D MM5. One case was forced by only surface buoyancy fluxes while the other case was forced by radiative forcing at

the top of the cloud. The results compared favorably with those published by Duynkerke and Driedonks (1987). Results from these preliminary evaluations are not shown in this report.

An example from a 3-D MM5 simulation using the improved formulation for in-cloud turbulence is shown in Figure 4.1.1, which shows cloud water mixing ratio and TKE for a vertical cross section from San Clemente to Point Magu, off the west coast of the U.S. in August of 1993. The marine stratus layer shown in Figure 4.1.1.a is associated with a region of enhanced TKE in Figure 4.1.1b. The larger in-cloud turbulence (compared to a similar experiment without the improved formulation, not shown) produces greater in-cloud mixing which affects the amount and distribution of the grid-resolved cloud, which in turn interacts with the PBL via the radiative flux divergence near the top of the cloud.

MM5 results using the Blackadar PBL are compared with those using the new TKE sub-model for a sounding location midway along this cross section (Figure 4.1.2). Both model simulations used identical initial conditions and boundary conditions. The Blackadar PBL solution (Figure 4.1.2a) shows an absolutely unstable profile near the base of the cloudy region within the PBL, while the TKE simulation (Figure 4.1.2b) shows a more realistic moist-adiabatic profile through the cloud layer as expected.

4.1.4. Discussion

Significant errors can occur in model simulations which do not properly account for turbulence in saturated layers. The PSU TKE-predicting sub-model for turbulence, now available in MM5V3, has been reformulated and used to demonstrate the sensitivity of the model

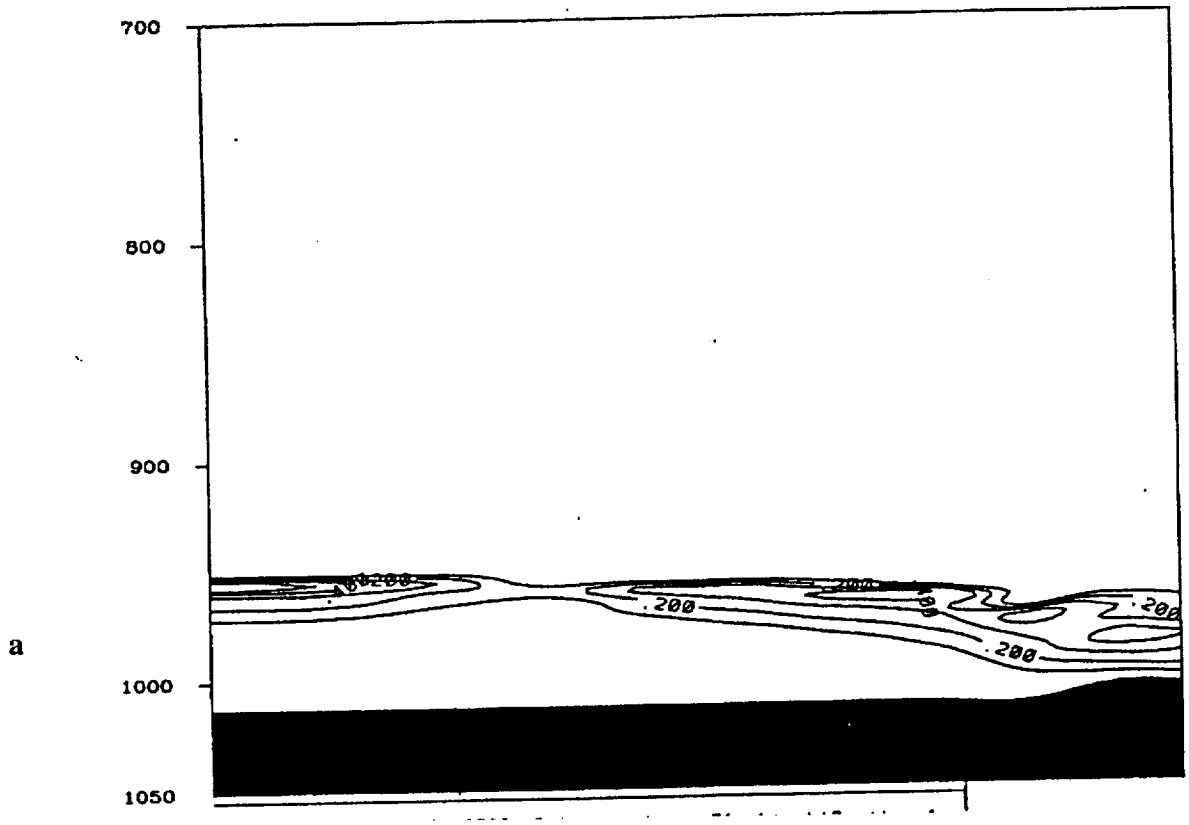

Figure 4.1.1. 3-D MM5 TKE-sub-model simulation for a vertical cross section from San Clemente to Point Magu, California, off the west coast of the U.S., at 6 h (0600 UTC 25 August 1993). (a) cloud-water mixing ratio (contour interval of 0.05 g kg^{-1}) and (b) TKE (contour interval of 0.1 J kg^{-1}).

b

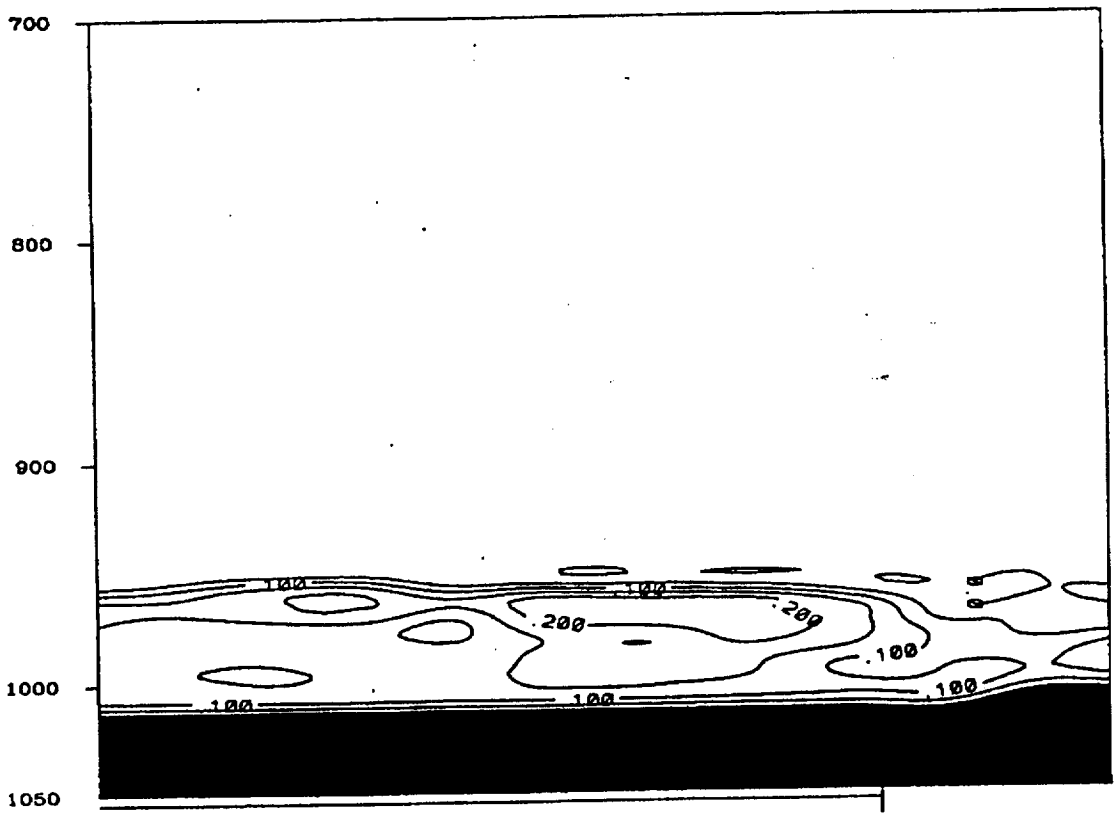

Figure 4.1.1 (Continued)

a.

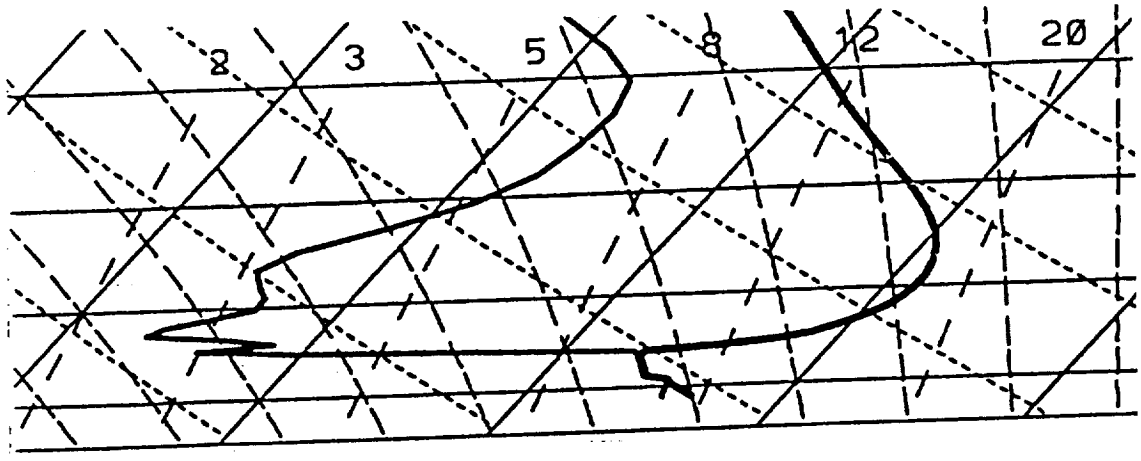

b.

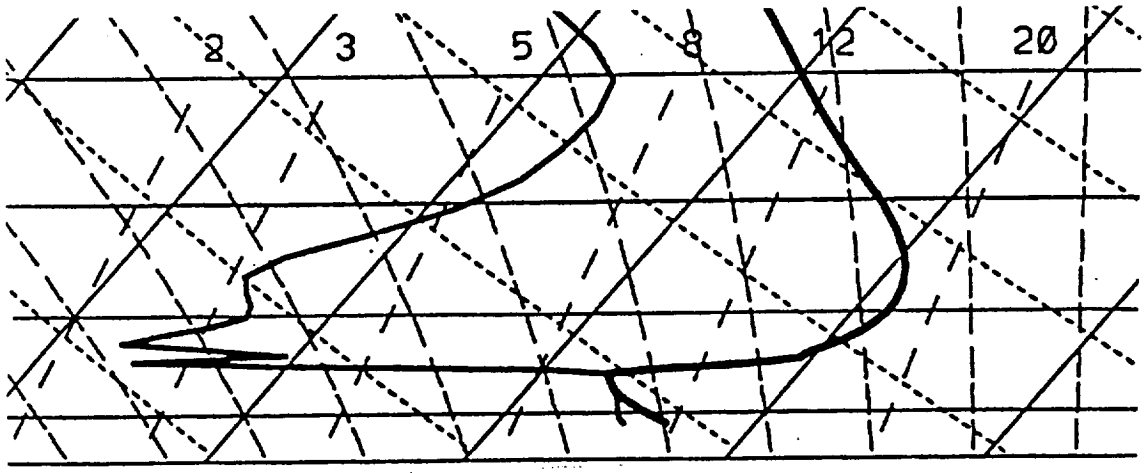

Figure 4.1.2. MM5 simulated sounding located midway along the cross section shown in Figure 4.1.1 at 6 h (0600 UTC 25 August 1993) using (a) Blackadar PBL and (b) PSU TKE sub-model.

solution to proper treatment of in-cloud turbulence, and its complex interaction with the moist microphysics and radiative forcing associated with a saturated layer. The recent improvements to the scheme, beyond that described in Shafran et al. (2000), include better representation of buoyant production and dissipation of TKE in saturated layers, including layers saturated with respect to ice. The mixing of ice-liquid potential temperature, total water mixing ratio and cloud water/ice mixing ratio conserves water mass and energy during vapor-liquid-ice phase changes.

In a future release, the TKE sub-model will be adapted to mixed-phase microphysics, where the sum of the vapor and cloud liquid mixing ratios will be computed as a residual from the total water mixing ratio minus the cloud ice mixing ratio. The individual vapor and cloud liquid mixing ratios will then be recovered using an equilibrium assumption.

4.2 Shallow Convection in the 3-D MM5

4.2.1 Introductory Remarks

Shallow clouds exert strong influences on the radiation budget of the earth-atmospheric system. They also play an important dynamic role in the transport of heat and moisture from the well-mixed planetary boundary layer to the free troposphere. In addition, by modifying the thermal and moisture structure of their environment, shallow clouds may affect the onset of deep convection and the subsequent development of mesoscale circulations. Furthermore, convective clouds may have strong influences on air pollution by causing boundary layer pollutants to be vented into higher levels, by altering chemical reaction rates through aqueous processes, and by

strongly affecting the actinic radiation flux. It is important that the influences of shallow clouds are included in the numerical models. However, most 3-D meteorological models used for air-quality and other mesoscale applications have treated shallow convective processes in inadequate ways. Often, shallow convection is represented as a simple mixing process, with cloud fraction diagnosed directly from the environmental relative humidity. While this approach is fairly reliable for global models, it is not accurate for regional models, especially for the applications associated with air-quality studies which require more detailed information on cloud properties such as cloud-base mass flux, number of clouds, cloud depth, entrainment and detrainment profiles.

In order to more accurately represent the effects of shallow clouds in mesoscale numerical models, a shallow-convection parameterization scheme has been developed at Penn State University (PSU). The scheme is closely associated with boundary layer turbulent processes and can transition to either a deep convection scheme (Kain-Fritsch) in convectively unstable environments or to an explicit moisture scheme in moist stable environments. The scheme's closure assumption uses a hybrid formulation based on boundary layer turbulent kinetic energy (TKE) and convective available potential energy (CAPE), while its convective trigger is primarily a function of boundary layer TKE. The scheme determines updraft characteristics using the vertical velocity calculated from the parcel buoyancy equation for entraining/detraining convective clouds. Using the updraft detrainment profile as a source term, neutrally buoyant cloud (NBC) is predicted by two governing equations (one for cloud fraction and one for liquid water content), with dissipation processes including precipitation, horizontal and vertical turbulent mixing, ice settling and cloud-top entrainment instability. A detailed

description of the shallow-convection scheme is given in Deng et al. (2002a) and in Section 2 of this report.

Following earlier evaluations in a 1-D version of the Penn State/NCAR MM5 model (Deng et al. 2002b), the shallow-convection scheme has been installed and tested against observed data sets in marine environments in the 3-D MM5 (Deng et al. 2000). The evaluations over the mid-Atlantic convective environment using the observational data from the ASTEX has shown that the scheme is able to reproduce the shallow fog-stratus of mid-latitudes and the subtropical trade-cumulus environment over the ocean (Deng, et al. 2000). This section of the final report focuses on evaluating the shallow-convection scheme in a continental stratocumulus environment over the Southern Great Plains (SGP) region.

4.2.2 Model Description

Version MM5v3 of the 3-D non-hydrostatic Penn State/National Center for Atmospheric Research (PSU/NCAR) mesoscale model is used for these experiments. The model is configured with the PSU shallow-convection parameterization and the 1.5-order turbulence sub-model that includes saturation effects in the prediction of turbulent kinetic energy (TKE) (Stauffer et al. 1999, Shafran et al. 2000). The turbulence scheme also is used to determine the planetary boundary layer (PBL) depth. Additional model physics include an explicit moisture scheme that predicts resolved-scale cloud and precipitation processes for water and ice (Dudhia 1989). For radiation, a two-stream broad-band atmospheric radiation scheme that calculates radiation fluxes in the column (Dudhia 1989) is used. As explained in Section 2, use of the shallow-convection scheme requires the column radiation subroutine to be called three times at a given time step

(every 15 minutes) to account for sub-grid portions of the column having clear or cloudy air. This is intended to calculate the radiative fluxes more accurately by considering partial cloudiness in the grid column.

For these experiments, the MM5 was configured with nested domains of 108-km (37x43 grid points) and 36-km (73x73 grid points), both centered at 35°N and 100°W. Vertically, we used 30 vertical layers, with 80-m layers from the surface to about 1400 m AGL. The layer thickness gradually increased above this height. The top of the model's reference-state pressure field was fixed at 100 hPa. Initial and boundary conditions were specified from NCEP global spectral model analysis enhanced by surface and rawinsonde data.

4.2.3 Methodology and Case Description

In this part of the study, we chose the case of 12-13 April 1997. Figure 4.2.1 shows MM5 initial sea-level pressure (hPa) at 1200 UTC, 12 April 1997 on the 36-km domain. Figure 4.2.2 shows a visible satellite image of stratocumulus clouds over the Southern Great Plains (SGP) region at 1709UTC, 12 April, centered on the ARM-CART central facility (36.61°N, 97.49°W). The entire domain of the satellite image covers the rectangular region in Fig. 4.2.1. A strong cold front had passed the central facility around 0000UTC, 11 April, bringing north-northwesterly winds and sharply falling temperatures. By early morning, at 1200 UTC, the surface temperature dropped from ~20 °C on the previous afternoon to -3 °C at the central facility, and post-frontal stratus clouds covered the region. Cold advection and north-

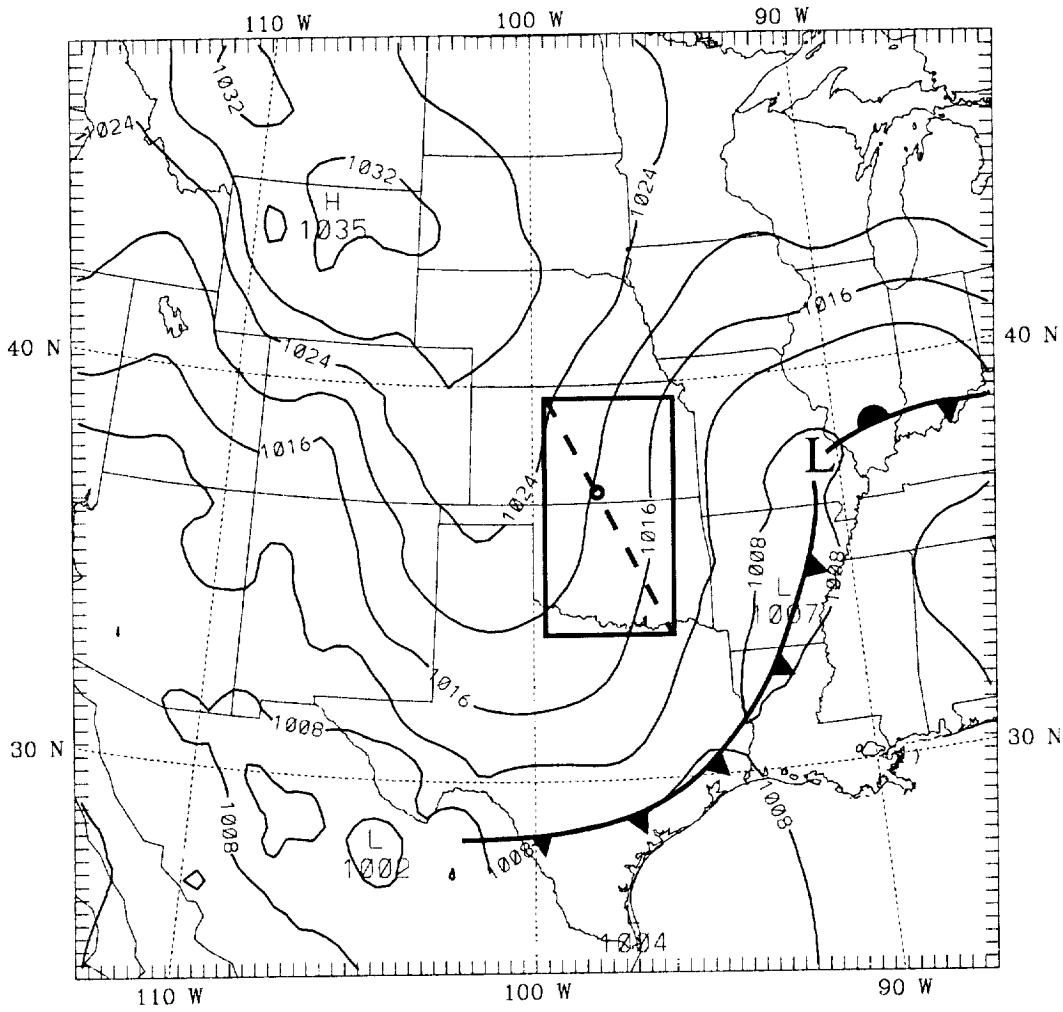

Figure 4.2.1. Analysis of sea-level pressure (hPa) at 0000 UTC, 12 April 1997 on the 36-km domain. The rectangular area over Kansas-Oklahoma region corresponds to the area covered by the observed satellite image in Fig. 4.2.2. Dashed line in the rectangular area shows the location for the cross sections in Fig. 4.2.6. The open circle on the dashed line indicates the location where vertical profiles in Fig. 4.2.7 are created.

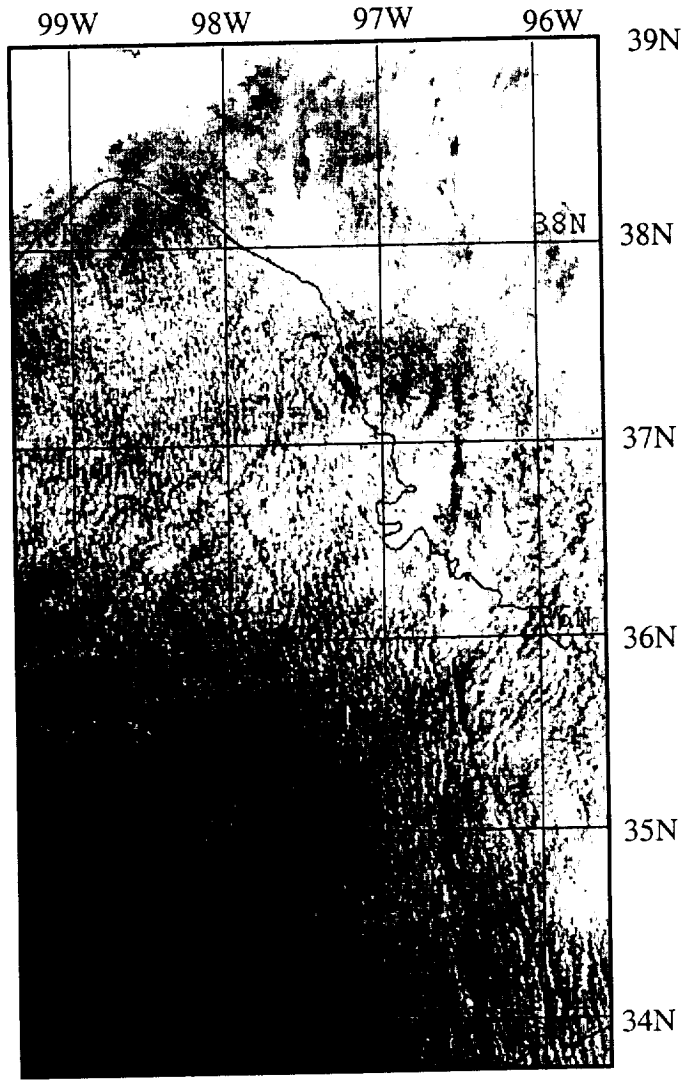

Figure 4.2.2. Visible satellite image at 1709 UTC, 12 April 1997, showing widespread stratocumulus clouds over the Kansas-Oklahoma region, and decreasing cloud cover towards the southwest.

northwesterly winds prevailed over the site through the next 36 h as high surface pressures were established over KS and OK. Following sunrise, heating of the surface led to the growth of the PBL and lifting of the cloud base. Extensive stratocumulus clouds evolved during the period in response to the diurnal heating cycle and boundary layer forcing. Figure 4.2.3 shows the observed cloud base, cloud top and PBL depth at the central facility, measured using a laser ceilometer, micropulse lidar and 35-GHz cloud radar. The cloud layer was initially very low, then gradually lifted as the boundary layer grew. As dry air was entrained from above into the growing PBL, the clouds changed from initial low stratus to broken stratocumulus clouds that extended across most of the region. These stratus and stratocumulus clouds accompanying the cold-air outbreak (Fig. 4.2.2) persisted through the day (12 April) and then dissipated near sunset as the surface heat flux became negative and a stable boundary layer replaced the daytime turbulent mixed layer.

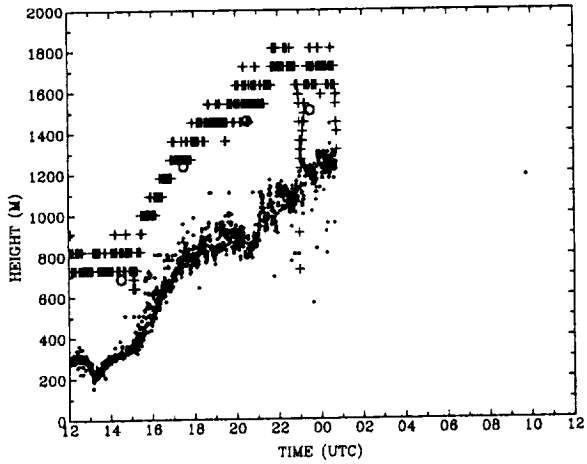

Figure 4.2.3. Observed cloud base (dots, m), cloud top (crosses, m) and mixed-layer depth (open circles, m) from 1200UTC, 12 April to 1200 UTC, 13 April 1997, at the Southern Great Plains ARM-CART central facility (36.61°N, 97.49°W).

To demonstrate the performance of the PSU shallow-convection scheme, we focus on the 36-km domain and conduct two 3-D experiments on this domain. The first (Exp. 4.2.1) experiment is run without the shallow-convection sub-model, so that all clouds must be represented on the resolved scale using MM5's explicit microphysics scheme (in this case a simple water/ice parameterization is used). The second (Exp. 4.2.2) experiment adds the shallow-convection sub-model, so that the sub-grid scale distribution of fractional cloud area and water/ice content are predicted. Both experiments are initialized at 0000UTC, 12 April and run for 24 hours. Simulated results are discussed in the following section.

4.2.4 Results for the Stratocumulus Case

The following discussions will focus on results after sunrise between 1200 UTC, 12 April and 0000 UTC, 13 April on the 36-km domain. Figure 4.2.4a and 4.2.4b show the resolved scale liquid water content (scaled by 10000) of low clouds in Exp. 4.2.1 at 1800 UTC (local noon) and 2100 UTC (mid-afternoon), respectively. The first contour, 0.005 g kg^{-1} gives the approximate outline of the low stratus for Exp. 4.2.1. Since there is no mechanism in Exp. 4.2.1 for producing partial cloudiness, Fig. 4.2.4a and 4.2.4b show solid stratus clouds with low water content across northern KS, but virtually no clouds over OK. That is, there are only two options: completely cloudy or completely clear. While the model captures the general observed trend of less cloudiness to the south and more to the north over the SGP, the true character of this case cannot be represented in the model (without a shallow-convection parameterization).

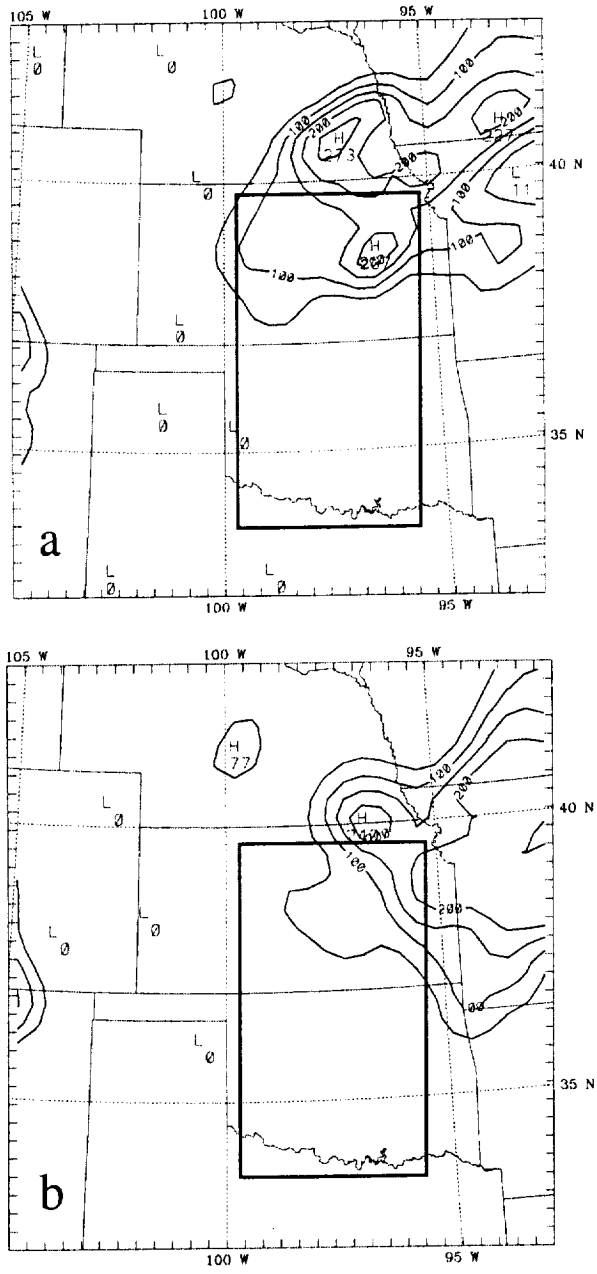

Figure 4.2.4. MM5-predicted liquid/ice water content (g kg^{-1}) of explicit cloud (scaled by 10000) at 1 km AGL in Exp. 4.2.1: a). 1800 UTC. b). 2100 UTC, 12 April 1997. Contour interval is 0.005 g kg^{-1}. Rectangular area corresponds to the area covered by the satellite image in Fig. 4.2.2.

Next, Fig. 4.2.5a and 4.2.5b give the fractional cloud area (%) for low clouds predicted in Exp. 4.2.2, with the PSU shallow-convection scheme, at 1800 UTC and 2100 UTC, 12 April 1997. Contour interval is 10%. Comparing Figs. 4.2.4 and 4.2.5, we find that the difference is dramatic. Both experiments show 100% cloud cover in northeastern KS gradually trending toward fewer clouds to the south, with clear skies over central TX (beginning at the southwest corner of the box indicating the domain of the satellite image in Fig. 4.2.2). Comparison with Fig. 4.2.2 confirms that this pattern is correct. Although Fig. 4.2.5b is valid about 4 hours after the satellite picture, it shows that the model generates the strongest gradient in the cloud fraction over the central part of the verification region.

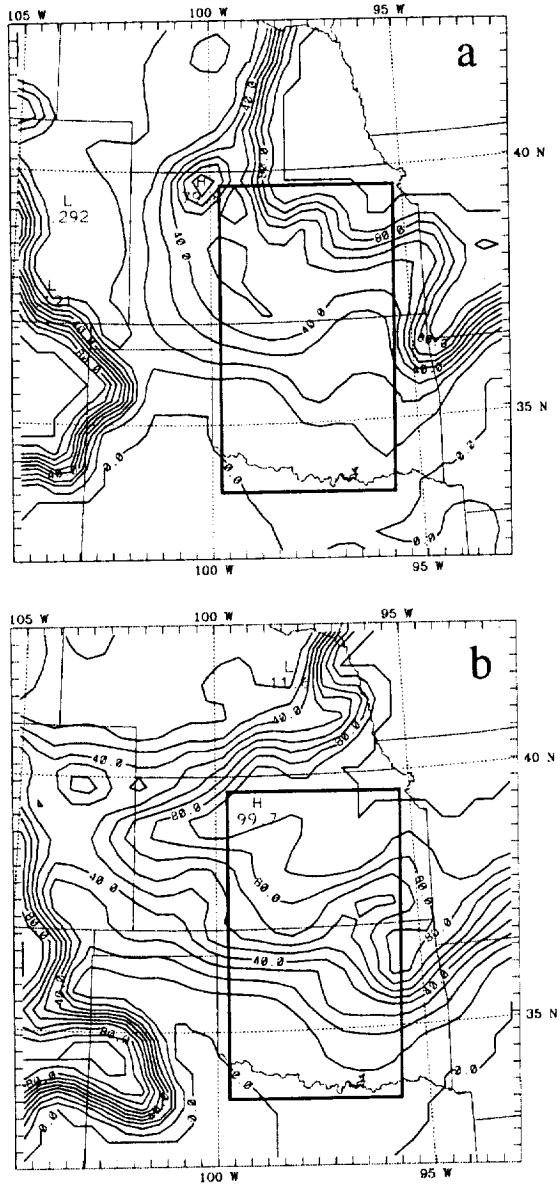

Figure 4.2.5. MM5-predicted fractional cloud area (%) for low clouds in Exp. 4.2.2: a). 1800 UTC. b). 2100 UTC, 12 April 1997. Contour interval is 10%. Rectangular area corresponds to the area covered by the satellite image in Fig. 4.2.2.

In order to examine the evolution of the 3-D cloud fields, we make a northwest-southeast cross section along the dashed line in the box covered by the satellite picture. Figure 4.2.6a, b, c and d show the cross sections of fractional cloud area (%) in Exp. 4.2.2 at 1500UTC, 1800UTC, 2100UTC, 12 April and 0000UTC, 13 April, respectively. Initially at 1500UTC (shortly after sunrise, Fig. 4.2.6a), solid stratus dominates the entire region. By 1800UTC (local noon) the stratus layer has broken and the cloud layer has risen significantly. This is consistent with the observation shown in Fig. 4.2.3. The maximum cloud fraction is less than 50%. By mid-afternoon (Fig. 4.2.6c), as updrafts continue to detrain their mass into their environment to form NBC, the maximum cloud fraction gradually increased to 85-90% that is consistent with the observed stratocumulus clouds in the satellite images shown in Fig. 4.2.2. Around sunset at 0000 UTC, 13 April, stratocumulus clouds start to dissipate, and eventually disappear over the entire region as the PBL collapses.

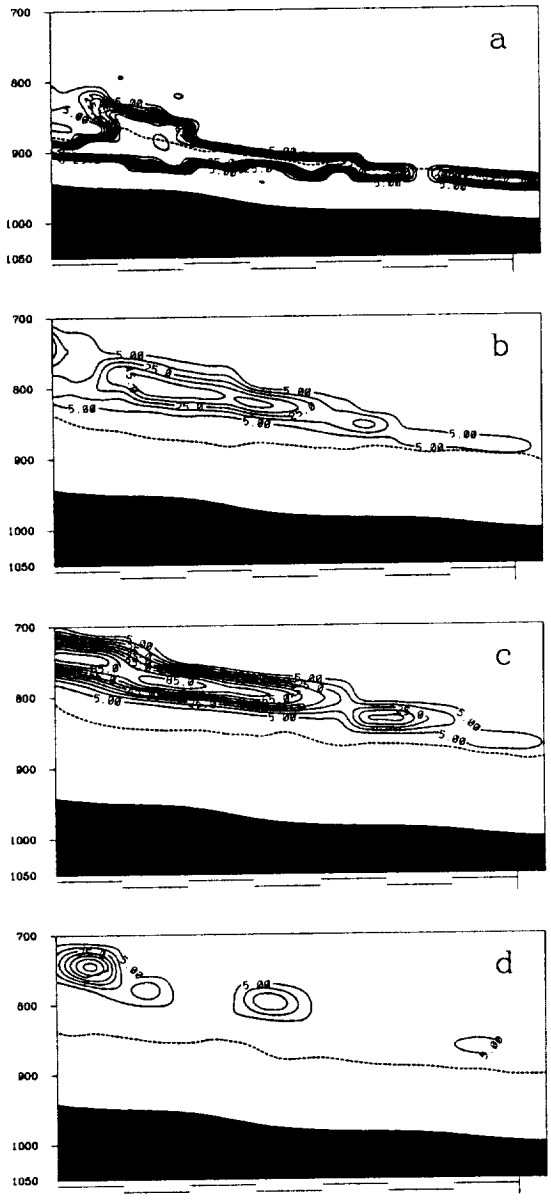

Figure 4.2.6. MM5 north-south cross section of predicted fractional cloud area (%) versus pressure (hPa) in Exp. 4.2.2 along the dashed line in Figure 4.2.1: a). 1500UTC, b) 1800UTC, c) 2100 UTC, 12 April 1997,d) 0000 UTC, 13 April 1997. Contour interval is 10%. Dashed curve is the MM5 predicted PBL depth.

The behavior of the shallow-convection scheme is further examined by looking at vertical profiles of cloud fraction and cloud water calculated using a prognostic scheme (Deng et al. 2002a). Figure 4.2.7a shows the vertical profile of cloud fraction at location on the cross section described above (shown as open circle on the dashed line in Fig. 4.2.1) at 1800 UTC. At this time the maximum NBC fraction is about 50% although the environment relative humidity is about 90%, with cloud top at 1570m and LCL at 634m. It is also shown in this figure that the fraction of updraft is only less than 5%. In the vertical profile of cloud water/ice content (Fig. 4.2.7b) at this time, the maximum cloud water content in the updraft is about 0.9 g kg^{-1} (shown as L_u), while the water/ice content in the NBC is less than 0.01 g kg^{-1} shown as L_c). These values are expected in this type of cold-season stratocumulus clouds.

4.2.5 Discussion

The PSU shallow-convection scheme has been tested in a stratocumulus environment over the Southern Great Plains (SGP) region during a case of 12-13 April 1997. Comparison between simulations with and without the shallow-convection scheme was performed. With the shallow-convection scheme, the MM5 model was able to reproduce the observed characteristics of the stratocumulus environment over land. The simulated results including the cloud fraction, cloud water/ice content were generally consistent with the observations from the field experiments (including radar and satellite imageries).

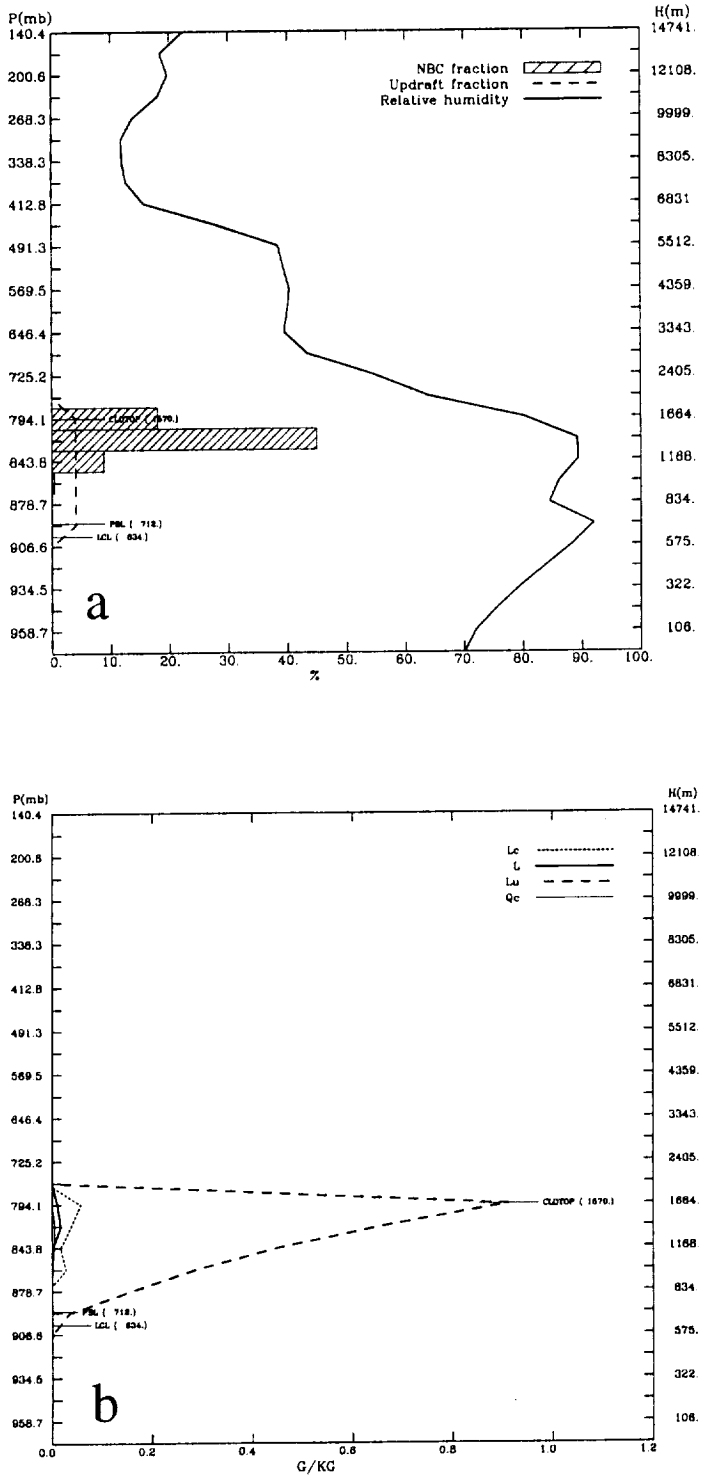

Figure 4.2.7 MM5 predicted cloud vertical profiles in Exp. 4.2.2 at 1800 UTC, 12 April 1997 at location marked by an open circle on the dashed line in Fig. 4.2.1. a). Cloud fraction (%) and resolved-scale relative humidity (%), b). Cloud water/ice content (g kg^{-1}).

4.3 PLACE and Shallow Convection in the 3-D MM5

4.3.1 Overview of the System

The basis of the MM5-PLACE development at Penn State is version 3 of the MM5 modeling system (Dudhia 1993, Grell et al. 1994). This version has the capability of using the Oregon State University (OSU) land-surface model, so that its preprocessor programs can produce several types of data that are required by PLACE or other complex land-surface models. The implementation of PLACE into MM5 has been designed so as to minimize the number of changes necessary in the standard public-release version of the MM5 modeling system. The input data that are specific to PLACE are ingested through an input file with the same data format as the standard MM5 input files, but which has appended all required PLACE variables. For example, these variables include the initial soil moisture and temperature fields that come from the offline version of PLACE described in Section 3.2.

When PLACE is not used, the simpler Blackadar force-restore Slab model (Zhang and Anthes 1982) is used to predict ground temperature. In the Slab land-surface model, the ground temperature of a thin "slab" representing both soil and vegetation effects changes in time according to a surface energy balance. This predictive ground-temperature equation accounts for differences in surface characteristics (e.g., roughness, albedo, moisture availability) as represented through a lookup table based on climatology, and the cloud and radiation effects computed by the MM5 explicit moisture and column radiation submodels. The surface moisture availability is specified at each grid cell and it does not change with time as the soil moisture

content profile does in PLACE. Thus, the surface moisture in slab does not respond to model-predicted precipitation or the lack thereof as it does in PLACE.

The 3-D MM5 system is used in this section to investigate the interactions between surface processes, the boundary layer and shallow clouds. In addition to the PLACE land-surface model, study of these interactions depends on two additional physical parameterizations: the Penn State 1.5-Order TKE turbulence scheme (Stauffer et al. 1999, Shafran et al. 2000), and the Penn State shallow-convection parameterization developed by Deng et al. (2002a). The TKE scheme and the improvements introduced during this study were described in Section 4.1. The shallow-convection scheme was described fully in Section 2, and improvements to the original scheme developed under this project were described in detail in Section 3.3.

The shallow-convective scheme can be considered an extension of the Kain-Fritsch (K-F) deep-convective parameterization, for cases of non-precipitating clouds. The shallow-convection scheme considers the effects of sub-grid clouds that are too shallow to activate the standard K-F scheme. Shallow clouds are triggered when parcels having thermodynamic properties defined in the near-surface layers are able to reach their lifting condensation level. The closure algorithm that determines the magnitude of the cloud-base mass flux distinguishes between a shallow, a hybrid, and a deep convection regime. In the purely shallow regime the mass flux is related to the TKE in the boundary layer (BL). In the deep convection regime the CAPE-removal closure of K-F is adopted, while in the hybrid regime an interpolation between the two extreme regimes is used. The cloud model used to calculate the cloud-environment interaction is similar to the one used in K-F. Finally, the shallow-convection scheme allows for sub-grid cloud water to be detrained from the active updrafts computed by the cloud model into sub-grid neutrally buoyant clouds (NBCs). Prognostic equations for the evolution of the sub-grid

NBC water content and cloud fraction are solved. These equations include the effects of evaporation, turbulent mixing, drizzle, etc. These sub-grid cloud fields in turn are also considered by the radiative parameterization and therefore can affect the energy input at the surface.

4.3.2 Case Description

In this section we show the results from the coupled MM5v3-PLACE with shallow convection for the day of 6 July 1997, focusing on the Central Great Plains region. Figure 4.3.1 shows the sea-level pressure analysis at the initial time (12 UTC) on the 36-km MM5 domain. Synoptic pressure gradients over the Central Plains were weak on this day, with a trough extending from the Great Lakes to northeastern Kansas. Through the night deep convection developed over northeastern Texas and spread into southeastern Oklahoma during the day. The rest of Oklahoma developed a field of shallow convection on 6 July with no precipitation. This spatial gradient of convective conditions represents an interesting and challenging environment for testing and improving the parameterizations used in this work.

4.3.3 Experimental Design

The numerical experiments described here are designed to assess how these different physical processes interact and affect the dynamics of the BL. There are four basic runs for different combinations of the surface and convective parameterizations (runs R04, R06, R13, and R14). Run R04 uses PLACE and the Kain-Fritsch (K-F) deep convection parameterization, R14

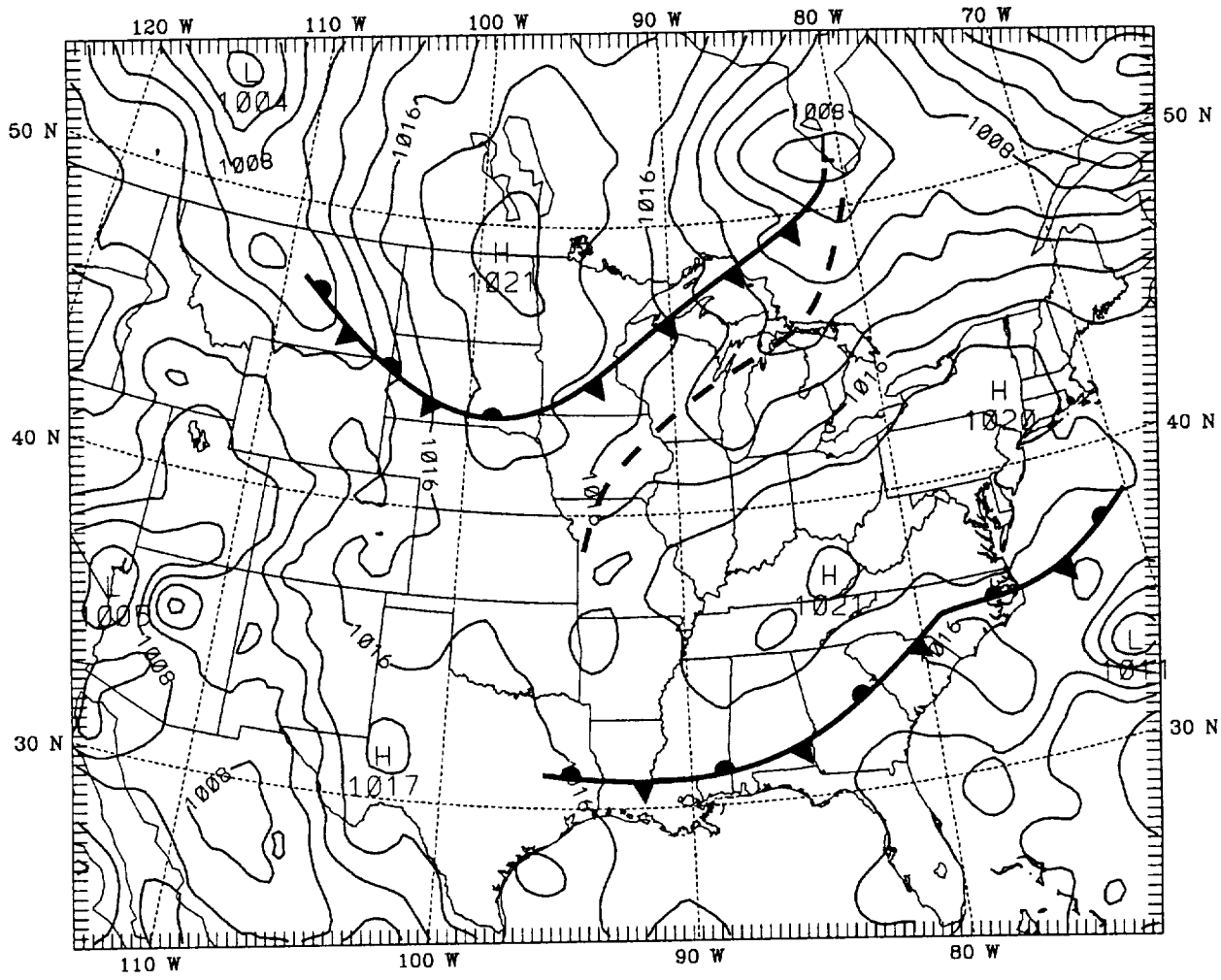

Figure 4.3.1 Model domain map and sea level pressure analysis at 12 UTC 6 July 1997 (contours in hPa).

uses PLACE and K-F with the Penn State shallow-convective parameterization. Run R06 uses the slab force-restore model and the K-F deep convective scheme, and R13 uses slab with the K-F deep convective scheme and the shallow-convective scheme. There are two additional sensitivity runs. Run R15 is similar to R04, but the model precipitation is not allowed to affect the soil moisture. Run R17 is similar to R13, but the shallow cloud-base mass flux has been augmented by a factor of three. All runs have been made with a 36-km grid and 32 levels in the vertical extending up to 50 hPa and with 15 levels below 850 hPa. All runs are integrated from 12 UTC 6 July 1997 to 0000 UTC 7 July 1997.

4.3.4 Results

4.3.4.1 Shallow Cloud Fields and Their Effects

Figure 4.3.2 shows the model's low-level sub-grid cloud area fractions predicted at 18 UTC July 6, 1997, 6 hours after initialization. The plotted field corresponds to the maximum cloud fraction predicted by the model for the pressure levels between 970 and 800 hPa. Figure 4.3.3 shows the low cloud amounts derived from GOES satellite data by Patrick Minnis at NASA Langley Research Center (data obtained from `http://www-pm.larc.nasa.gov/`). Comparison of Figs. 4.3.2 and 4.3.3 shows that the spatial distribution of low-level cloudiness has been partially captured by the parameterization. The SW-NE band that crosses Oklahoma is reproduced in the model, although shifted eastwards somewhat. The predicted cloud amounts, however, are much smaller than those derived from satellite. The sensitivity run R17 (with an augmented cloud mass flux) shows the same spatial pattern, but peak amounts around 40% compared to the peaks around 30% shown in Fig. 4.3.2. The runs that used PLACE as the land-

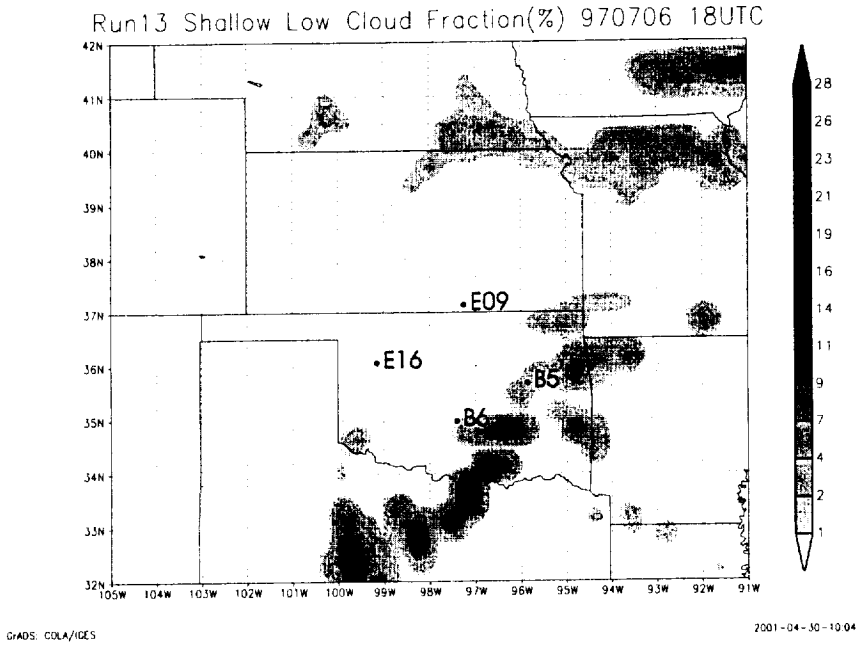

Figure 4.3.2 Model calculated sub-grid low-level cloud fractions in run R13 for 6 July 1997 at 18 UTC. Run R13 uses SLAB surface model and Kain-Fritsch convective parameterization.

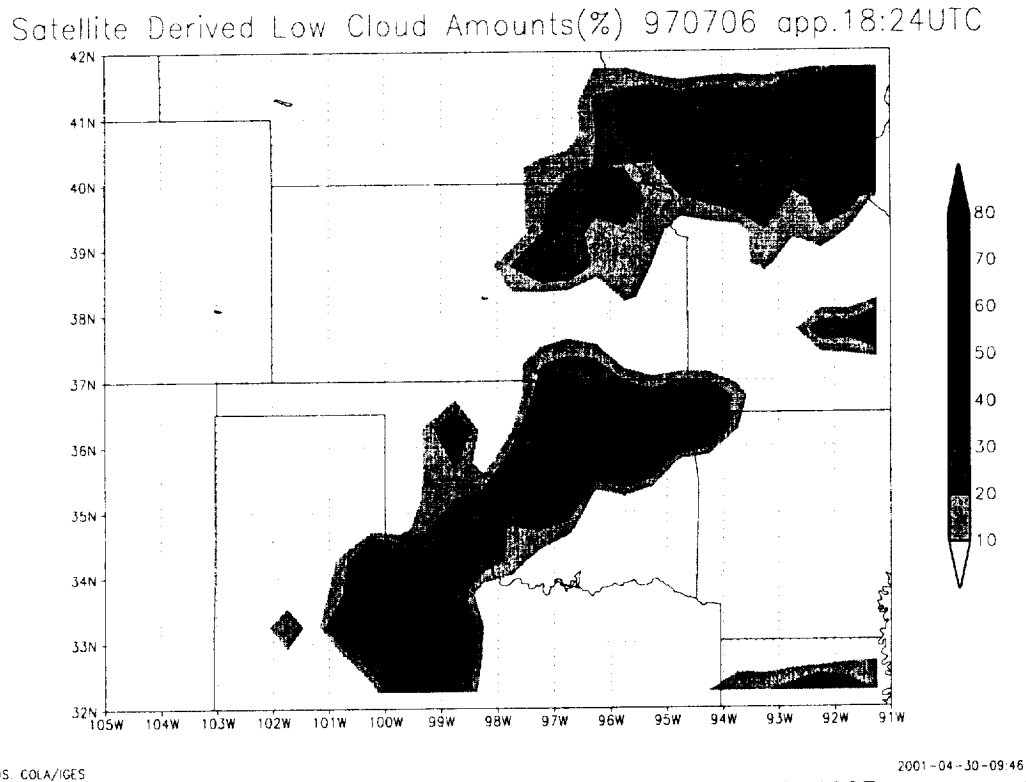

Figure 4.3.3 GOES derived low level cloud fractions for 6 July 1997 at approx. 18:24 UTC.

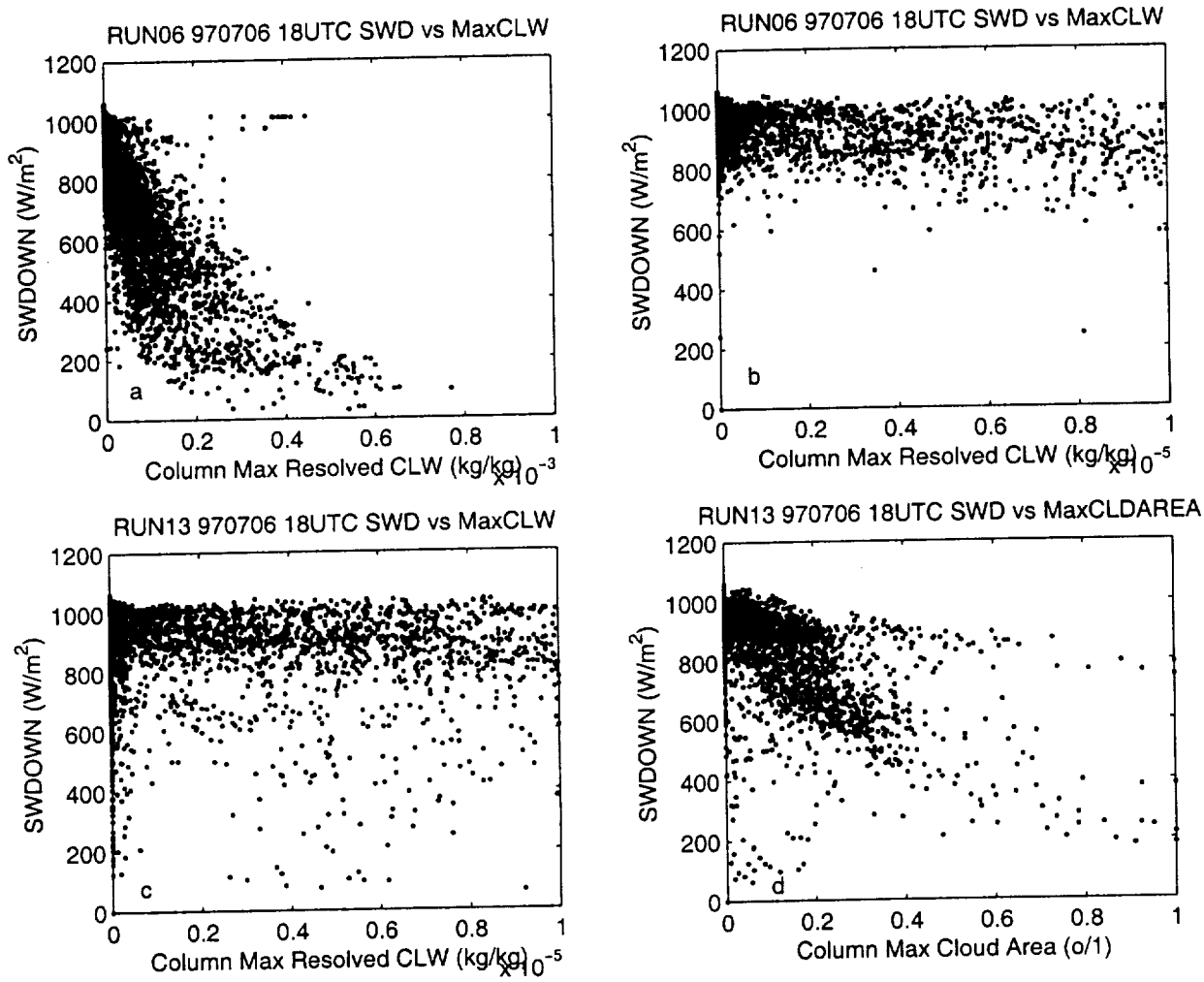

Figure 4.3.4 Scatter plots of model downward shortwave radiation fluxes at the surface for 6 July 1997 at 18 UTC. a) Abscissa variable is column maximum resolved-scale cloud water content in run using KF convective scheme only, b) as a) but for grid points with maximum cloud water content below 10^{-5} kg/kg, c) as b) but for run that uses shallow convective scheme, d) as c) but abscissa variable is sub-grid cloud area fraction.

surface parameterization showed a more extensive region of shallow clouds, associated with larger evaporation rates computed in those runs (not shown).

One of the physical processes that a sub-grid cloudiness scheme tries to represent is to account for the effect of unresolved clouds on the solar radiation reaching the surface. Figure 4.3.4 shows the dependence of model downward solar radiation (SWDOWN) as a function of resolved and sub-grid cloud variables, for all grid points at 18 UTC. Panel a shows SWDOWN versus the maximum resolved cloud water content in the column, for a run without the shallow convection scheme. As expected, larger cloud water amounts are associated with reduced radiative fluxes at the surface. Panel b is a blowup of the same plot, but for maximum cloud water amounts lower than 10^{-5} kg/kg. In these clear and almost-clear conditions the standard model computes radiative fluxes that are consistently large, since there is no sub-grid cloudiness to produce attenuation. Panel c is constructed as panel b, but for results of run R13, that includes the use of the shallow-convection parameterization. In this case there is more variability in the radiative fluxes for the grid points that are almost clear with respect to resolved cloud water. Finally, panel d uses the same quasi-clear points of panel c, but the scatter is between SWDOWN and sub-grid cloud area fraction. The latter variable explains much of the computed attenuation of the solar radiation reaching the surface.

The effects of the shallow-convection parameterization on the vertical redistribution of water vapor and temperature are illustrated by the vertical profiles shown in Fig. 4.3.5. Panels a) and b) show the thermodynamic profiles for point B5 in east-central Oklahoma, and panels c) and d) are for point B6 in central-southern Oklahoma (locations shown in Fig. 4.3.2). Observed soundings are plotted in each panel as bold lines. Especially over point B5, where shallow clouds were more prevalent in the model, the shallow convection parameterization appears to dry

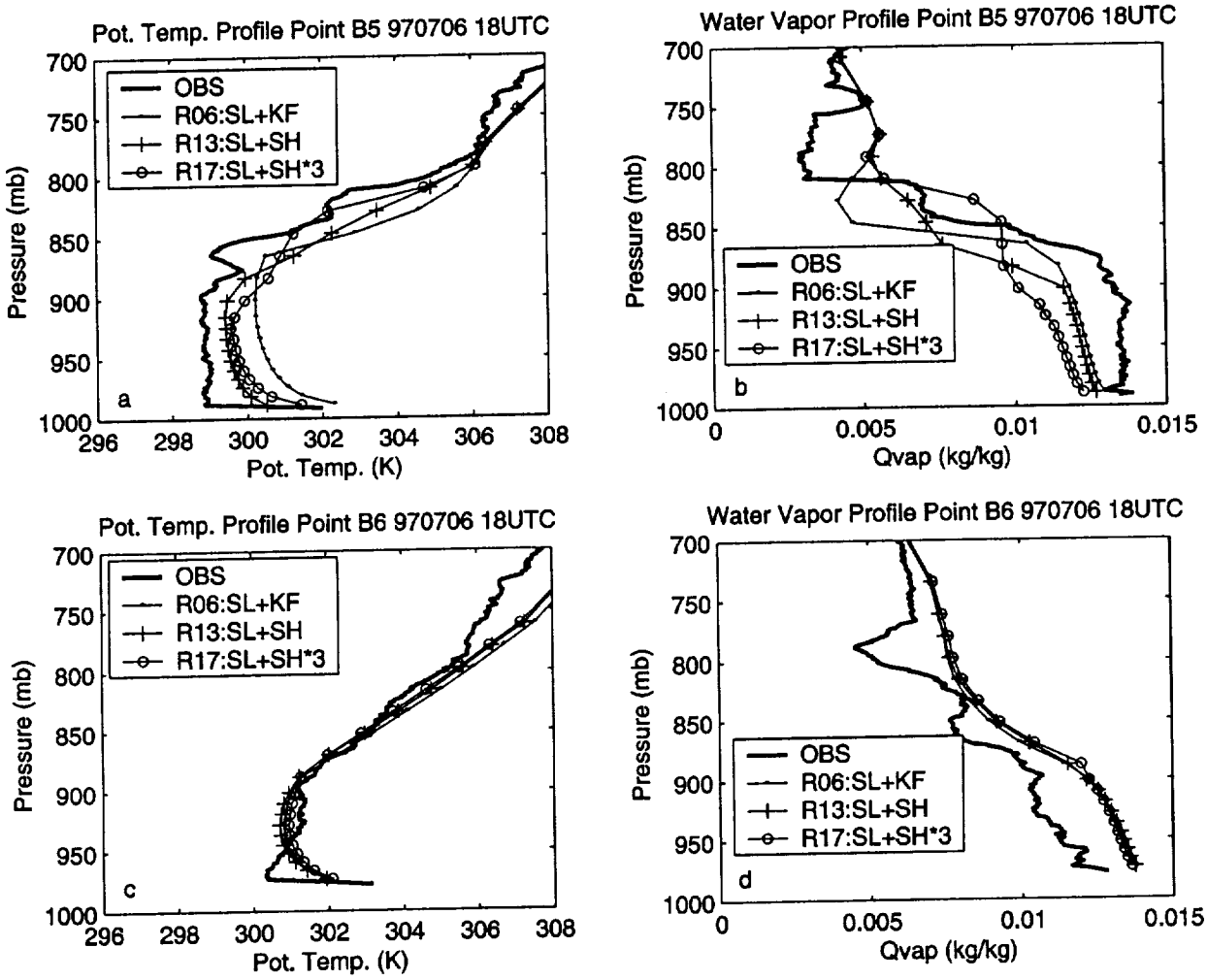

Figure 4.3.5 Observed and modeled vertical profiles of thermodynamics variables. a) potential temperature at point B5, b) water vapor mixing ratio at point B5, c) as a) but for point B6, d) as b) but for point B6. Results are for runs with different convective schemes.

the upper portion of the boundary layer in R13 and moisten the layers above it. With the cloud-base mass flux artificially increased in R17, the drying effect extends throughout the BL. The temperature profile is affected by the vertical transport and also the radiative effects described earlier, and the net result compared to B5 appears to be a cooling of the boundary layer and the air above it. In these three-dimensional runs advection can also be important, so that these preliminary effects have to be studied further.

4.3.4.2 Effects of Surface Processes

In this section we describe the effects of using different treatments of the surface boundary conditions. As discussed in Section 4.3.1, the standard MM5 model uses the Slab parameterization to calculate the surface fluxes, including a prognostic equation for the soil surface temperature (only one layer) and a fixed climatological moisture availability field to calculate the latent heat fluxes. The alternative scheme uses the PLACE land-surface model, which includes tendency equations for five soil moisture layers, and seven soil temperature layers.

During this time of the year Oklahoma has a strong longitudinal gradient in vegetation cover and soil moisture. Figure 4.3.6b shows longitudinal averages of water vapor mixing ratios derived from surface Oklahoma Mesonet stations. Each point is constructed by averaging the measurements of all stations located in a 1 degree latitude by 1 degree longitude box centered at 36° N and moving –99.5° W to –95.0° W. The measured vapor gradients at 12 UTC and 18 UTC show that the eastern part of the state develops a moister boundary layer at 18 UTC than the central and western parts, consistent with the vegetation cover gradient. Model results shown in

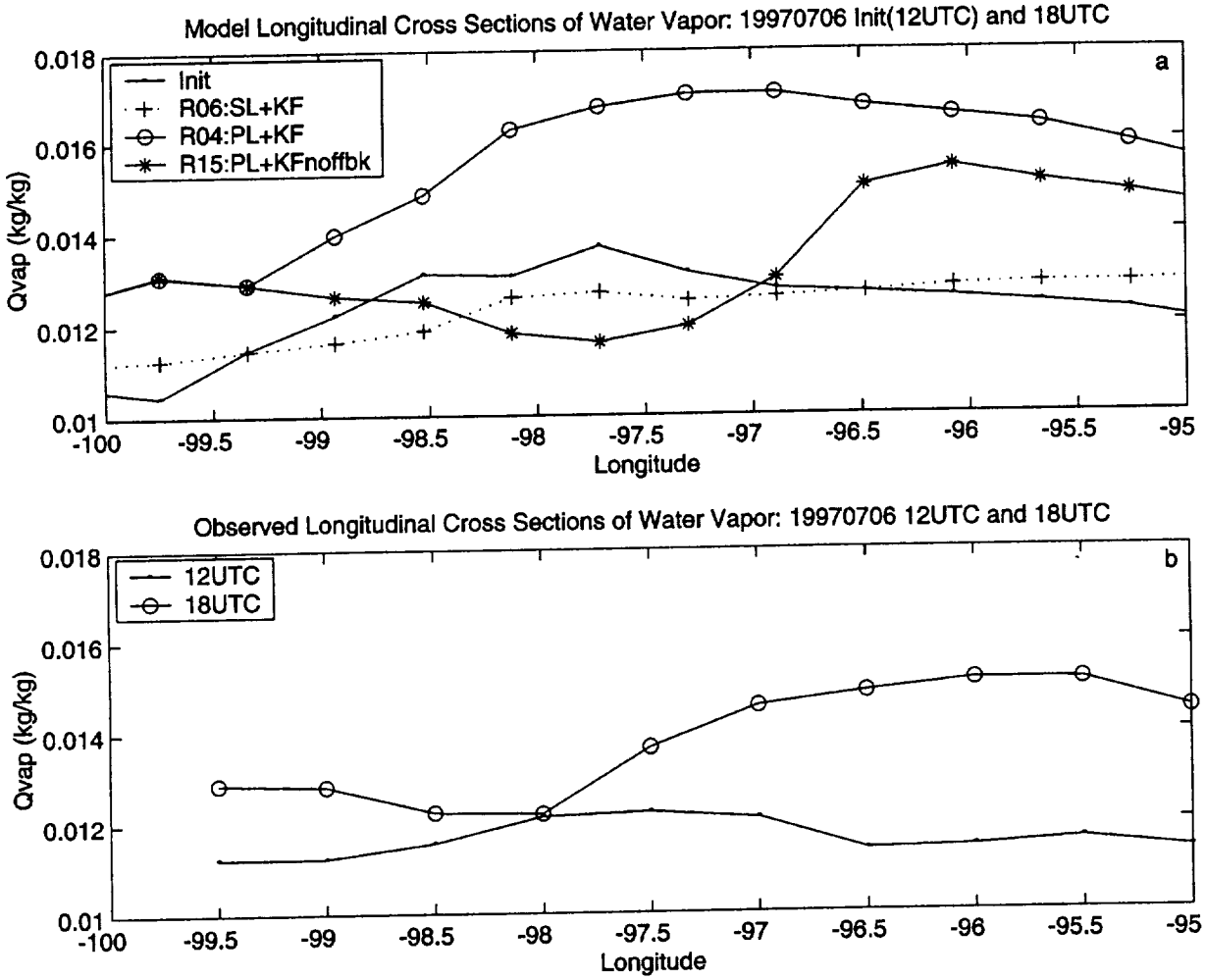

Figure 4.3.6 Longitudinal cross sections of surface layer water vapor at 36 N for 6 July 1997 at 12 UTC and 18 UTC. a) Model results at first layer. b) Averages derived from MESONET observations.

Fig. 4.3.6a indicate that the standard slab surface model does not capture this gradient in moisture (run R06). The run R04 that uses PLACE does indeed produce more moistening in the eastern part of the state, although the mixing ratios appear to be too high. In Run R04, the K-F deep-convection scheme produced widespread light rainfall over Oklahoma (largely due to inaccurate initialization of the precipitation already occurring at the intial time, 12 UTC), which caused an increase of the surface soil moisture and subsequent high evaporation rates calculated by PLACE. This contributed to the excessive boundary-layer water vapor in R04 at 18 UTC. Run R15 does not include the rain feedback on the soil moisture (and therefore on the evaporation rates). Thus, experiment R15 also shows the longitudinal gradient of moisture, but with lower overall values of mixing ratio and perhaps too much drying in the central region of the state. Dynamic initialization can be used in the future to minimize these initialization errors.

The diurnal cycle of water vapor mixing ratio in the convective boundary layer usually shows a moistening in the early morning hours and a subsequent drying due to entrainment of the drier air from above the BL. If the moisture supply at the surface is high, this later drying can be reduced. Figure 4.3.7 shows in bold lines the surface temperature and mixing ratio measured at the Mesonet stations closest to points B5 (panels a and b) and B6 (panels c and d). The second station near B6 shows a more pronounced drying in the afternoon than the first station near B5 does. From the model runs, the run R15 that uses the PLACE model with no rain feedback appears to produce the best time series of temperature and mixing ratio over both points.

Figure 4.3.8 shows potential temperature and water vapor mixing ratio vertical profiles at 18 UTC 6 July 1997, over points B5 (panels a and b) and B6 (panels c and d), measured and calculated by the model runs that used the PLACE land-surface sub-model.

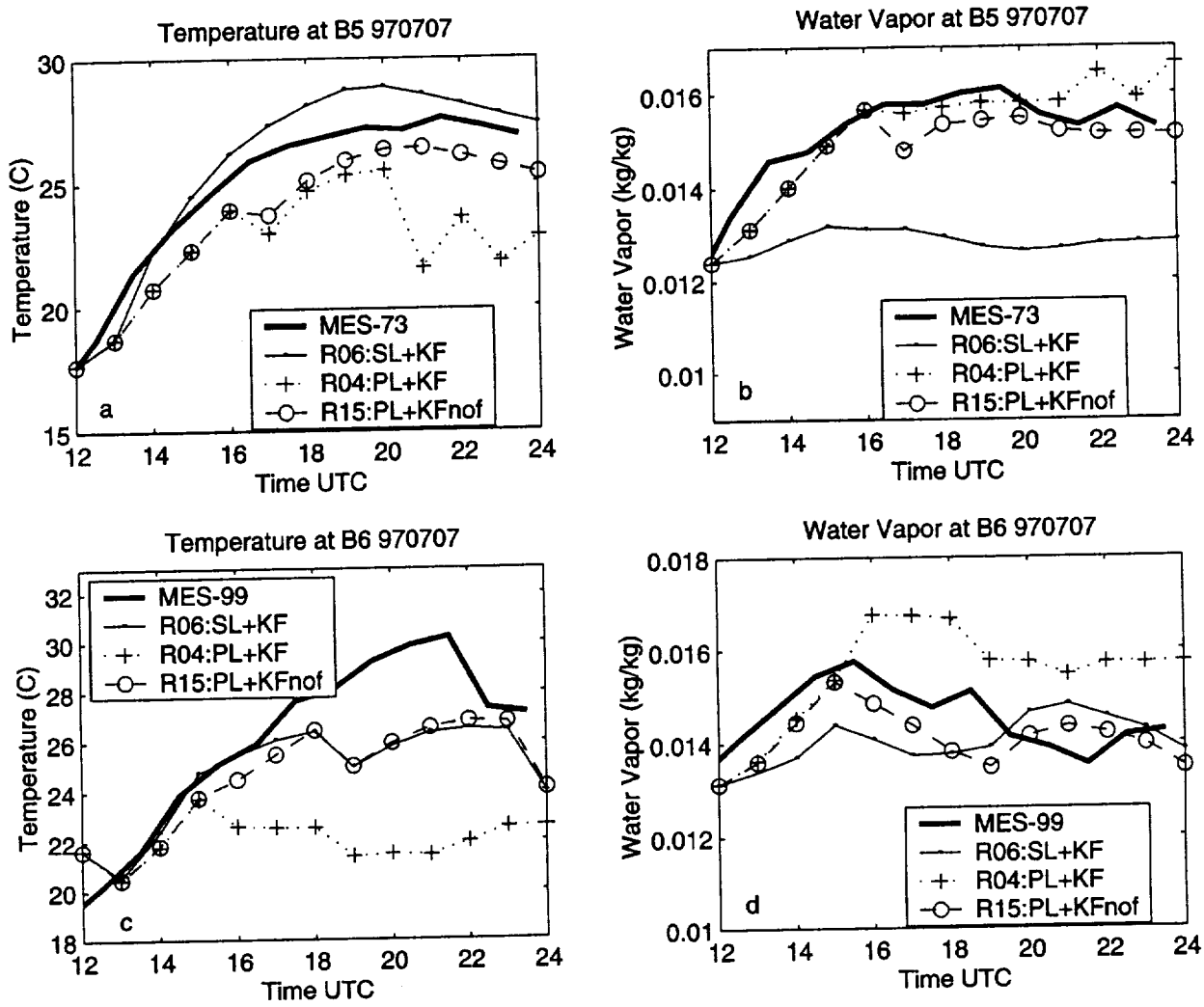

Figure 4.3.7 Time series of temperature and water vapor mixing ratio. a) Mesonet station and model grid point closest to point B5, b) as a) but for water vapor mixing ratio, c) Mesonet station and model grid point closes to point B6, d) as c) but for water vapor mixing ratio.

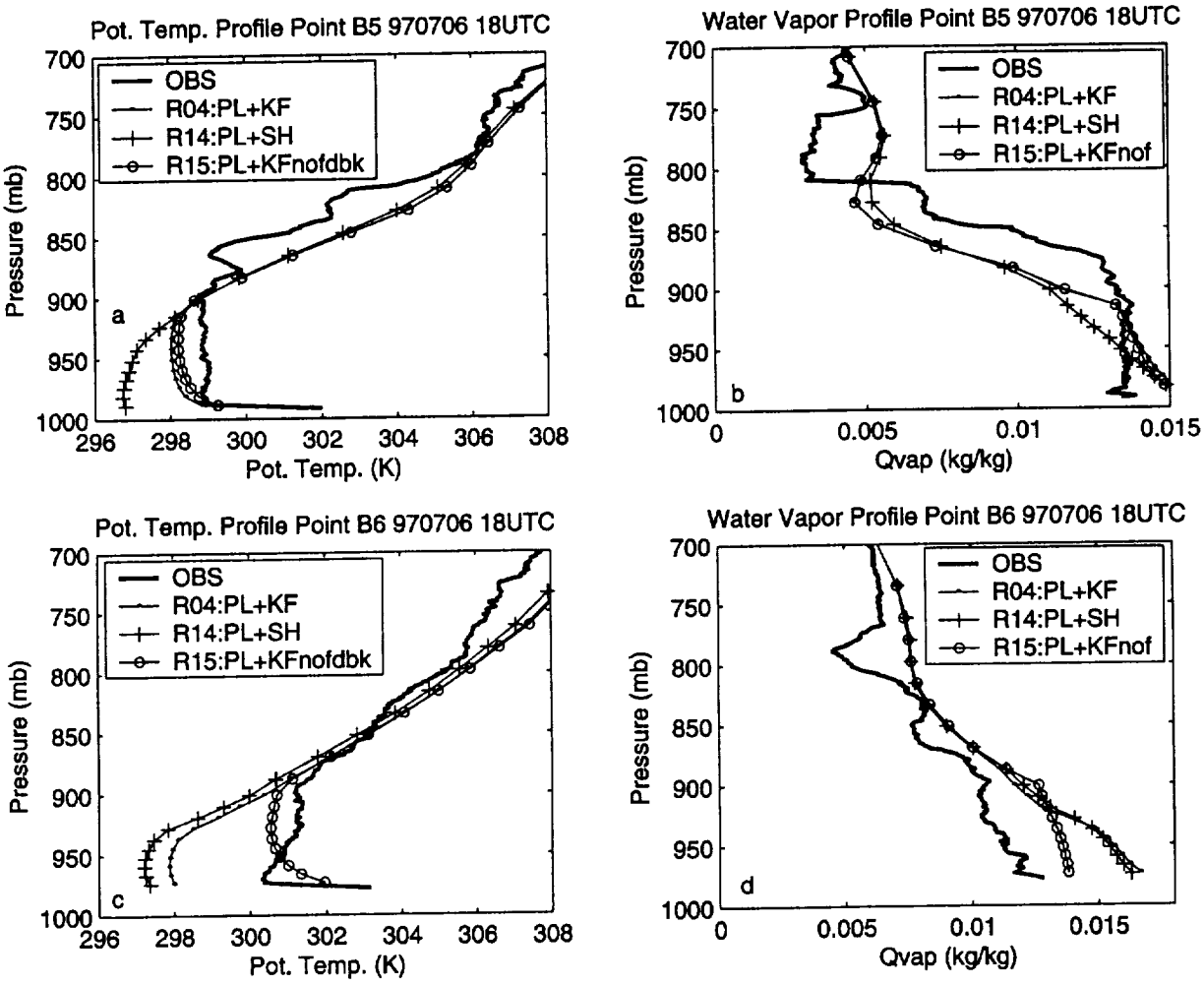

Figure 4.3.8 Observed and modeled vertical profiles of thermodynamics variables. a) potential temperature at point B5, b) water vapor mixing ratio at point B5, c) as a) but for point B6, d) as b) but for point B6. Results for runs with different surface schemes.

Comparison of these soundings with those in Fig. 4.3.5 shows a tendency for the boundary layer calculated by PLACE to be moister and cooler than the observations. The bias is reduced when the rain feedback on the evaporation is eliminated (run R15). The measured temperature profile over point B6 has the peculiarity of having a strong unstable surface layer, but a stably stratified and not well-mixed boundary layer. It is possible that this condition is due to advection that is not captured adequately by the model results.

The best way to test the performance of the surface parameterizations would be by comparing predicted surface fluxes with observations. However, reliable measurements of surface fluxes are scarce. For the period of interest the SGP data archive provides only 8 flux measurement points with no quality flags. Figure 4.3.9 shows modeled and measured surface-flux time series for points E09 (panels a and b) and E16 (panels c and d) (locations shown in Fig. 4.3.2). In the region where these and the rest of the measurements are available, the model using PLACE tends to underestimate the evaporation rates, as in the case of the results for station E09. The comparison of the measurements with the PLACE runs is better at station E16. However at these points we see a tendency for the modeled latent fluxes to peak earlier in the morning and then decrease, a feature that has to be better understood with more detailed analysis of the results.

4.3.4.3 Effects of Sub-grid Soil Moisture Heterogeneity

The latent heat fluxes calculated by the 3-D MM5-PLACE model in the previous section show some features that we will try to describe and explain here in more detail. The time series of modeled latent heat fluxes in panels a) and c) of Fig. 4.3.9 show an early peak in evaporation and then a tendency for near-constant or declining values in the afternoon. Although in some

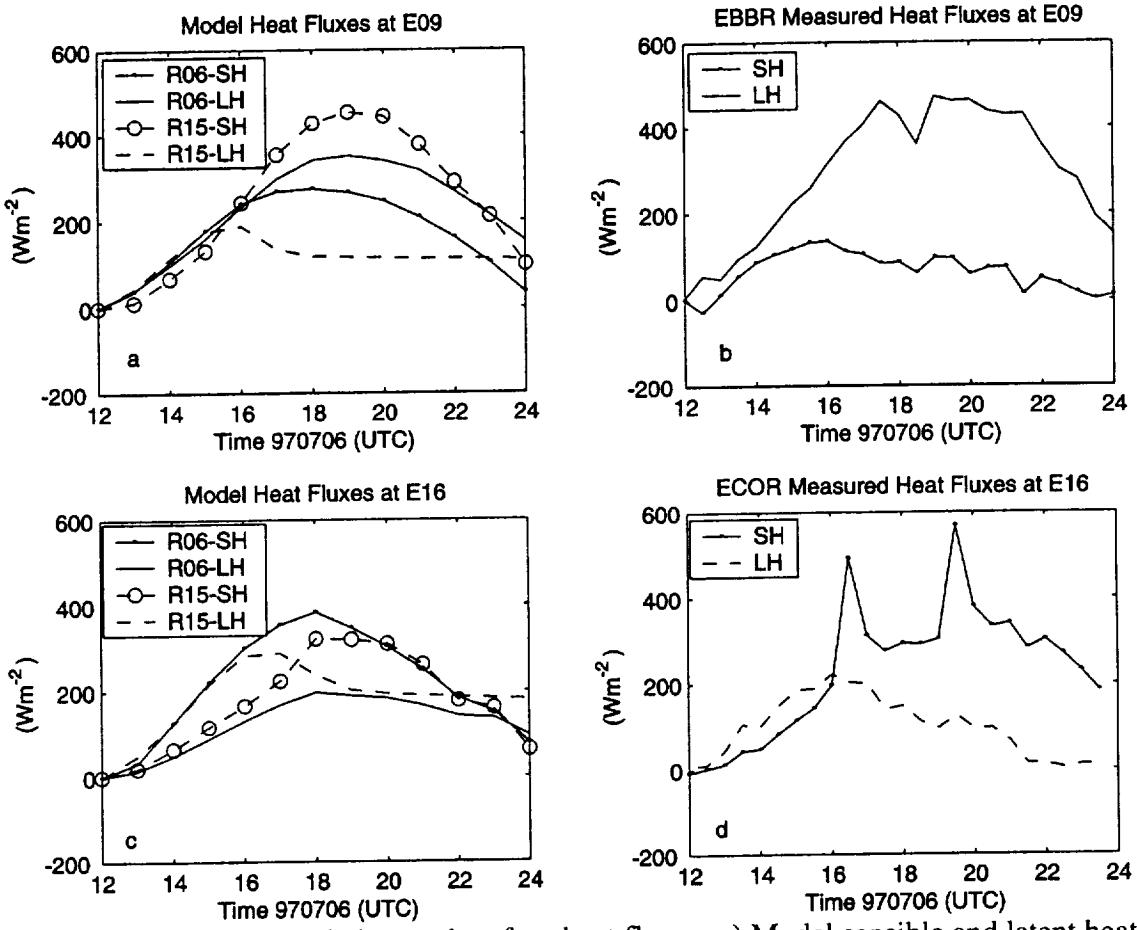

Figure 4.3.9 Model and observed surface heat fluxes. a) Model sensible and latent heat fluxes at station E09, b) observed fluxes at E09 with Energy Balance-Bowen Ratio (EBBR) instrument, c) model sensible and latent heat fluxes at station E16, d) observed fluxes at E16 with eddy correlation instrument. See Fig. 4.3.2 for location of stations.

cases the observations show a similar behavior (panel d of the same figure), in many other cases the diurnal cycle of evaporation is more symmetric with respect to noon (panel b). Also, in visualizing horizontal maps of calculated evaporation rates, there is a tendency to see sharp gradients between zones of little evaporation and other zones in which evaporation rates are large. We try to understand these model results and explore the effect that sub-grid soil moisture variability can have in this respect.

To illustrate two different types of model results, we present in Fig. 4.3.10 modeled latent heat fluxes for two grid points, those closest to ARM-CART stations C1 and B5. Panels a) and c) present results for Run R15 that did not include precipitation feedback into the soil moisture, and also did not include sub-grid soil moisture variability. In each panel we present the total evaporation rate, as well as the parts due to evaporation from the soil (very small in both cases) and vegetation. Panels b) and d) show the same results, but for Run 04s4 that includes consideration of sub-grid soil moisture. The discussion of how we estimated soil moisture variability is presented in the following section. For now we concentrate on panels a) and c) and try to explain the significant difference in the diurnal cycle of evaporation in these two grid points. In particular we would like to understand for C1 (panel a) its early peak in evaporation rate and the leveling off in the afternoon, and for B5 (panel c) its well defined diurnal cycle and higher values of evaporation rates.

The different time traces of model evaporation at points C1 and B5 can be due to differences in the soil and vegetation types (and associated parameters), or different states of the soil variables (moisture and temperature), or a combination of both. Figures 4.3.11 and 4.3.12 show the time evolution of soil moisture and soil temperature (upper layer) for the same model

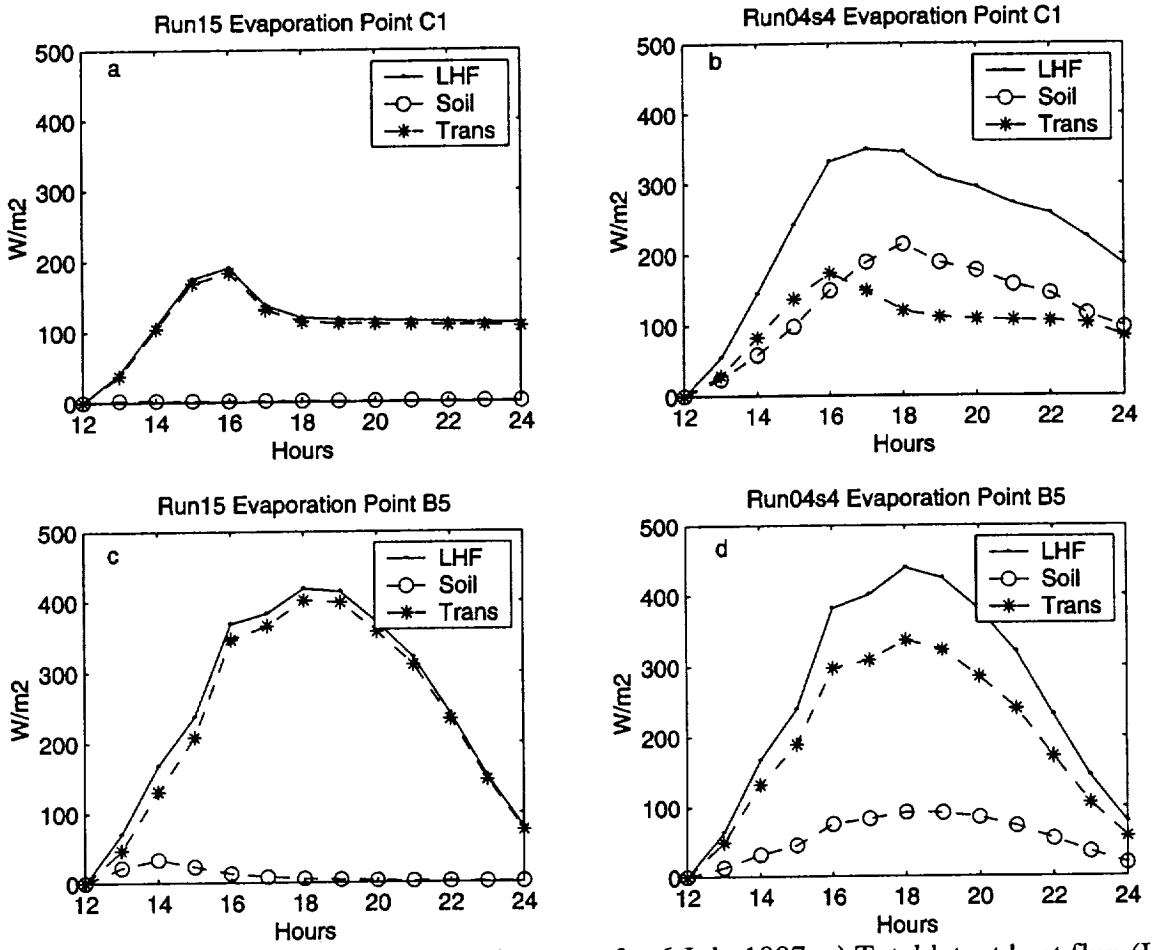

Figure 4.3.10 Time series of evaporation rates for 6 July 1997. a) Total latent heat flux (LHF), soil evaporation (Soil), and plant transpiration (Trans) at grid point closes to C1 for Run15 that has no rain feedback on soil moisture and no soil moisture heterogeneity. b) as a) but for Run 04s4 that considers soil moisture heterogeneity. c) as a) but for gridpoint closest to point B5. d) as b) but for gridpoint closest to point B5.

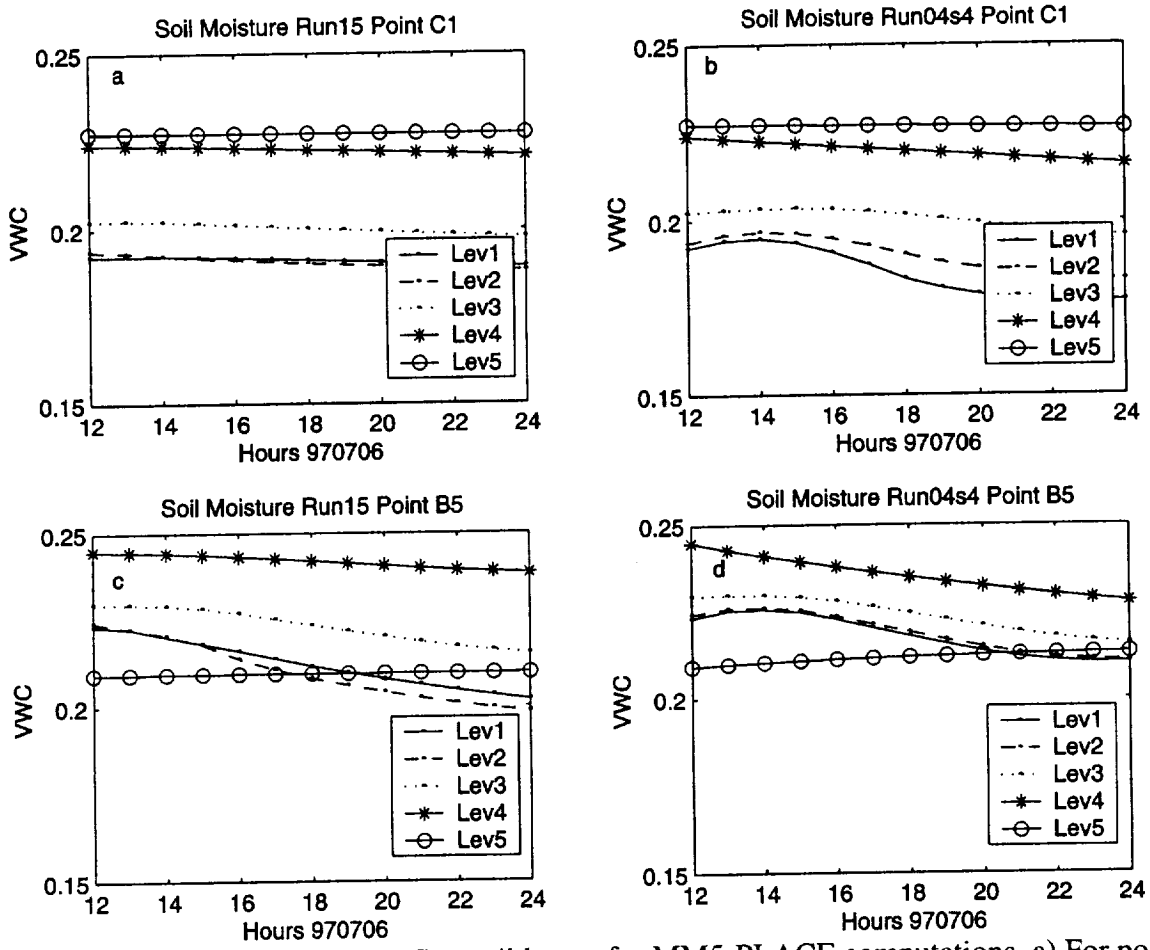

Figure 4.3.11 Soil moisture at five soil layers for MM5-PLACE computations. a) For point closes to C1 and run R15 that does not include variability in soil moisture, b) as a) but for run R04 that includes soil moisture variability, c) as a) but for point B5, d) as b) but for point B5.

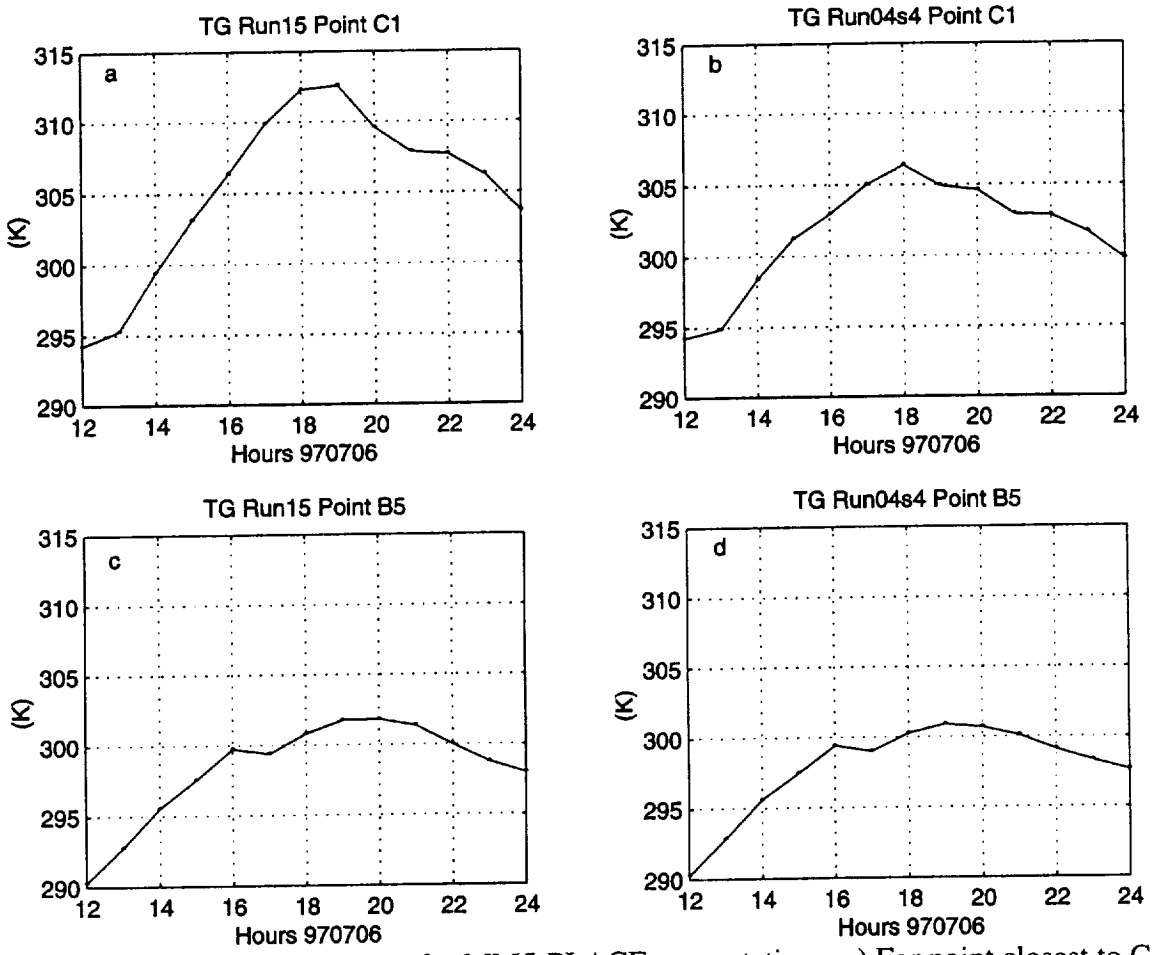

Figure 4.3.12 Soil temperature for MM5-PLACE computations. a) For point closest to C1 and run that does not include variability in soil moisture, b) as a) but for run that includes soil moisture variability, c) as a) but for point B5, d) as b) but for point B5.

runs as in Fig. 4.3.10. It is apparent that the upper soil layers are initially moister at point B5 than at point C1. Soil temperature reaches higher values at C1 than at B5, consistent with the smaller evaporation fluxes at C1. In terms of differences of the parameters characterizing soil and vegetation at both grid points, both points have the same soil type (silt loam) and this eliminates a potentially important source of differences between them. However, point C1 has mixed dryland/irrigated cropland and pasture and point B5 has savanna, and the vegetation fraction at C1 is 0.41 and that at B5 is 0.79.

In order to study in detail the behavior of the evaporation rates calculated by PLACE, we isolated its evaporation subroutine and constructed a Matlab graphical user interface (GUI) that allows for easy interactive computation of evaporation rates for different conditions in the surface parameters and forcings. In particular we calculated evaporation rates as function of soil temperature, soil moisture, or soil moisture variability. Figure 4.3.13 shows evaporation rates as a function of soil temperature for points C1 (panel a) and B5 (panel b). The bold lines indicate total evaporation. The dash-dotted line indicates the fraction that is due to evaporation from plant storage. The GUI results presented in Fig. 4.3.13a show for point C1 a pattern similar to that of the 3-D MM5-PLACE computations (Fig. 4.3.10a). Total evaporation peaks early and then flattens out to a nearly constant value. (Note that the temperature abscissa in the figure can be considered also a time variable, since we started the computation with the temperature and plant storage conditions similar to the 12 UTC conditions, shortly after the daily minimum temperature, and we finished with the maximum temperature observed around 18 UTC.) A detailed analysis of the GUI results shows that the early peak in evaporation rate is due to depletion of plant water storage in the model. Evaporation of plant storage in the model occurs when a layer of soil reaches its maximum evaporation rate. Plants are assumed to continue

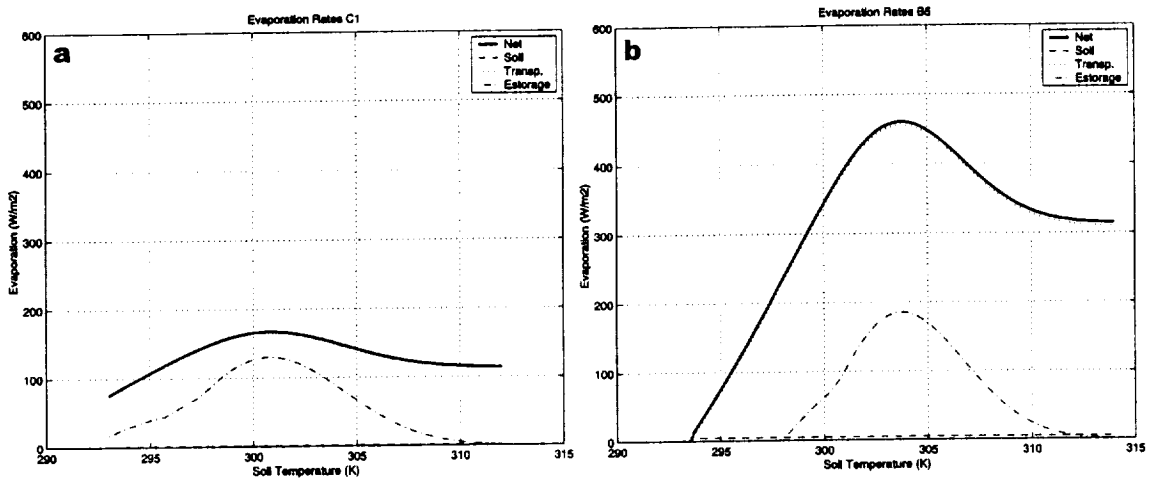

Figure 4.3.13 Computed evaporation rates as a function of soil temperature. a) for conditions similar to point C1, b) for conditions similar to point B5.

evaporating at the potential rate, so that any stored water is depleted. After some time the plant storage vanishes and the evaporation rate returns to the maximum sustainable rate that can be taken by the plants directly from the soil (threshold evapotranspiration). Results for point B5 in panel b) show that the threshold plant evaporation is larger than for C1. This is due to a moister soil and to a larger vegetation cover fraction. Consistently, the depletion of plant storage occurs later than for point C1. The results in the 3-D MM5-PLACE simulation for B5 (Fig. 4.3.10c) do not show the peak and flat regimes of the evaporation rates because the soil temperature (Fig. 4.3.12c) reaches a maximum of only about 301 K, and Fig. 4.3.13b shows that the peak and flat regime occurs at temperatures several degrees warmer.

In summary, the diurnal cycle of evaporation in the PLACE model is seen to occur in three stages. In the early morning the evaporation rates increase at the potential rate (stage 1). At some point some of the soil levels reach their threshold evaporation rates. At this point plant storage begins to be depleted, so that the net evaporation rate continues to increase at the potential rate (stage 2). Finally, when plant storage is depleted, the total evaporation rate returns back to the threshold value (stage 3).

Next, we turn to the question of how the inclusion of sub-grid soil moisture variability may alter the diurnal cycle of evaporation in the model. Figure 4.3.14 shows the results obtained with the GUI for evaporation rates as a function of soil moisture (panels a and b), and as function of the standard deviation of soil moisture (panels c and d). The latter are calculated for conditions similar as those at 18 UTC in the 3-D MM5-PLACE model results. In each panel

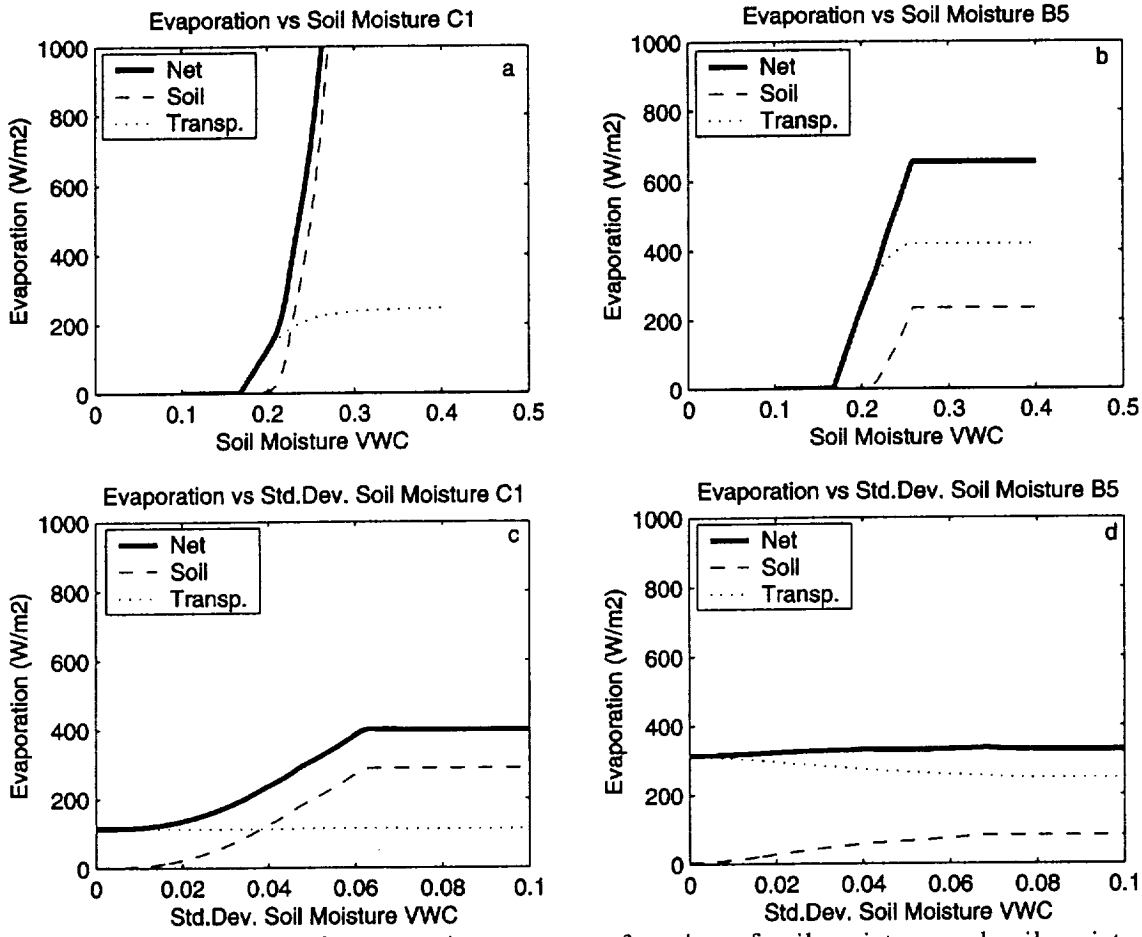

Figure 4.3.14 Computed evaporation rates as a function of soil moisture and soil moisture variability. a) Conditions like in point C1, abscissa is soil moisture, b) as a) but for B5, c) conditions like in point B5, abscissa is standard deviation of soil moisture, d) as c) but for B5.

we plot the total evaporation rate as a bold line along with the fractions from soil versus vegetation. Soil and vegetation evaporations have a very different sensitivity to soil moisture. Soil evaporation increases rapidly, while vegetation evaporation increases a little bit slower. Depending on the shape of the curves in panels a) and b), the inclusion of soil moisture variability can produce an increase, a decrease or not greatly affect the evaporation rates for soil and vegetation. Analysis of panels c) and d) shows that for conditions similar to point C1 the inclusion of soil moisture variability greatly increases evaporation from soil, but it hardly changes the vegetation evaporation. For point B5 the effects in soil and vegetation evaporations have different signs and therefore the total evaporation is little affected by inclusion of soil moisture variability. These results explain the differences in the latent heat fluxes shown in Fig. 4.3.10.

4.3.4.4 Methodology to Define Subgrid Soil Moisture Heterogeneity

Subgrid heterogeneity is addressed in PLACE either through mosaic tiling, where each model grid cell is divided into smaller tiles for flux calculations, and then a composite flux is computed for the grid cell, or a statistical specification of the variability is performed. Either methodology or both can be used. We use the latter statistical methodology. In order to define realistic subgrid soil moisture heterogeneity statistics within the 3-D MM5-PLACE model run that included its effects (Run04s4), we used high-resolution soil moisture data available from ESTAR measurements for some days of July 1997 during SGP97. Figure 4.3.15 shows scatter plots of the standard deviation of soil moisture versus mean soil moisture for 36 X 36 km and 12 X 12 km averages. Based on the 36-km panel (Fig. 4.3.15a) we assigned for our 36-km MM5-PLACE work a maximum standard deviation of 0.10 and a coefficient of variation of 0.33

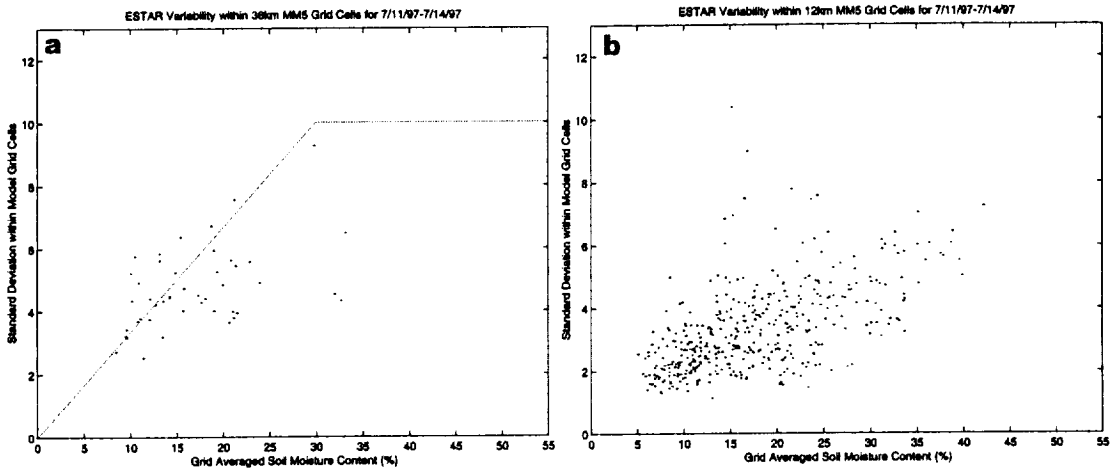

Figure 4.3.15 Soil moisture variability as derived from ESTAR data. Abscissa is mean soil moisture and ordinate is standard deviation of soil moisture. a) for 36x36 km^2 averages, b) for 12x12 km^2 averages.

defined from the slope of the pattern; that is, the standard deviation divided by the mean, as defined in Wetzel and Chang (1988).

The effects of including subgrid variability in the soil moisture are assessed in Figs. 4.3.16 and 4.3.17. In the first we show histograms for latent heat fluxes at 18 UTC calculated over the grid points covering Kansas and Oklahoma. Panels a and b show results for total evaporation rates for the run without soil moisture variability and the one with it, respectively. When subgrid variability is not considered the histograms have a double peak structure, with maxima at lower and higher values of fluxes.

Inclusion of variability reduces the peak at low values. Panels c and d shows the respective histograms for soil evaporation and panels e and f do the same for evaporation from vegetation. In both cases the frequency of very small fluxes is decreased, especially for soil evaporation. The corresponding histograms for sensible heat fluxes (Fig. 4.3.17) show a similar behavior. A double peak structure is present when no soil moisture sub-grid variability is considered and the histogram is more unimodal histogram as sub-grid variability is included.

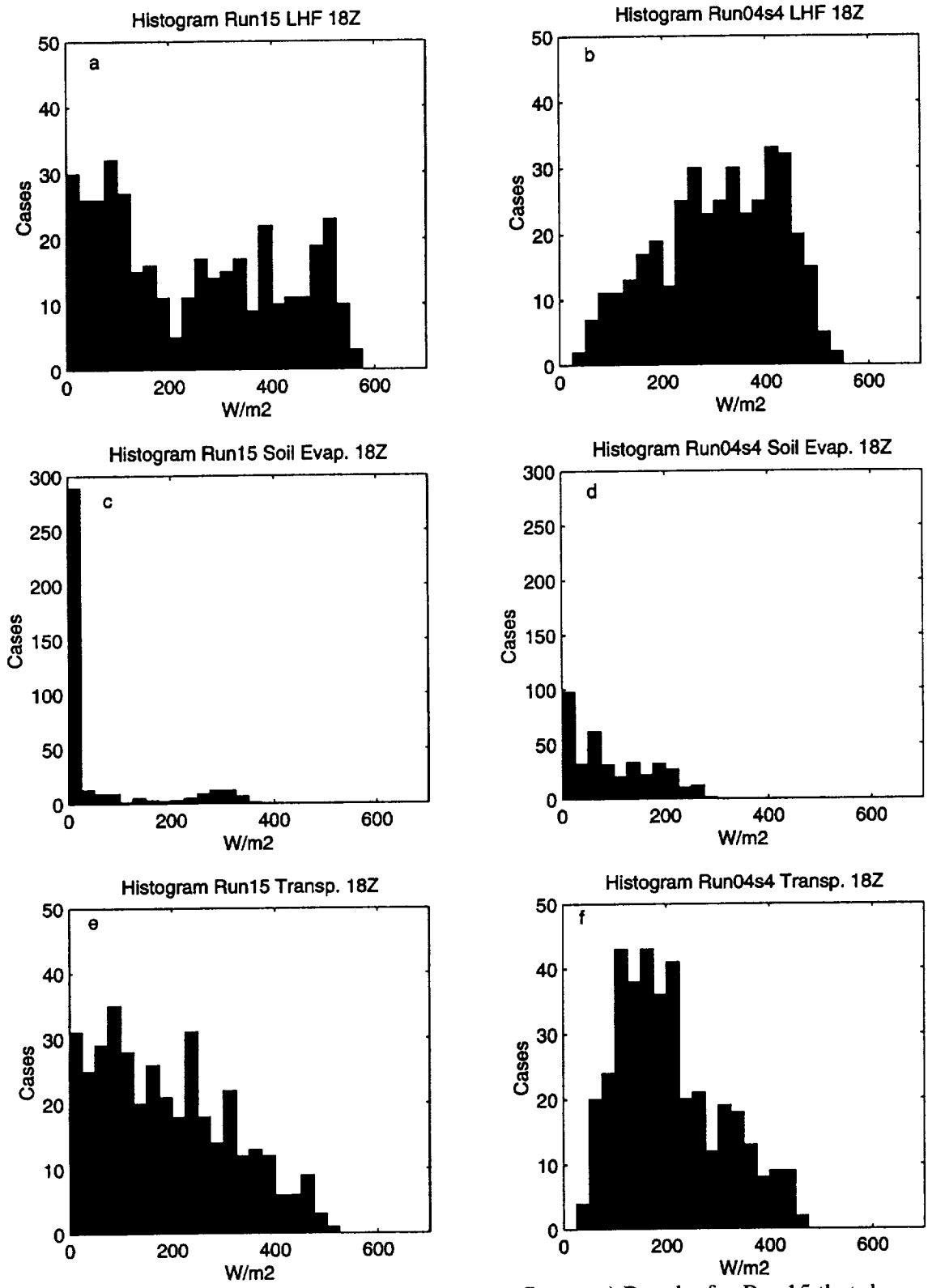

Figure 4.3.16 Histograms of modeled latent heat fluxes. a) Results for Run15 that does not include soil moisture variability, b) as a) for Run14s4 that includes soil moisture variability, c) as a) but for evaporation of soil, d) as b) but for evaporation of soil, e) as c) but for evaporation from plants, f) as d) but for evaporation from plants.

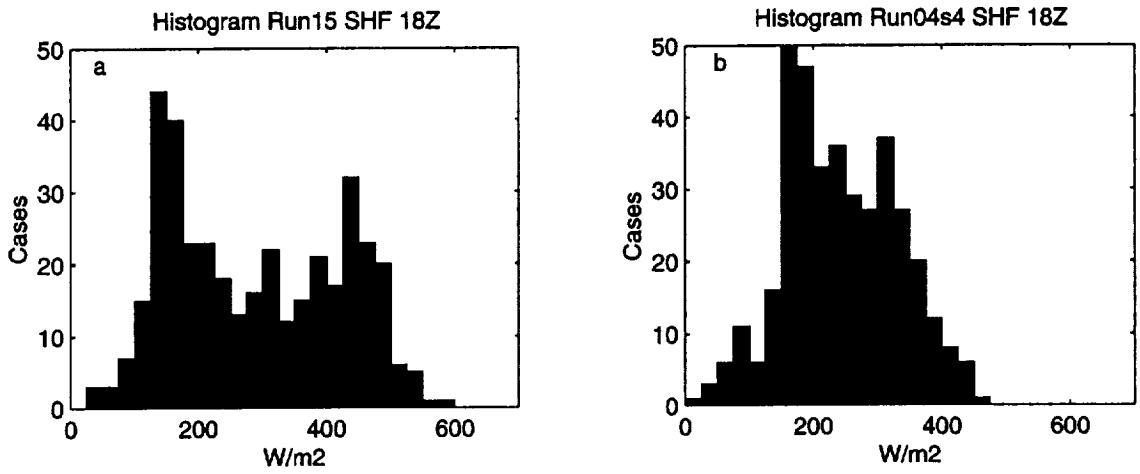

Figure 4.3.17 Histograms of modeled sensible heat fluxes. a) results for Run15 that does not include soil moisture variability, b) as a) for Run14s4 that includes soil-moisture variability maxima at lower and higher values of fluxes.

5. SUMMARY

The **objective** of this investigation has been to study the role of shallow convection on the regional water cycle of the Mississippi and Little Washita Basins of the Southern Great Plains (SGP) using a 3-D mesoscale model, the PSU/NCAR MM5. The underlying premise of the project was that current modeling of regional-scale climate and moisture cycles over the continents is deficient without adequate treatment of shallow convection.

At the beginning of the study, it was hypothesized that an improved treatment of the regional water cycle can be achieved by using a 3-D mesoscale numerical model having high-quality parameterizations for the key physical processes controlling the water cycle. These included a detailed land-surface parameterization (the Parameterization for Land-Atmosphere-Cloud Exchange [PLACE] sub-model of Wetzel and Boone, 1995), an advanced boundary-layer parameterization (the 1.5-order turbulent kinetic energy [TKE] predictive scheme of Shafran et al., 2000), and a more complete shallow convection parameterization (the hybrid-closure scheme of Deng et al., 2002a,b) than are available in most current models. PLACE is a product of researchers working at NASA's Goddard Center in Greenbelt, MD. The TKE and shallow-convection schemes are the result of model development at Penn State.

The work conducted in this study provided the first insertion of the PLACE scheme into the MM5v3 model (the latest version of the MM5). It was found through extensive testing in 3-D and 1-D frameworks that the PLACE land-surface scheme performed at about the same level of accuracy as other land-surface schemes used to represent the surface fluxes over the Great Plains in normal operations. In some cases, PLACE was able to perform better than alternative schemes. However, in many situations, it was found that a more simple land-surface contained

in the Blackadar boundary layer parameterization (Zhang and Anthes 1982), known as the Blackadar slab scheme, generally provided about the same level of skill or better. Thus, while the results of MM5-PLACE simulations were as good or better than any others known to be done with PLACE, it proved difficult to show an overall clear advantage when PLACE is used.

The underlying reason for this result is attributed mostly to the uncertainty involved in defining many of the key soil and vegetation parameters that must be defined in order to run PLACE. Even with the best soil-characteristic data sets currently available, such as the STATSGO data base, PLACE produced soil-moisture evolutions that did not always agree well with soil-moisture measurements over the Great Plains. Work is currently underway at Penn State to evaluate MM5-PLACE during July 1997 using ESTAR soil moisture and NDVI-based leaf-area index and vegetation fraction.

The 1.5-order TKE-predicting turbulence scheme of Shafran et al. (2000) worked reasonably well in dry (unsaturated) conditions, but was found to have deficiencies in saturated layers. A reformulation was introduced that now accounts for the effects of saturation on the calculations in the buoyancy-production term of the turbulent kinetic energy equation, and the stability parameters and turbulent length scales. This saturation dependency is missing in many current numerical models. The change allows the turbulence sub-model to generate more intense mixing in clouds, especially near cloud tops where the longwave radiative flux divergence leads can cause intense cooling. The consequence of this improvement is a more realistic thermodynamic and moisture structure in cloudy regions and better representation of fog layers.

Extensive evaluations and testing of the shallow-cloud parameterization also were conducted in the course of this investigation. It was found that this convection sub-model contained several layer-dependent formulations for some key quantities related to the cloud-base

mass flux. In particular, the discrete thickness of the model layers tended to cause a discontinuous behavior of the mass-flux calculations that sometimes led to erratic behavior of the convection scheme. This behavior occurred even for vertical configurations that are considered to be very good for 3-D models (e.g., layer thickness of only ~40 m in the boundary layer and the cloud layer). Further work led to changes in the formulations of the shallow convection scheme so that the dependency on discrete layer thickness was reduced or eliminated. The consequence was that the key quantities of the shallow-convection scheme, including mass flux and detrainment rates, now evolve in a generally smooth manner as the clouds develop and grow. Not only does the reformulation provide a more realistic shallow-cloud structure, but it also makes the evolution of calculated water-budget terms smoother and much easier to interpret.

Following the extensive testing of each individual parameterization, several combined experiments were conducted in the 3-D MM5 using the PLACE or Blackadar Slab land-surface scheme, and the improved versions of the PSU 1.5-order TKE-predicting turbulence scheme and shallow-convection scheme. These experiments showed that the MM5 can produce fairly realistic distributions of shallow convective cloud fields in stratocumulus and fair-weather cumulus (humilis) conditions. Cloud area and liquid water content are reasonable and are within the accuracy expected, given typical uncertainties in the initial atmospheric and soil states. The vertical structure for the resolved-scale temperature and moisture fields in the cloud layer appear to evolve in a generally realistic way, although further testing is required.

An offline PLACE system forced by observations was constructed and refined for this study. This stand-alone version of PLACE appears to produce realistic soil moisture fields useful in initializing the 3-D MM5-PLACE model. We have compared the forcings and the results of the stand-alone PLACE with available data and obtained reasonable results. We also

have carried out a test of improved physical parameterizations in the framework of the MM5v3 mesoscale modeling system. The case chosen was characterized by rather weak synoptic forcing typical of summer conditions over the SGP. This July case presented complex mesoscale variation in convective and surface conditions and therefore posed a considerable challenge to getting realistic modeling results.

Model results obtained with the new shallow convection parameterization scheme in this advanced MM5 system produced realistic spatial patterns of clouds, although cloud amounts appear to be low when compared to satellite derived data. We also examined the effects of parameterized clouds on the vertical structure of the BL and on the radiation forcing at the surface. The preliminary results show physically plausible effects, although more evaluation is needed to better ascertain the quantitative skills of the parameterization. Model results that used improved initialization and modeling approaches for the surface processes, especially soil moisture and vegetation cover, showed that the spatial and temporal structure of moisture in the boundary layer is positively affected by the inclusion of the improved surface treatments. In particular, the model was able develop an east-west gradient in moisture over central Oklahoma that was absent in an experiment using the more standard Slab land-surface scheme. The modeled results, however, suffered from sub-grid convective precipitation that was predicted over Oklahoma, but did not occur. This precipitation, which was a result of the atmospheric initialization, affected in turn evaporation rates in the runs that included the dynamic soil moisture parameterization. When this feedback was eliminated (in effect, eliminating the impact of the faulty initial thermal stability and moisture fields), the soil moisture values produced by the model appeared closer to the observations and the spatial and temporal variation of moisture compares better with observations. Moreover, we have completed a preliminary study of the

effects of considering sub-grid moisture variability in the MM5-PLACE model results. The results of these experiments show that it appears to be necessary to include the sub-grid variability of soil moisture in order to avoid un-realistic diurnal cycles in evaporation rates, at least for the 36-km grid size that we have used.

More analysis of model results is needed to better evaluate these complex parameterization schemes and their interactions. Of special importance appears to be the interaction of sub-grid cloudiness, precipitation, radiation and evaporation parameterizations. Without adequate interaction of these processes in the model, the results can rapidly diverge from the observations. Another point of interest is to determine if the development of a more intense shallow cloud field over Oklahoma in nature had an impact in suppressing the convective precipitation that developed so rapidly in the model solutions.

Due to the extensive development, testing and refinement work related to improving the key parameterizations used in this study, it was impossible to perform as many 3-D experiments with the finished system as were originally intended. We had expected to conduct and evaluate MM5 runs for 1-3 months in the summertime environment in the Southern Great Plains (SGP), but had to restrict the experimentation to two cases in April and July of 1997. Now that the parameterizations have been enhanced, it is recommended that future numerical work be conducted to expand the testing to seasonal time scales so that meaningful water budgets can be calculated over the SGP.

Two major accomplishments were achieved on the basis of the research conducted through this GEWEX/GCIP grant. First, a set of advanced parameterizations designed for the simulation of the physical processes critical to the atmospheric water budget have been

developed, tested and refined. These parameterizations for land/atmosphere exchanges, turbulence, and shallow convection work together smoothly as a unit. They have been evaluated against observations in a variety of situations and show good agreement with measurements and physical expectations. The second accomplishment is that this set of physics, applied in the 3-D MM5, was used to show the impact of shallow convection on the vertical structure of temperature and mixing ratio over the Great Plains. Although there were insufficient time and resources in the current project to complete numerical experiments on the seasonal time scale, as intended, the present work shows a favorable result upon which further studies of regional climate can be based.

6. REFERENCES

Agee, E. M., 1987: Mesoscale cellular convection over the oceans. *Dynamic of Atmospheric Oceans,* **10**, 317-341.

Albrecht, B. A., 1979: A Model of the thermodynamic structure of the trade-wind boundary layer. Part II: Applications. *J. Atmos. Sci.,* **36**, 90-98.

Arakawa, A., and W. H. Schubert, 1974: Interaction of a cumulus cloud ensemble with the large-scale environment, Part I. *J. Atmos. Sci.,* **31**, 674-701.

Ballard, S.P., B.W. Golding and R.N.B. Smith, 1991: Mesoscale model experimental forecasts of the Haar of northeast Scotland. *Mon. Wea. Rev.*, **119**, 2107-2123.

Betts, A.K., 1973: Non-precipitating cumulus convection and its parameterization. *Quart. J. Roy. Meteor. Soc.*, **99**, 178-196.

Betts, A.K., and M. Miller, 1986: A new convective adjustment scheme. Part II: Single column tests using GATE Wave, BOMEX, ATEX and arctic air-mass data sets. *Quart. J. Roy. Meteor. Soc.*, **112**, 693-709.

Deardorff, J.W., 1976: On the entrainment rate of a stratocumulus-topped mixed layer. *Q. J. Roy. Meteor. Soc.*, **102**, 563-582.

Deardorff, J. W., 1980: Cloud top entrainment instability. *J. Atmos. Sci.,* **37**, 131-146.

Deng, A., 1999: A shallow convection parameterization scheme for mesoscale models. Ph. D. Thesis, The Pennsylvania State University, 152 pp.

Deng, A., N. L. Seaman and A. Lario-Gibbs, 2000: A shallow-convection scheme for 3-D regional-scale air-quality applications. 11th Joint Conference on the Applications of Air Pollution Meteorology with the A&WMA, American Meteorological Society, 9-14 January, Long Beach, California, 102-106.

Deng, A., N. L. Seaman and J. S. Kain, 2002a: A shallow-convection parameterization for mesoscale models. Part I: Sub-model description and preliminary applications. Submitted to *J. Atmos. Sci.*, 36 pp.

Deng, A., N. L. Seaman and J. S. Kain, 2002b: A shallow-convection parameterization for mesoscale models. Part II: Verification and sensitivity studies. Submitted to *J. Atmos. Sci.*, 35 pp.

Dickinson, R.E., 1995: Land processes in climate models. *Remote Sens. Environ.*, **51**, 27-38.

Dudhia, J., 1989: Numerical study of convection observed during the winter monsoon experiment using a mesoscale two-dimensional model. *J. Atmos. Sci.,* **46**, 3077-3107.

Dudhia, J., 1993: A non-hydrostatic version of the Penn State/NCAR mesoscale model: Validation tests and simulation of an Atlantic cyclone and cold front. *Mon. Wea. Rev.*, **121**, 1493-1513.

Duynkerke, P.G. and A.G.M. Driedonks, 1987: A model for the turbulent structure of the stratocumulus-topped atmospheric boundary layer. *J. Atmos. Sci.*, **44**, 43-64.

Fritsch, J. M., and C. F. Chappel, 1980: Numerical prediction of convectively driven mesoscale pressure system. Part I: Convective parameterization. *J. Atmos. Sci.*, **37**, 1722-1733.

Gayno, G.A., 1994: Development of a higher-order, fog-producing boundary layer model suitable for use in numerical weather prediction. M.S. Thesis, The Pennsylvania State University, Dept. of Meteorology, 104 pp.

Gayno, G.A., N.L. Seaman, A.M. Lario and D.R. Stauffer, 1994: Forecasting visibility using a 1.5-order closure boundary layer scheme in a 12-km non-hydrostatic model. Preprints, Tenth Conference on Num. Wea. Pred., Portland, OR, July 18-22, 18-20.

Grell, G.A., J. Dudhia and D.R. Stauffer, 1994: A description of the fifth-generation Penn State/NCAR Mesoscale Model (MM5). NCAR Tech. Note, NCAR/TN-398+STR, 122 pp.

Jackson, T. J., D. M. Le Vine, A. Y. Hsu, A. Oldak, P. J. Starks, C. T. Swift, J. D. Isham, and M. Haken, 1994: Soil moisture mapping at regional scales using microwave radiometry: The Southern Great Plains Experiment. *IEEE Trans. Geosci. Remote Sensing*, **37**, 2136-2151.

Kain, J. S., and J. M. Fritsch, 1990: A one-dimensional entraining/detraining plume model and its application in convective parameterization. *J. Atmos. Sci.*, **47**, 2784-2802.

Kain, J. S., and J. M. Fritsch, 1993: Convective parameterization in mesoscale models: the Kain-Fritsch scheme. *In the representation of cumulus convection in numerical models, A.M.S. Monograph, K.A. Emanuel, and D. J. Raymond, EDS.*, 165-170.

MacVean, M. K., and P. J. Mason, 1990: Cloud-top entrainment instability through small-scale mixing and its parameterization in numerical models. *J. Atmos. Sci.*, **47**, 1012-1030.

Mellor, B.L. and T. Yamada, 1974: A hierarchy of turbulence closure models for planetary boundary layers. *J. Atmos. Sci.*, **31**, 1791-1806.

Muñoz, R.C., 2002: Vertical transport by shallow convection over land. Ph.D. Dissertation, The Pennsylvania State University, In preparation.

Muñoz, R.C., D.R. Stauffer and N.L. Seaman, 2000b: Treatment of buoyancy production at a cloudy-clear interface in a TKE model. 14th AMS Symp. on Bound. Layer and Turbulence. Aspen, CO, 7-11 Aug., 62-65.

Muñoz, R.C., N.L. Seaman, D.R. Stauffer and A. Deng, 2001: Modeling the interaction between boundary layer and shallow clouds using a TKE and a shallow convection parameterization. 9th AMS Conf. on Mesoscale Proc.., Ft. Lauderdale, FL, 30 July - 2 Aug., 26-30.

Musson-Genon, L., 1987: Numerical simulation of a fog event with a one dimensional boundary layer model. *Mon. Wea. Rev.*, **115**, 592-607.

Randall, D. A., 1980: Conditional Instability of the First Kind Upside-Down. *J. Atmos. Sci.*, **37**, 125-130.

Reen, B. P., D. R. Stauffer, K. J. Davis, A. R. Desai, and R. J. Dobosy, 2001: On the added value of high-resolution remotely sensed soil moisture data in a mesoscale model. *Ninth Conference on Mesoscale Processes*, American Meteorological Society, in-print.

Schlesinger, R.E., 1984: Effects of the pressure perturbation field in numerical model of unidirectionally sheared thunderstorm convection: Two versus three dimensions. *J. Atmos. Sci.*, **52**, 1571-1587.

Seth, A. and F. Giorgi, 1996: Three-dimensional model study of organized mesoscale circulations induced by vegetation. *J. Geophys. Res., Sec. D*, **101**, 7371-7391.

Shafran, P.C., N.L. Seaman and G.A. Gayno, 2000: Evaluation of numerical predictions of boundary-layer structure during the Lake Michigan Ozone Study (LMOS). *J. Appl. Meteor.*, in press.

Siebesma, A. P., and J. W. M. Cuijpers 1995: Evaluation of parametric assumptions for shallow cumulus. *J. Atmos. Sci.*, **52**, 650-666.

Simpson, J., 1983: Cumulus clouds: Interactions between laboratory experiments and observations as foundations for models. *Mesoscale Meteorology*, D.K. Lilly and T. Gal-Chen, Eds., Reidel, 399-412.

Smith, C. B., M. N. Lakhtakia, W. J. Capehart, and T. N. Carlson, 1994: Initialization of soil water content in regional-scale atmospheric prediction models. *Bull. American Met. Soc.*, **75**, 585-593.

Sommeria, G., and J.W. Deardorff, 1977: Subgrid-scale condensation in models of nonprecipitating clouds. *J. Atmos. Sci.*, **34**, 344-355.

Stauffer, D. R., R. C. Muñoz and N. L. Seaman, 1999: In-cloud turbulence and explicit microphysics in the MM5, Preprints, Ninth PSU/NCAR MM5 modeling System User's Workshop, Boulder, Colorado, 23-24 June, 177-180.

Stull, R. B., 1988: A Introduction to Boundary Layer Meteorology. Kluwer Academic Publishers, 666 pp.

Tiedtke, M., 1989: A comprehensive mass flux scheme of cumulus parameterization in large-scale models. *Mon. Wea. Rev.*, **117**, 1779-1800.

Tiedtke, M., 1993: Representation of clouds in large-scale models. *Mon. Wea. Rev.*, **121**, 3040-3060.

Tripoli, G.J. and W.R Cotton, 1981: The use of ice-liquid potential temperature as a thermodynamic variable in deep atmospheric models. *Mon. Wea. Rev.*, **109**, 1094-1102.

Wetzel, P.J., S. Argentini, and A. Boone, 1996: Role of land surface in controlling daytime cloud amount: Two cases in the GCIP-SW Area. *J. Geophys. Res., Sec. D.*, **101**, 7359-7370.

Wetzel, P.J. and A. Boone, 1995: A parameterization for Land-Atmosphere-Cloud Exchange (PLACE): Documentation and testing of a detailed process model of the partly cloudy boundary layer over heterogeneous land. *J. of Climate*, **8**, 1810-1837.

Wetzel, P.J. and J.-T. Chang, 1988: Evapotranspiration from nonuniform surfaces: a first approach for short-term numerical weather prediction. *Mon. Wea. Rev.*, **116**, 600-621

Wyant, M.C., C.S. Bretherton, H.A. Rand, and D.E. Stevens, 1997: Numerical simulations and a conceptual model of the stratocumulus to trade cumulus transition. *J. Atmos. Sci.*, **54**, 1680-192.

Xu, K., and D. A. Randall, 1996: A semiempirical cloudiness parameterization for use in climate models. *J. Atmos. Sci.*, **53**, 3048-3102.

Yamada, T., 1977: A numerical experiment on pollutant dispersion in a horizontally homogeneous atmospheric boundary layer. *Atmos. Environ.*, **11**, 1015-1024.

Young, G. S., 1987: Mixed layer spectra from aircraft measurements. *J. Atmos. Sci.*, **44**, 1251-1256.

Zhang, D.L and R.A. Anthes, 1982: A high resolution model of the planetary boundary layer: Sensitivity tests and comparisons with SESAME-79 data. *J. Appl. Meteor.*, **21**, 1594-1609.